

UNIVERSITY OF CALGARY

Mapping organic contaminant plumes in groundwater using spontaneous potentials

by

Sarah Forté

A THESIS

SUBMITTED TO THE FACULTY OF GRADUATE STUDIES  
IN PARTIAL FULFILMENT OF THE REQUIREMENTS FOR THE  
DEGREE OF DOCTOR OF PHILOSOPHY

DEPARTMENT OF GEOSCIENCE

CALGARY, ALBERTA

MARCH, 2011

© Sarah Forté 2011



UNIVERSITY OF  
CALGARY

The author of this thesis has granted the University of Calgary a non-exclusive license to reproduce and distribute copies of this thesis to users of the University of Calgary Archives.

Copyright remains with the author.

Theses and dissertations available in the University of Calgary Institutional Repository are solely for the purpose of private study and research. They may not be copied or reproduced, except as permitted by copyright laws, without written authority of the copyright owner. Any commercial use or re-publication is strictly prohibited.

The original Partial Copyright License attesting to these terms and signed by the author of this thesis may be found in the original print version of the thesis, held by the University of Calgary Archives.

Please contact the University of Calgary Archives for further information:

E-mail: [uarc@ucalgary.ca](mailto:uarc@ucalgary.ca)

Telephone: (403) 220-7271

Website: <http://archives.ucalgary.ca>



## **ABSTRACT**

Increased water demands have raised awareness of its importance. One of the challenges facing water resource management is dealing with contaminated groundwater; delineating, characterizing and remediating it. In the last decade, spontaneous potentials have been proposed as a method for delineating degrading organic contaminant plumes in groundwater. A hypothesis proposed that the redox potential gradient due to degradation of contaminants generated an electrical potential gradient that could be measured at the ground surface. This research was undertaken to better understand this phenomenon and find under what conditions it occurs.

Spontaneous potentials are electrical potentials generated by three sources that act simultaneously: electrokinetic, thermoelectric and electrochemical sources. Over contaminant plumes electrochemical sources are those of interest. Thermoelectric sources are negligible unless in geothermal areas, but we hypothesized that electrokinetic potentials could be impacted by contaminants altering sediment surface properties. We built and calibrated a laboratory apparatus to make measurements that allowed us to calculate streaming current coupling coefficients. We tested sediment from hydrocarbon impacted sites with clean and hydrocarbon polluted groundwater and found a measurable though inconsistent effect. Moreover, numerical modelling was used to demonstrate that the impact of these changes on field measurements was negligible.

Spontaneous potential surveys were conducted on two field sites with well characterized degrading hydrocarbon plumes in groundwater. We did not find a correlation between redox conditions and spontaneous potential, even after the electrical measurements were corrected for anthropogenic noise. In order to determine why the expected signal was not seen, we undertook numerical modelling based on coupled fluxes using two hypothesized

types of current: redox and diffusion currents. The only scenarios that produced spontaneous potential anomalies at the ground surface were those using the redox hypothesis with a relatively resistive transition zone and strong Eh gradients. These conditions are paradoxical because they imply low and high reaction rates respectively.

Surface spontaneous potential anomalies do not occur on all sites with degrading contaminant plumes in groundwater. The models currently available cannot explain why SP and redox potentials are correlated on certain sites and further research would be necessary to explain this phenomenon.

## ACKNOWLEDGEMENTS

Help from many people made it possible for me to do this work and I would like to thank them for their assistance.

For many discussions, critical questions and thinking aloud: Larry Bentley.

For access to the field sites and data from the sites: Gord Jesse, Patrick Todd, Scott Eagleson, Jeff Swingler and Renée Bellavance.

For work in the field: Jackie Randell, Jennifer Macdonald, Ian Anderson, Greg Langston, Trevi Lough, Mehran Gharibi, Blake Hiebert, Hadi Samimi, Nathan Green, Amy Perrin, Jordan Frank, Nicole Willson and Charlene Avery.

For work in the laboratory: Michael Nightingale, Farzin Melekani, John Juigalli, Malcolm Bertram, Yves Forté and Jane Simmons.

For the use of their programmes or data: Kevin Hayley, Uli Mayer, Burke Minsley, Doug Oldenburg and André Revil.

For helping me find information in the library: Pat, Claudette, Sandy and Adriana.

For discussions: Dr Swaddle, Maurice Shevalier, Dr. Haslett, Dr Shaw, Kevin Hayley, Dr. Taylor and Len Hills.

For editing: Yves Forté and Len Hills.

For evaluating my work and recommending corrections: Dr. Estella Atekwana, Dr. Angus Chu, Dr. Cathy Ryan and Dr. Patrick Wu.

For financial support: Alberta Ingenuity Fund and National Science and Engineering Research Council.

En dernier lieu je tiens à remercier mes amis, Ann, Adriana, Kevin et Emma, qui rendirent Calgary un lieu plus agréable, et les membres de ma famille, qui par leur amour, support, soins, intérêt et encouragements me permirent de terminer ce projet.

## TABLE OF CONTENTS

<b>Abstract</b> .....	<b>iii</b>
<b>Acknowledgements</b> .....	<b>v</b>
<b>Table of Contents</b> .....	<b>vi</b>
<b>List of Tables</b> .....	<b>xi</b>
<b>List of Figures</b> .....	<b>xiv</b>
<b>List of Symbols</b> .....	<b>xxx</b>
<b>List of Symbols</b> .....	<b>xxx</b>
<b>Epigraph</b> .....	<b>xxxiii</b>
<b>1 Introduction</b> .....	<b>1</b>
<b>1.1 Goals</b> .....	<b>2</b>
<b>1.2 Contributions of this work</b> .....	<b>2</b>
<b>1.3 Layout of thesis</b> .....	<b>3</b>
<b>2 Background</b> .....	<b>5</b>
<b>2.1 Streaming potential</b> .....	<b>6</b>
2.1.1 Surface charges .....	7
2.1.2 Electrical layer models .....	8
2.1.3 Zeta and streaming potentials.....	10
2.1.4 Experimental apparatus .....	15
2.1.4.1 <i>Sample and sample holder</i> .....	15
2.1.4.2 <i>Pressure system</i> .....	17
2.1.4.3 <i>Electrodes</i> .....	18
2.1.4.4 <i>Measurement methods</i> .....	19
2.1.4.5 <i>Auxiliary measurements</i> .....	19
2.1.5 Effect of parameters on streaming potential .....	20
2.1.5.1 <i>Fluid electrical conductivity</i> .....	22
2.1.5.2 <i>pH</i> .....	23
2.1.5.3 <i>Temperature</i> .....	24
2.1.5.4 <i>Water saturation</i> .....	25
2.1.5.5 <i>Grain size, porosity and permeability</i> .....	26

2.1.5.6	<i>Formation factor and clay content</i> .....	29
2.1.6	Coupling coefficients from the field.....	30
2.1.6.1	<i>Effect of water saturation</i> .....	33
2.1.7	Field-lab comparisons.....	33
2.1.8	Streaming current coupling coefficient.....	35
2.1.9	Summary.....	36
<b>2.2</b>	<b>Spontaneous potential of electrochemical origin</b> .....	<b>37</b>
2.2.1	Membrane and diffusion potentials.....	38
2.2.2	Redox potentials and terminology.....	40
2.2.3	SP over ore bodies.....	45
2.2.4	SP over oil fields.....	52
2.2.5	SP over contaminated areas.....	53
2.2.6	Relationship between spontaneous and redox potentials.....	61
2.2.6.1	<i>Stoll, Bigalke &amp; Grabner, 1995</i> .....	62
2.2.6.2	<i>Timm &amp; Möller, 2001</i> .....	63
2.2.6.3	<i>Naudet, Revil &amp; Bottero, 2003</i> .....	64
2.2.6.4	<i>Hamilton, Cameron, McClenaghan &amp; Hall 2004a</i> .....	64
2.2.6.5	<i>Castermant, Mendocça, Revil, Trolard, Bourrié &amp; Linde, 2008</i> .....	65
2.2.6.6	<i>Hamilton &amp; Hattori, 2008</i> .....	66
2.2.6.7	<i>Revil, Trolard, Bourrié, Castermant, Jardani &amp; Mendocça, 2009</i> .....	67
2.2.7	Discussion.....	68
<b>2.3</b>	<b>Quantitative interpretations of spontaneous potentials</b> .....	<b>72</b>
2.3.1	First analytical methods.....	73
2.3.2	Methods based on monopole or dipole distributions.....	74
2.3.2.1	<i>Simple geometric shapes</i> .....	74
2.3.2.2	<i>Anisotropy</i> .....	75
2.3.2.3	<i>Inversion</i> .....	75
2.3.3	Methods based on coupled fluxes.....	82
2.3.3.1	<i>Electrokinetic effect</i> .....	87
2.3.3.2	<i>Thermoelectric effect</i> .....	94
2.3.3.3	<i>Electrochemical effect</i> .....	95
2.3.4	Summary.....	102
<b>3</b>	<b>Finite element forward model</b> .....	<b>105</b>
<b>3.1</b>	<b>Governing equations</b> .....	<b>105</b>

<b>3.2</b>	<b>Implementation.....</b>	<b>109</b>
3.2.1	Meshes.....	110
3.2.2	Construction of matrix equation from governing equations .....	111
3.2.3	Multiple sources .....	114
3.2.4	Source and potential solutions.....	115
3.2.5	Error .....	115
<b>3.3</b>	<b>Electrical source in anisotropic medium.....</b>	<b>116</b>
<b>3.4</b>	<b>Streaming potential through a dam.....</b>	<b>117</b>
<b>3.5</b>	<b>Summary .....</b>	<b>121</b>
<b>4</b>	<b>Laboratory measurements .....</b>	<b>123</b>
<b>4.1</b>	<b>Apparatus for measuring streaming current coupling coefficient .....</b>	<b>124</b>
<b>4.2</b>	<b>Measurement procedures .....</b>	<b>128</b>
4.2.1	Streaming potential coupling coefficient .....	128
4.2.2	Hydraulic conductivity .....	133
4.2.3	Electrical resistivity.....	134
4.2.4	Geochemical measurements.....	136
<b>4.3</b>	<b>Calibration of measurement procedures.....</b>	<b>137</b>
4.3.1	Calibration of electrical measurements.....	137
4.3.2	Calibration of hydraulic conductivity measurements.....	147
4.3.3	Calibration of geochemical measurements .....	148
<b>4.4</b>	<b>Experimental results .....</b>	<b>150</b>
4.4.1	Sample descriptions.....	150
4.4.2	Electrical measurements.....	152
4.4.3	Hydraulic conductivity measurements .....	154
4.4.4	Geochemical measurements.....	154
<b>4.5</b>	<b>Discussion.....</b>	<b>158</b>
4.5.1	Electrical results .....	159
4.5.2	Hydraulic conductivity results .....	160
4.5.3	Geochemical results .....	161
4.5.4	Synthesis.....	161
4.5.5	Streaming current modelling over contaminant sites.....	165
<b>4.6</b>	<b>Summary .....</b>	<b>169</b>
<b>5</b>	<b>Field data.....</b>	<b>171</b>
<b>5.1</b>	<b>Field and processing methods .....</b>	<b>171</b>

5.1.1	Spontaneous potential measurements .....	172
5.1.1.1	<i>Electrodes</i> .....	172
5.1.1.2	<i>SP surveying</i> .....	173
5.1.1.3	<i>Telluric monitoring</i> .....	177
5.1.1.4	<i>Processing</i> .....	179
5.1.1.5	<i>Error</i> .....	180
5.1.2	Resistivity and induced polarization measurements .....	182
5.1.3	Geochemical measurements and sediment sampling.....	183
<b>5.2</b>	<b>RIVER site</b> .....	<b>185</b>
5.2.1	Hydrogeological and geochemical data .....	186
5.2.2	Geophysical data.....	189
5.2.3	RIVER site model .....	194
<b>5.3</b>	<b>KNOLL site</b> .....	<b>198</b>
5.3.1	Hydrogeological and geochemical data .....	199
5.3.2	Geophysical data.....	202
5.3.3	Corrections to spontaneous potential data .....	208
5.3.4	KNOLL site model .....	215
<b>5.4</b>	<b>Discussion</b> .....	<b>221</b>
<b>5.5</b>	<b>Summary</b> .....	<b>226</b>
<b>6</b>	<b>Numerical modelling of electrochemical SP over contaminant plumes</b> .....	<b>227</b>
<b>6.1</b>	<b>Theoretical models</b> .....	<b>227</b>
6.1.1	Diffusion model .....	227
6.1.2	Eh model .....	228
<b>6.2</b>	<b>Data set used</b> .....	<b>231</b>
<b>6.3</b>	<b>Calculation results</b> .....	<b>241</b>
6.3.1	Ten year data with plume and transition zone at water table.....	243
6.3.2	Ten year data with transition zone at water table.....	246
6.3.3	Ten year data with transition zone at plume edge.....	248
6.3.4	Twenty year data with transition zone at plume edge.....	250
6.3.5	Ten year data with transition zone at plume edge and reduced model resistivity.....	252
6.3.6	Ten year data with transition zone at plume edge and anisotropic transition zone resistivity .....	254

6.3.7	Ten year data with transition zone at plume edge and Eh calculated differently .....	256
6.3.8	Ten year data with transition zone all around plume .....	257
6.3.9	Synthesis.....	259
<b>6.4</b>	<b>Discussion.....</b>	<b>265</b>
6.4.1	Interpretation of RIVER and KNOLL site data .....	265
6.4.2	Current density and reaction rate considerations for Eh model .....	266
6.4.3	Mechanisms causing large SP anomalies over contaminant plumes .....	271
6.4.3.1	<i>Electric field anomalies.....</i>	<i>271</i>
6.4.3.2	<i>Current anomalies with electrons as charge carriers.....</i>	<i>272</i>
6.4.3.3	<i>Current anomalies with ions as charge carriers.....</i>	<i>274</i>
<b>6.5</b>	<b>Summary .....</b>	<b>276</b>
<b>7</b>	<b>Closing remarks.....</b>	<b>279</b>
7.1	<b>Principle results .....</b>	<b>279</b>
7.2	<b>Summary .....</b>	<b>281</b>
7.3	<b>Future work .....</b>	<b>282</b>
	<b>References .....</b>	<b>285</b>
	<b>APPENDIX A: Streaming potential coupling coefficient measurements .....</b>	<b>311</b>

## LIST OF TABLES

Table 2.1 Electrokinetic phenomena. All involve the movement of a solid and a liquid relative to each other. This list specifies which parts are stationary and which are in motion. (Dukhin, 1974) .....	10
Table 2.2 Typical values for terms in the streaming potential coupling coefficient equation. There are empty spaces in the table because the formulae for clay-free and clay-rich aquifers have different variables. (Revil et al., 2003).....	15
Table 2.3 Summary of coupling coefficients calculated from field results with a linear model.....	31
Table 2.4 Summary of coupling coefficients calculated from field results with a Fournier model.....	32
Table 2.5 Summary of coupling coefficients measured in both the field and laboratory. The model used for calculating field values is specified. ....	33
Table 2.6 Summary of measured streaming current coupling coefficients.....	36
Table 2.7 Summary of the effect of different parameters on the coupling coefficient measured in the lab. ....	37
Table 2.8 Examples of spontaneous potential surveys over ore bodies.....	46
Table 2.9 Spontaneous potential surveys over environmental targets with positive anomalies. Abbreviations: meas.–measurements, PCE–tetrachloroethylene, conc.–concentration, SVE–soil vapour extraction, IP–induced polarization, TEM–time domain electromagnetics.....	54
Table 2.10 Spontaneous potential surveys over environmental targets with both positive and negative anomalies. Abbreviations: meas.–measurements, SVE–soil vapour extraction, IP–induced polarization, GPR–ground penetrating radar. ....	55
Table 2.11 Spontaneous potential surveys over environmental targets with negative anomalies. Abbreviations: meas.–measurements, SVE–soil vapour extraction, IP–induced polarization, DO–dissolved oxygen, neg.–negative.....	56
Table 2.12 Articles where authors have measured spontaneous and redox potentials at the same locations. Spearman correlation coefficient between redox and SP. Abbreviation: n.s.–not significant at the 95% level, KTB–German Continental Deep Drilling Program.....	62

Table 2.13 Formulations for different driving forces all with the form $f = \phi + CY$ . (Nourbehecht, 1963).....	86
Table 2.14 Studies where the total potential method of calculating streaming potential is applied. ....	90
Table 2.15 Comparison of Nourbehecht's and Sill's methodologies. (modified from Sill, 1983).....	92
Table 2.16 Studies where the current method of calculating streaming potential is applied. .....	93
Table 3.1 Variables for the different SP problems. Abbreviations: $\mathcal{F}$ –Faraday’s constant, $z_i$ – valence of ion $i$ , $D_i^*$ –effective diffusion coefficient of ion $i$ . ....	106
Table 3.2 Properties of different dam regions.....	118
Table 4.1 Dimensions of three cylinders along flow path in end plates. ....	139
Table 4.2 Concentrations of the standards used for the liquid ion chromatograph.....	149
Table 4.3 Surrogates and their recovery for the hydrocarbon analyses. ....	149
Table 4.4 Sample descriptions including mineralogical composition.....	151
Table 4.5 Measurements of sample electrical properties. The x.C sub-samples had clean water and x.P had hydrocarbon polluted water. ....	152
Table 4.6 $C$ values measured for sample KNOLL1.P at different temperatures. ....	153
Table 4.7 Measured hydraulic conductivities. ....	154
Table 4.8 Chemical characteristics of sample fluids measured during experiments. The error associated with pH measurements is 0.01 units. Abbreviations: symbol(–)–not measured. ....	155
Table 4.9 Results of chemical analyses of sample fluids. The error associated with the measurements is 5% Abbreviations: symbol(–)–not measured.....	156
Table 4.10 Hydrocarbon analyses of sample fluids and sediments. Abbreviations: symbol(–)–not measured, n.d.–concentrations below the detection limit. ....	157
Table 4.11 Cation exchange capacity of samples. ....	158
Table 4.12 Compilation of test results for clean and polluted samples. Abbreviations: n.s.–not significant. ....	162
Table 4.13 Properties used for numerical modelling. ....	167

Table 4.14 Range of differences in potential for different tests of scenario 2.....	169
Table 5.1 Statistics of contact resistances for surveys on both sites.....	176
Table 5.2 Statistics of standard deviations of the readings at each station for surveys on both sites. ....	181
Table 5.3 Statistics of electrical resistivity and IP surveys at RIVER site. Abbreviations: res.–resistivity.....	192
Table 5.4 Statistics of electrical resistivity surveys at KNOLL site. Abbreviations: $\rho_a$ –apparent resistivity, Q–quality factor: standard deviation between measurements.....	205
Table 6.1 Toluene biodegradation model domain dimensions. ....	233
Table 6.2 Ionic diffusion coefficients at infinite dilution at 25°C. Values are from Li & Gregory (1974), unless followed by an asterisk, in which case they were estimated from thermodynamic data. Activity coefficients are those calculated by MIN3P for the aquifer.....	236
Table 6.3 Redox potential ranges of different redox couples calculated using the Nernst equation and the 10 year time step data. ....	239
Table 6.4 Description of eight numerical modelling tests to explain motivations for each modification. Abbreviations: T-zone–transition zone, Res.–resistivity, vad.–vadose zone, sat.–saturated zone. ....	242
Table 6.5 Amplitude of sources and potentials for different tests with toluene biodegradation data. The resistive and conductive qualifiers for the Eh models refer to the relative resistivity of the transition zone. Abbreviations: T-zone–transition zone, Res.–resistivity, Surf. SP–SP anomaly at the ground surface, vad.–vadose zone, sat.–saturated zone, D–dipole.....	260
Table 6.6 Compilation of experiments with instances of electrochemical SP where current densities and power densities were reported. Abbreviations: med.–median. ....	267

## LIST OF FIGURES

Figure 2.1 Schematic diagram of ion distribution and potential profile for the Gouy-Chapman model. The whole medium is electrically neutral and since the solid interfaces are negatively charged, the fluid has excess positive ions that are concentrated near the solid interfaces. ....	8
Figure 2.2 Electrical double layer models of ion distributions and potential profiles. A) At the electro-capillary maximum, when the surface has no polarization. B) With negative polarization. C) With positive polarization. Abbreviations: OHP–outer Helmholtz plane, IHP–inner Helmholtz plane. (modified from Grahame, 1947) ..	9
Figure 2.3 Summary of electrical double layer with shear/slipping plane indicated. Fluid movement is parallel to the mineral surface.(modified from Ogilvy et al., 1989)	11
Figure 2.4 Capillary model of porous media. (Ishido & Mizutani, 1981) .....	12
Figure 2.5 Different pressure systems. A: Constant head reservoirs at different heights (Ahmad, 1964) B: Membrane on side of reservoir vibrated using loudspeaker (Pengra et al., 1999) C: Air tight water reservoirs into which gas can be injected (Ishido & Mizutani, 1981).....	17
Figure 2.6 Streaming potential measured by running water through a fissure with a variable opening width (d). (Bogolovsky & Ogilvy, 1972) .....	21
Figure 2.7 Effect of fluid conductivity on the coupling coefficient.....	22
Figure 2.8 Effect of pH on coupling coefficient. ....	23
Figure 2.9 Effect of temperature on coupling coefficient. ....	24
Figure 2.10 Effect of water saturation on coupling coefficient.....	25
Figure 2.11 Effect of grain size on coupling coefficient.....	26
Figure 2.12 Effect of porosity on coupling coefficient. ....	27
Figure 2.13 Effect of permeability on coupling coefficient. ....	28
Figure 2.14 Effect of formation factor on coupling coefficient. ....	29
Figure 2.15 Effect of clay content of coupling coefficient. ....	30

Figure 2.16 Field results plotted with all laboratory results. Diamonds: $C'$ calculated with Fournier model. Triangles: $C'$ values calculated with linear model. Lab results are those in Figure 2.7.....	34
Figure 2.17 Electrolytic and voltaic cells. (modified from Seese & Daub, 1981; Hess, 1984).....	42
Figure 2.18 The relationship between calculated Eh and carbon-14 age of groundwater samples. The Eh values of different redox couples are based on measured concentrations of the individual oxidation state of a given element. The carbon-14 age gives an indication of the water age. (Stefánsson et al., 2005) .....	43
Figure 2.19 Redox data recorded by a platinum sensor in reference to an Ag/AgCl electrode in the KTB (German Continental Deep Drilling Program) pilot hole. (Stoll et al., 1995).....	44
Figure 2.20 Laboratory measurements of: a) redox potential (RP), b) electric potential (EP), and c) total potential (TP) of various solutions filled in tubes fixed to various hand specimen of rock. (Timm & Möller, 2001) The electrodes with a black tip are platinum electrodes whereas those with a line in the centre are Ag/AgCl electrodes. ....	45
Figure 2.21 Sketch of geo-battery set up. ....	48
Figure 2.22 Proposed electrochemical mechanism for self-potentials. (from Sato & Mooney, 1960).....	49
Figure 2.23 a) Down hole SP in hole 65 intersecting the Kimheden ore body, Sweden. Redrawn from Parasnis (1970). (Corry, 1985) b) SP and litho-logs of borehole MUL-16A. (Rao et al., 2000).....	51
Figure 2.24 Equipotential lines on both blocks are SP contours in mV measured at the ground surface. a) Distribution of electrotelluric currents generated by an oil field before drilling and its associated self-potential sink at the surface of the ground as delineated by equipotential lines with possible disturbances by pipelines. b) Effect of electrotelluric currents on the SP curves of the wells drilled in and around an accumulation of oil and on the radioactivity of shale beds. (Pirson, 1981).....	52
Figure 2.25 Redox potential measured with an error of $\pm 50$ mV versus the residual self-potential estimated with an error of $\pm 20$ mV. Data point #15 is excluded from the slope calculation. (Naudet et al., 2003).....	59

Figure 2.26 Sketch of two possible electron transfer mechanisms in a contaminant plume. a) In model I, the presence of minerals facilitates electronic conduction. b) In model II, only bacteria populations are connected by conductive pili. At the “bacterial anode”, electrons are gained through the oxidation of the organic matter, iron oxides or Fe-bearing phyllosilicates. The electrons are conveyed to the “bacterial cathode” through a network of pili. At the “bacterial cathode”, the reduction of oxygen and the nitrate prevails as electron acceptors. In this system, bacteria act as catalysts. The transport of electrons through the anode to the cathode of the microbattery may involve different bacterial communities and different electron transfer mechanisms including external electron shuttles. (Revil et al., 2010)..... 60

Figure 2.27 Scatter plot of data obtained from Stoll et al. (1995). The data show anti-correlation between Eh and SP..... 63

Figure 2.28 Scatter plot of data obtained from Timm & Möller (2001). ..... 63

Figure 2.29 Scatter plot presented by Naudet et al. (2003)..... 64

Figure 2.30 Scatter plot of data obtained from Hamilton et al. (2004a). ..... 65

Figure 2.31 Scatter plot of data from Castermant et al. (2008)..... 66

Figure 2.32 Scatter plot of data obtained from Hamilton & Hattori (2008). ..... 67

Figure 2.33 Scatter plot of data obtained from Revil et al. (2009) ..... 67

Figure 2.34 Sketch of the different redox zones in groundwater due to a landfill leachate plume. Above the ground surface the set-up for an SP survey is illustrated, and both electrodes are located in the vadose zone, which will have a relatively uniform Eh..... 70

Figure 2.35 Data fit for three iterations of the compact source solution with the 1D resistivity structure. Note the rough fit for the first iteration, which has strong smoothness constraint to avoid near-surface artifacts due to the noisy data. This constraint is relaxed in later iterations, which is evident by the improved data fit. (Minsley et al., 2007b) ..... 78

Figure 2.36 Example of the application of the self-potential 3D tomography in the volcanological area of the Mt. Somma-Vesuvius (Naples, Italy) for the configuration of the volcano venting system. The topmost horizontal slice shows the anomaly map of the self-potential field in mV. The following horizontal slices show the results of the 3D tomography at increasing depths from ground level.

	The bottom colour scale gives the range for the charge occurrence probability values. (Patella, 1997a).....	80
Figure 2.37	SP data along a profile across the Vulcarolo fissure (around $x = 22$ ). The calculated wavelet transform (with $\gamma = 2$ ) exhibits maximum in the space-altitude domain above the fracture area (see the centre contour at 45 mV and the line of modulus maxima. Data from Aubert (1999). (Sailhac & Marquis, 2001).....	82
Figure 2.38	a) Cross-section of the southern limit of the axial graben according to the resistivity sounding data. The vertical columns represent the resistivity sounding log, figures inside them indicate the true resistivity in $\Omega\text{m}$ , and the zone of crosses corresponds to the bedrock. b) Proposed model for computations. The striped zone corresponds to the saturated zone of the volcanic aquifer. c) Two measured SP profiles and the theoretical curve obtained from the model of b) with $C' = 1.25$ mV/m. (Fournier, 1989).....	89
Figure 2.39	a) Physical properties used to model the data at Red Hill. Symbols: $\rho_T$ —thermal resistivity, $C$ —voltage coupling coefficient, $\rho$ —electrical resistivity. b) Comparison of the observed and calculated temperatures at Red Hill. c) Comparison of the observed and modelled SP anomaly at Red Hill. (Sill, 1983).94	94
Figure 2.40	A) Schematic circuit for the galvanic corrosion of sulphides showing the current flow. B) The same corrosion cell showing the resistances. $R_1$ is the resistance to electronic current flow within the sulphides; $R_3$ is the resistance to charge transport by ionic flow in the electrolyte fluids contained within the rocks; $R_4$ represents the kinetic parameters controlling the anodic oxidation processes taking place at the corrosion interface between sulphide and electrolyte; and $R_2$ similarly represents the kinetic parameters controlling the reducing processes taking place on the cathodic interface between sulphide and electrolyte. (Thornber, 1975b).....	97
Figure 2.41	Measured (meas.) and calculated (calc.) SP and Redox potential data in relation to the geology. a) Measured and calculated distribution of redox potential. b) Geological settings after Hirschmann (1993). c) Measured and calculated borehole data. d) Measured and calculated surface data. (Stoll et al., 1995).....	99
Figure 2.42	a) Measured self-potential anomaly (full circles) and theoretical anomalies provided by the inert electrode model with electrode resistance of 1, 5, 10, and 15 $\Omega$ . b) Distribution of the redox potential obtained from self-potential current sources and the distribution of the measured redox potential. We assume $\sigma =$	

0.0025 S m <sup>-1</sup> (400 Ωm) for the conductivity of the crust coating the iron bar. (Castermant et al., 2008).....	100
Figure 3.1 Example of rectilinear structured grid. One element is divided into six tetrahedra, the shape used for finite element modelling.....	110
Figure 3.2 Comparison of electrical potential calculated with analytical (solid line) and numerical (dotted line) methods. Different panels are sections through the centre of the model domain for the isotropic (TOP) and z anisotropy (BOTTOM) cases. The source is located at 0,0 in each panel. ....	117
Figure 3.3 TOP: Cross-section of dam with different regions for hypothetical problem. BOTTOM: hydraulic head distribution through dam. ....	118
Figure 3.4 Comparison of potentials calculated with two methods for the hypothetical dam model. All cross-sections and profiles are through the centre of the dam at y=50 m. The solid and dashed black lines in the top two panels are the locations of the profiles found in the bottom two panels. TOP: Cross section of potentials calculated with SP3D. TOP CENTRE: Cross-section of potentials calculated with finite element programme. BOTTOM CENTRE: profile through cross-section at 5 m elevation. BOTTOM: profile along top of dam. ....	120
Figure 4.1 Apparatus consisting of a PVC cylinder and two end plates. The end plates are held in place by long bolts.....	125
Figure 4.2 End plates. On the right plate semi-transparent cylinders have been added to illustrate the hollow chamber and its three ports.....	126
Figure 4.3 PVC cylinder with stainless steel discs for resistivity measurements. Discs are held in place with silicone. ....	127
Figure 4.4 Support for packing the sample with the ram. LEFT: Set up for packing the sample. RIGHT: Close-up of ram. ....	129
Figure 4.5 Methods of pushing fluid through the sample. LEFT: Compressed air is brought from the bench to the valve, at the front of the image, which controls which reservoir the air is sent to. RIGHT: See-saw to balance the reservoirs, operated using a string attached to the cross bar in two places. Abbreviations: DAQ–data acquisition device. ....	131
Figure 4.6 Bias resistor set-up for reducing noise in potential measured between two electrodes. Abbreviations: DAQ–data acquisition device. ....	132
Figure 4.7 Set-up for falling head hydraulic conductivity test.....	133

Figure 4.8 LEFT: Sketch of set-up to measure sample resistivity. RIGHT: Equivalent circuit diagram. Abbreviations: DAQ–data acquisition device.....	135
Figure 4.9 Test comparing copper (Cu) and Ag/AgCl electrodes with a box waveform of 0.1 Hz frequency and 0.5 mV amplitude. LEFT: Entire test. RIGHT: Close up of one second during the test.....	138
Figure 4.10 Laboratory set-up used to measure voltages. LEFT: Cartoon sketch. MIDDLE: Equivalent circuit diagram. RIGHT: Cross-section of end plate. White areas are hollow and filled with fluid. Three coloured rectangles are drawn to show cylinders used for resistance calculations. Abbreviations: DAQ–data acquisition device.....	139
Figure 4.11 Pressure sensor calibrations using water columns of known height. Linear regressions used for conversions are noted on the graphs. ....	141
Figure 4.12 Streaming potential coupling coefficient data for sample RIVER1.C. LEFT: Data for the whole test. MIDDLE: Close up of data used to determine $C$ . RIGHT: Cross-plot of $\Delta V$ vs. $\Delta P$ from the middle panel, used to calculate the ratio.....	143
Figure 4.13 Streaming potential coupling coefficient data for empty apparatus. The three panels are as described in Figure 4.12. ....	143
Figure 4.14 Calibrating resistivity measurements with three solutions of known resistivity. The thickness of the 'EC probe' line encompasses the error in this measurement. ....	146
Figure 4.15 Comparison of measured $C$ values (+) with those from literature (o). The values are plotted against fluid conductivity since this is the most important controlling factor.....	159
Figure 4.16 Comparison of measured $L'$ values with those from literature. The data are shown as crosses on box-and-whisker plots. The averages of each measurement series are shown as thick coloured lines at the right side of the plots so they can be compared.....	160
Figure 4.17 Compilation of most coherent lab results as compiled in Table 4.12 for six samples tested. Outlined circles (○) are for clean sub-samples and filled circles (●) are for polluted sub-samples. Vertical bars indicate error associated with each measurement and pairs circled with dotted lines are clean and polluted sub-samples where measurements are the same within error. ....	163

Figure 4.18 Change in electrical properties after addition of hydrocarbons. The bars represent the possible ranges given the errors and the black horizontal line at the centre of each bar is the percentage change using measured values. .... 163

Figure 4.19 Hypothetical model used for investigating the effect of contaminants on streaming potential. LEFT: Topography of model and extent of contaminant plume. RIGHT: Model cross-sections with different zones and hydraulic head contours (1 m spacing). Ten of the hydraulic head contours in scenario 2 are so close together that they appear as a thick black bar. .... 166

Figure 4.20 Streaming potentials calculated at the surface of hypothetical model drawn in Figure 4.19 for scenario 1. LEFT: No plume. MIDDLE: With plume, thick white line outlines plume extent. RIGHT: Difference of left panel minus centre panel, thick white line outlines plume extent..... 168

Figure 4.21 Streaming potentials calculated at the surface of hypothetical model drawn in Figure 4.19 for scenario 2. LEFT: No plume. MIDDLE: With plume, thick white line outlines plume extent. RIGHT: Difference of left panel minus centre panel, thick white line outlines plume extent..... 169

Figure 5.1 Copper-copper sulphate electrodes used for SP surveying. An assembled electrode is in the centre and the top and bottom are on either side. The ceramic on the bottom piece on the right is stained green by copper sulphate..... 172

Figure 5.2 Variation in electrode potential caused by watering of copper-copper sulphate electrodes, Raft River, Idaho. Electrode separation was 200 m. (Corwin & Hoover, 1979)..... 174

Figure 5.3 Repeated SP measurements along a survey line. For “no clay” measurements the electrodes were directly in contact with the soil. For “with clay” measurements the electrodes were set in holes filled with salted bentonite. Measurements series were made 16 days apart. .... 175

Figure 5.4 Histograms of contact resistances for surveys on both sites..... 175

Figure 5.5 Potential readings made after an electrode is set into the ground. The period of high drift during the first hour is due to the electrode equilibrating with the ground..... 176

Figure 5.6 Base station set-up for telluric monitoring. The electrode in the NW corner serves for both dipoles. This is done by using a jumper wire at the data logger. 178

Figure 5.7 Telluric monitoring record for October 2 <sup>nd</sup> , 2006 at the KNOLL site. Each dipole has $\pm 0.5$ mV high frequency chatter due to noise and a lower frequency signal from telluric current variations is visible as a trend. In the north-south dipole the variation is a 2 mV rise over the course of the day followed by a 1 mV decrease at the end of the afternoon.....	179
Figure 5.8 Example of drift corrections applied to SP measurements. TOP: Potential measured at tie location at different times. BOTTOM: Raw measurements made between tie point readings and the same measurements with corrections applied. ....	179
Figure 5.9 Histograms of standard deviations of the readings at each station for surveys on both sites. ....	180
Figure 5.10 Repeat measurements at three stations every fortnight. The boxes around the central points are the standard deviation of the readings and the error bars are $\pm 5$ mV. The readings at the 10 and 30 m stations are the same within error whereas at the 50 m station the measurements from 13.10.06 and 27.10.06 do not overlap.	181
Figure 5.11 Timing of resistivity and induced polarization (IP) measurements with respect to current injection and potential produced.....	182
Figure 5.12 Variations of groundwater field parameters with depth for six wells at the RIVER site. The different colours for the profiles represent different wells.....	184
Figure 5.13 Topographical map of the RIVER site. Elevation contours are every metre. The black dots are data locations used to make the contour map. ....	186
Figure 5.14 Groundwater elevation maps for four seasons of 2005. Elevation contours are every half metre. The black dots are data locations used to make the countour maps. ....	187
Figure 5.15 Chromatographs of hydrocarbons found on the RIVER site. LEFT: Free phase. RIGHT: Dissolved phase. The distinct peaks at 9.5 and 14.5 are surrogates used for quality control. (EBA Engineering Consultants Ltd., 2006) .....	187
Figure 5.16 Free phase petroleum hydrocarbon thickness maps for four seasons of 2005. The black dots are data locations used to make the countour map. ....	188
Figure 5.17 June 2006 data for RIVER site. LEFT: Groundwater elevation map with contours are every half metre. The black dots are data locations used to make the countour map. RIGHT: Hydrocarbon distribution and redox potentials measured	

in wells. A dashed line is drawn around the edge of the plume. The red markers indicate where our geophysical work was done.....	189
Figure 5.18 Spontaneous potential measurements at RIVER site.....	190
Figure 5.19 High frequency (6000 Hz) measurements of transient voltages and spectral analyses for locations C (TOP) and G (BOTTOM). LEFT: Time series data showing the sum of a high frequency signal and a lower frequency one. RIGHT: Periodograms to show the dominant signal frequencies. ....	191
Figure 5.20 Electrical resistivity and IP inversion results for three of the lines at the RIVER site. The warm coloured bodies on the resistivity profiles are continuous and coherent within each profile but cannot be mapped between profiles. The chargeability values are generally low with an exception at 115 m and possibly something at 10 m though the second anomaly is poorly constrained because of sparse data. The small location maps on the left highlight the line corresponding to the presented data. ....	193
Figure 5.21 Interpreted resistivity sections for the RIVER site with the water table and well logs. The small location maps on the left highlight the line corresponding to the presented data. ....	195
Figure 5.22 Picture of flare stack and pit at KNOLL site. ....	198
Figure 5.23 Topography and infrastructure at the KNOLL site. Elevation contours are every metre. Only the portions of the pipelines nearest to the plant are drawn though they extend across the whole site. ....	199
Figure 5.24 November 2006 groundwater elevation map with contours every metre for the KNOLL site. ....	200
Figure 5.25 November 2006 hydrocarbon distribution with dissolved oxygen (DO) concentrations measured in wells at the KNOLL site. A thick dashed line is drawn around the edge of the free phase plume and a thin dashed line delineates the dissolved phase plume.....	201
Figure 5.26 Chromatograph of hydrocarbons found at the KNOLL site. (Matrix Solutions Inc., 2006) .....	202
Figure 5.27 Spontaneous potential measurements at the KNOLL site. Small black dots are measurement locations. ....	202
Figure 5.28 Transient voltage measurements and spectral analyses for locations A (TOP) and B (BOTTOM). They were acquired at frequencies of 600 Hz for A and 6000	

Hz for B. LEFT: Time series data showing a sinusoidal signal. The dashed lines are drawn at the average potential, which is equal to the DC values measured in the field. RIGHT: Periodograms to show the dominant signal frequency, 120 Hz. ....	203
Figure 5.29 Location of resistivity lines surveyed at the KNOLL site. Small red diamonds are electrode locations.....	204
Figure 5.30 Electrical resistivity inversion results for lines R01-R08 at the KNOLL site. The warm and green coloured shapes form a continuous body between the profiles with the top at ~945 m. This is overlain by blue coloured material which thickens towards the east (decreasing R numbers) as the ground surface elevation increases. The small location maps on the right highlight the line corresponding to the presented data.....	206
Figure 5.31 Electrical resistivity inversion results for lines R06, R08, R10 and R11 at the KNOLL site. Both R10 and R11 have green coloured bodies with a top ~957 m. The inversion profiles are not deep enough to map bodies from the south lines to the north ones but the dark blue wedge at y = 400 to 425 m on R11 below a warm coloured zone indicates the green and warm coloured bodies in the north are likely distinct from those in the south. The small location maps on the right highlight the line corresponding to the presented data.....	207
Figure 5.32 Electrical resistivity inversion results for line R12 and the line it intersects, R10. The pink rectangles are drawn at the intersection. On both lines there is a green coloured body with a top at ~958 m. The small location maps on the right highlight the line corresponding to the presented data. ....	208
Figure 5.33 Detailed SP survey over and next to a pipeline. If anthropogenic noise from the pipeline was contributing to the measured spontaneous potential, contours would have a NW-SE trend parallel to the pipeline. Instead the contours are N-S, mapping a more regional trend. ....	209
Figure 5.34 Isosurface contours of charge occurrence probability tomogram at the KNOLL site. The south-east corner has been cut out to show the maximum and (310, 440, 935), which has removed the contours of the minimum just east of the map at (470,340,930). ....	210
Figure 5.35 Slices through the source inversion results for the KNOLL site. The N-S slice is drawn through the maximum. The small black dots on the surface of the cube are locations of data points used in inversion. ....	211

Figure 5.36 Location and intensity of the sources used to model the anode bed. The sources are 10-23 m below ground and their surface projections have been included to help locate them relative to the plant fence line..... 212

Figure 5.37 Profiles to demonstrate fit between anode model potential signal and measured SP at the KNOLL site. There is a close fit between measured and modelled SP for the 75 m on either side of the anomaly. SP measured further from the anomaly could have contributions from sources other than the anode bed so a close fit with the model is not necessary..... 213

Figure 5.38 Corrections to the spontaneous potential data for the anode bed at the KNOLL site. Locations of sources for corrections are represented by black triangles. TOP LEFT: SP data measured in the field. TOP RIGHT: SP signature of anode bed created with finite element code. BOTTOM: Residual SP (measured – modelled SP). The dashed lines emphasize inflections in the contour lines that demark the SW corner where data were gathered under wetter field conditions. The dotted line at  $y=75$  m delimits data gathered under colder field conditions, visible by an excursion in the 50 m contour..... 214

Figure 5.39 Electrical resistivity inversion images for four lines in the south with water table and lithologies from logs of nearby wells. The small location maps on the right highlight the line corresponding to the presented data. .... 216

Figure 5.40 Electrical resistivity inversion images for three lines in the north with water table and lithologies from logs of nearby wells. The small location maps on the right highlight the line corresponding to the presented data. .... 217

Figure 5.41 Three dimensional drawing of all the electrical resistivity inversions at the KNOLL site..... 218

Figure 5.42 Streaming potential signature at the KNOLL site, calculated with the finite element code..... 220

Figure 5.43 Chemical data overlain on the residual SP map at the KNOLL site..... 221

Figure 5.44 SP profiles at the RIVER site with information on the contaminants. The vertical rectangles are wells on or near the survey line. The wells drawn in grey had hydrocarbons above the water so redox parameters could not be measured. SP decreases slightly away from the plume. Abbreviations: LNAPL–light non-aqueous phase liquid. .... 223

- Figure 5.45 SP profiles at the KNOLL site with information on the contaminants. The vertical rectangles are wells on or near the survey line. The wells drawn in grey had hydrocarbons above the water so redox parameters could not be measured. Dashed line is measured SP and solid line is SP corrected for the effect of the anode bed. SP increases with distance from the pollutants but as a trend rather than a sharp anomaly. Abbreviations: LNAPL–light non-aqueous phase liquid, DO–dissolved oxygen.....224
- Figure 5.46 Cross-plots of dissolved oxygen in groundwater measured in wells and SP measured next to the wells for both sites studied. ....225
- Figure 6.1 Problem definition for biodegradation problem showing location of contaminant source and flow boundary conditions. (Mayer et al., 2002) This sketch is a cross-section parallel to the groundwater flow direction in the centre of the plume. The horizontal line in the centre of the rectangle represents the water table. Abbreviations:  $q$ –surface recharge,  $h_w$ –height of the water table. ....232
- Figure 6.2 MIN3P simulation data from the 10 year time step of toluene biodegradation. These are cross-sections parallel to the groundwater flow direction through the centre of the plume. The white line is the water table. Above the water table the concentration contours mark an area through which the toluene is percolating below the spill site at a distance of 100 m. Below the water table the concentration contours outline the plume. In the vadose zone all the species apart from carbonate ( $\text{CO}_3^{2-}$ ) have elevated concentrations below the spill site and the contours are stretched to the bottom right under the influence of advection. The carbonate distribution is the opposite with the lowest values at the centre of the plume because initially it is present everywhere and the low pH in the plume transforms it into bicarbonate. The iron hydroxide ( $\text{FeOH}^+$ ) has highest concentrations at the toe of the plume in the bottom right because it is produced by secondary reactions, which are reactions of species such as  $\text{Fe}^{2+}$  produced during the toluene biodegradation.....234
- Figure 6.3 MIN3P simulation data from the 20 year time step of toluene biodegradation. The white line is the water table. For a detailed description of the plume see caption from Figure 6.2. This plume stretches further to the right because the longer period of time has allowed further transport.....235
- Figure 6.4 Resistivity profile for the 10 year time step calculated using Waxman-Smiths equation. The vadose zone appears with resistivities above 700  $\Omega\text{m}$  (yellow to red colours). The exception is below the spill site at a distance of 100 m where the

resistivity is reduced by the high ionic concentrations. In the groundwater the plume is defined by resistivities below 250  $\Omega\text{m}$  (blue colours)..... 238

Figure 6.5 Estimation of redox potential distribution using 10 year time step data of simulated toluene biodegradation. The white line is the water table. The cool colours represent low Eh and reduced redox conditions. TOP: With  $\text{Fe}^{2+}/\text{Fe}^{3+}$  redox couple. The redox calculated with iron has lower Eh values (orange colour) above the water table outside the area impacted by toluene. This is an artefact caused by differences in iron ion concentrations that are on the order of  $10^{-13}$  mol/L. BOTTOM: Combination of  $\text{O}_2/\text{H}_2\text{O}$  couple outside the plume and  $\text{CH}_4/\text{CO}_2$  couple inside the plume..... 239

Figure 6.6 Schematic redox zonation in an originally aerobic aquifer down gradient from a landfill. (Christensen et al., 2001) The zones are defined by the predominant redox reactions. The most reduced zone is to the left (lowest Eh) and it becomes progressively more oxidized to the right..... 240

Figure 6.7 Simulation data from the 10 year time step modified so that the centre of the plume is at the water table. The white line is the water table. For a detailed explanation see caption from Figure 6.2..... 243

Figure 6.8 Position of transition zone for Eh model relative to the plume outline and water table for the modified 10 year data..... 244

Figure 6.9 Source currents calculated with the modified 10 year data. The profiles are maps of the current source in amperes at each node. Both the centre of the plume and the transition zone are at the water table. The sources of the diffusion model (TOP) are throughout the plume where there are strong concentration gradients. The two Eh models (CENTRE and BOTTOM) have sources restricted to the transition zone, which was defined as the elements spanning the water table above the plume..... 245

Figure 6.10 Potentials calculated using the modified 10 year data with the plume centre and transition zone at the water table. The profiles are contour maps of the potential at each node generated by the source currents in Figure 6.9 given a resistivity distribution calculated with the Waxman-Smits equation. The top panel is SP as it would be measured at the surface of the model domain, at 15 m elevation. The three bottom profiles are contour maps of the electrical potential in millivolts at each node. The strongest potentials are found where the sources are. In the diffusion (TOP CENTRE) and Eh model with conductive transition zone

(BOTTOM) the potential anomaly is restricted to the area immediately adjacent to the sources. In the Eh model with resistive transition zone (BOTTOM CENTRE) the potential anomaly spreads further. ....246

Figure 6.11 Position of transition zone for Eh model relative to the plume outline and water table with sources at the water table and normal 10 year data.....247

Figure 6.12 Source currents calculated with the 10 year data and sources at the water table for the three models. ....247

Figure 6.13 Potential generated by the source currents in Figure 6.12, calculated with the 10 year data and sources at the water table for the three models. The top panel is SP as it would be measured at the surface of the model domain.....248

Figure 6.14 Position of transition zone for Eh model relative to the plume outline and water table with sources at plume edge and normal 10 year data.....249

Figure 6.15 Source currents calculated with the 10 year data and sources at the plume edge for the three models.....249

Figure 6.16 Potential generated by the source currents in Figure 6.15, calculated with the 10 year data and sources at the plume edge for the three models. The top panel is SP as it would be measured at the surface of the model domain.....250

Figure 6.17 Source currents calculated with the 20 year data and sources at the plume edge for the three models.....251

Figure 6.18 Potential generated by the source currents in Figure 6.17, calculated with the 20 year data and sources at the plume edge for the three models. The top panel is SP as it would be measured at the surface of the model domain.....252

Figure 6.19 Resistivity profile for the 10 year time step calculated by adding a conductivity of 0.033 S/m to the conductivity calculated using the Waxman-Smits equation.....252

Figure 6.20 Potential generated by the source currents calculated with the 10 year data with reduced resistivity and sources at the plume edge for the three models. The top panel is SP as it would be measured at the surface of the model domain. ....254

Figure 6.21 Resistivity distribution in the z direction for the 10 year time step calculated from using Waxman-Smits equation with a 0.1  $\Omega$ m transition zone added. ....255

Figure 6.22 Potential generated by the source currents calculated with the 10 year data with sources at the plume edge. The top panel is SP as it would be measured at the

surface of the model domain. CENTRE TOP: Resistive transition zone. CENTRE BOTTOM: Conductive transition zone (0.1 $\Omega\text{m}$ ) BOTTOM: Anisotropic resistivity in transition zone (resistive in x and y, 0.1 $\Omega\text{m}$ in z). .....	256
Figure 6.23 Potential generated by the source currents calculated with the 10 year data with sources at the plume edge. The top panel is SP as it would be measured at the surface of the model domain. CENTRE Modelled using Eh calculated with the iron couple. BOTTOM: Modelled using Eh distribution made from a combination of those calculated with oxygen and methane couples. ....	257
Figure 6.24 Position of transition zone for Eh model relative to the plume outline and water table with sources all around the plume and normal 10 year data. ....	258
Figure 6.25 Source currents calculated with the 10 year data with sources at the plume edge and a resistive transition zone. TOP: Modelled using sources just at the top of the plume. BOTTOM: Modelled using sources all around the plume.....	258
Figure 6.26 Potential generated by the source currents in Figure 6.25, calculated with the 10 year data with sources at the plume edge. The top panel is SP as it would be measured at the surface of the model domain. CENTRE Modelled using sources just at the top of the plume. BOTTOM: Modelled using sources all around the plume.....	259
Figure 6.27 SP calculated at the surface for the four tests using the diffusion model. Abbreviations : yr.–year, w.t.–water table, res.–resistivity. ....	261
Figure 6.28 SP calculated at the surface for the seven tests using the Eh model with resistive transition zone. Abbreviations :T-zone–transition zone, yr.–year, w.t.–water table, res.–resistivity. ....	262
Figure 6.29 SP calculated at the surface for the six tests using the Eh model with conductive transition zone. Abbreviations: T-zone–transition zone, yr.–year, w.t.–water table, res.–resistivity. ....	263
Figure 6.30 Effect of changing the model resistivity on the SP anomaly measured at the surface. LEFT: Background conductivity is varied while transition zone is fixed at 10 S/m. The mean conductivity of elements in the transition zone is used as background. MIDDLE: Transition zone conductivity is varied while the background is fixed at 0.0046 S/m. RIGHT: The data of the first two graphs plotted against the transition zone to background conductivity ratio.....	264

Figure 6.31 Magnitude of surface SP anomaly associated with varying current density (LEFT), toluene degradation rate (MIDDLE) and transition zone to background conductivity ratio (RIGHT). The gray boxes are plausible limits from: compiled data (LEFT), an order of magnitude either side of the value reported by Baker et al. (2000) (dashed line) (MIDDLE), and implications of model assumptions (RIGHT).....269

Figure 6.32 SP logs with units of millivolts. The gradual decrease in the response with depth at TH2 from 220 to 200 m is not thought to represent lithological change. The sand-clay boundary is seen as a gradual transition in all cases. Curve a at TH1, measured immediately after drilling was complete, appears to respond to the contaminant plume. Curve b, measured 2 days later, may also respond to the plume but more weakly and over a broader zone. This change in response probably reflects borehole mixing during the intervening time. (Greenhouse & Harris, 1983) This figure is a cross-section through the centre of the plume parallel to the direction of groundwater flow. The stippled area is the contaminant plume, defined as the area enclosed by the 1000  $\mu\text{S}/\text{cm}$  conductivity contour. ...274

## LIST OF SYMBOLS

Variables that use the same symbol are listed together and the correct variable is always identified in the text. Symbols are separated into three alphabetically arranged tables: greek symbols, capital letters and small letters.

### *Greek symbols*

<b>symbol</b>	<b>variable</b>	<b>units</b>
$\beta$	transfer coefficient for overpotential current	–
$\gamma$	activity coefficient	1/mol
$\varepsilon$	dielectric permittivity	F/m
$\zeta$	zeta potential	V
$\eta$	dynamic viscosity	kg/m·s
$\eta$	overpotential	V
$\theta$	volumetric water content	–
$\mu_i$	chemical potential of ion $i$	J/mol
$\xi$	tortuosity factor	–
$\rho$	electrical resistivity	$\Omega\text{m}$
$\rho_w$	fluid density	kg/m <sup>3</sup>
$\sigma_{f,s,b,r}$	electrical conductivity: fluid, surface, bulk, relative	S/m
$\phi$	electrical potential	V
$\varphi$	connected porosity	–
$\Delta V$	difference in electrical potential	V
$\Delta P$	difference in pressure	Pa

*Capital letters*

<b>symbol</b>	<b>variable</b>	<b>units</b>
$C, C', C_{sat}$	streaming potential coupling coefficient, for the field, at saturation	V/Pa ( V/m <sub>H<sub>2</sub>O</sub> )
$C_H$	redox coupling coefficient	–
$D_i, D_i^*$	diffusion coefficient of ion $i$ , effective coefficient	m <sup>2</sup> /s
$E$	electric field	V/m
Eh	redox potential	V
$F, F_0, F_a$	formation factor, in a saturated medium, apparent	–
$\mathcal{F}$	Faraday's constant	A·s/mol <sub>charge</sub>
$I$	ionic strength	mol/kg
$I$	electrical current	A
$J_{q,s,a,c}$	flux of heat: solvent, anions, cations	J/m <sup>2</sup> s, m <sup>3</sup> /m <sup>2</sup> s, mol/m <sup>2</sup> s
$K$	hydraulic conductivity	m/s
$L'$	streaming current coupling coefficient	A/m <sup>2</sup> (= A/m · m <sub>H<sub>2</sub>O</sub> )
$L_{ii,ij}$	primary and cross coupling terms	units variable
$M$	polarization	C/m <sup>2</sup>
$P$	pressure	Pa
$P$	power	W
$\overline{Q}_V$	excess charge per unit pore volume	C/m <sup>3</sup>
$R$	universal gas constant	J/mol·K
$R$	resistance	Ω
$S_w$	water saturation	–
$T$	temperature	K
$V$	potential	V

*Small letters*

<b>symbol</b>	<b>variable</b>	<b>units</b>
$a_i$	activity of ion $i$	(mol/L)
$a, A$	cross-sectional area	$\text{m}^2$
$c_i$	concentration of ion $i$	mol/L
$e^-$	electron	–
$g$	gravitational constant	$\text{m/s}^2$
$g$	specific electrode area	$\text{m}^2$
$h$	hydraulic head	$\text{m}_{\text{H}_2\text{O}}$
$j$	electric current density	$\text{A/m}^2$
$j_0$	exchange current density when system is at equilibrium	$\text{A/m}^2$
$k$	geometric factor	m
$k_b$	Boltzmann's constant	J/K
$k_r$	relative permeability	–
$\ell$	length	m
$m$	electrical cementation exponent	–
$n$	number of electrons	–
$q_i$	charge of species $i$	C
$r$	radius	m
$s_x$	sample standard deviation of $x$	units of $x$
$t$	time	s
$t_i$	Hittorf transport number of ion $i$	–
$\mathbf{u}$	volumetric fluid flux, Darcy velocity	$\text{m/S}$
$u_i$	mobility of ion $i$	$\text{m}^2/\text{V}\cdot\text{s}$
$v$	solution velocity	$\text{m/s}$
$z$	elevation head	m
$z_i$	valence of ion $i$	$\text{mol\_charge/mol\_ion}$

*How sorry the world would be if all the times to come could not find in it questions to tend to.*

Seneca, Natural Questions



## 1 INTRODUCTION

Growing human populations are increasing pressure on water resources everywhere in the world, which has led to an interest in the study and characterization of these resources. This work focuses on a method for delineating and characterizing groundwater contaminant plumes rich in organic carbon, as might be found in landfill leachate or in oil spills. The method studied is spontaneous potential, which has been used in the mineral exploration industry since the 1830s (Fox, 1830), but has only been applied to environmental problems in the last decade (Nyquist & Corry, 2002; Naudet et al., 2003). Currently groundwater plumes are delineated by drilling many wells to determine where the contaminants are, an intrusive and costly procedure. If spontaneous potential mapping on the ground surface could help delineate the polluted zones it would be useful by reducing the number of wells needed, though some wells would be necessary to support the geophysical data.

Spontaneous potentials (SP) are natural electrical potential differences between different locations on the earth's surface or in boreholes. There are three known causes: the electrokinetic, electrochemical and thermoelectric effects. The electrokinetic effect is commonly referred to as streaming potential and occurs when a hydraulic gradient in a liquid filled porous medium creates an electric field. We measure the gradient of the electrical field as electrical potential. The electrochemical effect can be further subdivided into membrane, diffusion and redox potential, and for these cases it is the gradient in ionic concentrations which generate the electrical field. Finally, thermoelectric effects are due to temperature gradients.

SP measurements are easy to make, requiring only two electrodes and a voltmeter, but the data analysis and interpretation are more challenging. Some of the complication stems from the fact there are several sources. Anthropogenic noise can also be problematic because SP is a potential method so the magnitude of the signals are generally very small. The potential method also implies that the inverse problem is always under-determined.

### **1.1 Goals**

This work aims to better understand the processes creating spontaneous potential anomalies over organic carbon rich contaminant plumes in an effort to model them quantitatively and determine under which field conditions they occur. Most of the work with SP done to date is qualitative, and if this method is to be applied more rigorously, as would be necessary for regulatory monitoring, a quantitative approach must be taken. It is understood that organic contaminants in groundwater get degraded by abiotic and biotic reactions and typically a redox zonation will form depending on the dominant reactions. Redox measurements are invasive and difficult to make, so if SP measurements could be used to approximate the redox distributions, they would be helpful in delineating a contaminant plume. This research suggests that contaminant electrochemical sources will only produce SP anomalies in very specific conditions so that the method is not always useful.

### **1.2 Contributions of this work**

This work includes three contributions. First, the impact of hydrocarbon contamination on streaming potential is quantified. When studying SP of electrochemical origin, streaming potentials are considered noise and are modelled and subtracted from the measured signal. Presently this is done assuming that the contaminants do not alter the streaming potential and laboratory tests described here can be used to justify and support this assumption.

Secondly, spontaneous potential surveys on two field sites with degrading hydrocarbon plumes in groundwater are described. These add to the limited number of contaminated field sites where SP measurements and redox conditions are reported and sources of anthropogenic noise have been addressed. Neither site had a significant correlation between SP and redox or had a large negative surface SP anomaly as has been reported on some sites.

Finally, numerical modelling is used to determine the conditions necessary for producing SP anomalies at the ground surface above a degrading plume based on two current

hypotheses explaining electrochemical SP. With the data set used, the diffusion model cannot produce anomalies greater than a few millivolts. This supports what is reported in literature with detailed calculations that include all ions. The redox model, which links spontaneous and redox potentials by assuming electronic current conduction in a transition zone, can only produce significant surface anomalies under specific circumstances: large redox gradients and a relatively resistive transition zone. These two requirements seem at odds with each other because they imply high and low reaction rates respectively, which suggests the redox model may be incorrect.

### 1.3 Layout of thesis

Chapter 2 includes a literature review to introduce past and present work on three aspects: streaming potential, SP of electrochemical origin and quantitative analysis of SP. Data from literature are compiled and different theories are discussed in detail in the section on SP of electrochemical origin as this is the focus of the thesis. Some computer modelling is included in all the areas of this work so the finite element code used for these calculations is introduced and validated in chapter 3.

Laboratory work investigating the effect of hydrocarbon contaminants on streaming potential is presented in chapter 4. An instrument for measuring streaming current coupling coefficient was built and used to measure samples from two field sites. These sites are described in chapter 5 and are both hydrocarbon contaminated sites where SP and resistivity surveys were performed over actively degrading plumes. Neither site showed the negative anomaly expected, as found in some literature examples.

To better understand the causative mechanisms, numerical modelling was used and is discussed in chapter 6. Since the modelling required more chemical data than was available at the field sites, we used simulation data from the programme MIN3P for a hypothetical hydrocarbon spill and its degradation. Conclusions and suggestions for future work are found in chapter 7.



## 2 BACKGROUND

Spontaneous potential is the electrical potential ( $\phi$ ) measured between two points ( $p_1$  and  $p_2$ ), which is the integral of the electric field ( $E$ ) on any path between the two points.

$$\phi_2 - \phi_1 = - \int_{p_1}^{p_2} E dl \quad [2.1.]$$

The inverse relationship shows that the electric field is the negative gradient of the electric potential.

$$E = -\nabla \phi \quad [2.2.]$$

The electric field in the earth can be due to polarization of portions of the subsurface or it can be generated by the flow of current. In the second case it is related to the current density ( $j$ ) and the resistivity ( $\rho$ ) or conductivity ( $\sigma$ ). Conductivity is the inverse of resistivity and both will be used in this work.

$$E = \rho j = \frac{j}{\sigma} \quad [2.3.]$$

The phenomena that polarize portions of the subsurface and cause currents to flow are coupled fluxes as described by a system of phenomenological equations (Marshall & Madden, 1959). Coupled fluxes occur when more than one force affects the flux of a given quantity. For example, when groundwater moves in response to a pressure gradient, the matter moving contains electrical charges so it alters both hydraulic and electrical potentials. Temperature gradients will give rise to thermoelectric coupling and chemical concentration gradients produce electrochemical coupling.

This review aims to provide a background on methodologies and models used for SP. Since this project focuses on sites with contaminant plumes, which are rarely located in geothermal areas, only streaming and electrochemical potentials will be discussed. The section on streaming potentials (2.1) details laboratory work and methods of measuring the streaming potential coupling coefficient as a background for chapter 4. Though the focus of this thesis is SP of electrochemical origin, field measurements will include a streaming potential component so it is necessary to understand them well enough that their contribution can be subtracted from the total signal. When discussing

electrochemical potentials in section 2.2, the emphasis is on different theories and the field data that support them to lead into chapters 5 and 6. The final section (2.3) describes methods for quantitative analysis of SP, and particularly the use of coupled fluxes in order to present numerical modelling used in chapter 3.

## **2.1 Streaming potential**

Streaming potential is the electrical potential generated by the flow of a liquid past a solid or through porous media. It is an electrokinetic phenomenon, first formally described by Helmholtz (1879), that exists because the solid surfaces are charged and interact with ions in the liquid. Streaming potential occurs in natural systems as groundwater flows through sediment and porous rock. It has been studied extensively and has been the subject of numerous lab experiments. The models developed to describe streaming potential have mostly focused on very simple systems, like pure quartz sand with a NaCl electrolyte. With any departure from these simple systems, things quickly become more complex.

The information in this section was principally gathered in order to build an apparatus for measuring the streaming current coupling coefficient. At first, the streaming potential phenomenon is explained before a detailed description of laboratory apparatus. Experimental results are then compiled to gain an understanding of important parameters. Some links with field measurements are made before a summary. The first sub-section (2.1.1) discusses how mineral surfaces become charged, before describing models developed to explain the effect of the charged surface on ions in the liquid in the next sub-section (2.1.2). Through the Helmholtz-Smoluchowski equation found in sub-section 2.1.3, some models can be used to estimate streaming potential and predict the effect of different parameters such as temperature and pH.

The models have been tested against a large body of laboratory data. The measurement of streaming potential in the laboratory involves measuring the electrical potential difference across a sample while a liquid is flowing through it, and since there are many ways of doing this, experimental apparatus will be discussed in sub-section 2.1.4. Following this,

sub-section 2.1.5 presents laboratory results of many authors to describe the dependence of streaming potential on parameters such as: pH, temperature, electrolyte valence and concentration, material porosity and multiphase flow.

Ultimately it is interesting to understand streaming potential in natural environments so sub-section 2.1.6 describes qualitative field studies of streaming potential and how they relate to laboratory studies. A summary is drawn in sub-section 2.1.7.

### *2.1.1 SURFACE CHARGES*

Surface charges are of interest when studying streaming potentials, but also in many other fields such as chemical oceanography, aquatic toxicology, water and wastewater treatment and chemical, metallurgical and mining engineering. There are three types of surface charge (Davis & Kent, 1990):

- 1) Permanent structural charge: due to isomorphous substitutions in minerals
- 2) Coordinative surface charge: associated with the reactions of potential determining ions with surface functional groups
- 3) Dissociated surface charge: counter-ions that accumulate near the particle surface to preserve electro-neutrality

Permanent structural charge occurs most commonly in aluminosilicates. In tetrahedral sites  $\text{Si}^{4+}$  can be replaced by  $\text{Al}^{3+}$ , while in octahedral sites  $\text{Al}^{3+}$  can be replaced by divalent cations such as  $\text{Ca}^{2+}$  or  $\text{Mg}^{2+}$  (Parks, 1990). As a result of these substitutions, the mineral has a net negative charge and will attract cations. Structural charge is a component contributing to the cation exchange capacity of clays.

Coordinative surface charges are the result of reactions of surface functional groups and these are dependent on the type of mineral and electrolyte involved. The most common reaction is hydroxylation and hydration of oxides. Oxides are very common in geological materials, with quartz ( $\text{SiO}_2$ ) being the most abundant. The surface of a fractured quartz crystal has broken covalent Si-O bonds, which have a very high surface energy, so these

immediately react with water to form silanol groups, Si-OH. This means that the surface of quartz is in fact covered in silanol groups. Further reactions include (Glover et al., 1994):



Dissociated surface charge will be discussed in more detail in the next sub-section.

### 2.1.2 ELECTRICAL LAYER MODELS

Electrical charges do not occur in isolation and the surface charges discussed in the previous sub-section are counterbalanced by counter-ions present in the fluid adjacent to the surfaces to ensure electrical neutrality. Several models have been used to describe the arrangement of ions next to a surface.

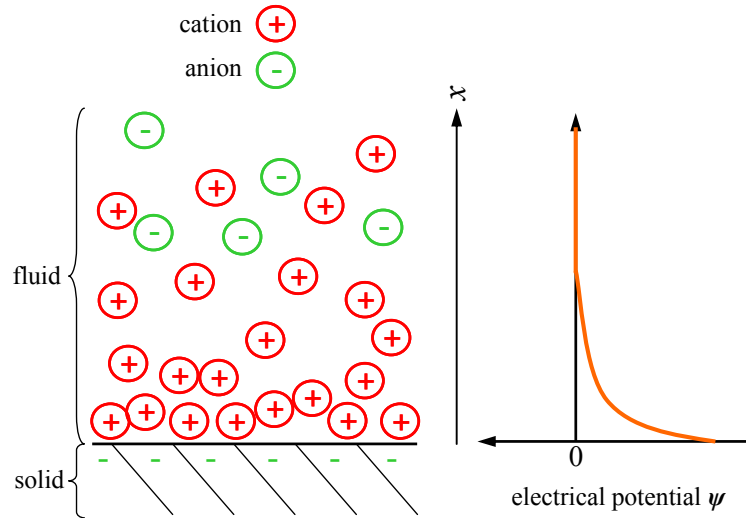


**Figure 2.1 Schematic diagram of ion distribution and potential profile for the Gouy-Chapman model. The whole medium is electrically neutral and since the solid interfaces are negatively charged, the fluid has excess positive ions that are concentrated near the solid interfaces.**

One of the first explanations of the microscopic scale arrangements was the Gouy-Chapman model (Figure 2.1), where ions in solution next to the charged surface form a cloud and are assumed to have a Boltzmann distribution (Gouy, 1910; Chapman, 1913). This model breaks down at high electrolyte concentrations or when the electrolyte is not symmetrical (cations and anions do not have the same valence) because it neglects the interaction between ions (Sposito, 1990).

The next model, proposed by Stern (1924), was a refinement of the Gouy-Chapman model consisting of a constant capacitance layer near the surface and a diffuse layer further out. The plane separating the Stern layer from the diffuse layer is called the slipping or shear plane. The electrical potential between this plane and the neutral solution is termed zeta ( $\zeta$ ) potential and is of interest for streaming potential. Grahame's (1947) contribution was to subdivide the Stern layer into the inner and outer Helmholtz planes, a more detailed description of the ion distribution (Figure 2.2). The inner Helmholtz plane is the locus of electrical centres of a layer of adsorbed ions, whether adsorbed by covalent bonds or van der Waals forces. The outer Helmholtz plane is the locus of electrical centres of hydrated or solvated ions in contact with the surface.

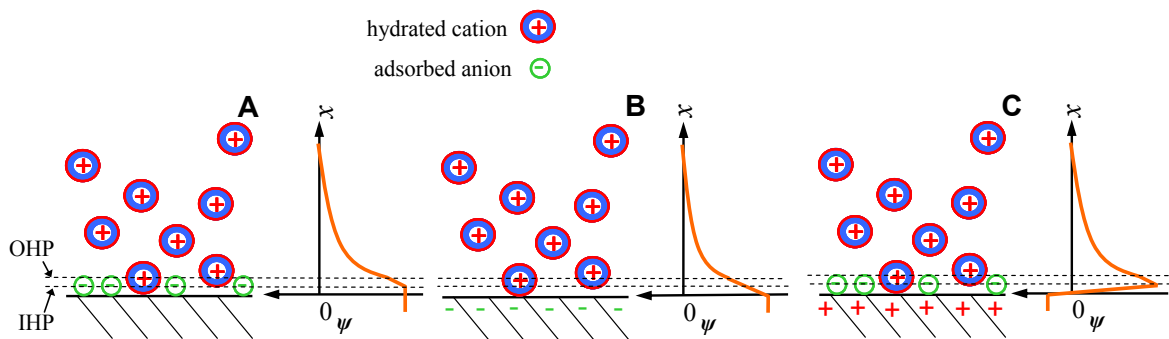


**Figure 2.2** Electrical double layer models of ion distributions and potential profiles. A) At the electro-capillary maximum, when the surface has no polarization. B) With negative polarization. C) With positive polarization. Abbreviations: OHP—outer Helmholtz plane, IHP—inner Helmholtz plane. (modified from Grahame, 1947)

Many double layer models used presently are essentially the same as Grahame's (1947) model. A triple layer model has also been proposed, which adds a layer of adsorbed  $H^+$  and  $OH^-$  ions right next to the surface (Davis et al., 1978).

Electrical double layer models have been developed for all electrokinetic phenomena (Table 2.1) though most of the pioneering studies have been done with electrophoresis.

**Table 2.1 Electrokinetic phenomena. All involve the movement of a solid and a liquid relative to each other. This list specifies which parts are stationary and which are in motion. (Dukhin, 1974)**

<b>Name</b>	<b>External force</b>	<b>Moving component</b>	<b>Stationary component</b>
electrophoresis	electrical field	solid	liquid
electro-osmosis	electrical field	liquid	solid
Dorn potential	pressure gradient	solid	liquid
streaming potential	pressure gradient	liquid	solid

The models have helped explain how the properties of a pore fluid are altered. For example, the dielectric constant of water in the interlayer region of swelling clays is 3-4 when the water thickness is 5-6 Å and 25-40 when the film thickness is 15-80Å (Parks, 1990). Normally the dielectric constant of water is 80.

The work has also had repercussions on the understanding of resistivity of materials. The movement of ions, particularly protons, can occur within the Stern layer. Revil & Glover (1998) stated that the surface conduction could be accounted for by the movement of ions in the Stern layer. They developed a formula to calculate the influence of surface conductivity on bulk conductivity of a saturated sample, with the aim of refining the empirical formula developed by Waxman & Smits (1968).

### 2.1.3 ZETA AND STREAMING POTENTIALS

Discussion from the two preceding sub-sections is valid whether the fluid in the porous medium is stationary or moving. Streaming potential only occurs where there is a pressure gradient causing the fluid to move through the porous medium. It is at this point that the shear plane becomes relevant.

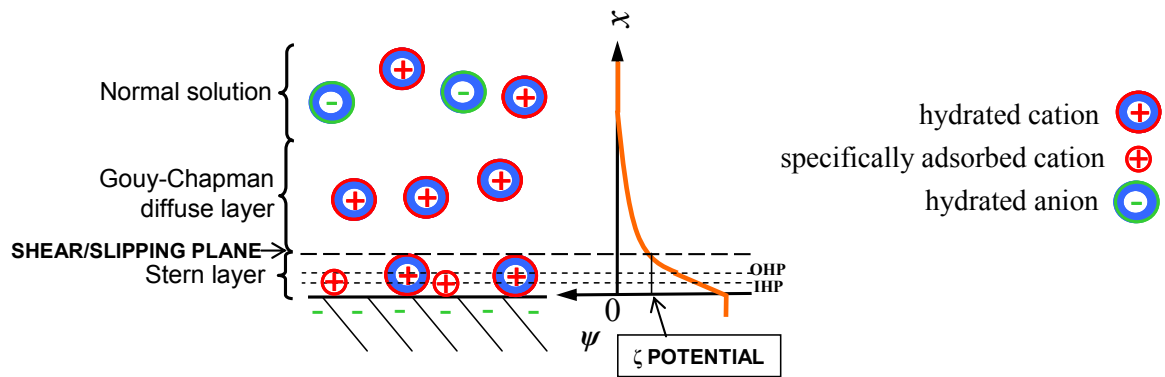


**Figure 2.3 Summary of electrical double layer with shear/slipping plane indicated. Fluid movement is parallel to the mineral surface.(modified from Ogilvy et al., 1989)**

Flow of the fluid drags the portion of the diffuse layer that is further from the surface than the shear plane (Figure 2.3), producing a current flow because there is an imbalance of mobile ionic species (Fitterman, 1978). Since surface charges are typically negative, the diffuse layer is usually composed of cations and when these get dragged by the convection current, an electrical anomaly is created that gets more positive down gradient. The relaxation time of the diffuse layer, which is the time it takes to regenerate after it is disarranged, is less than 1 ns so it is always present even though the cations are dragged away since it renews itself almost instantaneously (Jiang et al., 1998). The charge separation sets up an electric field that causes a counter current through the pore fluid called the conduction current (Fitterman, 1978).

Helmholtz (1879) was the first to describe streaming potential with formulae, working with data gathered by Quincke (1861). He formalised the idea of an electrical double layer, suggesting that there were two oppositely charged planes close together that acted as a capacitor. He developed a formula for a capillary which Smoluchowski (1903) generalised for a porous medium that was modelled as a bundle of capillaries entering the medium at one side and exiting the other following a tortuous path (Figure 2.4).

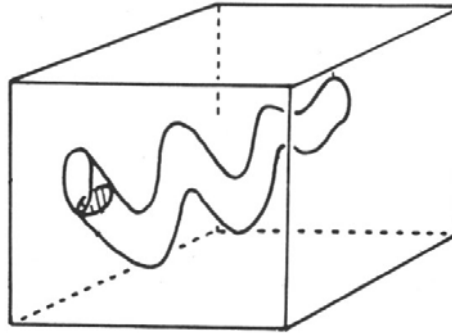


**Figure 2.4 Capillary model of porous media. (Ishido & Mizutani, 1981)**

The Helmholtz-Smoluchowski equation, which forms the basis of electrokinetic and electro-osmotic work, is given by:

$$\frac{\Delta V}{\Delta P} = \frac{\varepsilon \zeta}{\eta \sigma_f} \quad [2.6.]$$

where  $\Delta V$  is the difference in electrical potential,  $\Delta P$  is the difference in pressure,  $\zeta$  is the zeta potential,  $\varepsilon$ ,  $\eta$  and  $\sigma_f$  are the dielectric permittivity, the dynamic viscosity and the conductivity of fluid, respectively.

Conditions under which this equation is valid according to Morgan (1989) are:

- 1) Flow is fully established and laminar.
- 2) Geometrical parameters of flow are equivalent for convection and conduction currents.
- 3) The thickness of the double layer is much smaller than the radius of the capillaries.
- 4) The fluid is so much more conductive than the surface that electrical conduction by the surface can be neglected.

In natural systems these assumptions do not always hold, which has led to some modifications of the equation. For example, in fine sediments such as clays, which have sizes of  $20\text{\AA}$  or less with pore spaces of similar dimensions, the third condition does not hold so correction factors have been calculated (Rice & Whitehead, 1965; Levine et al., 1975). The fourth condition is violated when there is surface conductance. Corrections for this problem have been calculated either using extremely simple geometries (Morgan,

1989), using the empirical electrical formation factor ( $F$ ) as in equation 2.7 (Revil et al., 2003) or using the excess electrical charge per unit volume contained in the pore water of shale (Revil et al., 2005b).

$$\frac{\Delta V}{\Delta P} = \frac{\varepsilon \zeta}{\eta F \sigma_s} \quad [2.7.]$$

where  $F = \varphi^m$ ,  $\varphi$  is the connected porosity,  $m$  is the electrical cementation exponent, and  $\sigma_s$  is the surface electrical conductivity. This equation holds when  $\sigma_f \ll \sigma_s$  and the contribution due to fluid conductivity is neglected.

The ratio  $\Delta V/\Delta P$  is called the streaming potential coupling coefficient ( $C$ ). The streaming potential coupling coefficient was developed from laboratory studies where the difference in pressure was equal to the difference in hydraulic head ( $h$ ). In some cases, particularly in the field, there may be a non-negligible contribution from elevation head so a more rigorous formulation of the streaming potential coupling coefficient is  $C'$ :

$$C' = \frac{\Delta V}{\Delta h} \quad [2.8.]$$

and its units are mV/m<sub>H<sub>2</sub>O</sub> instead of mV/kPa. The conversion from pressure ( $P$ ) to hydraulic head ( $h$ ) can be done using (Domenico & Schwartz, 1998):

$$h = z + \frac{P}{\rho_w g} \quad [2.9.]$$

where  $z$  is elevation head,  $\rho_w$  is water density and  $g$  is the gravitational constant. If there is no elevation head, then:

$$C' = C \rho_w g \quad [2.10.]$$

In the following discussion  $C$  will be used when referring to values measured in the laboratory because this is the convention and  $C'$  will be used for field values.

The streaming potential coupling coefficient allows the calculation the electrical potential difference given a head difference, or vice versa. It is of particular interest when applying streaming potentials to hydrogeological problems because if  $C'$  and the subsurface electrical resistivity distribution are known in an area, a map of the electrical streaming

potential distribution can be converted to a map of hydraulic head distribution. This is appealing because both the SP and electrical resistivity can be measured non-intrusively, while typically hydraulic head distributions are calculated from water level measurements made in piezometres, which are invasive and expensive to install.

For the case of  $\sigma_f \gg \sigma_s$ , the streaming potential coupling coefficient is equal to the right hand side of equation 2.6. Of the four terms in this expression,  $\zeta$  is the most difficult to determine.  $\sigma_f$  is easily measured, while  $\varepsilon$  and  $\eta$  are well tabulated and can be found given a liquid's ionic concentration and temperature.

The  $\zeta$  potential is typically calculated using the Helmholtz-Smoluchowski equation (2.6) and electrokinetic data measured in the laboratory. Any electrokinetic phenomena can be used, but electrophoresis has been the most popular. For such measurements, an electrical potential difference is imposed across the ends of a fluid and the velocity of charged particles in the fluid is measured and used to calculate the equivalent pressure difference. Streaming potential measurements can also be used, and they are done by imposing a pressure difference across the ends of a sample and measuring the resulting potential difference.

Typical values for the terms in the streaming potential coupling coefficient expression are given in Table 2.2. The first column is for a clay free aquifer and the second is one for shaley sands with smectite.

**Table 2.2 Typical values for terms in the streaming potential coupling coefficient equation. There are empty spaces in the table because the formulae for clay-free and clay-rich aquifers have different variables. (Revil et al., 2003)**

<b>Term (units)</b>	<b>Clay-free aquifer</b>	<b>Shaley sands</b>
$\varepsilon_f$ (F/m)	$80\varepsilon_0$	$80\varepsilon_0$
$\zeta$ (V)	-0.030	-0.030
$\eta$ (kg/ms)	$8.8 \cdot 10^{-4}$	$8.8 \cdot 10^{-4}$
$\sigma_f$ (S/m)	0.02	
$F$		20
$\sigma_s$ (S/m)		0.1
<b><math>C</math> (mV/kPa)</b>	<b>-1.21</b>	<b>-0.0121</b>

The calculated coupling coefficient is two orders of magnitude smaller in the case of shaley sands. In natural environments  $C$  can cover a wide range of values and can be both positive and negative (Levine et al., 1975). It is typically negative since the  $\zeta$  potential is negative because of negative surface charges. Positive surface charges do sometimes occur, which results in positive coupling coefficients.

#### 2.1.4 EXPERIMENTAL APPARATUS

Many efforts have been spent measuring coupling coefficients from streaming potential in the laboratory. Unfortunately there are no standard techniques so it is often difficult to compare results between studies. There is a consensus that these measurements are difficult to make and they require meticulous work so that the signal is not lost in noise, as it has such a small amplitude. Every research group seems to build their own apparatus which they describe in varying detail, often emphasizing different aspects. This section will describe the different elements of the apparatus and some methods used to make the measurements.

##### 2.1.4.1 Sample and sample holder

Ahmad (1964) concluded that the geometry of flow was unimportant after making streaming potential measurements in three experimental set-ups: a rectangular box, a flow

tube and a 60° radial sector. Since then, most studies have been done using flow tubes because it is easier to ensure uniform flow and to pack properly. However, work done using tanks has had equal success (Maineult, 2004).

Most studies have been done on unconsolidated sediment using rigid sample holders that have been carefully packed. Packing of the material is critical as the sample must not contain air. There are large effects on the measured coupling coefficients if the sample is not fully saturated and several authors have outlined the difficulties encountered because of trapped air bubbles (Morgan et al., 1989; Sprunt et al., 1994; Sheffer, 2005).

When the material under study is rock, it is typically crushed before being packed into the sample holder (Ishido & Mizutani, 1981; Morgan et al., 1989; Lorne et al., 1999a). Lorne et al. (1999b) did experiments on both intact cores and crushed rock of two different quartzite samples. They found that for electrolyte conductivities smaller than  $\sim 10^6 \mu\text{S}/\text{cm}$ , the coupling coefficients were the same for the rock and crushed samples.

## 2.1.4.2 Pressure system

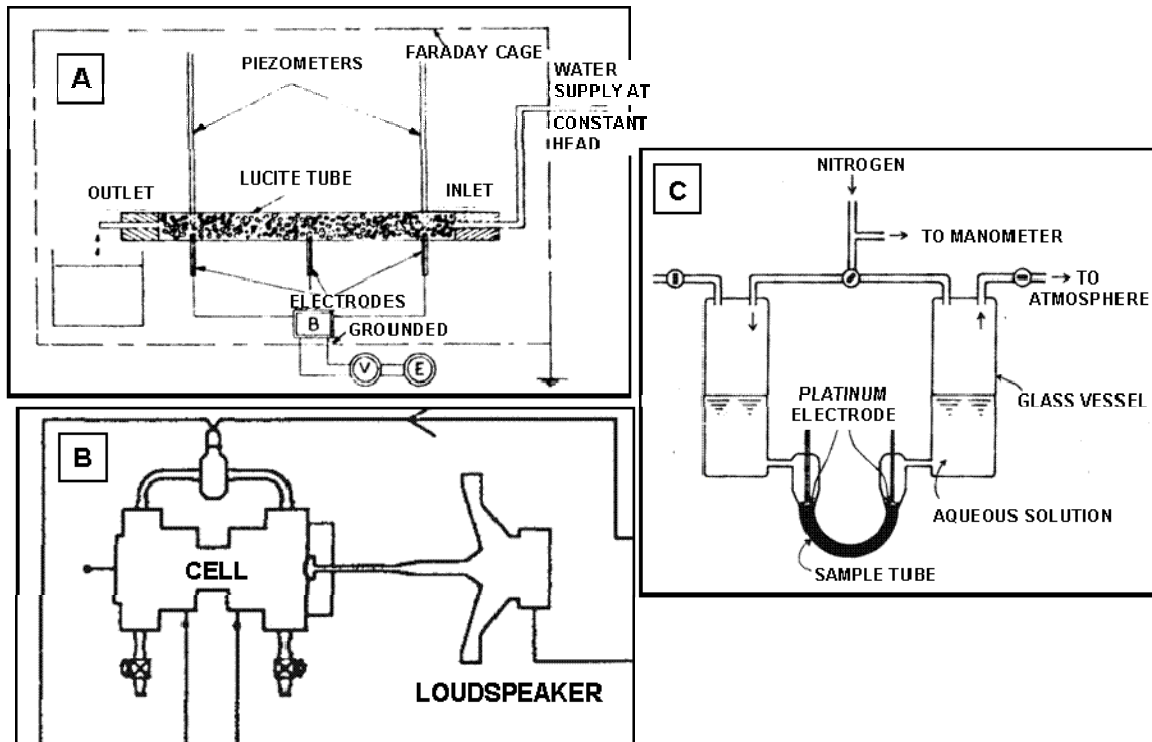


**Figure 2.5** Different pressure systems. **A:** Constant head reservoirs at different heights (Ahmad, 1964) **B:** Membrane on side of reservoir vibrated using loudspeaker (Pengra et al., 1999) **C:** Air tight water reservoirs into which gas can be injected (Ishido & Mizutani, 1981).

In order to create a streaming potential, it is necessary to impose a pressure difference across the sample that will cause the saturating liquid to flow. Most often the pressure difference is created by having the inlet and outlet water reservoirs at different heights (Figure 2.5A). In some examples the pressure variations were produced by a loudspeaker pushing on a membrane siding of one of the reservoirs, as shown in Figure 2.5B (Li et al., 1995; Pengra et al., 1999). Another method consists of using air tight water reservoirs and injecting gas in one reservoir while the other is open to the atmosphere as in Figure 2.5C (Somasundaran & Kulkarni, 1973; Ishido & Mizutani, 1981; Reppert & Morgan, 2003). Measuring the pressure at either end of the sample has been done using water levels, piezometres or manometers (Ahmad, 1964; Ogilvy et al., 1969; Olsen, 1972; Ishido & Mizutani, 1981; Morgan et al., 1989; Revil et al., 2002a; Revil et al., 2005b) or by using

pressure sensors, transducers or hydrophones (Lorne et al., 1999a; Pengra et al., 1999; Revil et al., 2002b; Guichet & Zuddas, 2003; Guichet et al., 2006).

#### *2.1.4.3 Electrodes*

It is necessary to have electrodes at both ends of the sample to measure the streaming potential across it. The reference electrode is placed in the upstream reservoir (Morgan, 1989).

Metal electrodes are subject to polarization and to the motoelectric effect, caused by fluid moving past the electrodes (Ogilvy et al., 1969). The motoelectric effect can be avoided if electrodes are placed outside the flow path (Morgan, 1989). The most common metal electrodes are stainless steel (Lorne et al., 1999b; a; Bernabé et al., 2003; Reppert & Morgan, 2003) and platinum (Schriever & Bleil, 1957; Somasundaran & Kulkarni, 1973; Sears & Groves, 1978; Ishido & Mizutani, 1981). Other metals used include beryllium bronze (Jouniaux & Pozzi, 1995b; a) and gold (Heister et al., 2005).

The most popular electrode type is the liquid junction electrode because it does not undergo as much polarization. In almost all cases Ag/AgCl electrodes are used, but in a few studies Cu/CuSO<sub>4</sub> electrodes have been used (Kassel et al., 1989; Antraygues & Aubert, 1993; Mainault, 2004).

It is important for the metal of both metal and liquid junction electrodes to be inert because electrodic potentials will be generated if it participates in chemical reactions. For example, the silver in Ag/AgCl electrodes can react with HS<sup>-</sup>, producing potentials that will be combined with targeted potentials in measurements (Zhang et al., 2010). Electrodic potentials can be a significant problem in environments with high temperatures, high pH or high ionic strength (Reppert & Morgan, 2003).

There is considerable variation as to the electrode locations, they may be in contact with a small point on the sample, they may be a disc on either end of the sample, they may be a ring around the sample or they may not be directly in contact with the sample, but rather

in the fluid immediately on either end of the sample. The potential gradient throughout the sample was found to be homogeneous, whether in a core or a tank (Lorne et al., 1999a; Mainault, 2004), so the electrode positioning should not have an impact on the measurements.

The magnitude of the signal measured with the electrodes is always small, a few mV or less, so it is important to have a high signal-to-noise ratio. The impedance of the voltmeter must be an order of magnitude larger than the contact resistance in order to avoid loading the measurement circuit (Corwin, 1990). Using coaxial cable between the electrodes and the voltmeter offers shielding to the inner wire transmitting the signal if the surrounding conductor is left isolated or grounded (Glover et al., 1994; Mainault, 2004). Building the whole apparatus with amagnetic materials can help reduce spurious signals (Jouniaux & Pozzi, 1995a). When working in electrically noisy environments, some researchers have found that it is necessary to build a faraday cage around their apparatus (Ahmad, 1964; Reppert et al., 2001; Sheffer, 2005). In one experiment, it was necessary to reconfigure interface circuitry to remove ground loops related to the standard wiring of pressure transducers and power supply units to reduce noise (Sheffer, 2007).

#### *2.1.4.4 Measurement methods*

There are three methods for collecting streaming potential data: DC, AC and transient. The DC method is the easiest to set up, but requires large volumes of fluid. The AC method requires more complex apparatus, but can measure lower magnitude signals because it allows for data stacking. Finally, the transient method is appropriate for sediment with very low hydraulic conductivity. For data analysis there are four methods, using raw data, rms processing, cross-correlation and spectral analysis, though they are not all applicable to each collection method. Reppert & Morgan (2001) discuss the different methods and their processing in detail. They demonstrate that with careful measurements all methods give equivalent results.

#### *2.1.4.5 Auxiliary measurements*

Natural sediment and rock samples have complex chemistry and can take a long time to reach chemical equilibrium when put in contact with liquids prepared in a lab. For

experiments with Berea sandstone, Reppert & Morgan (2001; 2003) reported zeta potentials calculated from coupling coefficient measurements that were very dependent on equilibration time; for 2-3 days  $\zeta = -30$  mV and for 19 days  $\zeta = -1.2$  mV. Mainault (2004) found that the degradation of biotite, which made up less than 2% of the sediment he worked with, caused the signal to change during an experiment lasting several months. When working with montmorillonite clays, Demir (1988) found that it took 6-7 weeks to achieve a constant chemical composition in the effluent.

Monitoring the evolution of the liquid chemistry is therefore important for determining when the sample has reached equilibrium and if it changes through the course of the experiment. In most apparatus a liquid sample is taken from one of the reservoirs for tests, but in a few, the measurement devices are integrated into the apparatus. Relevant measurements include the resistivity of the sample, the fluid conductivity, the pH and the temperature.

#### *2.1.5 EFFECT OF PARAMETERS ON STREAMING POTENTIAL*

Streaming potential can be generated in a relatively simple system, however there are a surprising number of parameters affecting the result. These parameters are interconnected and it is not possible to investigate the effect of one parameter in isolation. For example, when trying to create high pH solutions to look at the effect of pH, one will also be changing the solution conductivity and perhaps causing minerals to precipitate, thus changing the mineralogy, porosity and permeability.

This section is a compilation of data from many laboratory studies. Since many of the data were read off graphs the values are not precise. All the values  $C$  were converted to units of mV/kPa. Though the standard requires the negative electrode to be upstream, typically producing negative  $C$ , both negative and positive coefficients are reported in literature. For consistency the positive values have been changed into negative ones, unless there was reason to believe the positive values were not due to a difference in convention.

Most of the tests were done using DC streaming potential apparatus, but low frequency AC results were used as well, since Reppert & Morgan (2001) have shown that they are comparable. All works assume that the streaming potential is linearly dependent on the applied pressure difference so that the relationship between the two can be entirely explained by the streaming potential coupling coefficient. In experiments with pressure differences over 0.1 kPa the relationship is linear, but Bogolovsky & Ogilvy (1972) demonstrated that at small pressure differences it is no longer linear (Figure 2.6). The works reported in this section are from experiments well above these pressures.

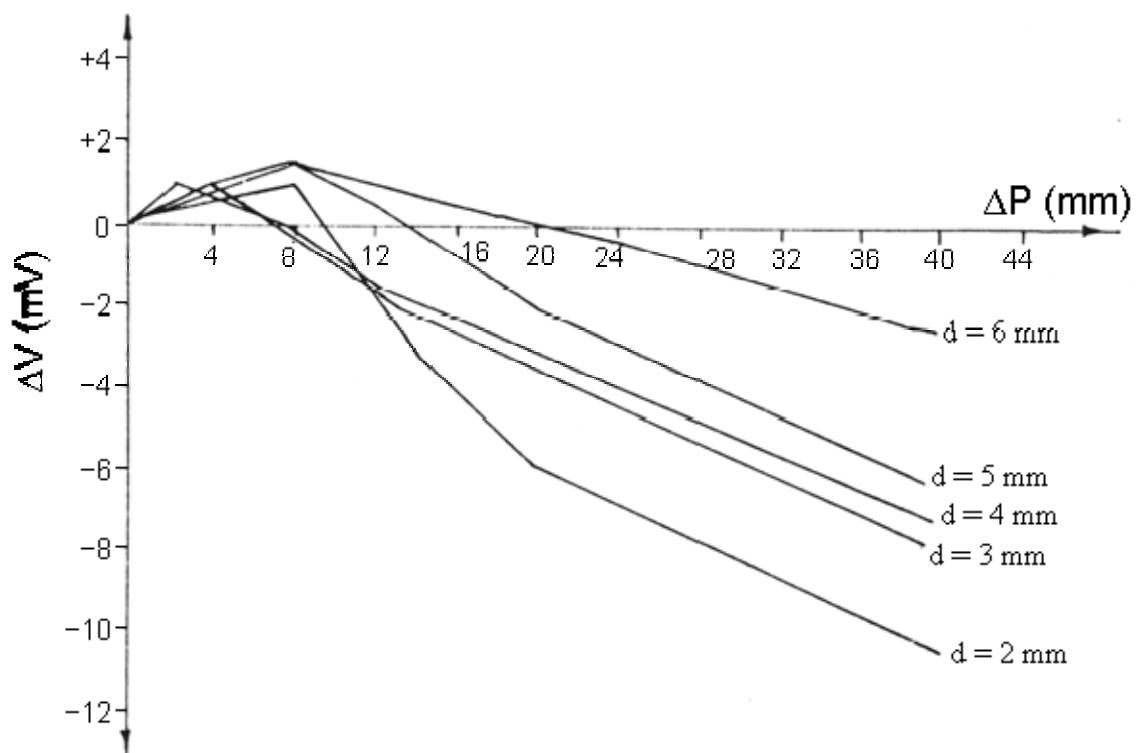


**Figure 2.6 Streaming potential measured by running water through a fissure with a variable opening width (d). (Bogolovsky & Ogilvy, 1972)**

The effect of the properties of the fluid; electrical conductivity, electrolyte type and pH, will be described first. Temperature and water saturation will be discussed next as they affect both the liquid and the sediment. The last parameters considered will be those related to the sediment: grain size, porosity, permeability, formation factor and clay content. The effect of all these parameters are presented as graphs of the parameter vs.



The electrolyte dissolved in the fluid has an effect on the coupling coefficient measured. In general, electrolytes with cations and anions with the same valence will have a larger magnitude  $C$  than electrolytes with ions of different valences (Schriever & Bleil, 1957; Morgan et al., 1989). Lorne et al. (1999b) presented results obtained from different electrolytes in terms of  $\zeta$  potential and the cation seemed to be the important ion for determining the  $\zeta$  potential. Salts with the same cation but different anions (ex. KCl &  $K_2SO_4$  or  $CaCl_2$  &  $CaSO_4$ ) produced very similar  $\zeta$  potentials. The precise effect of a mixture of ions, such as are found in natural waters, is not known although the relationship of decreasing magnitude of  $C$  with increasing salinity still holds (Sheffer, 2005).

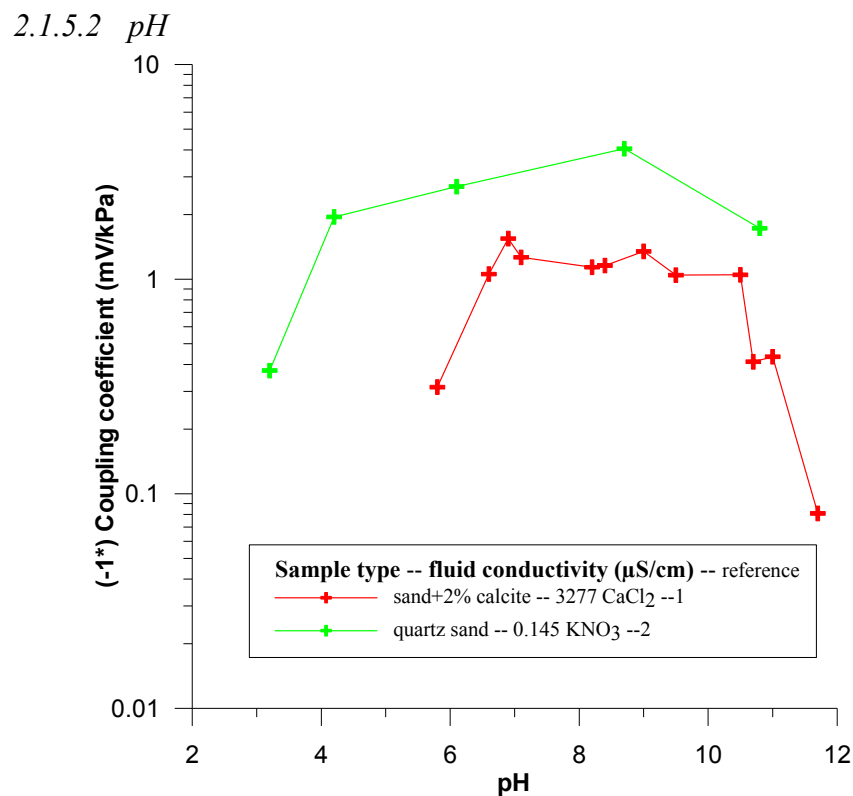


**Figure 2.8 Effect of pH on coupling coefficient.**  
 References: 1 (Guichet et al., 2006) 2 (Ishido & Mizutani, 1981)

Both studies on the effect of pH show that the magnitude of  $C$  increases with increasing pH until  $\sim$ pH 9, after which it decreases (Figure 2.8). When doing these studies it is

impossible to keep a constant fluid conductivity. Guichet (2002) explained that at higher pH, certain minerals will begin to precipitate, coating the original sediment and altering the surface properties and the  $C$ . In his study calcite precipitated at pH above 10. Guichet & Zuddas (2003) propose that  $\text{Al}(\text{NO}_3)_3$  in the system precipitated as Al-hydroxides at high pH in the study by Ishido & Mizutani (1981).

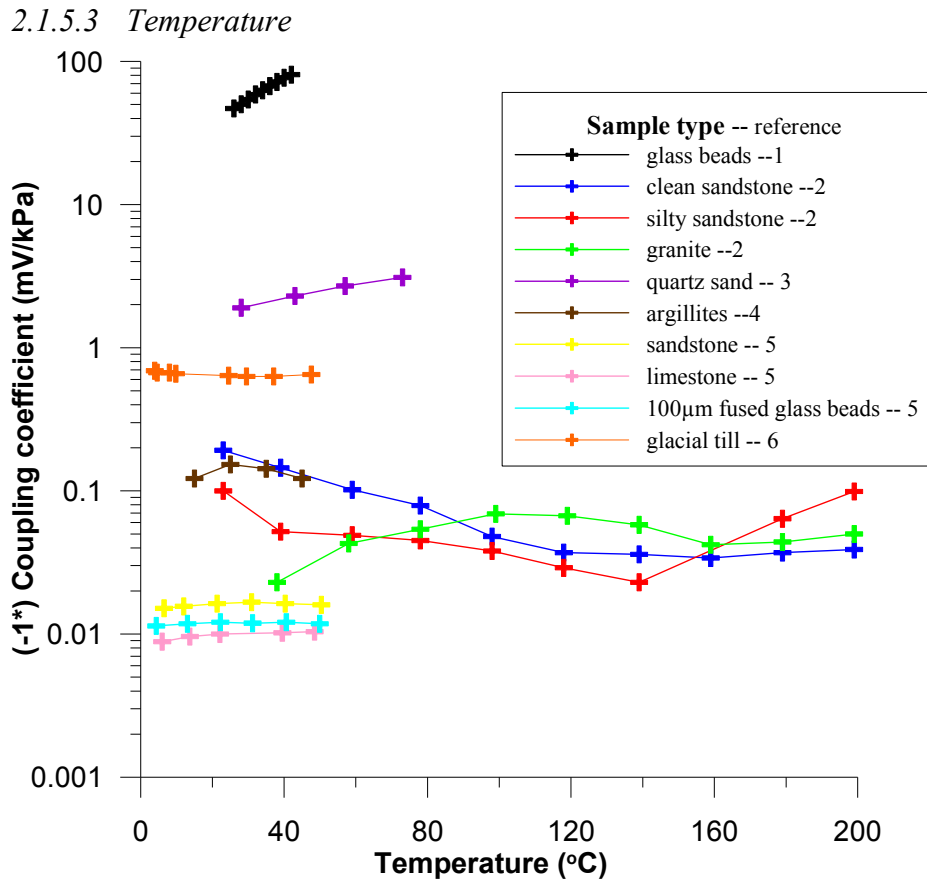
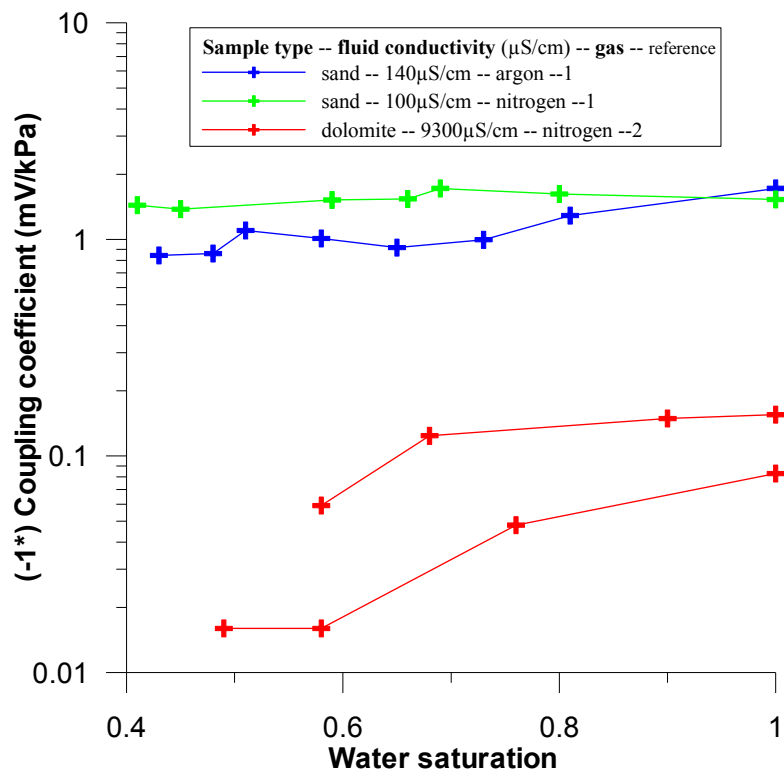


Figure 2.9 Effect of temperature on coupling coefficient.  
References: 1 (Schriever & Bleil, 1957) 2 (Reppert & Morgan, 2003)  
3 (Ishido & Mizutani, 1981) 4 (Revil et al., 2005b)  
5 (Pengra et al., 1999) 6 (Friborg, 1996)

The effect of temperature on coupling coefficient is not consistent across studies by different authors (Figure 2.9). Work by Schriever & Bleil (1957) and Ishido & Mizutani (1981) show that the magnitude of  $C$  increases with temperature, whereas studies by Friborg (1996), Pengra et al. (1999) and Revil et al. (2005b) indicate that  $C$  is independent of temperature. The only investigation at high temperature shown is that of

Reppert & Morgan (2003) and it does not show any clear trend. Increasing the temperature will facilitate certain reactions between the sample and the fluid, making it difficult to maintain constant fluid conductivity and pH. The studies by Schriever & Bleil (1957) and Ishido & Mizutani (1981) used very fresh water (distilled water and  $0.15\mu\text{S}/\text{cm}$   $\text{KNO}_3$  respectively) compared to the other studies (all  $\sigma_f > 3800\mu\text{S}/\text{cm}$ ), so perhaps only systems with low conductivity solutions are sensitive to temperature changes.

#### 2.1.5.4 Water saturation



**Figure 2.10 Effect of water saturation on coupling coefficient.**

References: 1 (Guichet et al., 2003) 2 (Revil & Cerepi, 2004)

Not many studies with quantitative results have looked at the effect of water saturation ( $S_w$ ). Morgan et al. (1989) detailed the difficulties they had with air bubbles passing through their system and causing erroneous readings. They found that the magnitude of  $C$  increased with the air bubbles, which contradicts the data presented in Figure 2.10, where the magnitude of  $C$  decreases with decreasing water saturation and falls to zero at a water saturation of 0.4. Two models have been developed to describe the dependence of  $C$  on

$S_w$  and both state that it is not linear. In the equation of Revil et al. (1999),  $C$  increases with decreasing water saturation, supporting the observations of Morgan et al. (1989). Linde et al.'s (2007) equation (2.11) states the opposite,  $C$  decreases with decreasing water saturation, and the authors used it to accurately simulate measured laboratory data.

$$C = \frac{C_{sat} k_r}{\sigma_r S_w} \quad [2.11.]$$

where  $C_{sat}$  is the streaming potential coupling coefficient at saturation,  $k_r$  is the relative permeability of water, often modelled using a van Genuchten equation (van Genuchten, 1980),  $S_w$  is the water saturation, and  $\sigma_r$  is the relative electrical conductivity.

#### 2.1.5.5 Grain size, porosity and permeability

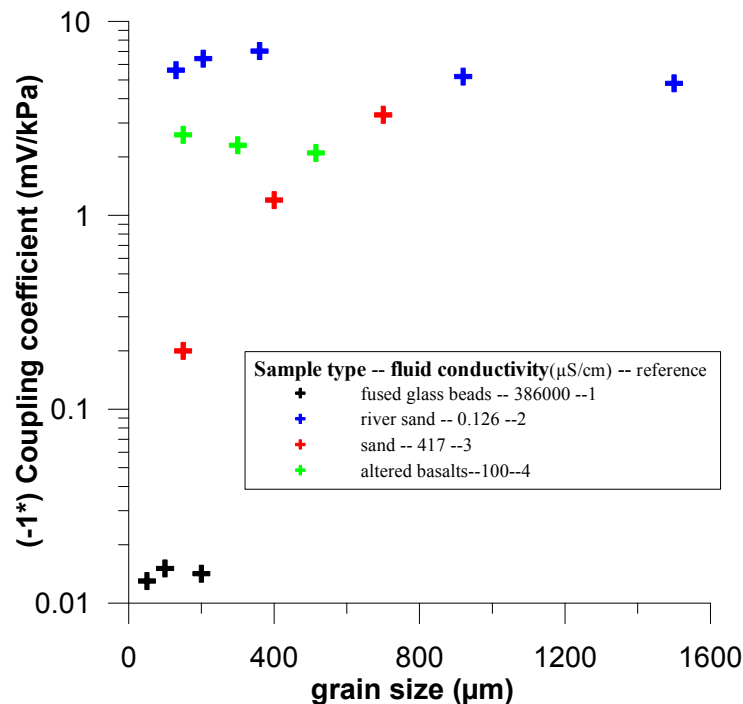
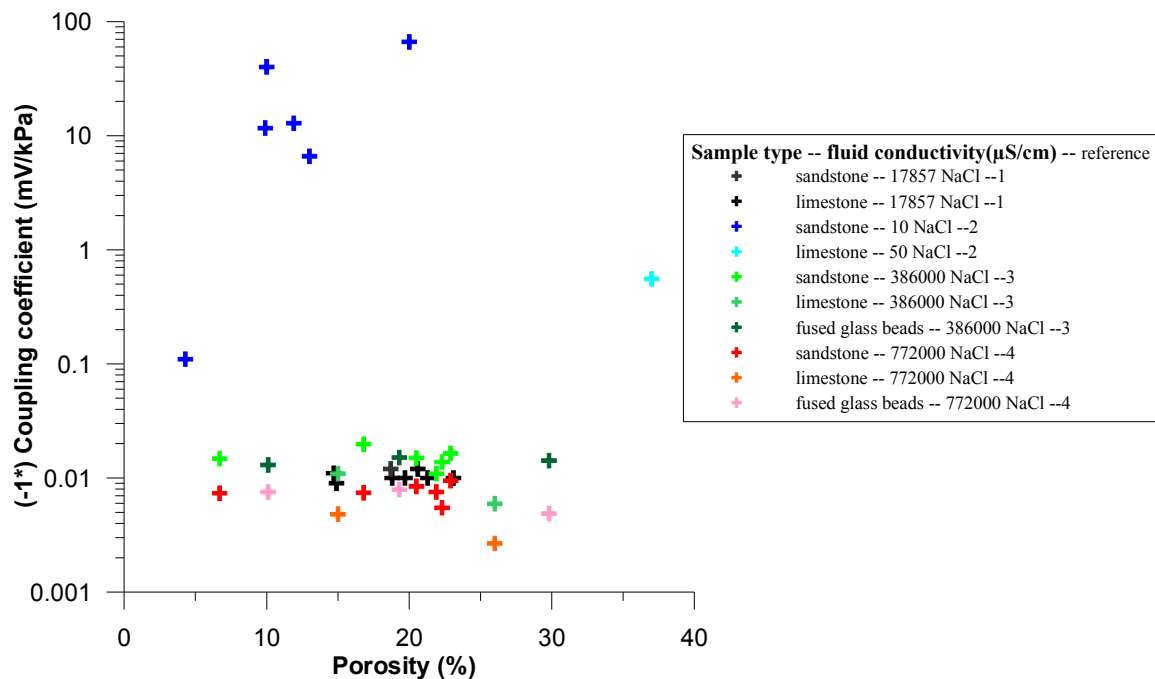


Figure 2.11 Effect of grain size on coupling coefficient.  
References: 1 (Li et al., 1995) 2 (Ogilvy et al., 1969)  
3 (Ahmad, 1964) 4 (Revil et al., 2004)



**Figure 2.12 Effect of porosity on coupling coefficient.**  
**References: 1 (Sprunt et al., 1994) 2 (Jouniaux & Pozzi, 1995a)**  
**3 (Li et al., 1995) 4 (Pengra et al., 1999)**

Grain size, porosity and permeability are properties of the sediment that are inter-related. There are no clear patterns on the plots of their effects on the coupling coefficient (Figure 2.11, Figure 2.12, Figure 2.13). The first study on the effect of grain size by Ahmad (1964) shows a clear increase in the magnitude of  $C$  with increasing grain size. However, three further studies do not support these findings (Figure 2.11). When the porosity data of several authors are plotted together, they do not have a pattern, but show that a wide range of  $C$  is possible for a given porosity (Figure 2.12). The permeability plot (Figure 2.13) shows a lack of correlation similar to what is found in the porosity data, perhaps with the exception of very low permeabilities. Based on Jouniaux & Pozzi's (1995a) data, it appears as though the magnitude of  $C$  decreases with decreasing permeability at permeabilities below  $10^{-14} \text{ m}^2$ . This contradicts the Helmholtz-Smoluchowski equation, since the equation has no term to account for variations in permeability. However their data has been supported by modelling results. Bernabé (1998) created a 2-D model of interconnected capillaries of which he could vary the diameter. He would fix the hydraulic pressure on each side of the network and calculate the hydraulic pressure and

streaming potential at each node. Using this model, he found that  $C$  was dependent on permeability.

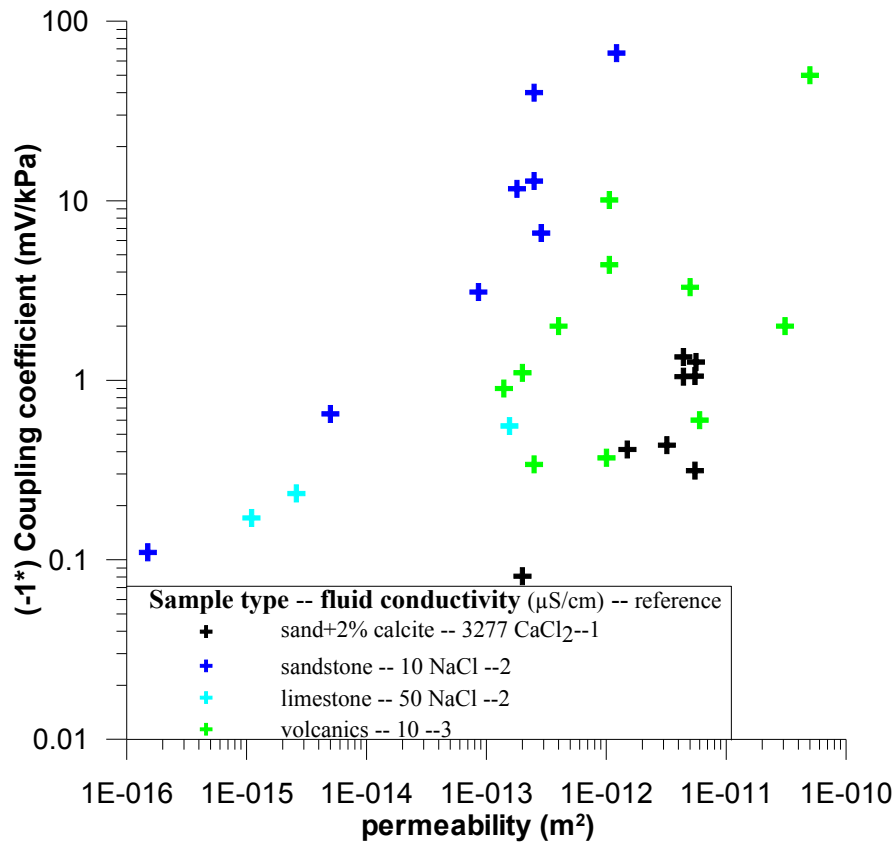
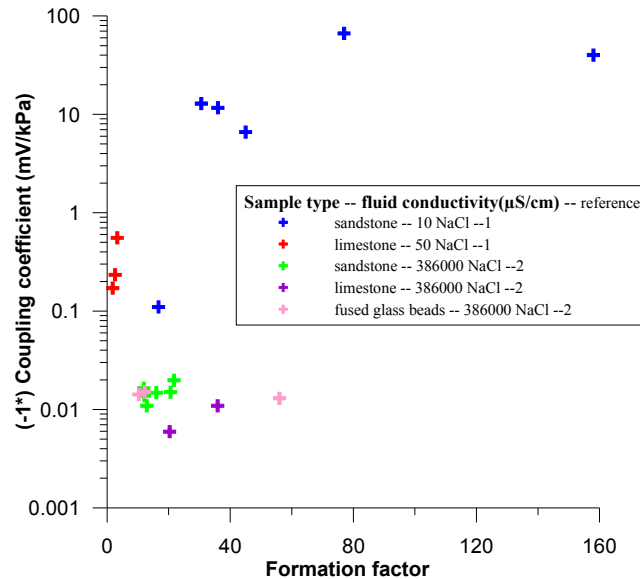


Figure 2.13 Effect of permeability on coupling coefficient.  
References: 1 (Guichet et al., 2006) 2 (Jouniaux & Pozzi, 1995a)  
3 (Jouniaux et al., 2000a)

### 2.1.5.6 Formation factor and clay content



**Figure 2.14 Effect of formation factor on coupling coefficient.**  
References: 1 (Jouniaux & Pozzi, 1995a) 2 (Li et al., 1995)

The mineralogy of the sample has an effect on the electrical potential generated. In all previous plots the different sediment types have been separated and identified. In general, calcite rich sediment such as limestone or dolostone will have smaller magnitude  $C$  given the same fluid conductivity, but these rocks react more readily so the solutions permeating through them tend to be more conductive. Two ways of roughly quantifying the sediment mineralogy are the formation factor and the percent clay content. The formation factor is  $\sigma_{fluid}/\sigma_{sample}$  and if the fluid conductivity is kept constant, it quantifies the conductivity of the samples. Increased sample conductivity is usually associated with increased clay content and these samples will have smaller formation factors.

There is a trend towards smaller magnitude  $C$  for smaller formation factors (Figure 2.14). This is supported by the results of Bogolovsky & Ogilvy (1972) for coupling coefficients measured across a fissure filled with sand containing varying amounts of clay (Figure 2.15). As the clay content increases the magnitude of  $C$  decreases. The discussion on  $\zeta$  potentials when there is surface conductance (sub-section 2.1.3) agrees with these laboratory results. For example, the calculations of Revil et al. (2003) (Table 2.2) predict smaller magnitude  $C$  when clay is present. Kulesa et al. (2003) counter this by claiming

that the  $\zeta$  potential, and therefore  $C$ , is larger where clay minerals are abundant. The sources they cite do not seem to support their statement because these sources found smaller magnitudes of  $C$  as clay percentages increased (Ogilvy et al., 1969; Ishido & Mizutani, 1981).

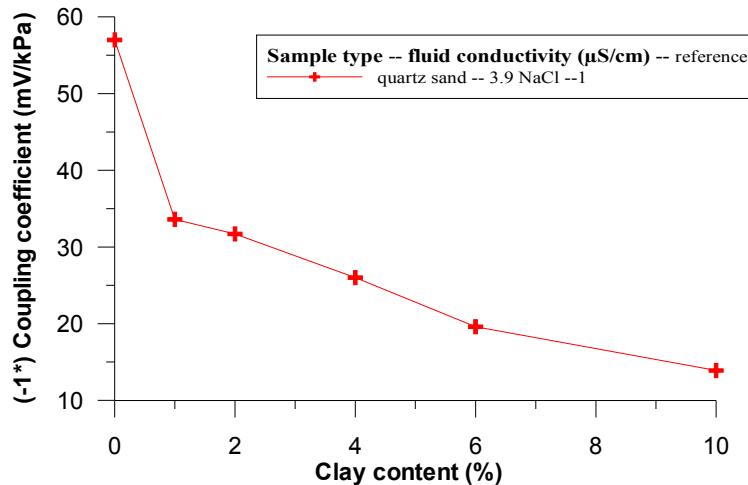


**Figure 2.15** Effect of clay content of coupling coefficient.  
References: 1 (Bogolovsky & Ogilvy, 1972)  
(Note that  $C$  is not on a logarithmic scale)

### 2.1.6 COUPLING COEFFICIENTS FROM THE FIELD

Although many laboratory experiments have quantified the streaming potential coupling coefficient, fewer field studies have quantified it. As shown in the previous sub-section (2.1.5), many parameters affect the coupling coefficient, and in the field these are uncontrolled and often unmonitored. Additionally, the electrical potential signal measured as spontaneous potential includes three components: streaming, electrochemically sourced and thermoelectric potential. On most sites, the magnitude of the streaming potential is so much greater than that of other sources, the other sources are negligible (Ishido & Pritchett, 1999). Even geothermal field sites are modelled with streaming potential (ex. Fitterman, 1978) as the signal from convection of warm water is greater than that due to the thermoelectric effect. All the studies presented in this section assumed that the SP signal was entirely due to streaming potential.

$C'$  cannot be measured directly so it is estimated by fitting field data to a model. Two approaches have been used:

- 1) Linear model: Slope of the best fit line on a cross-plot of measured SP vs. measured water levels. This approach has been used in natural environments and in forced situations such as pumping and infiltration tests.
- 2) Fournier model: More detailed model, developed by Fournier (1989), where SP signal source is assumed to be at the water table. Both  $C'$  and water table elevation are adjusted for best fit.

The coupling coefficients at a few field sites have been calculated using the linear model. This method is appropriate if the hydraulic head has been measured in many places. It has been done in natural settings and forced situations where the water table level was altered by pumping or infiltration tests. Forced situations provide more accurate results since a background SP which includes the effects of variations in lithology and fluid conductivity can be subtracted from the data. Results from these studies are summarised in Table 2.3.

**Table 2.3 Summary of coupling coefficients calculated from field results with a linear model.**

<b>Authors</b>	<b>Setting</b>	<b>Location / material</b>	<b>Water conductivity (<math>\mu\text{S}/\text{cm}</math>)</b>	<b>Calculated <math>C'</math> (<math>\text{mV}/\text{m}</math>)</b>
Baker & Cull (2004)	natural	King River, Tasmania / river sediments including mine tailings	55700	-1500
Bogolovsky & Ogilvy (1970)	natural	Water reservoir on Kalya River, Northern Caucasus / strongly fractured karstified limestones	-	-9
Ishido et al. (1983)	natural	Takinova geothermal area, Japan	~50000	-1.5
Titov et al. (2000)	natural	Neva river bank, St. Petersburg / sand with gravel & clay	-	-2.5
Revil et al. (2002b)	forced	drainage ditch / carbonate rich silty mud	600	-10.8
Rizzo et al. (2004)	forced	silty sand layer between 2 shale layers	915	-0.8

The results of Baker & Cull (2004) are very different from the others, which are almost all encompassed in one order of magnitude, between  $-1$  and  $-10$  mV/m. Apart from the

calculated  $C'$ , the distinguishing feature of the Baker & Cull study seems to be that it was done at a site contaminated with massive sulphides mine tailings rich in copper and base metals. The salinity and pH in the study area are known to be highly variable and it is plausible that electrochemically sourced potentials could be important. This may explain the unexpectedly high  $C'$ .

The Fournier model is discussed in subsection 2.3.3.1 with quantitative analysis of electrokinetic effects. This modelling method is appropriate for sites where hydraulic head is only known in a limited number of places. A summary of sites where Fournier modelling was used to calculate  $C'$  is presented in Table 2.4.

**Table 2.4 Summary of coupling coefficients calculated from field results with a Fournier model.**

<b>Authors</b>	<b>Location / material</b>	<b>Water conductivity (<math>\mu\text{S}/\text{cm}</math>)</b>	<b>Modelled <math>C'</math> (mV/m)</b>
Fournier (1989)	Puy-de-Dôme, France / acid volcanics	90-150	-1.25
Birch (1993)	4 drumlins in New Hampshire, U.S.A. / glacial till	-	1, 2, 2 and 4
	2 deltas in New Hampshire, U.S.A. / sand & gravel	-	-16, -17
Revil et al. (2003)	Bogolovsky & Ogilvy's (1973) data from a pumping well	-	-3.2 and -14.2
	Jackson & Kauahikaua's (1987) data at Kilauea volcano, Hawaii	-	-1.4 and -9.4
Revil et al. (2004)	Piton de la Fournaise volcano, Ile de la Réunion	80	-5.7

It is interesting to note that Birch obtained positive  $C'$  when working over clay rich tills and negative  $C'$  in sands and gravels. The data discussed in sub-section 2.1.5.6 indicated  $C$  would have a smaller magnitude when clays were present but did not propose a sign reversal.

### 2.1.6.1 *Effect of water saturation*

In an attempt to measure the effect of water saturation on the streaming potential signal, Doussan et al. (2002) compared SP and unsaturated water flux measured in the field on a sandy loam and a clay loam plot. For single rainfall events, they found a good correlation during the infiltration phase, but the correlation was no longer present during the drainage phase. Over longer periods, they did not find correlations and believed this was due to electrode drift. It is difficult to compare these results to those presented in section 2.1.5.4 as they are reported as water fluxes rather than % saturation, but they concur qualitatively because the largest potential signal is associated with the largest flux, which would occur at the highest water saturation.

### 2.1.7 *FIELD-LAB COMPARISONS*

The reported  $C'$  values have a much smaller range than the values reported for laboratory experiments, as they have magnitudes smaller than 20 mV/m apart from Baker & Cull's (2004) data. For three of the field studies presented, the authors also measured  $C'$  of the sediment from their sites in the laboratory to compare with field derived values. These are described in Table 2.5. There is more variation between the field and lab results than between field results at different sites. The two  $C'$  values calculated with the linear model show better agreement with the lab results than the  $C'$  calculated with the Fournier model. Part of the disagreement could be explained by the fact that the lab experiments used NaCl or KCl solutions with similar conductivities to those measured in the field, rather than actual groundwater.

**Table 2.5 Summary of coupling coefficients measured in both the field and laboratory. The model used for calculating field values is specified.**

<b>Authors</b>	<b>Field <math>C'</math> (mV/m)</b>	<b>Laboratory <math>C'</math> (mV/m)</b>
Baker & Cull (2004)	(linear) -1500	-1800
Revil et al. (2002b)	(linear) -10.8	-3.2
Revil et al. (2004)	(Fournier) -5.1	-22.6

The field values are compared with the laboratory results in Figure 2.16. Most fall reasonably close to the lab data, given the already important scatter in the data. The value of Baker & Cull (2004) seems erroneous.

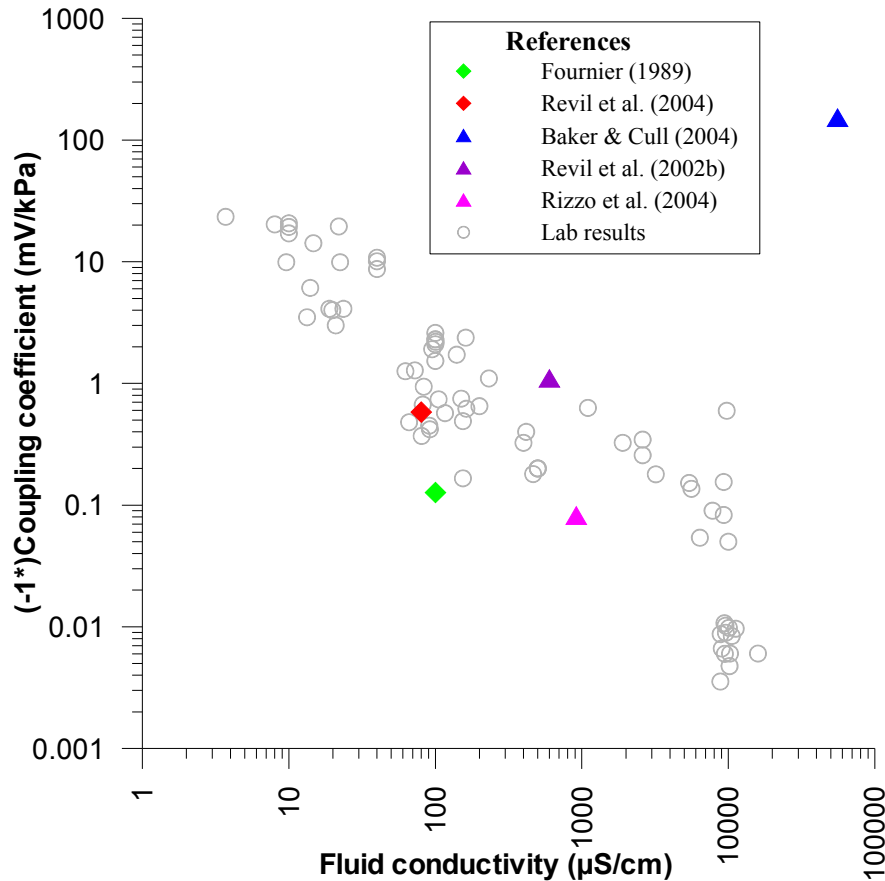


**Figure 2.16** Field results plotted with all laboratory results. **Diamonds:**  $C'$  calculated with Fournier model. **Triangles:**  $C'$  values calculated with linear model. Lab results are those in Figure 2.7.

Guichet (2002) provides a detailed comparison of field and laboratory data from six volcanoes using SP, coupling coefficient, geochemistry and water temperature data from different sources. Since the data are from hydrothermal areas he does a temperature correction so that all data can be compared at 25°C. Of the six volcanoes discussed, he has both field SP data to calculate  $C'$  and laboratory measured  $C$  from three of them, and the values reported differ by 1-2 orders of magnitude. A large part of these discrepancies are certainly due to the fact the laboratory samples did not necessarily come from the precise field measurement locations and the field and laboratory fluids were different.

### 2.1.8 STREAMING CURRENT COUPLING COEFFICIENT

The discussion up to date has focused on the streaming potential coupling coefficient ( $C$ ). When modelling streaming potential and relating it to hydraulic head distributions, it is necessary to use the streaming current coupling coefficient ( $L$ ).  $L$  cannot be measured directly so it is calculated using the equation:

$$L = -\sigma C \quad [2.12.]$$

where  $\sigma$  is the electrical conductivity. When working with hydraulic head instead of pressure, the formula is:

$$L' = -\sigma C' \quad [2.13.]$$

$L'$  is typically reported in units of  $A/m^2$ , which could be written more precisely as  $A/m \cdot m_{H_2O}$ .

Only a few experiments have measured both  $C$  and  $\sigma$  to allow the calculation of  $L'$  and they are listed in Table 2.6. The values of  $L'$  have a much smaller range than those of  $C$  and seem to be influenced by the mineralogy of the porous medium. Most values are between 10 and 50  $\mu A/m^2$ . The  $L'$  values found by Jouniaux et al. (2000b) are an order of magnitude lower than most of the others and are the only experiments with intact core. It is not clear if it is the lithology or sample type that causes the difference. The last two studies report values an order of magnitude larger than the average. Suski et al. (2006) and Jardani et al. (2006) used the same apparatus to measure  $C$  and found values close to what they had estimated in the field. Their laboratory resistivity measurements were also close to what they found with electrical resistivity tomograms.

**Table 2.6 Summary of measured streaming current coupling coefficients.**

<b>Authors</b>	<b>Material</b>	<b># of measurements</b>	<b>standard deviation (<math>\mu\text{A}/\text{m}^2</math>)</b>	<b>average <math>L'</math> (<math>\mu\text{A}/\text{m}^2</math>)</b>
Friberg (1996)	glacial till	35	8.3	15
Jouniaux et al. (2000b)	volcanic rocks	11	2.7	2.2
Sheffer (2005)	glass beads	9	17.2	85
Sheffer (2005)	dam sediments	7	5.8	17
Revil et al. (2005)	sands	8	9.2	54
Suski et al. (2006)	carbonate silt	6	69.4	228
Jardani et al. (2006)	loess	3	222.3	174

### 2.1.9 SUMMARY

Streaming potential is an electrokinetic phenomenon caused by the flow of a liquid past a solid due to electrical interactions between the charged surface and ions in the fluid. The interactions on an atomic level are described by electrical double layer models and by the Helmholtz-Smoluchowski equation at a larger scale.

Streaming potential coupling coefficient determination has been the subject of many laboratory experiments. The effects of different parameters of the fluid-solid system have been studied and fluid conductivity has the largest effect on  $C$ . The parameters which have clear effects are summarised in Table 2.7.

**Table 2.7 Summary of the effect of different parameters on the coupling coefficient measured in the lab.**

<b>Parameter</b>		<b>magnitude of <math>C</math></b>
fluid conductivity	$\uparrow \sigma_f$	$\downarrow$
mineralogy	$\uparrow$ clay content	$\downarrow$
	$\downarrow$ Formation factor	$\downarrow$
water saturation	$\downarrow S_w$	$\downarrow$
pH	$\uparrow$ 3-9	$\uparrow$
	$\uparrow$ 9-12	$\downarrow$

It is difficult to translate the laboratory measured values to the field and only a few studies have been done where both were measured. In these examples the correspondence between the values is no better than the differences between sites. Part of this lack of correspondence may be due to the difficulty of reproducing field conditions in the lab. If both the streaming current coupling coefficient and the subsurface electrical resistivity of a site are known, they can be used to calculate the hydraulic head distribution from an SP map.

Since this research focuses on SP of electrochemical origin, the streaming potential contribution to SP is considered as noise. Therefore we aim to model the streaming potential to subtract it from the total measured SP. To do this it is necessary to know  $L$  and the subsurface resistivity distribution. In order to calculate  $L$  it is necessary to build a laboratory apparatus that can measure both  $C$  and  $\sigma$  of field sediment samples. We have not found literature examples discussing the impact of contaminants on  $L$ , and this is an important aspect investigated in chapter 4.

## 2.2 Spontaneous potential of electrochemical origin

Spontaneous potentials of electrochemical origin can be divided into three types: membrane, diffusion and redox potentials. Redox electrochemical potentials are not yet fully understood and are the subject of several hypotheses. The term electrochemical potential has a precise definition in chemistry that is different from the phenomenon

discussed here so the phrases electrochemical SP or SP of electrochemical origin will be used.

Membrane and diffusion potentials will be discussed briefly in sub-section 2.2.1 before focusing on redox potentials. Redox terminology is presented in sub-section 2.2.2 before the discussion of redox SP data from different environments. Along with the data, proposed mechanisms causing SP anomalies are described. This research focuses on SP over contaminants but other targets are discussed as well. Examples over ore bodies are presented in sub-section 2.2.3 because they have been studied for a longer period so there are more published data and generally accepted causative mechanisms. Oil fields examples are touched on in sub-section 2.2.4 as they have similarities with contaminant targets, which are discussed in sub-section 2.2.5. Data from different surveys are compiled to study the relationship between spontaneous and redox potentials (sub-section 2.2.6), before a discussion in subsection 2.2.7. The discussion reviews the mechanisms proposed as this study aims to investigate them further.

### 2.2.1 MEMBRANE AND DIFFUSION POTENTIALS

Membrane potentials, also called shale potentials, refer to the electric potentials that can be measured by immersing identical electrodes in solutions of differing concentrations. In living cells, membranes can separate fluids of different conductivities, while in the geological context, it might be the contact between a sandstone and a shale, because the shale is permeable to  $\text{Na}^+$  ions but not  $\text{Cl}^-$  ions (Nyquist & Corry, 2002). The equation describing this potential for different concentrations of an ion  $\text{M}^+$  is (Bockris & Reddy, 1998, eq. 3.104):

$$\phi = \frac{RT}{\mathcal{F}} \ln \frac{a_{\text{M}_1^+}}{a_{\text{M}_2^+}} \quad [2.14.]$$

where  $\phi$  is the electrical potential,  $R$  is the universal gas constant,  $T$  is the temperature,  $\mathcal{F}$  is Faraday's constant and  $a_{\text{M}_{1,2}^+}$  are the activity of ion  $\text{M}^+$  in solutions 1 and 2.

Diffusion potentials, also called liquid junction potentials, arise because ions have different mobilities. For example, if a solution containing NaCl is put in contact with pure water, the  $\text{Na}^+$  and  $\text{Cl}^-$  ions will diffuse into the pure water region because of the concentration gradient.  $\text{Cl}^-$  ions have a higher mobility than the  $\text{Na}^+$  ions (Keller & Frischknecht, 1966), so they will move into the region faster, creating a charge separation which creates an electrical potential. This potential will act to speed up the  $\text{Na}^+$  ions and slow down the  $\text{Cl}^-$  ions so that ultimately they will move at the same velocity though a separation remains.

The diffusion potential in its general form is too complex to solve analytically but if certain simplifying assumptions are made it yields the Plank-Henderson equation (Bockris & Reddy, 1998, eq. 4.289):

$$\phi = \frac{RT}{\mathcal{F}} \sum_i \frac{t_i}{z_i} \frac{c_i(l)}{c_i(0)} \quad [2.15.]$$

where  $t_i$  and  $z_i$  are the transport number and valence of ion  $i$  and  $c_i(0,l)$  are the concentrations of ion  $i$  at distances 0 and  $l$ . The assumptions are (Bockris & Reddy, 1998, p. 501):

- 1) Activity coefficients are taken as unity.
- 2) Transport numbers are assumed constant.
- 3) A linear variation of concentration with distance is assumed.

In the case of an electrolyte with ions of the same valence ( $z:z$ ),  $z_+=z_-=z$ , the concentrations are also the same,  $c_+=c_-=c$  so that equation 2.15 reduces to a form similar to what is found in geophysics texts such as Telford et al. (1990).

$$\phi = \frac{RT}{z\mathcal{F}} (t_+ - t_-) \ln \frac{c(l)}{c(0)} \quad [2.16.]$$

The transport number ( $t_i$ ) depends on the mobility of the ion  $i$  ( $u_i$ ). It is the proportion of the total current being carried by that ion. In the case of a  $z:z$  valent electrolyte:

$$t_+ = \frac{u_+}{u_+ + u_-} \text{ and } t_- = \frac{u_-}{u_+ + u_-} \quad [2.17.]$$

These simpler equations can be derived from the phenomenological equations, yet many geoscientists have chosen to work directly with the phenomenological equations (Marshall & Madden, 1959; Nourbehecht, 1963; Olsen, 1972; Fitterman, 1976; Sill, 1982; Yeung, 1990; Marino et al., 2001; Kulesa et al., 2003). In almost all cases a  $z:z$  valent electrolyte is assumed. This is because if a solution with multiple cations and anions is used, the equations quickly become too complex. In his introduction, Nourbehecht (1963) explains how to proceed for calculations with multiple ions, but his own calculations are with pairs. Using average values he calculates that the maximum plausible potentials generated by diffusion are on the order of 18 mV. Following Nourbehecht's example, Kulesa et al. (2003) use anions and cations but assume their chemical potentials are equal ( $\nabla\mu_c \approx \nabla\mu_a \approx \nabla\mu$ ) since their gradients cannot be very different without large electrical fields developing.

### 2.2.2 REDOX POTENTIALS AND TERMINOLOGY

Oxidation-reduction reactions, also called redox reactions, are chemical reactions in which electrons are exchanged and the participating elements change oxidation state. An example is the oxidation of iron half-reaction:



reduced state  $\Rightarrow$  oxidised state +  $ne^{-}$

Redox potential is the electron exchanging propensity of a medium and is measured as Eh, the electrical potential between an environment and a standard hydrogen half-cell. The Nernst equation describes the electrical potential expected if the oxidation and reduction half reactions of a redox reaction are physically separated, set up as a galvanic cell with a wire and salt bridge connecting both half cells and operated reversibly (Krauskopf & Bird, 1995, eq. 9-17).

$$\text{Eh} = \text{Eh}^0 + \frac{RT}{n\mathcal{F}} \ln \left( \frac{\prod_i [\text{products}]^{n_i}}{\prod_j [\text{reactants}]^{n_j}} \right) \quad [2.19.]$$

where  $\text{Eh}^0$  is the redox potential at standard state,  $n$  is the number of electrons exchanged,  $[x]$  is the concentration of element  $x$  and  $n_{i,j}$  are the coefficients of the products and

reactants in the balanced redox equation. If the cell is not operated reversibly the measured potential will be less than the predicted potential.

Confusion with the terms oxidising and reducing zones stems from the fact that oxidation reactions always occur simultaneously with reduction reactions. In the same reaction organic matter is oxidised while oxygen is reduced, which means the designation of the environment depends on which compound you choose to focus on.

When two half reactions are set up as described for the Nernst equation, the result is a galvanic cell (or voltaic cell). It is one of the two types of electrochemical cells that are similar enough to cause confusion, the other type are electrolytic cells (Figure 2.17). In galvanic cells current flows because of a spontaneous chemical reaction, while in electrolytic cells current flows because of an imposed outside current source. In both cells electrons flow from the anode to the cathode and in both cells reduction occurs at the cathode while there is oxidation at the anode. A difference is that in a galvanic cell the cathode is positive and the anode is negative, while the reverse is true for an electrolytic cell (Seese & Daub, 1981).

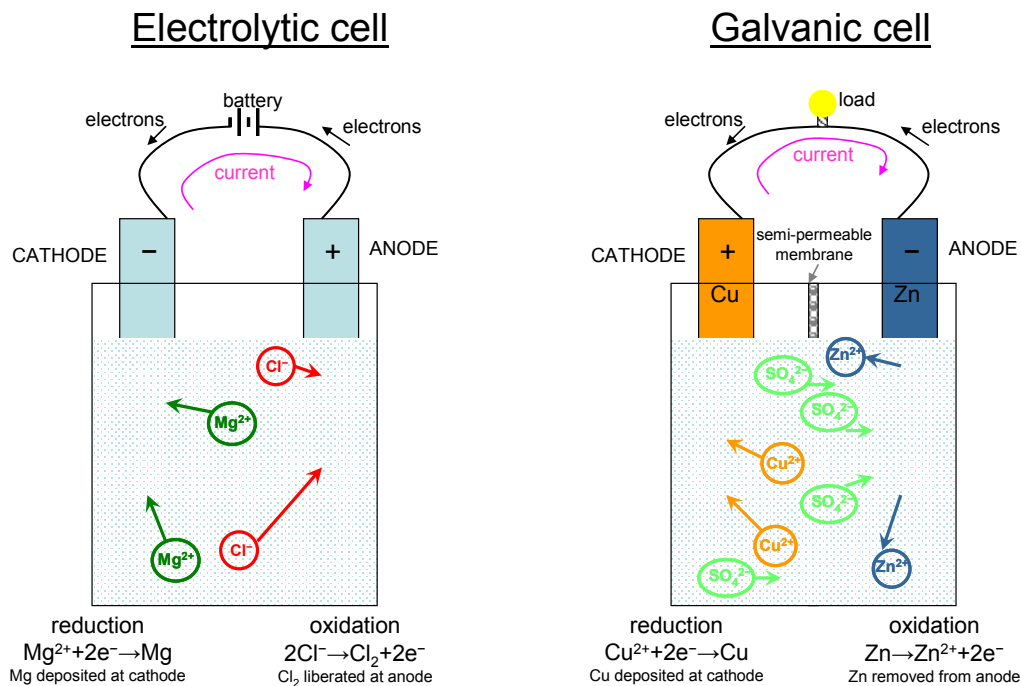


**Figure 2.17 Electrolytic and voltaic cells. (modified from Seese & Daub, 1981; Hess, 1984))**

In geophysics authors refer to natural electrochemical cells as geo-batteries. The galvanic nature of the mechanism was demonstrated by Lile (1996) who was able to find the load at which an SP anomaly developed the most power. Williams et al. (2007) made similar power measurements on a column with sulphate reducing bacteria during a lab experiment.

In the field, redox measurements are made by finding the electrical potential difference (in mV) between an inert electrode, typically platinum, and a reference half-cell immersed in the same medium. The standard reference is the hydrogen half-cell but any can be used if a correction is made. Often Ag/AgCl or Cu/CuSO<sub>4</sub> half-cells are used as they are handier.

Redox potentials are a concept developed in the laboratory that is applied to the field with difficulty. Redox reactions can be slow and natural systems are rarely in redox equilibrium (Lindberg & Runnells, 1984). When the system is in disequilibrium, Eh has

different values depending on the redox couple used to calculate it. This difference can persist longer than 15 000 years, as shown by the groundwater samples collected by Stefánsson et al. (2005) (Figure 2.18).

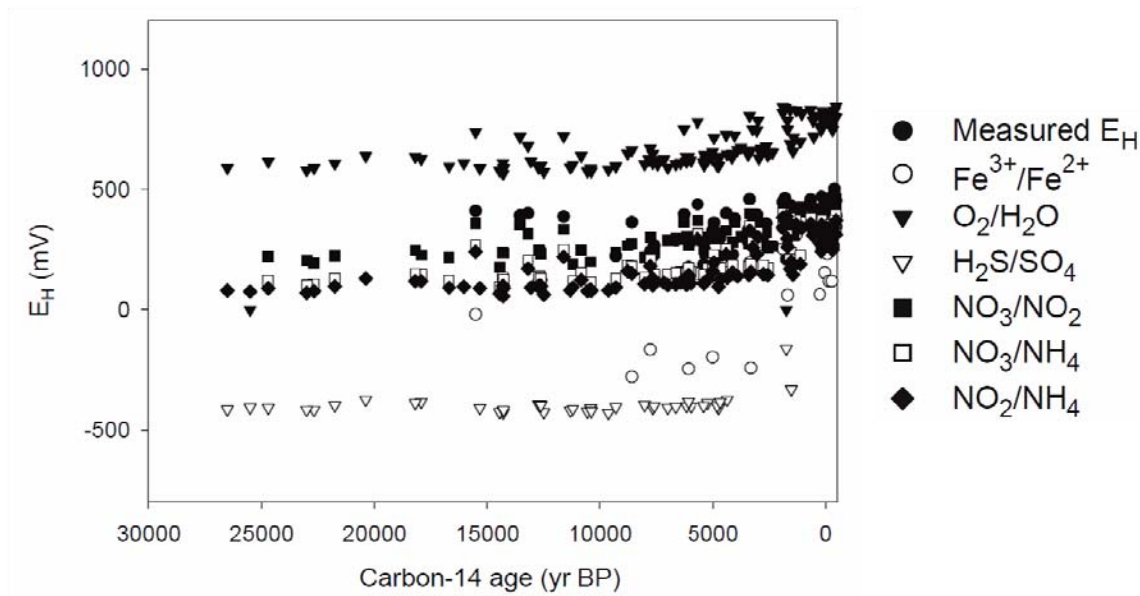


**Figure 2.18** The relationship between calculated Eh and carbon-14 age of groundwater samples. The Eh values of different redox couples are based on measured concentrations of the individual oxidation state of a given element. The carbon-14 age gives an indication of the water age. (Stefánsson et al., 2005)

Even if natural groundwater systems were at chemical equilibrium, it is possible that Eh could not be properly measured with an inert electrode, as suggested above, for three reasons (Hostettler, 1984):

- 1) Totally inert electrode: Electrons on electrode do not react with any aqueous, gaseous or solid species.
- 2) Coated electrode: If there is a coating of oxidation or sulphidation products forming on the electrode, electrochemical equilibrium is achieved between the electrode and coating, but not between the coating and solution.
- 3) Slow electrode: The electrons in the electrode are slow to interact with all oxidants and all reductants. This occurs because some important redox systems are not electroactive. These include the  $\text{NO}_3^-$ - $\text{NO}_2^-$ - $\text{NH}_4^+$ - $\text{H}_2\text{S}$  and  $\text{CH}_4$ - $\text{CO}_2$  systems (Stumm & Morgan, 1996). The  $\text{Fe}^{2+}$ - $\text{Fe}^{3+}$  couple requires

the transfer of a single electron and has the fastest kinetics, so it typically dominates redox measurements (Christensen et al., 2000).

There is general agreement that there is a redox gradient in the earth, similar to the temperature gradient. Eh is positive at the surface and gets negative with depth (Bølviken, 1979). An example is the data of Stoll et al. (1995) in Figure 2.19. Zobell (1946) and Baas Becking et al. (1960) also demonstrated that not only is Eh generally lower with depth, the pH is higher.

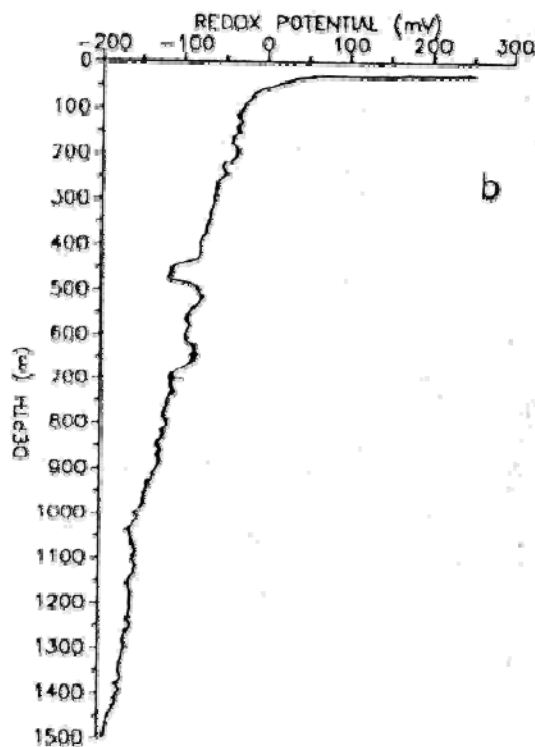


**Figure 2.19** Redox data recorded by a platinum sensor in reference to an Ag/AgCl electrode in the KTB (German Continental Deep Drilling Program) pilot hole. (Stoll et al., 1995)

A link can be made between redox and spontaneous potentials, which are also electrical potentials. SP measurements are made by finding the electrical potential difference (in mV) between two identical electrodes, typically liquid junction Ag/AgCl or Cu/CuSO<sub>4</sub>, at different locations. An electrode is left in one spot as a reference and the other is moved to different stations. The differences between redox and SP measurements may seem

subtle but the two important ones are: for redox both electrodes are at the same location whereas they are not for SP; and SP measurements use two half-cell electrodes while for redox one electrode is inert.

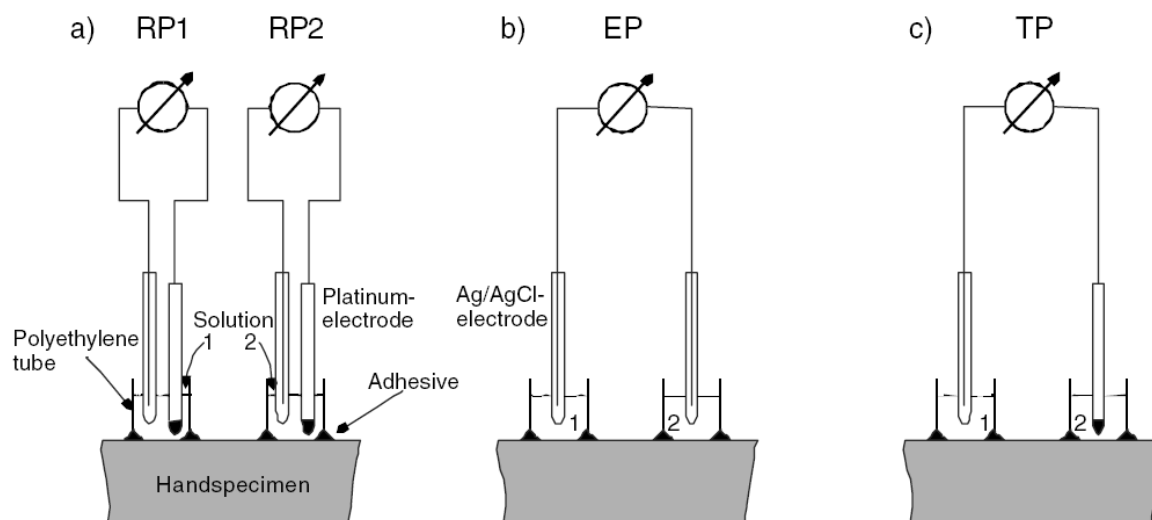


**Figure 2.20** Laboratory measurements of: a) redox potential (RP), b) electric potential (EP), and c) total potential (TP) of various solutions filled in tubes fixed to various hand specimen of rock. (Timm & Möller, 2001) The electrodes with a black tip are platinum electrodes whereas those with a line in the centre are Ag/AgCl electrodes.

Timm & Möller's (2001) investigation involved measuring both these potentials on the same samples. They also measured something they called total potential where the electrodes used for redox measurements are put at different locations (Figure 2.20). They found that the total potential was equal to SP plus one of the redox potentials, RP2 if the set-up is as in Figure 2.20. Timm & Möller did experiments in both the lab and field and Hamilton et al. (2004b) did field experiments that support the additive behaviour of SP and Eh to give total potential.

### 2.2.3 SP OVER ORE BODIES

Spontaneous potential has been used in mineral exploration since the early nineteenth century when the phenomenon was first described by Fox (1830). The results of a few surveys are summarised in Table 2.8. All surveys show a negative peak over ore bodies with magnitudes varying from  $-5$  to  $-1500$  mV.

**Table 2.8 Examples of spontaneous potential surveys over ore bodies.**

<b>Authors</b>	<b>Target</b>	<b>Survey type</b>	<b>Peak SP values (mV)</b>
Poldini (1938; 1939)	sulphides	surface	-150, -260
Sivenas & Beales (1982)	sulphides	surface	-20
		well log	-300
Corry (1985)	sulphides	surface	-800
	graphite	surface	-600
Stoll et al. (1995)	graphite	surface	-600, -800
		well log	-200
Lile (1996)	sulphides	surface	-380
Rao et al. (2000)	uranium deposits	well log	-200
Hamilton et al. (2004a)	sulphides	surface	-5, -10
Heinson et al. (2005)	banded iron formation	underwater	-50
Bhattacharya et al. (2007)	graphite	surface	-60, -540
	sulphides	surface	-130
Mendoça (2008)	disseminated sulphides	surface	-1500
Castermant et al. (2008)	rusting iron bar	laboratory	-50

Spontaneous potential anomalies are areas of anomalously high current density ( $j$ ). In a medium like the earth, the current density is described by:

$$j = E\sigma \quad [2.20.]$$

where  $E$  is the electrical field strength and  $\sigma$  is the conductivity. Hamilton (2000) explained that to get anomalously high current densities, it is necessary to have either anomalously high electric fields or conductivities. Cull (1985) demonstrated that an electric field from an outside source, which he did not characterise, would cause spurious current densities in the ground if there were contrasts in resistivity. Ore bodies are relatively conductive with respect to typical host rocks and vertical bodies are thought to link together zones from different depths with different redox potentials by a sort of short circuit. Conduction through the ore body is often referred to as occurring electronically, as opposed to the country rock where ions in groundwater filling fractures carries current

electrolytically. Though graphite may carry current electronically, most ores including sulphides and oxides are semi-conductors (Lile, 1994). However, with a few exceptions, metal sulphides and arsenides are nearly as conductive as true metals (Keller & Frischknecht, 1966).

Earlier authors (Schlumberger & Schlumberger, 1922; Poldini, 1938; 1939) believed that the ore had to be perfectly continuous in order to conduct electrons and create an SP anomaly. However many SP anomalies have been measured over disseminated sulphides which lack this electrical conductivity. Furness (1992) suggested that conduction could be both electronic through ore grains and ionic between them to produce significant anomalies. There are existing models, like that of Bigalke & Grabner (1997), that assume electronic conductors extending over some 100 metres up to kilometres.

Though ore bodies provide good conductors, it is still necessary to have an electrical field to generate an SP anomaly. This field is thought to be a result of redox reactions where the half-reactions are separated in space. There are three geo-battery hypotheses that involve different chemical reactions, though all include a near vertical ore body divided into a positively charged cathode at its apex and a negatively charged anode at depth (Figure 2.21). The electrical circuit is completed by ions in the groundwater beside the ore moving in response to the electrical field. This sets up two electrical dipoles, near the surface the ore itself is positively charged, but the environment around it is negatively charged because of an excess of anions, producing the negative SP anomalies. Likewise, at depth the ore anode is negative but the environment around it is positively charged. A fourth hypothesis assigns a critical role to the SP survey equipment. Each hypothesis will be discussed in turn.

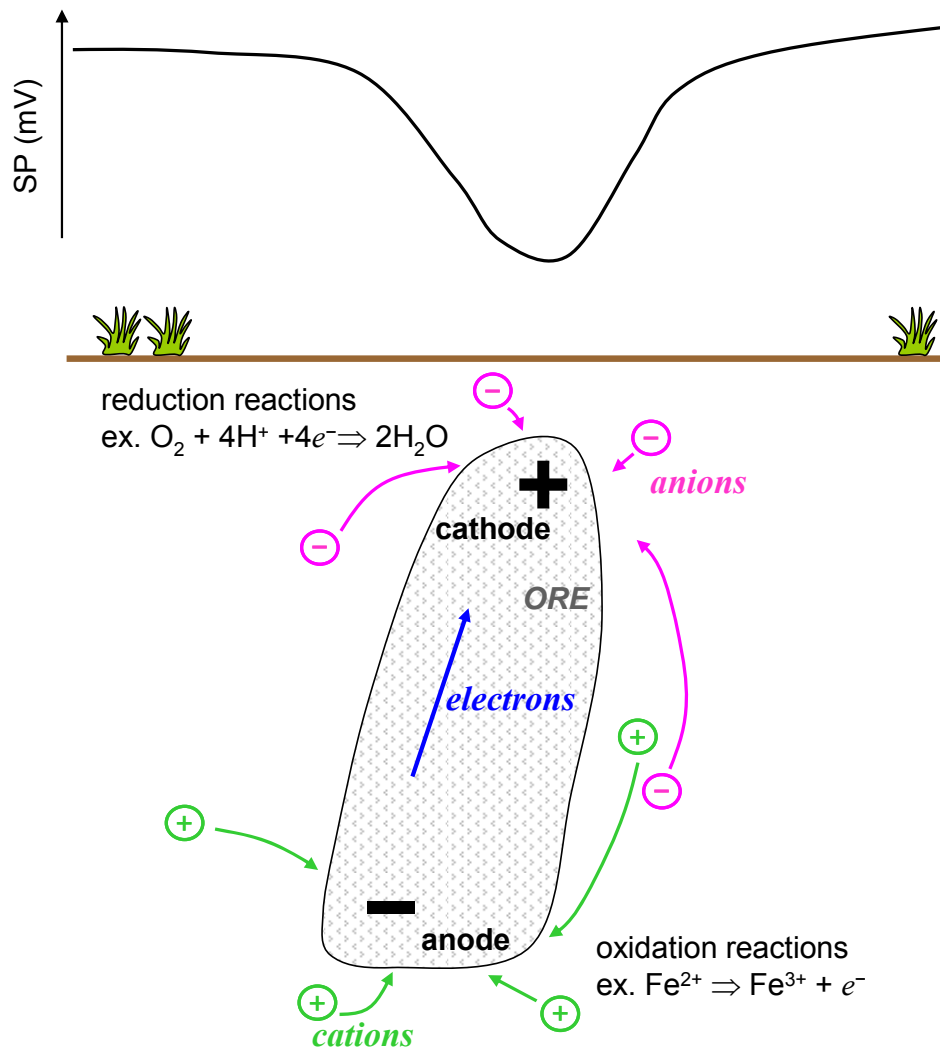
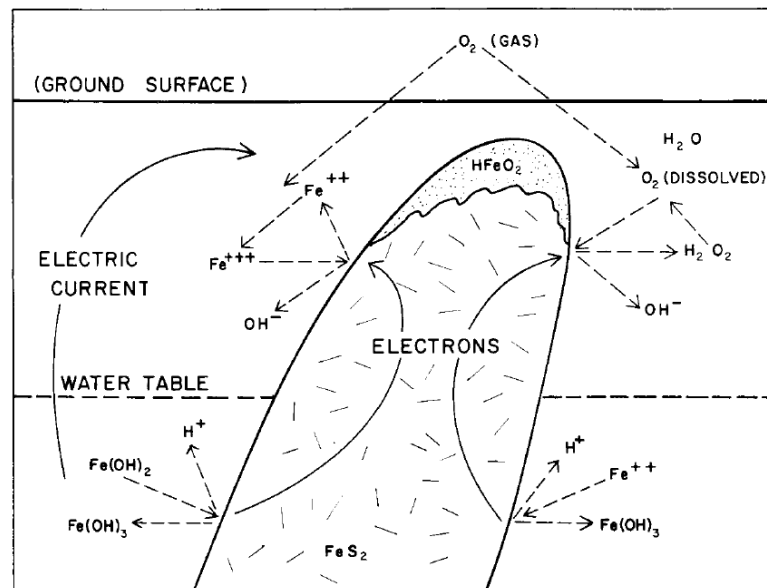


Figure 2.21 Sketch of geo-battery set up.

The first hypothesis was suggested by Schlumberger & Schlumberger (1922) and Poldini (1938; 1939) and further developed by Sato & Mooney (1960). The ore does not react but simply acts as “an inert medium for the transport of electrons”. Sato & Mooney (1960), whose model is illustrated in Figure 2.22, believed that the most probable reactions occurring above the water table were the ferrous-ferric ion and hydrogen peroxide-oxygen pairs, whereas below the water table it was again ferrous-ferric ions and possibly ferrous-ferric hydroxide.



**Figure 2.22 Proposed electrochemical mechanism for self-potentials. (from Sato & Mooney, 1960)**

The maximum potential difference across both ends of the conductor these authors calculated was 800 mV, and since SP is typically measured above ground the largest anomalies should be on the order of 400 mV. This is significantly less than several reported anomalies which can reach magnitudes of up to 1V. Sivenas & Beales (1982) suggested that other reactions could be chosen so long as they remain within the Eh stability field of water since we do not see hydrogen or oxygen gas evolving from ore bodies. This increases the maximum potential difference to 1.23 V across the conductor, but as Hamilton (2000) stressed this is unrealistically high as a maximum because the calculations assume a reversible thermodynamic reaction which is not the case in nature.

Schlumberger & Schlumberger (1922), Poldini (1938; 1939) and Sato & Mooney (1960) divided the underground into an oxidised zone above the water table and a reduced zone below it, implying that the water table had to intersect the ore body. They thought that the role of the water table and groundwater was essential so that SP anomalies would be unimportant in very arid climates or in arctic regions. Corry (1985) reports that this is not the case. The idea that everything is oxidised above the water table and reduced below it

may be too simple, suggesting that the Bølviken model of a redox gradient in the earth might be more appropriate.

Thornber (1975b; a) studied a massive nickel sulphide deposit in Australia and proposed the second hypothesis. The ore participates in the oxidation-reduction reactions, which leads to its alteration. The cathodic reaction is a series of reactions involving oxygen and the anodic reactions depend on the type of ore and its depth. They include pyrrhotite to pyrite and pentlandite to violarite. These reactions match the minerals he was able to find at different depths. Though he did not present a typical SP map, he did many Eh and pH measurements on samples taken from various depths and locations in the ore body. Thornber concluded: “The Eh-pH data reflect the condition of a galvanic cell after it has partially run down. The unreacted fully charged cell would have given a constant Eh and pH throughout the ore body.”

Sivenas & Beales (1982) take a middle road approach for the third hypothesis, suggesting both the mechanism proposed by Sato & Mooney (1960), which they call an oxygen concentration cell, and that of Thornber (1975b; a), which they call a sulphide galvanic cell, act simultaneously.

An incongruity between these first three models and field data that has been pointed out by Corry (1985) is the lack of positive poles. If these ore bodies are accepting electrons at depth, then there must be an area which is anodic. Surface SP surveys rarely show a positive pole, perhaps because it is masked by the cathode which is nearer to surface. However well logs through ore bodies should show positive peaks at depth, yet measured SP is negative when passing through ore zones (Figure 2.23). In a lab experiment with an iron bar rusting in a saturated sand tank, Castermant et al. (2008) measured a positive peak at depth, but there are no reported field examples.

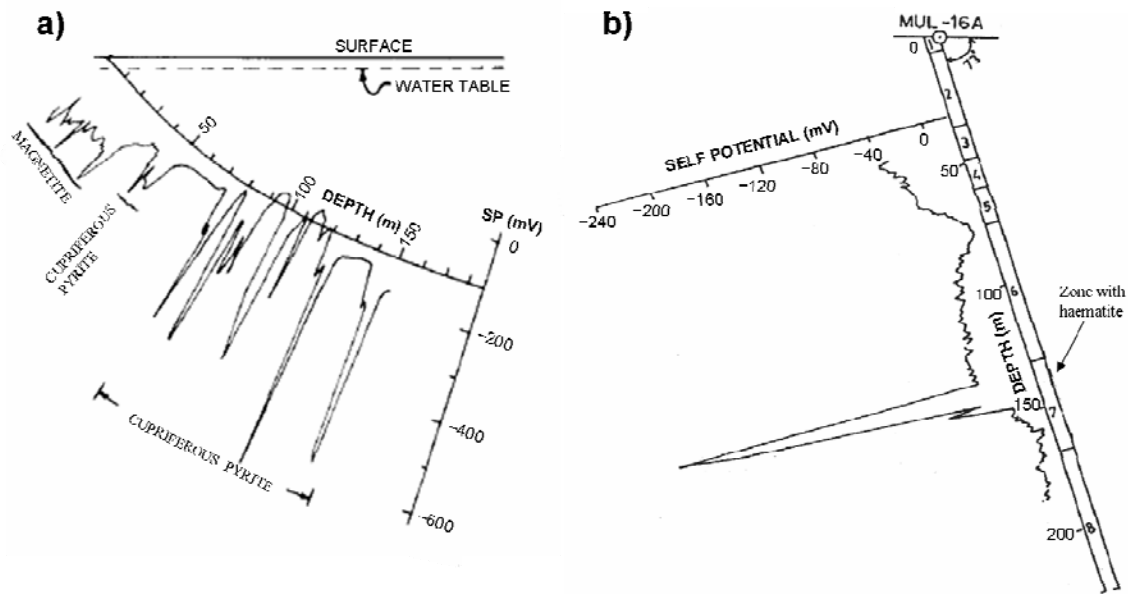


**Figure 2.23 a) Down hole SP in hole 65 intersecting the Kimheden ore body, Sweden. Redrawn from Parasnis (1970). (Corry, 1985) b) SP and litho-logs of borehole MUL-16A. (Rao et al., 2000)**

The last hypothesis is that of Corry (1985) where no current flows naturally. He suggests that “the measured potential must be the result of perturbing an otherwise stable field by making an electrical connection between the host rock and sulphide”. The survey electrodes planted in the ground and the wire between them creates a galvanic cell where the wire is the electronic conductor, instead of a conductive ore body. Corry believes that the SP measurement is the difference in oxidation potential between the two electrode locations. He suggested that ferroelectric effects may be important in setting up potential differences (Corry, 1994). Several sulphides are ferroelectric, which means that below their Curie temperature they hold permanent electrical polarization due to asymmetry in the position of anions and cations in their crystal lattice. The model proposed by Corry (1985) is similar to Thornber’s because the ore is altered as the rock weathers, which gives rise to different anomalies depending on the state of weathering.

These hypotheses outline general mechanisms and there seem to be two methods followed for calculating magnitudes of spontaneous potential anomalies associated with

specific sites: the apparent mobility and overpotential methods, which will be discussed in the sub-section about quantitative analysis of SP (2.3.3.3).

#### 2.2.4 SP OVER OIL FIELDS

Pirson (1981) found that SP typically decreases with depth in oil exploration well logs (water gradient). However, in wells over oil fields, the slope is reversed so that SP increases with depth (oil gradient). According to Pirson some oil leaks into the shales above the reservoir where it gets degraded, forming a zone that is reduced with respect to the surrounding oxidised sediment. This sets up a redox galvanic cell whose electric currents can be measured both at the surface and down hole (Figure 2.24). Tomkins (1990) uses the same model when discussing direct methods of finding oil deposits but does not develop it further.

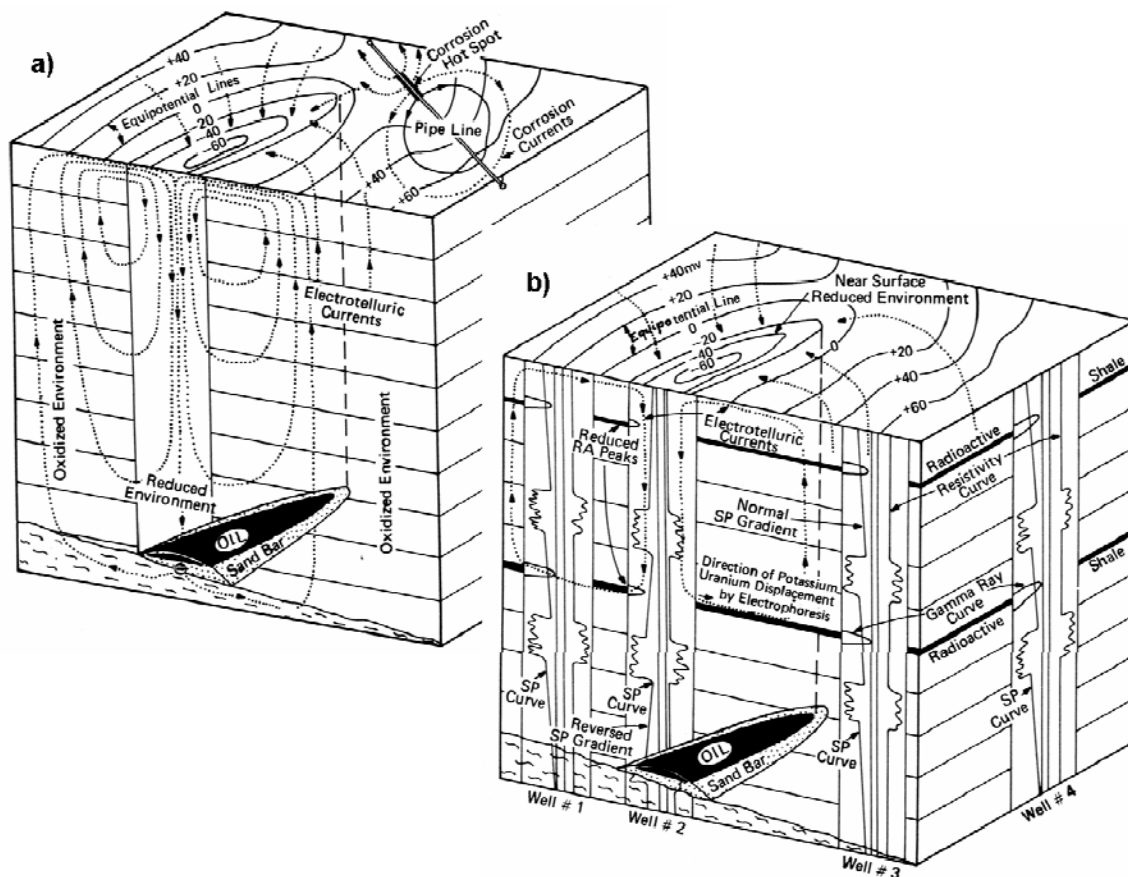


Figure 2.24 Equipotential lines on both blocks are SP contours in mV measured at the ground surface. a) Distribution of electrochemical currents generated by an oil field before drilling and its associated self-potential sink at the surface of the ground as delineated by equipotential lines with possible disturbances by pipelines. b) Effect

---

**of electrotelluric currents on the SP curves of the wells drilled in and around an accumulation of oil and on the radioactivity of shale beds. (Pirson, 1981)**

According to Hamilton (2000) spontaneous potential anomalies over oil fields are an example of anomalously high current densities due to anomalously high electric fields (equation 2.20).

#### *2.2.5 SP OVER CONTAMINATED AREAS*

The use of spontaneous potentials as a method of finding or delineating contaminants in environmental studies is relatively recent, the oldest reference to such a survey found was Weigel (1989) The targets of environmental studies are shallow zones (<50 m) impacted by redox-active pollution from several possible sources: landfill leachate, mine tailing pond effluent, hydrocarbons leaking from storage tanks and many others. Since the method is being developed and field data does not present as clear a pattern as SP over ore bodies, all articles I found with environmental SP targets are compiled in three tables. The fourteen studies are divided according to the polarity of the SP anomaly. Positive anomalies are found in Table 2.9, both positive and negative in Table 2.10 and negative ones in Table 2.11.

**Table 2.9 Spontaneous potential surveys over environmental targets with positive anomalies. Abbreviations: meas.–measurements, PCE–tetrachloroethylene, conc.–concentration, SVE–soil vapour extraction, IP–induced polarization, TEM–time domain electromagnetics.**

<b>Authors</b>	<b>Target</b>	<b>Peaks (mV)</b>	<b>SP data</b>	<b>SP anomaly characteristics</b>	<b>Other geophysics</b>	<b>Information on target</b>	<b>Bio-ventilation</b>
<i>Positive anomalies</i>							
Minsley et al. (2007a)	chlorinated solvent leaked from holding pond	+150	112 surface & borehole meas., interpolated in 3D	smooth	resistivity, IP	PCE conc. from wells	SVE
Naudet (2004)	oil from well blow-out	+40	440 profile & scattered meas., interpolated	bull's eyes around bioventing wells	resistivity	redox and geochemistry from wells	bio-ventilation
Buselli & Lu (2001)	acid mine drainage from tailing ponds	+30	30 meas. on grid, interpolated	relatively smooth <sup>1</sup>	resistivity, IP, TEM	limited geochemistry from adjacent wells	no

<sup>1</sup>Authors were unsure of source, may be due to streaming potential.

**Table 2.10 Spontaneous potential surveys over environmental targets with both positive and negative anomalies.**  
**Abbreviations: meas.–measurements, SVE–soil vapour extraction, IP–induced polarization, GPR–ground penetrating radar.**

<b>Authors</b>	<b>Target</b>	<b>Peaks (mV)</b>	<b>SP data</b>	<b>SP anomaly characteristics</b>	<b>Other geophysics</b>	<b>Information on target</b>	<b>Bio-ventilation</b>
<i>Positive and negative anomalies</i>							
Doherty et al. (2010)	hydrocarbons from tar pit at gas works	dipole –450- +350	110 meas. on grid, interpolated	relatively smooth dipole	resistivity, IP	redox and geochemistry from wells	no
Hämmann et al. (1997)	construction waste leachate	+75	profile	anomalies on noisy regional gradient	none	location of landfills	no
	household & industrial waste leachate	–30					
Nash et al. (1997) Che-Alota et al. (2009)	fuel in abandoned fire training area — 1996	+24	374 meas. on grid, interpolated	rather spotty <sup>1</sup>	resistivity, IP, GPR	redox and geochemistry from wells	no
	fuel in abandoned fire training area — 2007	–30	273 meas. on grid, interpolated	very spotty			SVE

<sup>1</sup>Authors believe part of anomaly is due to unmapped utility line, the portion they refer to has the same magnitude and size as principle anomaly.

**Table 2.11 Spontaneous potential surveys over environmental targets with negative anomalies. Abbreviations: meas.–measurements, SVE–soil vapour extraction, IP–induced polarization, DO–dissolved oxygen, neg.–negative.**

<b>Authors</b>	<b>Target</b>	<b>Peaks (mV)</b>	<b>SP data</b>	<b>SP anomaly characteristics</b>	<b>Other geophysics</b>	<b>Information on target</b>	<b>Bio-ventilation</b>
<i>Negative anomalies</i>							
Weigel (1989)	waste dump leachate	–15	profile	sharp trough on noisy background	none	limited geochemistry from wells	no
Bavusi et al. (2006)	landfill leachate	–40	107 & 93 scattered meas., interpolated	spotty	resistivity, IP	deduced from resistivity	no
Nyquist & Corry (2002)	leachate from canning plant	–80	? meas., interpolated	smooth	none	DO in wells	no
Vichabian et al. (1999)	leaks from pipeline, tank, spill	–100, –50, –60	1 profile per site	multi-step neg. peaks, most over targets	none	determination method unspecified	no
Perry (1997)	underground oil storage tank leaks	–220, –50	580, 1300 meas., contoured	smooth, very spotty	none	geochemistry from wells	no
Revil et al. (2010)	oil spill near a refinery	–160	70 meas. along profile	smooth profile with large clear anomaly	resistivity	determination method unspecified	no
Naudet et al. (2004) Arora et al. (2007) Linde & Revil (2007)	landfill leachate	–400	>2800 meas. along profiles, interpolated	smooth with 2 negative anomalies <sup>1</sup>	resistivity	redox and geochemistry from wells	no
Shi (1998)	jet fuel plume	–600	83 meas., gridded	? <sup>2</sup>	resistivity	geochemistry from wells	SVE & air sparging

<sup>1</sup> Only one anomaly is considered, second due to clay lens. <sup>2</sup> Characteristics cannot be seen because only a black & white photocopy of the coloured grid is available.

Contrary to SP surveys over ore bodies, those over contaminant targets do not have a characteristic anomaly pattern. If the same mechanisms are acting, one would expect negative anomalies as well. To produce a negative anomaly from a galvanic reaction, the area has to be cathodic relative to the surroundings, implying that it must be undergoing reduction. This fits with the knowledge that the degradation of organic contaminants produces reduced zones in the groundwater (Christensen et al., 2000).

Three of the fourteen studies presented had only positive anomalies. One of these studies is uncertain (Buselli & Lu, 2001) and the two others had bioventilation systems on site. The authors specified that they were no longer operating (Naudet, 2004) or turned off during the survey (Minsley et al., 2007a). These systems, either soil vapour extraction or air sparging, inject air into the subsurface to promote biodegradation. The oxygenated zone may become anodic relative to the surroundings, creating a positive SP anomaly at the surface. The data from two other studies on sites with soil vapour extraction systems provide contrary evidence. Shi (1998) reports a  $-600$  mV anomaly over such a system, specifying that it was turned off for the duration of the survey. In the case of Che-Alota et al. (2009) the system state is unspecified and a survey before soil vapour extraction initiation had a small positive anomaly whilst there is a small negative anomaly afterwards. It is not possible to draw conclusions about the effect of bioventilation on SP measurements.

The only two other studies that include positive anomalies are those by Hämmann et al. (1997) and Doherty et al. (2010). There is little detail in the study by Hämmann et al. (1997), but it is interesting to note that the different types of landfill waste produced different polarity anomalies. Household waste can be expected to contain more organic contaminants than construction waste and maybe that is what gave rise to the negative anomaly. Analogously, Greenhouse & Harris (1983) did not find any surface SP anomalies over the Borden landfill which has 80 % wood and construction waste. The dipole measured by Doherty et al. (2010) is unique and as an explanation they propose a model with a biological anode produced by hydrocarbon degradation at 5-7 m depth

separated by a thin clay aquiclude from an abiotic cathode where buried clinker and iron compounds are oxidised at 0-2.2 depth. A trial pit dug through the aquiclude and backfilled with conductive waste acts as a conductor between the two regions. It is surprising that the cathode below is not masked by the anode, but rather appears beside it, and that two adjacent trial pits do not have the same effect.

In general the polarity of SP anomalies over reduced contaminant zones seems to be negative. Weigel (1989) wrote that anthropogenic noise caused positive anomalies while real anomalies presented negative peaks.

The two mechanisms proposed for contaminant SP anomalies are similar to those for ore bodies in that they involve zones with different redox potentials.

The first hypothesis is that the spontaneous potentials are due to the difference between the redox potential at the two measurement locations. Vichabian & Morgan (1999) used this idea when they converted measured spontaneous potentials into oxygen partial pressure contrasts using the Nernst equation and they got reasonable agreement with measured data. Nyquist & Corry (2002) proposed the same idea, though they believed that there is no current flow before the SP survey is set up.

Empirical observations by Naudet et al. (2003; 2004) and Naudet & Revil (2005) bring a modulation to hypothesis, suggesting that instead of being equal, the potentials are linearly related. Measured spontaneous and redox potential for 8 locations showed a linear relationship (Figure 2.25).

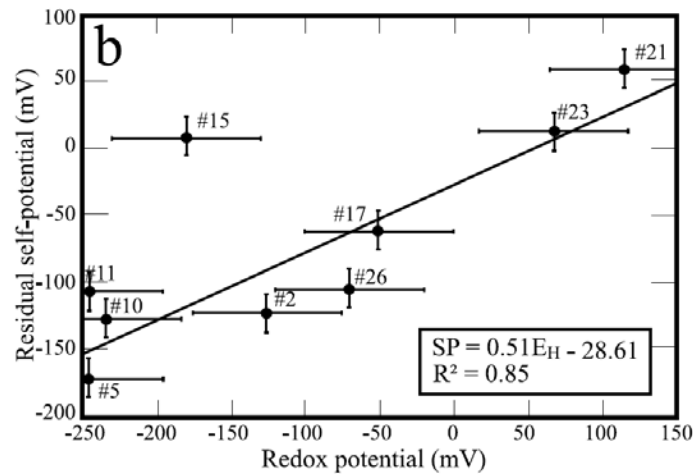


**Figure 2.25** Redox potential measured with an error of  $\pm 50$  mV versus the residual self-potential estimated with an error of  $\pm 20$  mV. Data point #15 is excluded from the slope calculation. (Naudet et al., 2003)

They proposed the equation

$$\phi_H - \phi_0 = C_H (E_H - E_{H_0}) \quad [2.21.]$$

where  $C_H$  is a dimensionless redox coupling coefficient and H and 0 are the measurement and reference locations. This is analogous to the streaming potential coupling coefficient.

$$\text{streaming potential : } C = \frac{\Delta V}{\Delta P} \quad \text{redox potential : } C_H = \frac{\Delta V}{\Delta E_H}$$

The theoretical foundation for the second hypothesis is explained in Revil et al. (2009). The authors work with a form of the diffusion equation (2.15) and assume that effectively all the current is being carried as electrons through microbial mats. They can therefore assign a transport number of one to the electrons and because the concentration of electrons can be expressed as Eh, they develop the equation:

$$\nabla \cdot (\sigma \nabla \phi_r) = -\nabla \cdot (\sigma \nabla E_H) \quad [2.22.]$$

where  $\nabla \phi_r$  is the SP due to redox. Given the complexity of this equation it is not possible to test its validity with a cross-plot, numerical modelling is necessary and was undertaken by Arora et al. (2007). This hypothesis is also discussed in Linde & Revil (2007), Castermant et al. (2008) and Revil et al. (2010). The implementation of this equation is further discussed in sub-section 2.3.3.3.

A critical element of the second hypothesis is the electronic conductor, an idea discussed further in Revil et al. (2010). The authors believe that it is found in a thin zone at the capillary fringe between the saturated and vadose zones and they call it the transition zone. They locate the transition zone very precisely in the capillary fringe because they believe this is where the strongest redox gradient will occur, between a contaminant plume in the groundwater and the oxygenated vadose zone. The two versions of this hypothesis they propose incorporate bacterial with pili to transfer electrons (Figure 2.26). The first version also includes certain semi-conducting minerals like sulphides that can precipitate under certain redox conditions.

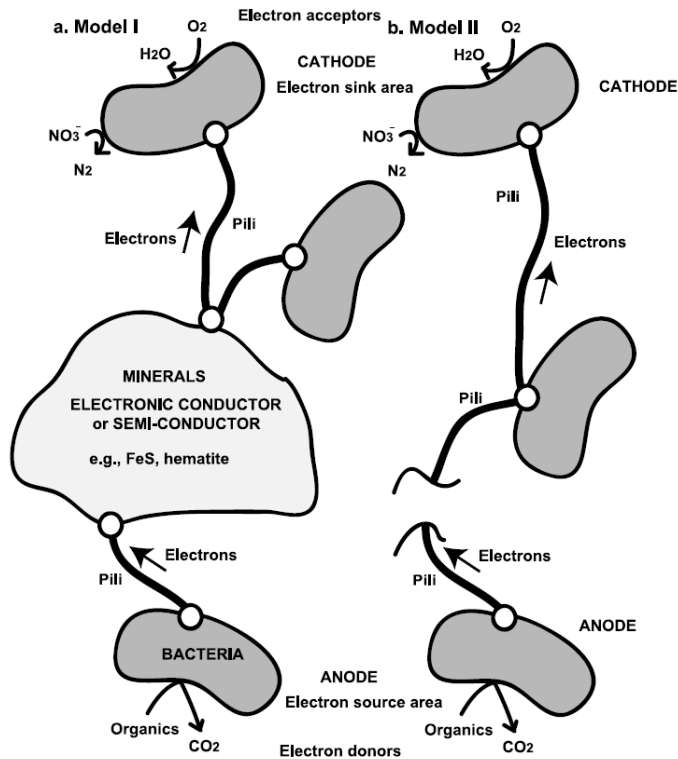


**Figure 2.26** Sketch of two possible electron transfer mechanisms in a contaminant plume. a) In model I, the presence of minerals facilitates electronic conduction. b) In model II, only bacteria populations are connected by conductive pili. At the “bacterial anode”, electrons are gained through the oxidation of the organic matter, iron oxides or Fe-bearing phyllosilicates. The electrons are conveyed to the “bacterial cathode” through a network of pili. At the “bacterial cathode”, the reduction of oxygen and the nitrate prevails as electron acceptors. In this system, bacteria act as catalysts. The transport of electrons through the anode to the cathode of the microbattery may involve different bacterial communities and different electron transfer mechanisms including external electron shuttles. (Revil et al., 2010)

Bacterial pili are hair-like protein structures projecting beyond the bacterial surface that are not involved in motility and the term fimbriae is sometimes used interchangeably with pili (Neidhardt et al., 1990; Prescott et al., 2005). The most common are sex pili that form the initial attachment between mating pairs of bacteria during conjugal transfer of DNA (Neidhardt et al., 1990; Becker & Deamer, 1991). The bacterial pili in Revil et al.'s (2010) model act like copper wires transferring electrons, and though this is not a typical function of pili, some bacteria appear to have electrically conductive nanowires (Reguera et al., 2005; Gorby et al., 2006).

Both the Eh difference between measurement points and the redox current hypotheses link spontaneous and redox potentials, but the second allows for the fact that the electrical and redox domains could be different.

#### *2.2.6 RELATIONSHIP BETWEEN SPONTANEOUS AND REDOX POTENTIALS*

All hypothesized mechanisms for SP anomalies of electrochemical origin link spontaneous and redox potentials. The first hypothesis for contaminant SP can be tested with a cross-plot of spontaneous and redox potentials, so such plots will be presented in this sub-section. Few studies have measured both types of potentials at the same locations and these are listed in Table 2.12, along with the Spearman correlation coefficient between redox and SP. They will each be described in the seven following sub-sections.

**Table 2.12 Articles where authors have measured spontaneous and redox potentials at the same locations. Spearman correlation coefficient between redox and SP. Abbreviation: n.s.—not significant at the 95% level, KTB—German Continental Deep Drilling Program.**

<b>Authors</b>	<b>Type/site</b>	<b>Target</b>	<b>Spearman correlation coefficient</b>
Stoll et al. (1995)	KTB deep drilling site	graphite bodies	−0.683
Timm & Möller (2001)	mine site	porphyry copper deposits	n.s.
Naudet et al. (2003)	Entressen landfill	landfill leachate	0.770
Hamilton et al. (2004a)	northern Ontario	sulphide deposits	n.s.
Castermant et al. (2008)	laboratory	rusting iron bar	−0.308
Hamilton & Hattori (2008)	northern Ontario	forest ring	n.s.
Revil et al. (2009)	laboratory	electrolytically induced redox gradient	−0.879

In some cases (Timm & Möller, 2001; Hamilton et al., 2004a) the redox potentials measured are not reported as Eh because they have not been referenced to the standard hydrogen electrode. If this referencing were done, a constant would be added to all Eh values, which would not change the slope of a possible correlation with SP.

#### 2.2.6.1 Stoll, Bigalke & Grabner, 1995

Stoll et al. (1995) present data from the KTB drill hole in northern Bavaria. Since the data are continuous, only the values every 50 m were noted. The redox potential at the surface SP reference electrode location was not specified, so +250 mV was used since it is the value recorded at the shallowest depth, it is plausible for an oxic surface environment, and typically the SP reference electrode is located next to the well at the surface. The authors do not discuss hydraulic gradients so it is difficult to know what the contribution from streaming potential might be.

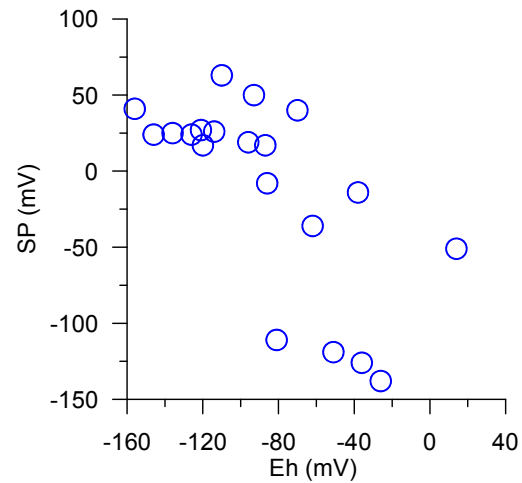


**Figure 2.27** Scatter plot of data obtained from Stoll et al. (1995). The data show anti-correlation between Eh and SP.

When plotted in a scatter diagram (Figure 2.27), SP and Eh are significantly correlated at the 95% level, with a Spearman correlation coefficient of  $-0.683$ . The four measurements with SP below  $-100$  mV were all from depths with negative excursions in the SP profile.

#### 2.2.6.2 Timm & Möller, 2001

In their field measurements, Timm & Möller (2001) refer to the redox potential as clay potential because they fixed the electrodes to the rock using bentonite and they have not compensated for the clay effect, which would be the same everywhere. There is no discussion of the role streaming potential might play in the field SP measurements.

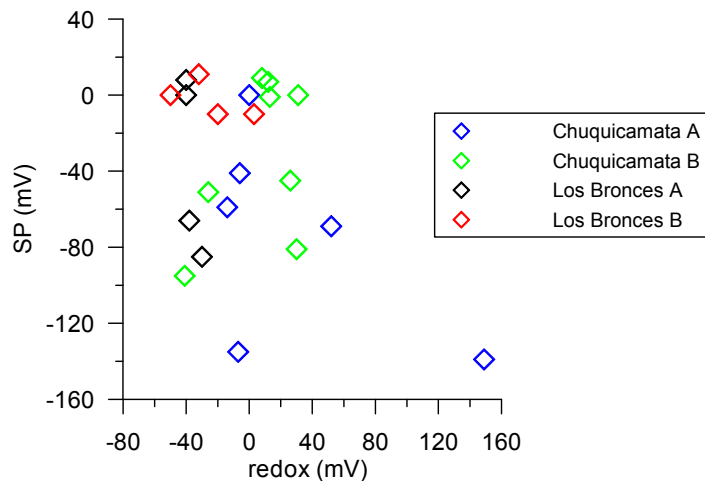


**Figure 2.28** Scatter plot of data obtained from Timm & Möller (2001).

The scatter plot (Figure 2.28) does not have any significant trends, whether the different measurement series are taken individually or as a whole.

## 2.2.6.3 Naudet, Revil &amp; Bottero, 2003

Naudet et al. (2003) did a large SP survey over the leachate plume of the Entressen landfill in southern France. They present their data in the form of a scatter plot of  $\nabla E_h$  vs. residual SP (Figure 2.29). The residual SP refers to the fact they have removed the estimated contribution due to streaming potential from the measured SP. The SP survey was done on the surface and Eh measurements were done on groundwater from wells where the water table was 2-12 m below ground.

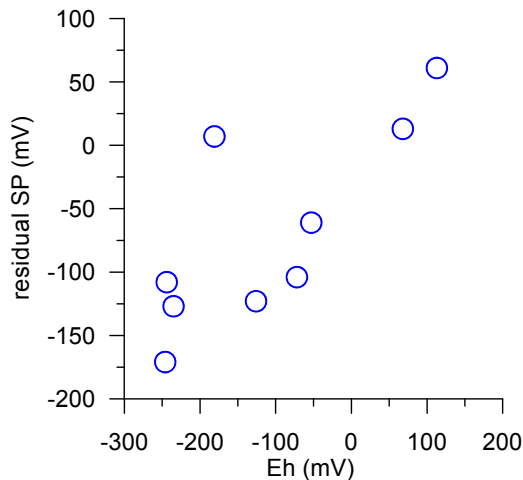


**Figure 2.29 Scatter plot presented by Naudet et al. (2003).**

SP and Eh are significantly correlated at the 95% level, with a Spearman correlation coefficient of 0.770 (Figure 2.29). The authors chose to disregard the data point at (-181, 7) because it is situated in a large negative SP anomaly above a clay lens. In this case the Spearman correlation coefficient is 0.924.

## 2.2.6.4 Hamilton, Cameron, McClenaghan &amp; Hall 2004a

Hamilton et al. (2004a) present spontaneous and redox potential data gathered in shallow wells in glacial sediment above a sulphide deposit near Timmins, Ontario. The wells are 9 m deep and the water table is within 4 m of the surface throughout the study area. The spontaneous and total potentials were measured down the wells by immersing Cu/CuSO<sub>4</sub> and platinum electrodes in the groundwater while using a surface Cu/CuSO<sub>4</sub> base station as reference. The redox potential measured was the voltage difference between the two immersed probes. The data points collected while the platinum electrode was depolarizing were not used. The water table seems relatively flat, which suggests that unless there are

large vertical hydraulic gradients, the hydraulic gradients are small and the streaming potential contribution to measured spontaneous potential will be minimal.

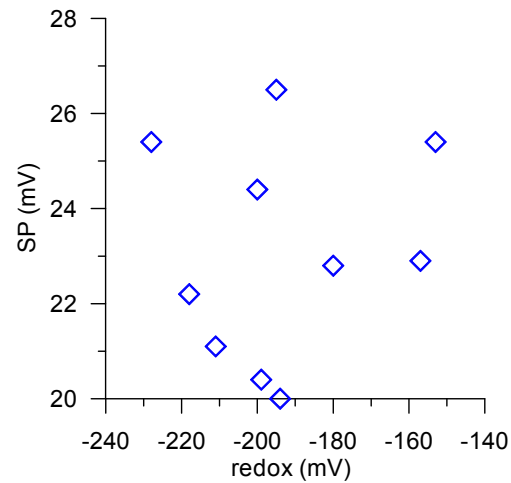


**Figure 2.30** Scatter plot of data obtained from Hamilton et al. (2004a).

When plotted in a scatter diagram (Figure 2.30) SP and redox do not show any correlation, though there is almost no variation in spontaneous potential. Field SP measurements typically have  $\pm 5$  mV error and the range of data is only 6.5 mV. The overburden at the site is  $\sim 30$  m of varved clay and silt, which would attenuate the response expected from a sulphide deposit.

#### 2.2.6.5 Castermant, Mendonça, Revil, Trolard, Bourrié & Linde, 2008

Poldini (1938; 1939) and Thornber (1975a) describe lab experiments with pieces of ore in sand tanks. Castermant et al. (2008) performed a similar lab experiment with detailed observations. They put an iron bar in a saturated sand tank and monitored SP, Eh and pH for six weeks as it rusted. There is no contribution from streaming potential to the SP signal. A. Revil graciously provided the data used for publication.

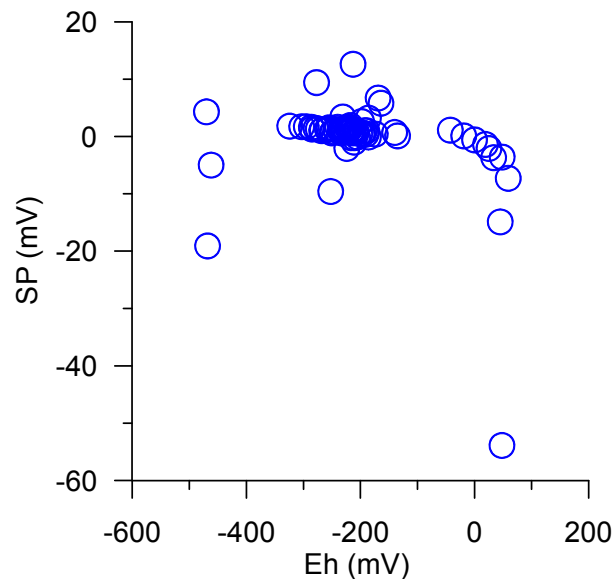


**Figure 2.31** Scatter plot of data from Castermant et al. (2008).

The cross-plot of Eh vs. SP has most of the data clumped together (Figure 2.31), but there is still a significant correlation at the 95% level, with a Spearman correlation coefficient of  $-0.308$ .

#### 2.2.6.6 *Hamilton & Hattori, 2008*

Hamilton & Hattori (2008) did an SP survey over a forest ring in north eastern Ontario. Forest rings are circular features in the boreal forest visible on aerial photographs because of a change in vegetation at the rims of the rings. They are typically hundreds of meters in diameter and centered on accumulations of reduced substances in groundwater, overburden or rock. The measurements were made in shallow wells in a set-up identical to that described by Hamilton et al. (2004a). In this case the redox potentials presented are calculated (total potential – SP) instead of being measured directly with a platinum electrode. The authors have disregarded one measurement (+120 m on E-W line) where they thought the SP measured was primarily due to streaming potential because of hydraulic gradients caused by a change in overburden from lacustrine clay to esker sand. This implies that they thought the other measurements were relatively unaffected by streaming potential.

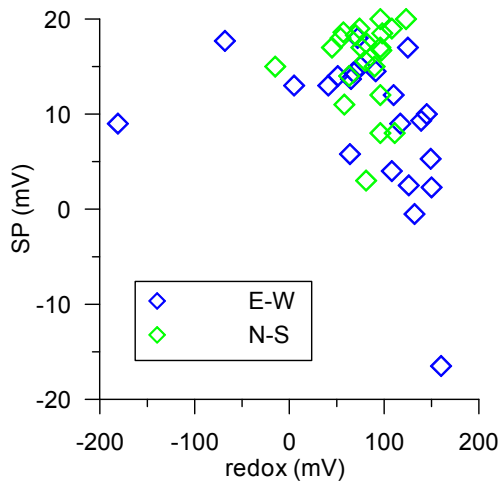


**Figure 2.32 Scatter plot of data obtained from Hamilton & Hattori (2008).** As can be seen on the scatter plot of redox vs. SP (Figure 2.32), there is no significant correlation at the 95% level. As with the other data of Hamilton, the range of the SP data is relatively small (36.5 mV).

#### 2.2.6.7 Revil, Trolard, Bourrié, Castermant, Jardani & Mendonça, 2009

The data of Revil et al. (2009) are from a laboratory experiment where an electrical potential of 3 V was maintained between 2 platinum electrodes in sand tanks connected by a saline bridge for 5 days. Eh and SP were measured after turning the potential off.

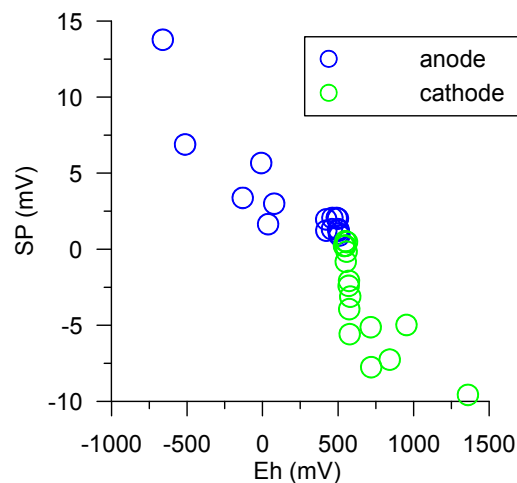


**Figure 2.33 Scatter plot of data obtained from Revil et al. (2009)** The data have a linear correlation (Figure 2.33) and the Spearman correlation coefficient for the combined data set is  $-0.879$ .

### 2.2.7 DISCUSSION

Spontaneous potential anomalies sometimes occur over ore bodies, oil fields and degrading contaminant plumes. Proposed mechanisms for generating SP anomalies of electrochemical origin are (1) a difference in redox potential between SP electrode locations and (2) various geo-batteries.

It seems clear that SP electrodes in locations with different redox conditions produce measurable SP anomalies. These could be called galvanic voltages and are due to electrons exchanged between species in the two redox zones. They are equivalent to the voltages measured in galvanic cells. In principle, the Nernst equation (2.19) could be used to calculate the voltage magnitude, but in practise there are too many species present in the field for such calculations. Additionally, the equation assumes the system is at equilibrium and usually the species are not in chemical equilibrium and there may be electrochemical disequilibrium between the electrodes and solution.

Ntarlagiannis et al. (2007), Williams et al. (2007), Slater et al. (2008) and Zhang et al. (2010) all presented data in support of this mechanism from laboratory experiments with sand columns in which sulphate reducing bacteria reduced  $\text{SO}_4^{2-}$  to  $\text{HS}^-$ . Using Ag/AgCl electrodes, they measured SP between different heights in the column. The potential differences between oxidised and reduced zones were 600, 750, 700 and 550 mV for the four studies, respectively.

The results compiled in the previous sub-section also tend to support the idea of galvanic voltages because the studies with a significant correlation between redox and SP are the ones where measurements were made within the target or very nearby. Those experiments where measurements were made at or near the surface to study buried features did not produce significant correlations, apart from the study by Naudet et al. (2003). Their buried target was not very deep as it was at the water table, 2-10 m deep (Naudet, 2004).

Whether electrical current flows naturally between zones with different redox states and if an electronic conductor is needed for this flux are still matters of debate. They are critical questions because several geo-battery models require something equivalent to electronic conduction. Corry (1985) and Nyquist & Corry (2002) believe that no current flows before the SP survey is set up. Ntarlagiannis et al. (2007) postulate that bacteria can act as electronic conductors based on their laboratory experiment mentioned earlier. SEM imaging of sediment from the sand column used revealed bacteria with pili had colonised the sand. The authors interpreted the bacteria as carrying current and creating the SP anomaly measured. Following the lead of Ntarlagiannis et al. (2007), the hypothesized bio-geobattery mechanism of Revil et al. (2009) requires conduction equivalent to electronic.

Williams et al. (2007) had an interpretation contrary to that of Ntarlagiannis et al. (2007) for their laboratory experiment. Once again SEM imaging of column samples at the end of the experiment showed extensive biofilm formation, but these authors believed the biofilms were not responsible for the electron flow necessary to produce the SP anomaly because the voltage anomaly dissipated once the cell was taken apart even though the biofilms were still present. Though Williams et al. (2007) thought some current might flow through these biofilms, as was shown by others, they did not believe it could carry the magnitudes of current necessary to produce the measured signal.

Zhang et al. (2010) modified the experiment with sulphate reducing bacteria in a sand column by including two types of Ag/AgCl electrodes. The first type was directly in contact with the sand column as in the three earlier experiments and these are the electrodes that measured signals up to 550 mV. The authors called the signals electrodic potentials and they are equivalent to galvanic potentials. The second type of Ag/AgCl electrode was separated from the sand column by KCl agar gel so that there was electrical contact without chemical contact. These electrodes did not measure potentials greater than 10 mV, providing an argument against the bio-geobattery mechanism which should have generated large electric fields if it was present.

The first geo-battery model, the oxygen concentration cell proposed by Sato & Mooney (1960) applies to mineral exploration and the ore acts as an inert electronic conductor. Thornber (1975b; a) proposes the next model, the sulphide galvanic cell, where ore is oxidised. Variations of Thornber's model are applied to oil fields and environmental targets by changing the matter being oxidised; in these cases they are readily degradable organic carbon. With the geo-battery model it is possible to produce SP anomalies that are not galvanic voltages and could be measured at a distance from the source.

For field studies of contaminant plumes, the SP measurements are typically made on the ground surface, while the reduced zone is found in the groundwater (Figure 2.34). The vadose zone is generally permeable to air and will be uniformly oxygenated. Since both SP electrodes will be in the vadose zone in areas with similar redox potentials, any SP signal measured is not a galvanic voltage. To produce SP anomalies at the ground surface it is necessary to create electrical potentials distant from the contaminant plume and this may be done with an electrochemical current.

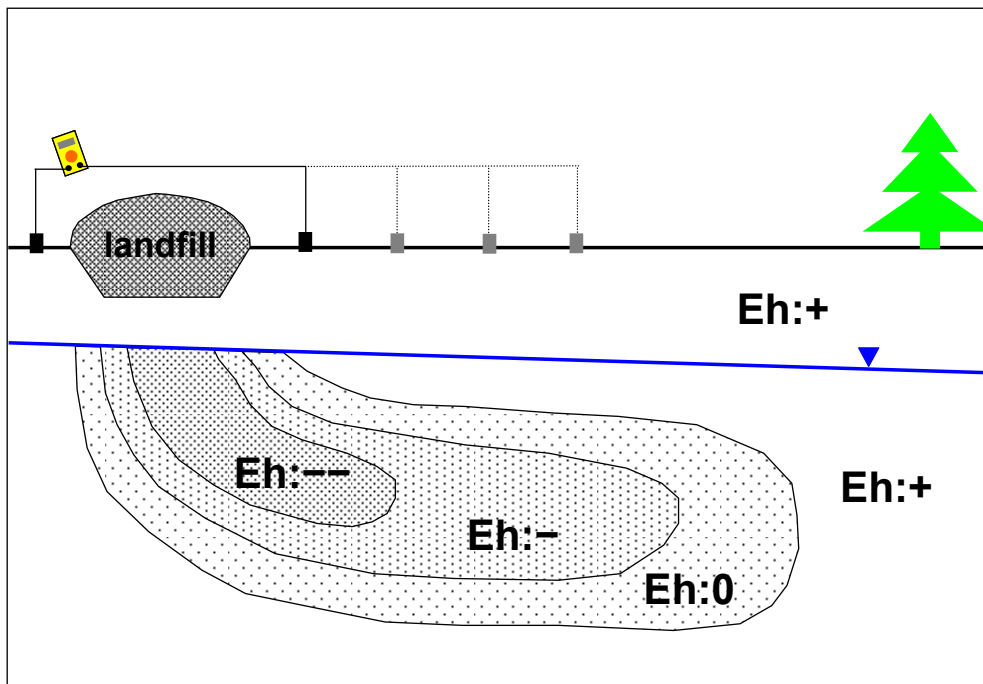


**Figure 2.34** Sketch of the different redox zones in groundwater due to a landfill leachate plume. Above the ground surface the set-up for an SP survey is illustrated, and both electrodes are located in the vadose zone, which will have a relatively uniform Eh.

An analogy may be drawn with streaming potentials, where there are convection and conduction currents. The convection current is caused by the displacement of ions in the double layer due to gradients in pressure in a fluid in a porous medium. It is counterbalanced by the conduction current which goes back through the fluid and porous media (Friborg, 1996). The currents balance in the whole space, but not at every point and the divergence of the convection and conduction in the whole space can be used to calculate the electrical potential at points of interest. For SP of electrochemical origin there could be an electrochemical current occurring principally in the contaminant plume whereas the counterbalancing conduction current could pass through all the sub-surface. The conduction current is what causes electrical potentials that can be measured at the surface. The nature of the electrochemical current is not known, but if it could be characterized, SP could be calculated using the methods presently applied to streaming potentials.

Three approaches for characterising the electrochemical current have been tried and though listed here, they will be discussed in more detail in sub-section 2.3.3.3. Nourbehecht (1963) and Fitterman (1976) assumed apparent or fictitious mobilities for ions through an ore body, which they believed carried current electronically. The second approach is that of Stoll et al. (1995) and Bigalke & Grabner (1997) who use an overpotential model to describe the current generated by disequilibrium at the surface of the conducting ore body. The third approach is the only one that can be applied to contaminant targets. Revil et al. (2009) propose that microbial mats of organisms degrading the plume carry current electronically and they call this electrochemical current a redox current. This is essentially the same as the fictitious mobilities used in the first approach, only in this case the conductor is micro-organisms rather than an ore body.

A fourth approach which has not been developed is that of calculating diffusion currents. Nourbehecht (1963) calculates the typical maximum value of potentials induced by diffusion as 18 mV, assuming a NaCl electrolyte and ion concentration difference of 2

orders of magnitude. In degrading contaminant plumes there are very sharp concentration gradients for redox active elements and many types of ions present, which may make larger spontaneous potentials possible.

Two mechanisms were proposed for generating electrochemical SP anomalies, galvanic voltages and geo-batteries. If they are applied to contaminant sites, it appears that only geo-batteries could produce surface SP anomalies. Galvanic voltages could not be used to map a plume in groundwater because SP electrodes are placed in the vadose zone where the redox potential is relatively uniform. If geo-battery mechanisms operate, plume delineation should be possible because electrical potentials can be generated at a distance. In chapter 6, I investigate two geo-battery mechanisms presented here; those with redox and diffusion currents.

### **2.3 Quantitative interpretations of spontaneous potentials**

The motivation for a better understanding of the location and shape of polarized bodies that give rise to spontaneous potential signals came primarily from the mineral exploration industry. Mineralised ore bodies containing sulphides or graphite often generate large negative spontaneous potential anomalies and people wanted to know the location and shape of the ore creating the anomalies which could be measured at the surface. The first quantitative interpretations were simple analytical methods discussed in sub-section 2.3.1. The 1960s to 1980s produced a series of papers where the initial methods were developed further to recognise the signatures of polarized bodies with diverse but simple geometric shapes. Inversion methods, which try to reproduce the underground polarization without constraints on the source shape, were not developed in earnest until the 1990s. These advances are presented in sub-section 2.3.2.

Work by Nourbehecht (1963) began a separate branch of SP data interpretation that was based on predicting the signal with the help of coupling coefficients and information about the cause of the SP signal (sub-section 2.3.3). These developments came with the use of SP over different types of targets, and in many of these cases the sources could no

longer be described by simple geometries. Beginning in the 1970s SP surveys were used for geotechnical studies at sites with leaky dams. In the 1980s spontaneous potential started being used for exploration of geothermal resources. Since the 1990s it has also been used for environmental studies at sites with organic carbon rich ground contamination. Modelling of streaming potential and the geo-battery phenomenon in chapters 4, 5 and 6 uses methods based on coupled fluxes.

Since the problem of solving the potential source from measured SP is ill defined, auxiliary data are always necessary. The conductivity of the medium is always required because of the relationship described in equation 2.3. Additional information is needed because survey data cannot be gathered in the three dimensional space in which the body of interest is found. This additional information may be an assumption about the body's shape, it may be smoothing functions imposed on inversions, or it may be associated driving force data if the potential is being calculated based on coupled fluxes.

### *2.3.1 FIRST ANALYTICAL METHODS*

Petrowsky (1928) was one of the first to address quantitative interpretation of SP data. He assumed the sphere was at a depth several times greater than its radius in a homogeneous isotropic conducting half-space separated from an upper free half-space by a flat horizontal plane. This allowed him to calculate the gradients in electrical potentials on the surface in the directions parallel and perpendicular to the plane of polarization of the sphere. He did not address why the sphere was polarized. The extrema and zero points of the SP gradient profiles parallel or perpendicular to the plane of polarization are characteristic so they can be used to obtain information about the buried sphere. Petrowsky offers a thorough explanation of his method but does not include examples.

de Witte (1948) applied a method very similar to Petrowsky's (1928) to field data. Yüngül (1950) also used the same method for field data and he improved it by first making a correction for topography. The field examples Yüngül used are in the Ergani copper district in the mountains of eastern Turkey and the topographic correction displace

the centre of the body by 24 m horizontally and the body's depth by 11 m with respect to the uncorrected model.

Bruckshaw (1931) and Stern (1945) developed equations for a buried dipping plane and dipping rod respectively. Their explanations were not thorough and both used absolute SP values, rather than their derivative, which makes these methods prone to error if the reference electrode is not at a proper background location. Neither published field data examples.

Meiser (1962) worked with both spheres and dipping planes and broke down complex SP profiles over graphitic ore bodies into a sum of profiles due to simple shapes.

### *2.3.2 METHODS BASED ON MONOPOLE OR DIPOLE DISTRIBUTIONS*

The works that continued calculating SP signatures based on dipole distributions in the subsurface began by modifying the works of Petrowsky (1928), Yüngül (1950) and Meiser (1962) to make their implementation easier, or to relax the restrictions on the shape of the polarized body. Anisotropy in the subsurface was also addressed. Finally, with the advent of computers it was possible to begin inversion schemes that assigned electrical pole distributions along a grid in the subsurface.

#### *2.3.2.1 Simple geometric shapes*

Bhattacharya & Roy (1981) used log-log plots of potential vs. distance and created a nomogram based on the potential formulae for a sphere and a horizontal cylinder. Data analysis was simplified; given the ratio of minimum to maximum potential and the ore body's shape it was possible to read off a chart the angle of polarization, the depth to the centre of the body and the location of the surface projection of the centre of the body.

Abdelrahman et al. (1997; 1998) used formulae similar to that of Petrowsky (1928) to describe the potential of a polarized body, but they described the body by a shape factor, which was one of the variables determined in the calculations. This was an improvement because it was no longer necessary to know the shape of the body a priori.

The authors mentioned in the two previous paragraphs as well as El-Araby (2004) and Asfahani & Tlass (2002) propose variations on processing and test their methods on the Ergani copper district data presented by Yüngül (1950). None of these five papers have models that follow the field data any better than that of Yüngül.

Sundararajan & Srinivas (1996) propose a different method, based on a modified Hilbert transform. Their method is restricted to the case of a horizontal cylinder and its origin must be known a priori. The SP profile and its modified Hilbert transform intersect at an  $x$  value equal to the depth of the body. The modified Hilbert transform can also be used to find the angle of polarization.

#### *2.3.2.2 Anisotropy*

Geological materials can rarely be qualified as homogeneous and heterogeneities in the material often result in heterogeneous electrical properties. All the methods discussed to date have assumed a simple body buried in a homogeneous electrically isotropic medium which simplifies the calculations. If a medium's electrical properties vary with direction but not with location, its anisotropy can be described by a symmetric and positive definite conductivity tensor.

Skianis & Hernández (1999) applied the work of Asten (1974), Eloranta (1988), and Lindell et al. (1993) on *mise-à-la-masse* surveys in anisotropic media to SP data, and only minor changes were required. They began by considering a vertical dipole with the first pole located at depth  $h$  and the second at infinity below it and made use of Lindell et al.'s formula. For a dipole of finite length they superimposed the potentials due to two single poles of opposite charge, assuming a homogeneous and transversely anisotropic ground.

#### *2.3.2.3 Inversion*

Just as geological media are rarely homogeneous and isotropic, geological bodies are rarely spheres, semi-infinite plates or horizontal cylinders. To address complex shapes,

numerical methods have been used to calculate the signals due to these bodies. The discretisation of space necessary for these methods can also be used to take into account heterogeneous electrical conductivities. As with the study of anisotropy, the first papers on this subject were for electrical resistivity surveys and their methods were later used for interpreting spontaneous potential data.

Numerical modelling aims to create a model of the area from which the signal was gathered. It involves two steps, the forward and inverse problems. The forward problem is to calculate the signal due to any arbitrary but known geometry of parameters. The inverse problem is to calculate the parameter geometry given a known signal, and it is usually solved by iteration: calculating the signal due to an assumed parameter geometry, comparing this with the known signal, adjusting the assumed parameters, recalculating the signal generated and continuing adjustments until the calculated and known signals are sufficiently similar.

The inverse problem in resistivity modelling consists of finding the resistivity distribution given a known source and a measured potential. It is ill posed; there are an infinite number of resistivity distributions that can properly fit the data. The inverse problem in modelling spontaneous potential data is even more underdetermined because neither the resistivity structure nor the sources are known. Furness (1994), Shi (1998) and Minsley et al. (2007b) have developed finite difference models for SP to find source distributions, working from known or assumed resistivity distributions and SP measurements. Other inversion methods available produce results that do not locate sources at specific points but rather probable locations.

Furness (1994) addressed the forward problem by solving an integral form of equation 2.3, where  $E$  is expressed as  $\partial\phi/\partial n$  and the current source is a body of polarization  $M$ :

$$\int_C \sigma \frac{\partial\phi}{\partial n} dc = \int_C M \cdot n dc \quad [2.23.]$$

where  $\sigma$  is conductivity,  $n$  is the unit normal vector and  $C$  is the model domain. He solved it using the discretisation by area approach developed by Dey & Morrison (1979).

Shi (1998), who developed a program to invert resistivity, induced polarization and SP data, addressed the non-uniqueness problem. She worked with a system of linear equations:  $\mathbf{R}\mathbf{v}=\mathbf{s}$ , where  $\mathbf{R}$  is a matrix that is a function of the geometry and physical property distribution of the grid,  $\mathbf{v}$  is a vector of potentials at each node, and  $\mathbf{s}$  is a vector with the source terms. While she did not provide details on the discretisation method, since her  $\mathbf{R}$  matrix is symmetric and positive definite, she likely used Dey & Morrison's (1979) discretisation by area approach. To solve the forward problem (finding  $\mathbf{s}$ ) she implemented a linear conjugate gradient algorithm with incomplete Cholesky preconditioning. The inverse problem was defined as finding  $\mathbf{G}$  where

$$\mathbf{v} = \mathbf{G}(\mathbf{s}) + \mathbf{e} \quad [2.24.]$$

where  $\mathbf{v}$  is the potential data,  $\mathbf{s}$  is the source,  $\mathbf{e}$  is the error and  $\mathbf{G}$  is the forward modelling operator ( $\mathbf{R}^{-1}$ ). Shi defined an objective function ( $\psi$ ) to be minimised with respect to  $\mathbf{s}$  that incorporated Tikhonov regularization to solve equation 2.24. A solution was defined to jointly minimize the data misfit and a stabilising function.

$$\psi = (\bar{\mathbf{d}} - \mathbf{G}(\bar{\mathbf{s}}))^T \mathbf{R}_{\text{dd}}^{-1} (\bar{\mathbf{d}} - \mathbf{G}(\bar{\mathbf{s}})) + \tau \|\mathbf{W}(\bar{\mathbf{s}} - \bar{\mathbf{s}}_0)\|^2 \quad [2.25.]$$

where  $\bar{\mathbf{d}}$  is the measured data,  $\mathbf{R}_{\text{dd}}$  is the data covariance matrix,  $\tau$  is the regularisation parameter,  $\mathbf{W}$  is a linear operator and  $\bar{\mathbf{s}}_0$  is the initial source distribution model. The stabilising function term could also be used to constrain the model with any known geologic information. SP inversions tend to find solutions near the surface because the potential has the highest sensitivities to this region. The  $\mathbf{W}$  term can constrain the current source intensity.

Minsley et al. (2007b) continued Shi's (1998) work and improved it by incorporating two modifications; sensitivity scaling and compact source constraints. They were able to model field data accurately (Figure 2.35) after adjusting the resistivity structure used. The authors demonstrated the effect of different resistivity structures on the model output, concluding that an unknown resistivity structure is an important source of error.

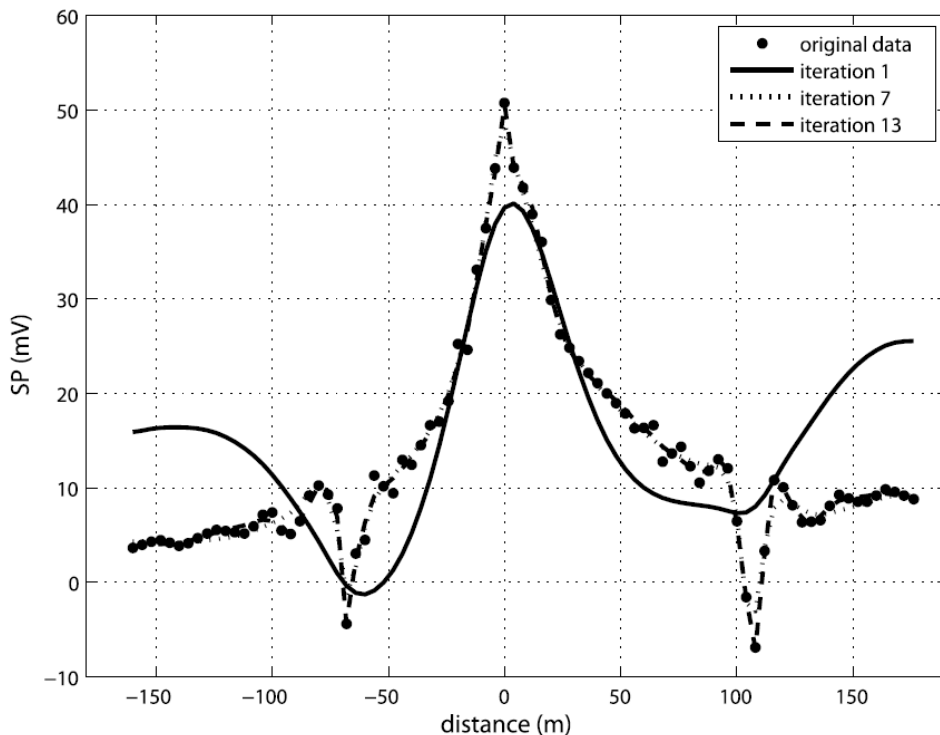


**Figure 2.35** Data fit for three iterations of the compact source solution with the 1D resistivity structure. Note the rough fit for the first iteration, which has strong smoothness constraint to avoid near-surface artifacts due to the noisy data. This constraint is relaxed in later iterations, which is evident by the improved data fit. (Minsley et al., 2007b)

All the inversion methods discussed so far are finite difference calculations developed on rectangular grids, though the node spacing was irregular. It is possible to accommodate the effects of topography in numerical methods by distorting the grid (Loke, 2004).

Patella (1997a; b) proposed a numerical method quite different from the ones discussed above because no a priori knowledge of the resistivity distribution in the model is necessary and the solution is not in source distribution space. Patella referred to his method as ground surface self-potential tomography and its result is a charge occurrence probability (COP) function. The plotted results showed regions with highest probabilities of having positive or negative charges instead of source locations as the method of Shi (1998). The COP is normalised cross-correlation product for each node, which ranges

---

from  $-1$  to  $+1$ . It is a measure of the likelihood of a source at each node producing the potential measured at the surface.

Using 3D tomography helps eliminate uncertainties present in 2D tomography where it is not possible to determine if the source or sink is located in the plane of the section or beside it at an equal radial distance away. Patella (1997b) further developed his method to make it applicable in areas with irregular topography. To demonstrate his technique he used the results from two field examples, for archaeological prospecting of chamber tombs and for locating the volcanic pathways of Mt. Somma-Vesuvius. In the first case he was able to image the voids left by the tombs as positive anomalies and in the second case an extended positive COP anomaly corresponded to the summit portion of the Vesuvius chimney (Figure 2.36).

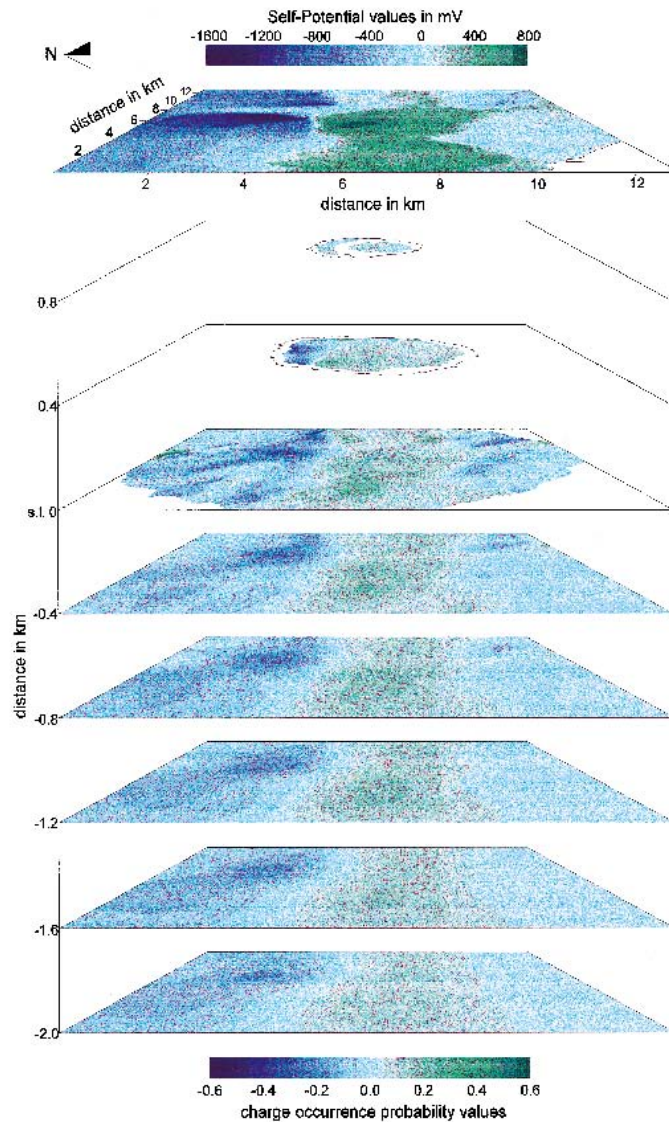


Figure 2.36 Example of the application of the self-potential 3D tomography in the volcanological area of the Mt. Somma-Vesuvius (Naples, Italy) for the configuration of the volcano venting system. The topmost horizontal slice shows the anomaly map of the self-potential field in mV. The following horizontal slices show the results of the 3D tomography at increasing depths from ground level. The bottom colour scale gives the range for the charge occurrence probability values. (Patella, 1997a)

Revil et al. (2001) criticised Patella's (1997a; b) method because it imaged monopole sources or sinks, while in nature electrical phenomena are due to dipolar sources. They proposed a modification to Patella's 2D dipole occurrence probability function, without including three dimensions or topography. They used it to process data over massive

---

graphite veins in steeply inclined fault zones and their tomography produced anomalies over faults confirmed by other methods.

Though technically electrical phenomena are dipoles, spontaneous potential surveys often show a single extremum that is a low. This can occur when the associated high is outside the study area or the polarized body has an axis of polarization that is near vertical and the associated high is at a great depth directly below the near surface negative pole and cannot be seen. For this reason, Patella's (1997a; b) method seems adequate as it does not force a positive source if it is not present in the data and can generate one if it is present.

The wavelet processing method (Moreau et al., 1999; Gibert & Pessel, 2001; Sailhac & Marquis, 2001) has similarities with Patella's method in that the output is not in the source distribution space. With this method the output is in wavelet transform space. The wavelet transform at a single dilation for a homogeneous function can be used to extrapolate the whole wavelet transform of the function, which has a cone-like structure with the apex at the homogeneity center. This center could be the point source of the potential signal.

To apply the method to spontaneous potential data, Sailhac & Marquis (2001) and Gibert & Pessel (2001) assumed a medium with a constant electrical conductivity. This simplifying assumption, as well as the fact the theory has been developed for point sources limits this method's use, but the authors suggested that it could be used as a pre-processing method to get a rough idea of the source distribution. An example of data analysis from the Vulcarolo fissure on Mt. Etna (Figure 2.37) shows that this method was able to resolve the source region, but perhaps not more than in a qualitative sense.

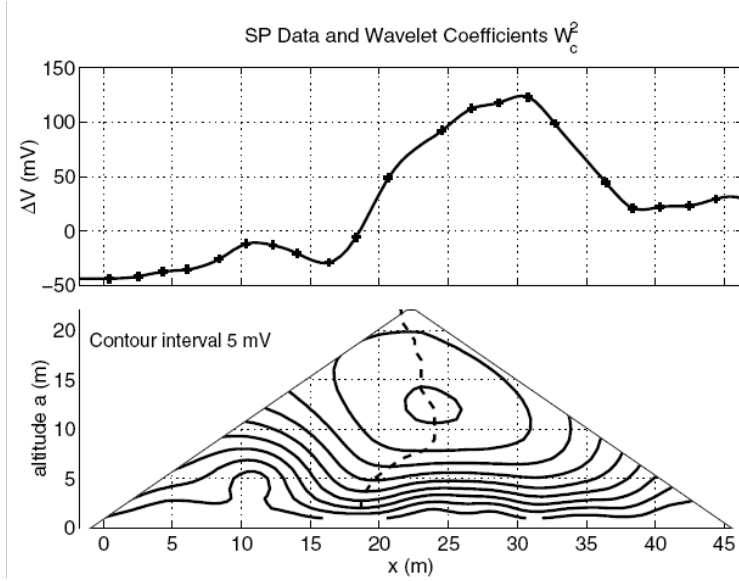


**Figure 2.37** SP data along a profile across the Vulcarolo fissure (around  $x = 22$ ). The calculated wavelet transform (with  $\gamma = 2$ ) exhibits maximum in the space-altitude domain above the fracture area (see the centre contour at 45 mV and the line of modulus maxima. Data from Aubert (1999). (Sailhac & Marquis, 2001)

### 2.3.3 METHODS BASED ON COUPLED FLUXES

The foundations for explaining the causes of spontaneous potential were laid down by Onsager (1931). He linked several irreversible thermodynamic forces acting simultaneously on a system and demonstrated how the cross-coupling terms were equal. The cross-coupling arises because though the overall reactions studied were irreversible, they were a result of innumerable microscopic reactions that were each reversible on an individual basis.

While trying to better understand the causes of induced polarization, Marshall & Madden (1959) investigated the possible effects of mechanical, thermal and chemical energy storage. They did so using a system of equations describing a general electrolyte system with coupling, the phenomenological equations:

$$\begin{bmatrix} \text{flow heat} \\ \text{flow solvent} \\ \text{flow cations} \\ \text{flow anions} \end{bmatrix} = \begin{bmatrix} J_q \\ J_s \\ J_c \\ J_a \end{bmatrix} = \begin{bmatrix} L_{11} & L_{12} & L_{13} & L_{14} \\ L_{21} & L_{22} & L_{23} & L_{24} \\ L_{31} & L_{32} & L_{33} & L_{34} \\ L_{41} & L_{42} & L_{43} & L_{44} \end{bmatrix} \begin{bmatrix} -\nabla T / T \\ -\nabla P \\ -\nabla \mu_c - \mathcal{F} z_c \nabla \phi \\ -\nabla \mu_a - \mathcal{F} z_a \nabla \phi \end{bmatrix} \quad [2.26.]$$

where  $P$  is the pressure,  $T$  is the temperature,  $\mu_{c,a}$  are the chemical potential of cations and anions,  $\phi$  is the electrical potential,  $\mathcal{F}$  is Faraday's constant,  $z_{c,a}$  are the ion valences and  $L_{ii}$  and  $L_{ij}$  are the primary and cross coupling terms, respectively. In this sub-section, pressure is used as the force driving solvent flux because this is the common notation. It is only accurate when there is no elevation head contributing to the hydraulic potential.

Nourbehecht (1963) thoroughly explored the relevance of these equations for spontaneous potential. He stressed that the above equations were valid when the system was displaced only slightly from equilibrium, because at larger displacements the assumption of linearity failed. For small fluctuations about equilibrium and for small flow densities, Onsager's theory stated that there was a symmetry in the coupling of various processes such that  $L_{ij} = L_{ji}$ . All forces and fluxes act simultaneously so that the potentials measured will be the sum of contributions. To simplify their study the contributions are separated into electrokinetic, thermoelectric and electrochemical coupling. Detailed explanations of the three types of coupling are introduced because these equations form the framework for the modelling done in further chapters. Each type of coupling will be discussed in more details in the sub-sections 2.3.3.1 to 2.3.3.3.

For electrokinetic coupling, there is no temperature gradient ( $\nabla T = 0$ ) or chemical gradient ( $\nabla \mu = 0$ ), so equation 2.26 can be simplified to:

$$J_s = L_{21}(0) + L_{22}(-\nabla P) + L_{23}(0 - \mathcal{F} z_p \nabla \phi) + L_{24}(0 - \mathcal{F} z_n \nabla \phi) \quad [2.27.]$$

$$J_c = L_{31}(0) + L_{32}(-\nabla P) + L_{33}(0 - \mathcal{F} z_c \nabla \phi) + L_{34}(0 - \mathcal{F} z_a \nabla \phi) \quad [2.28.]$$

$$J_a = L_{41}(0) + L_{42}(-\nabla P) + L_{43}(0 - \mathcal{F} z_c \nabla \phi) + L_{44}(0 - \mathcal{F} z_a \nabla \phi) \quad [2.29.]$$

Equations 2.28 and 2.29 can be combined to get the electrical current density ( $j$ ), given that  $j = \mathcal{F} \sum_i z_i J_i$ .

$$j = -\mathcal{F}(L_{32}z_c + L_{42}z_a)(\nabla P) - \mathcal{F}^2(L_{33}z_c^2 + (L_{34} + L_{43})z_c z_a + L_{44}z_a^2)(\nabla \phi) \quad [2.30.]$$

The notations of equations 2.27 and 2.30 can be simplified to:

$$J_s = -L_{22}' \nabla P - L_{23}' \nabla \phi \quad [2.31.]$$

$$j = -L_{32}' \nabla P - L_{33}' \nabla \phi \quad [2.32.]$$

The meanings of the coefficients are:

$$L_{33}' = \left( \frac{j}{-\nabla\phi} \right)_{\nabla P=0} = \text{electrical conductivity } (\sigma)$$

$$L_{22}' = \left( \frac{J_s}{-\nabla P} \right)_{\nabla\phi=0} = \text{permeability } (k)$$

$$-\frac{L_{32}'}{L_{33}'} = \left( \frac{\nabla\phi}{\nabla P} \right)_{j=0} = \text{streaming potential coupling coefficient}$$

$$-\frac{L_{23}'}{L_{22}'} = \left( \frac{\nabla P}{\nabla\phi} \right)_{J_s=0} = \text{electro-osmotic coupling coefficient}$$

Using typical values Nourbehecht calculated the size of each of the coefficients in 2.31 and 2.32.  $L_{23}'\nabla\phi$  is two orders of magnitude smaller than  $L_{22}'\nabla P$  so it can safely be neglected and equation 2.31 can be decoupled because it is not affected by the electrical potential. It is considered as the primary flux and is governed by Darcy's law

$$J_s \cong -L_{22}'\nabla P \quad [2.33.]$$

The two terms of equation 2.32 are of the same magnitude so the equation needs to be calculated as written.

The same steps could be used to show that when there is no pressure or chemical gradient, the thermal flux equation can be decoupled. For the thermoelectric case the equations equivalent to 2.31 and 2.32 are:

$$J_q = -L_{11}'\nabla T - L_{13}'\nabla\phi \quad [2.34.]$$

$$j = -L_{31}'\nabla T - L_{33}'\nabla\phi \quad [2.35.]$$

The meanings of the coefficients are:

$$L_{11}' = \left( \frac{J_q}{-\nabla T} \right)_{\nabla\phi=0} = \text{thermal conductivity } (K)$$

$$-\frac{L_{31}'}{L_{33}'} = \left( \frac{\nabla\phi}{\nabla T} \right)_{j=0} = \text{thermoelectric e.m.f. } (\theta)$$

$$-\frac{L_{13}'}{L_{33}'} = \left( \frac{J_q}{j} \right)_{\nabla T=0} = \text{Peltier heat } (\pi)$$

Using typical values  $L_{13}'\nabla\phi$  is three orders of magnitude smaller than  $L_{11}'\nabla T$  and can therefore be neglected.

For electrochemical coupling, since there is diffusion of ions which carry charge, the coupling with the primary flux cannot be neglected.

$$J_c = -L_{33}\nabla\mu_c - L_{34}\nabla\mu_a - \mathcal{F}(L_{33}z_c + L_{34}z_a)\nabla\phi \quad [2.36.]$$

$$J_a = -L_{43}\nabla\mu_c - L_{44}\nabla\mu_a - \mathcal{F}(L_{43}z_c + L_{44}z_a)\nabla\phi \quad [2.37.]$$

Two simplifications can be made. Firstly, the direct coupling effects are much larger than the cross-terms so the later can be neglected (Nourbehecht, 1963). Secondly, the chemical potential for positive and negative ions of the same valence can be approximated as equal because they cannot exist at very different concentrations ( $\mu_c \approx \mu_a \approx \mu$ ). With these assumptions the electrical current density may be written as:

$$j \cong -\mathcal{F}(L_{33}z_c + L_{44}z_a)\nabla\mu - \mathcal{F}^2(L_{33}z_c^2 + L_{44}z_a^2)\nabla\phi \quad [2.38.]$$

When there are several ionic species present their chemical potentials are no longer equal and equation 2.38 can be rewritten as

$$j \cong -\mathcal{F}\sum L_i z_i \nabla\mu_i - \mathcal{F}^2\left(\sum L_i z_i^2\right)\nabla\phi \quad [2.39.]$$

where  $L_i$  is the conductivity of ion  $i$ . The chemical potential gradient is dependent on the concentration ( $c_i$ ) gradient of the different species.

$$\nabla\mu_i \cong RT \frac{\nabla c_i}{c_i} \quad [2.40.]$$

where  $R$  is the gas constant and  $T$  is temperature. The conductivity terms are dependent on the mobility of each ionic species ( $u_i$ ).

$$L_i \cong \frac{u_i c_i}{\mathcal{F} z_i} \quad [2.41.]$$

The current density in equation can be rewritten as

$$j = -\mathcal{F}^2\left(\sum L_i z_i^2\right)\left(\nabla\phi + \frac{RT}{\mathcal{F}} \frac{\sum u_i \nabla c_i}{\sum u_i z_i c_i}\right) \quad [2.42.]$$

This states that the ions with the largest concentration gradients and mobilities will have the greatest contribution to the current.

The final equations for the current due to the three types of coupling may be written as  $j = -L_{33}' \nabla f$  where  $f$  is of the form  $f = \phi + CY$  as in Table 2.13.

**Table 2.13 Formulations for different driving forces all with the form  $f = \phi + CY$ .  
(Nourbehecht, 1963)**

Force	Function
pressure	$f = \phi + \left( \frac{L_{32}'}{L_{33}'} \right) P$
temperature	$f = \phi + \left( \frac{L_{31}'}{L_{33}'} \right) T$
chemical	$f = \phi + \left( \frac{L_{33}z_p + L_{44}z_n}{\mathcal{F}(L_{33}z_c^2 + L_{44}z_a^2)} \right) \mu$

In the absence of electrical sources,  $\nabla \cdot j = 0$ , which means that  $f$  satisfies Laplace's equation ( $\nabla^2 f = 0$ ) in each medium where  $L_{33}'$  is homogeneous and the value at the boundaries depends on  $\phi$  and  $Y$ . This is equivalent to saying that  $f$  is caused by sources distributed along the boundaries. At the boundaries between two media, 1 and 2, both  $\phi$  and  $Y$  are continuous so the difference between  $\phi_1$  and  $\phi_2$  is zero and  $Y$  refers to the common value at the boundary. The difference between the total potentials across the boundary can be expressed as:

$$f_1 - f_2 = (C_1 - C_2)Y \quad [2.43.]$$

The normal component of current flow across the boundary is continuous ( $j_1 \cdot n = j_2 \cdot n$ ) so a second boundary condition is:

$$\sigma_1 \frac{\partial f_1}{\partial n} = \sigma_2 \frac{\partial f_2}{\partial n} \quad [2.44.]$$

Nourbehecht's (1963) explanations are important because they show how to calculate the electrical potential given information about the primary flux and the coupling coefficients. Since it is sometimes easier to obtain information about the primary fluxes than about electrical source distributions, it is possible to get indirect information about the electrical potential. Modelling of SP signals can be done through modelling of

primary fluxes. Most of the work to date involving primary potential coupling for quantitative interpretation of SP data has been with electrokinetic coupling.

#### 2.3.3.1 *Electrokinetic effect*

Mechanisms causing the electrokinetic effect were described in section 2.1, as well as ways of measuring the streaming potential coupling coefficient. This sub-section will focus primarily on the application of streaming potential to field situations. It is necessary to have some water level data, as obtained in monitoring wells, but the more densely acquired SP data allow to fill in between observations points. Two approaches have been used for calculations: the total potential method (Nourbehecht, 1963) and the current method (Sill, 1983).

The total potential method is simpler, was developed first and used until the early 2000s. Advances in computer technology facilitated the complex calculations needed for the current method and its use has expanded greatly since the early 2000s.

Fournier (1989) used the total potential method and described it in detail so his research will be presented before a compilation of various studies. Fournier (1989) determined the depth to the water table in a volcanic region with an aquifer divided in three zones: the unsaturated, saturated and bedrock zones. Assuming the zones were homogeneous, any current source will be at the boundaries between the zones. No sources were at the surface because neither the air above nor the vadose zone below had the saturation necessary to produce an electrokinetic effect. The water table, which is the boundary between the unsaturated and saturated zones, would be a source because of the contrast in coupling coefficients and since the waters of the site were poorly mineralised with a conductivity of 90-150  $\mu\text{S}/\text{cm}$ , Fournier expected streaming potential cross-coupling coefficient ( $C'$ ) values of a few mV/m. The bedrock zone contrasted with the overlying aquifer by a permeability ten times smaller, but since  $C'$  is much more dependant on water conductivity than medium permeability and the water in both zones were well mixed, there was no big contrast likely to produce current sources. Therefore the main source of SP signals was the water table.

Fournier (1989) wrote Nourbehecht's (1963) equation 2.43 as a function of hydraulic head ( $h$ )

$$f_1 - f_2 = (C_1' - C_2')h \quad [2.45.]$$

where  $f_{1,2}$  are the total potentials at locations 1 and 2. Integrating  $h$  over the water table surface ( $S$ ) will give the total potential at the ground surface

$$f = -\frac{(C_2' - C_1')}{2\pi} \iint_S h \frac{r \cdot n}{r^3} ds \quad [2.46.]$$

where  $r$  is the vector between an observation point on the ground and a location at the water table surface. At the ground surface, the hydraulic head was assumed to be zero so that the total potential was equal to the electrical potential. Equation 2.46 is the one used to model  $C'$  for field results as presented in Table 2.4.

The work of Fournier (1989) was in two dimensions, assumed an unconfined aquifer and neglected the vertical component of flow to produce a simple discretised expression for the integral in equation 2.46. The author modelled the SP signal by adjusting the coupling coefficient and water table depth, using knowledge of the sub-surface gained with resistivity surveys (Figure 2.38).

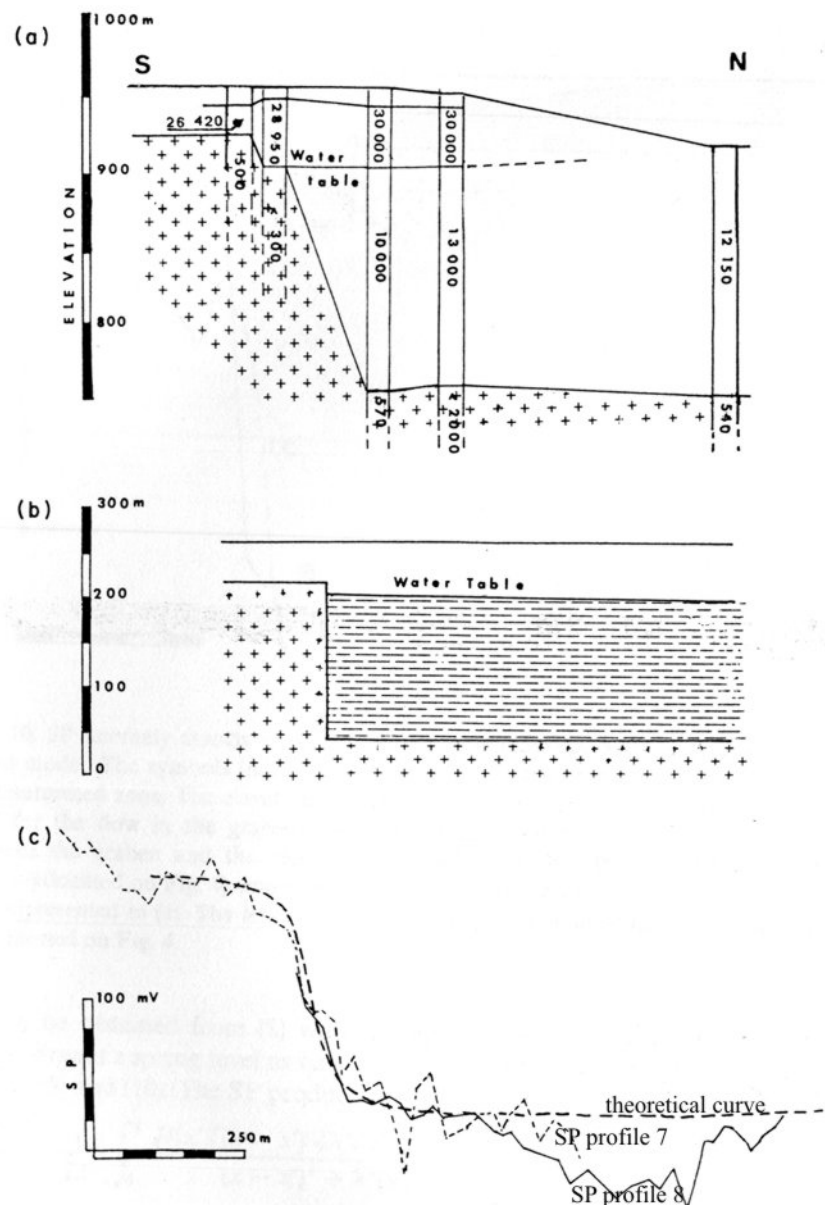


Figure 2.38 a) Cross-section of the southern limit of the axial graben according to the resistivity sounding data. The vertical columns represent the resistivity sounding log, figures inside them indicate the true resistivity in  $\Omega\text{m}$ , and the zone of crosses corresponds to the bedrock. b) Proposed model for computations. The striped zone corresponds to the saturated zone of the volcanic aquifer. c) Two measured SP profiles and the theoretical curve obtained from the model of b) with  $C' = 1.25$  mV/m. (Fournier, 1989)

Several other authors have used the total potential method for practical applications (Table 2.14).

**Table 2.14 Studies where the total potential method of calculating streaming potential is applied.**

<b>Authors</b>	<b>Application</b>
Bogolovsky & Ogilvy (1970)	Calculated seepage rates on a reservoir on the Kalya River in northern Caucasus, Russia, using relationship between the seepage potential anomaly and the water levels to determine target areas for seepage control measures.
Fitterman (1978; 1979)	Calculated type curves for a pressure source in a layered half-space (vertical & horizontal) as a function of: layer thickness, conductivity contrast and source region depth, extent and length.
Birch (1993; 1998)	Used Fournier's (1989) method at six sites in New Hampshire, U.S.A., and on five of the sites the SP profiles calculated based on the water table depth correlated well with measured profiles. In second paper, a programme to solve the inverse problem is presented.
Revil et al. (2002b)	Determined the coupling coefficient of a natural system with calibrations and then calculated the expected depth of the water table during an infiltration experiment with reasonable accuracy.
Rizzo et al. (2004)	Predicted the change in head during a pumping test using SP data.
Revil et al. (2004)	Modelled the depth to the water table on a volcano flank using data from an SP and a resistivity survey.

Sill (1983) noted that Fitterman (1978; 1979), and subsequently Fournier (1989) and Birch (1993; 1998), used zero pressure at the surface boundary, which is inappropriate because an uncritical use of the zero surface pressure boundary condition in potential flow problems often results in a non-zero normal gradient and therefore fluid flow at the air-earth interface. The more appropriate boundary condition is zero normal gradient at the surface. Sill proposed a modification to Nourbehecht's (1963) total potential approach, the current approach, where equation 2.32 is interpreted as the sum of currents. His methodology is presented before a second compilation of examples.

Potentials are caused by currents, which can be divided into convection ( $j_{convection}$ ) and conduction ( $j_{conduction}$ ) currents. The convection current is the charge movement caused by a pressure gradient displacing ions in the electrical double layer relative to the charges fixed on particles. The conduction current is the response to the electrical field generated by the convection current and occurs through electrolytic and surface conduction. Equation 2.32 is rewritten as:

$$j_{total} = -L_{32}'\nabla P - L_{33}'\nabla\phi = -j_{convection} - j_{conduction} \quad [2.47.]$$

In the absence of external current sources

$$\nabla \cdot j_{total} = 0 = \nabla \cdot (j_{convection} + j_{conduction}) = \nabla \cdot j_{convection} + \nabla \cdot j_{conduction} \quad [2.48.]$$

If the gradients of the primary and electrical potential are measured under conditions of zero total current, as is typical in the laboratory, the conduction current exactly cancels the convection current everywhere.

$$j_{conduction} = -j_{convection} = -L_{32}'\nabla P \quad [2.49.]$$

$$L_{33}'\nabla\phi = -L_{32}'\nabla P \quad [2.50.]$$

This allows the measurement of the streaming potential cross-coupling coefficient ( $C$ ) discussed in section 2.1.

$$C = -\left(\frac{\nabla\phi}{\nabla P}\right)_{j=0} = \frac{L_{32}'}{L_{33}'} = \frac{L_{32}'}{\sigma} \quad [2.51.]$$

To calculate the convection current it is necessary to use the term  $L_{32}'$ , also referred to as  $L$ , the streaming current coupling coefficient. This term is calculated by multiplying  $C$  by  $\sigma$ , so it is necessary to measure both properties on a sample to model streaming potential.

Sill (1983) approached the problem from an electrical potential point of view and his method is contrasted with Nourbehecht's (1963) in Table 2.15.

**Table 2.15 Comparison of Nourbehecht's and Sill's methodologies. (modified from Sill, 1983)**

<b>Author</b>	<b>Source</b>	<b>Parameter measured</b>	<b>Coefficient used</b>
Sill (1983)	divergence of convection current	gradients in primary potential	streaming current
Nourbehecht (1963)	boundaries	magnitude of primary potential	streaming potential

Sill's approach works equally well for gradients of pressure and temperature. For more complex problems where numerical solutions are necessary, he suggested solving the problems in three steps:

- 1) Use an appropriate programme to solve primary potential problem.
- 2) Calculate the sources of electrical current from equation 2.49 using the primary potential solution and a model of the cross-coupling coefficients.
- 3) Use the current sources and electrical resistivity model to determine the electrical potential

All the works listed (Table 2.16) are computer programmes for modelling SP from hydraulic head. Some calculate hydraulic head distributions while others are post-processors that work from hydraulic head distributions calculated elsewhere.

**Table 2.16 Studies where the current method of calculating streaming potential is applied.**

<b>Authors</b>	<b>Application</b>
Wilt & Butler (1990)	Programme that solved the pressure profile at the surface and used this to calculate the electrical potential. Served to calibrate permeabilities assigned to different parts of a leaking dam by allowing comparison of measured and calculated SP profiles.
Titov et al. (2002)	Programme developed for additional calibration of groundwater flow models.
Wurmstich & Morgan (1994)	3D finite difference programme to calculate the SP anomaly caused by pumping 500 bbl/day from an oil well. Very small signals were calculated and the well casing heavily disturbed the signal.
Ishido & Pritchett (1999)	Post-processor to be used with a reservoir simulation programme. An extended grid for SP calculations was necessary. Used to model the changes in an SP anomaly above an exploited geothermal field.
Sheffer & Oldenburg (2007)	Finite volume post-processor (SP3D) to calculate SP generated by hydraulic head distributions created with the software MODFLOW, with increased grid size for the electrical potential model.
Sheffer (2007)	Integrated SP3D into an inversion programme to successfully model data from a lab experiment of flow under a cut-off wall.
Bérubé (2007)	Finite element programme (SPiso3D) used to model flow through a mine tailings dam.

Jardani et al. (2008) use similar methods for inversion of SP data, but they define the conduction current as:

$$j_{conduction} = \overline{Q_v} \mathbf{u} \quad [2.52.]$$

where  $\overline{Q_v}$  is the excess charge per unit pore volume of the material and  $\mathbf{u}$  is the volumetric fluid flux. They were able to map the pattern of groundwater flow at a geothermal field.



Fitterman & Corwin (1982) had a simpler approach for modelling the SP signal at the Cerro Prieto geothermal field in Baja California, Mexico, and used a patch model, which consisted of a vertical rectangular heat source, corresponding roughly with a nearly vertical fault crossing the field. They used the Levenberg-Marquardt algorithm ZXSSQ as a non-linear least squares technique to adjust model parameters to minimise the sum of squared residuals between the modelled and measured SP profiles. The parameters adjusted were: depth to top of patch, depth to bottom of patch, length of patch and resistivity contrast on either side of the patch. They were able to obtain a fit with 28 mV RMS error.

One year later Fitterman (1983) published an article with explanations on how to account for more complex sources. He used Green functions to describe the SP sources and worked with two vertical rectangular sources, meant to represent the two sides of a dyke.

### 2.3.3.3 *Electrochemical effect*

Unlike pressure and temperature, the equation for the flux of ions due to chemical concentration gradients cannot be decoupled from the electrical potential. The four approaches for calculating electrochemical current described in sub-section 2.2.7 will be discussed again with the help of equations. All approaches calculate an electrochemical current which can be used to find spontaneous potential

$$\nabla \cdot j_{\text{electrochemical}} = -\nabla \cdot (\sigma \nabla \phi) \quad [2.53.]$$

The first approach is that of Nourbehecht (1963) and Fitterman (1976) who tried to apply the phenomenological equations to ore situations by assuming apparent mobilities for species participating in redox reactions such as iron ions. If iron is being oxidised at depth and reduced at the surface, it can be described as  $\text{Fe}^{2+}$  at depth giving up an electron to become  $\text{Fe}^{3+}$ , but this electron travels at high speed through the ore body to transform an  $\text{Fe}^{3+}$  ion at the surface into  $\text{Fe}^{2+}$ , therefore the  $\text{Fe}^{2+}$  ion apparently travels the whole length of the ore body almost instantaneously. The final formulation is

$$f = \phi + \frac{RT}{n\mathcal{F}} \ln \frac{[H^+]^m [B]^b}{[A]^a} = \phi + (Eh - Eh^0) \quad [2.54.]$$

where  $R$  is the gas constant,  $T$  is the temperature,  $n$  is the number of electrons exchanged in the reaction,  $\mathcal{F}$  is Faraday's constant,  $[i]^x$  is the concentration of  $i$ , with an exponent  $x$  equal to the stoichiometric proportion of  $i$  in the reaction, and  $Eh, Eh^0$  are the redox potential at measured and standard conditions. Both Nourbehecht (1963) and Fitterman (1976) used the total potential formulation with which Sill (1983) found fault because it often leads to models with inappropriate boundary conditions.

Kilty (1984) followed Sill's lead for modifications to the phenomenological equations and instead of using apparent mobilities for ions, used mobilities and concentrations of electrons and holes in the ore when calculating the potential. To estimate concentrations of electrons travelling through the ore Kilty used overpotential calculations, which is the second approach.

Overpotential ( $\eta$ ) is a deviation of the Galvani potential of the electrode ( $\Delta\phi$ ) from the value it has when the rate of charge flow across its interface with the solution is equal in each direction for the reaction concerned (Bockris et al., 2000, eq. 7.14).

$$\eta = \Delta\phi - \Delta\phi_e \quad [2.55.]$$

where  $\Delta\phi$  is the interfacial potential and  $\Delta\phi_e$  is the interfacial potential at equilibrium. In geological situations overpotentials are assumed to occur when current conduction switches from electronic to ionic or vice versa. Thornber (1975b) drew an electrical circuit representing a geo-battery (Figure 2.40) and included a drawing with the resistances. Across each resistance there is an electrical potential jump and those at  $R_2$  and  $R_4$  are called overpotentials, occurring at the interphase between electrolytic and electronic conductors.

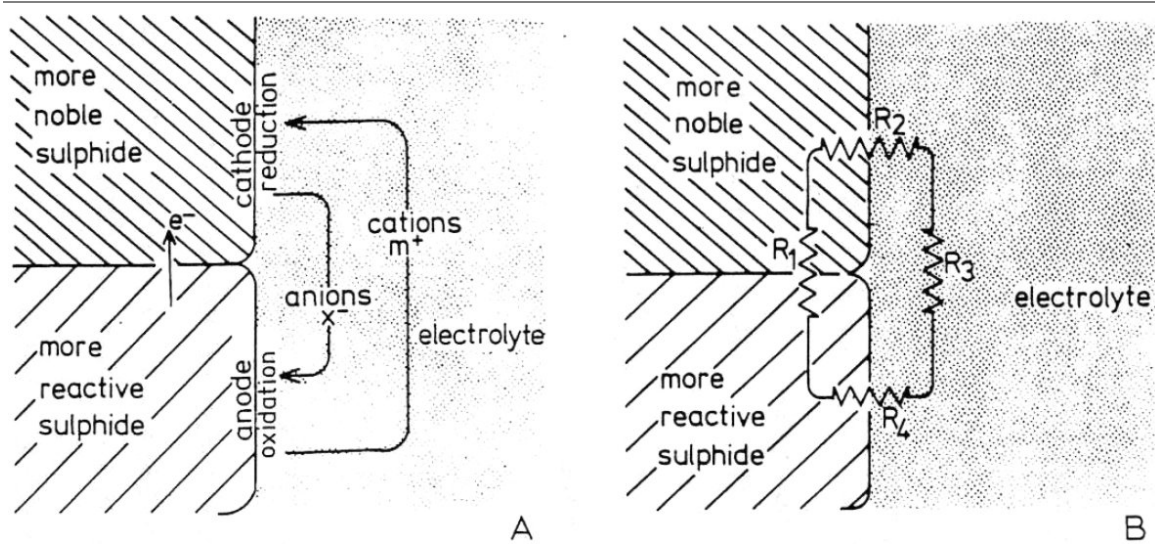


Figure 2.40 A) Schematic circuit for the galvanic corrosion of sulphides showing the current flow. B) The same corrosion cell showing the resistances.  $R_1$  is the resistance to electronic current flow within the sulphides;  $R_3$  is the resistance to charge transport by ionic flow in the electrolyte fluids contained within the rocks;  $R_4$  represents the kinetic parameters controlling the anodic oxidation processes taking place at the corrosion interface between sulphide and electrolyte; and  $R_2$  similarly represents the kinetic parameters controlling the reducing processes taking place on the cathodic interface between sulphide and electrolyte. (Thornber, 1975b)

The overpotential value is one of the terms necessary in the calculation of current density ( $j$ ) given by the Butler-Volmer equation:

$$j = j_0 \left( e^{-\beta \eta \mathcal{F} / RT} - e^{(1-\beta) \eta \mathcal{F} / RT} \right) \quad [2.56.]$$

where  $j_0$  is the exchange current density when the system is at equilibrium ( $\eta=0$ ),  $\beta$  is a transfer coefficient (between 0 and 1) related to the symmetry of the  $j$ -vs.- $\eta$  relationship, and dependent on the species reacting, though it is usually near 0.5,  $\mathcal{F}$  is Faraday's constant,  $R$  is the universal gas constant and  $T$  is temperature.

Two special cases are the low and high overpotentials. At low overpotentials, as is expected to occur around an ore body, the current density is linear with overpotential. This occurs when  $|\eta|$  is less than  $|RT/\beta \mathcal{F}|$  ( $\sim 50$  mV at room temperature). In this case the Butler-Volmer equation can be approximated using a Taylor MacClairin series to:

$$j = j_0 \frac{\eta \mathcal{F}}{RT} \quad [2.57.]$$

Stoll et al. (1995) and Bigalke & Grabner (1997) proposed an electrochemical model for SP anomalies due to conductive ore bodies based on electrode kinetics and the overpotential approach. It is a development of the method proposed by Eskola & Hongisto (1987) and altered by Furness (1992; 1994), who included an arbitrarily chosen potential jump across the ore body interface. Stoll et al. (1995) begin by expressing the overpotential in more easily measurable terms:

$$\eta(r) = -Eh(r) + Eh_m - \phi(r) \quad [2.58.]$$

The authors define  $Eh_m$  as the Eh at the depth at which  $\phi = 0$ , though they do not explain how one might find this. Using equation 2.58, the current flow across the ore-electrolyte interface as a function of depth ( $r$ ) is defined as:

$$j(r) = -j_0 \frac{\mathcal{F}}{RT} (Eh(r) - Eh_m + \phi(r)) \quad [2.59.]$$

At the interface, current conduction changes from electronic to ionic so the interface can be thought of as the source of ionic current. The electrical potential is measured outside the conductor with an SP survey. The relationship between potential and current the authors propose takes into account the size of the outer surface of the ore body.

$$-\nabla \cdot j = -gj_0 \frac{n\mathcal{F}}{RT} (Eh(z) - Eh_m + \phi) = \sigma \nabla^2 \phi \quad [2.60.]$$

where  $g$  is the specific electrode area. Stoll et al. (1995) solved this equation numerically by a finite difference method to model the expected SP signal in the zone of Erbendorf-Vohenstrauß, in Bavaria, Germany, from borehole Eh data and their results are shown in Figure 2.41.

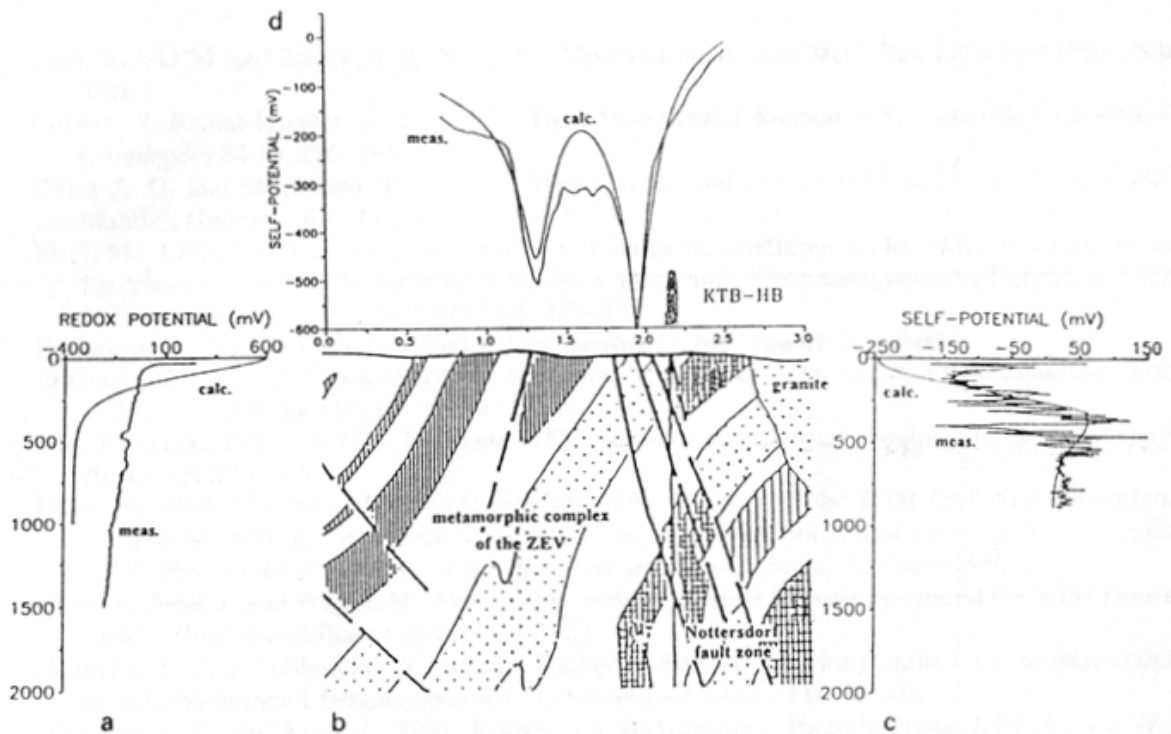


**Figure 2.41** Measured (meas.) and calculated (calc.) SP and Redox potential data in relation to the geology. **a)** Measured and calculated distribution of redox potential. **b)** Geological settings after Hirschmann (1993). **c)** Measured and calculated borehole data. **d)** Measured and calculated surface data. (Stoll et al., 1995)

A weakness of the overpotential method is the assumption that the ore is a continuously conducting body. Sulphides are often disseminated and these bodies also create large SP anomalies.

The third approach, proposed by Revil et al. (2009), defines the electrochemical current as the redox current

$$\nabla \cdot j_{\text{electrochemical}} = \nabla \cdot j_{\text{redox}} = \nabla \cdot (\sigma \nabla E_h) \quad [2.61.]$$

Castermant et al. (2008) tested both the overpotential and redox methods by modelling a laboratory experiment of an iron bar rusting in a wet sand tank. Stoll et al.'s (1995) model was used to predict SP with the resistivity distribution as a parameter to be optimised (Figure 2.42a). An inversion based on equation 2.61 was used to calculate the Eh distribution from measured SP and this was compared with the measured Eh distribution (Figure 2.42b). The authors concluded that both methods worked equally well.

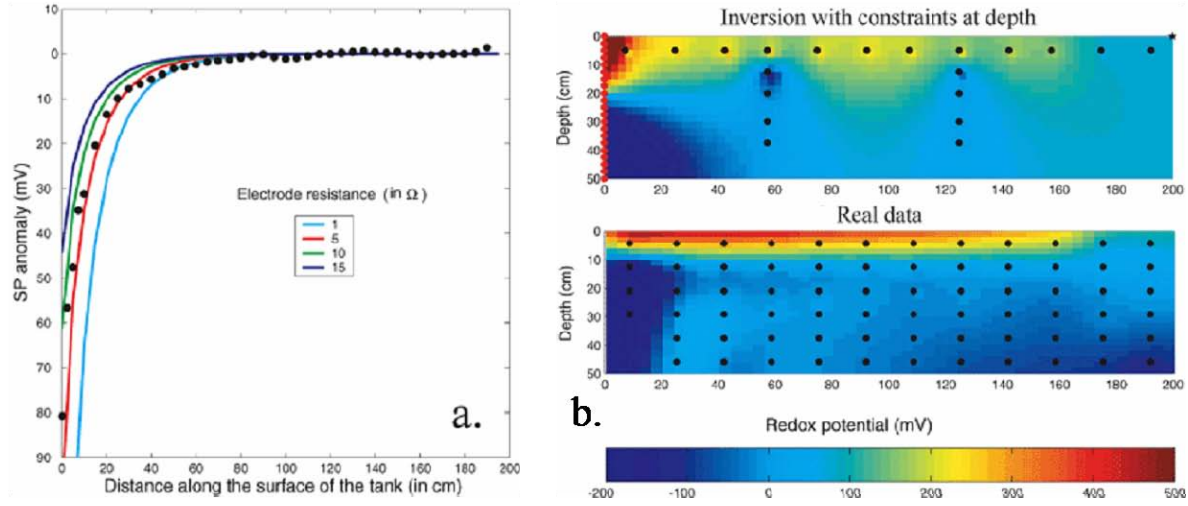


**Figure 2.42** a) Measured self-potential anomaly (full circles) and theoretical anomalies provided by the inert electrode model with electrode resistance of 1, 5, 10, and 15  $\Omega$ . b) Distribution of the redox potential obtained from self-potential current sources and the distribution of the measured redox potential. We assume  $\sigma = 0.0025 \text{ S m}^{-1}$  (400  $\Omega\text{m}$ ) for the conductivity of the crust coating the iron bar. (Castermant et al., 2008)

The last approach assigns the diffusion current as equivalent to the electrochemical current and its derivation is described in detail as it will be used for calculations in chapter 6. If one assumes a medium without electronic conductors and no surface conductance, the total electric current density ( $j$ ) in the medium is:

$$j = \mathcal{F} \sum_i z_i J_i \quad [2.62.]$$

where  $\mathcal{F}$  is Faraday's constant,  $z_i$  is the valence of ion  $i$ ,  $J_i$  is the mass flux of ion  $i$  and the sum over all  $i$  includes all ions. The next six equations are developed for fluxes in a liquid and corrections for the effect of a saturated porous medium are added afterwards. The mass flux of a molecule can be described by the Nernst-Planck equation (Bard & Faulkner, 2001, eq. 4.1.9):

$$J_i = -D_i \nabla c_i - \frac{z_i \mathcal{F} D_i}{RT} c_i \nabla \phi + c_i v \quad [2.63.]$$

where  $D_i$  is the diffusion coefficient of ion  $i$ ,  $c_i$  is the concentration of  $i$ ,  $z_i$  is the valence of ion  $i$ ,  $\mathcal{F}$  is Faraday's constant,  $R$  is the universal gas constant,  $T$  is temperature,  $\phi$  is electrical potential and  $v$  is the solution velocity, which will be the same for all ions. To

simplify equation 2.63, the quotient part of the second term can be expressed as mobility ( $u_i$ ) using the Einstein-Smoluchowski equation (Bard & Faulkner, 2001, eq. 4.2.2):

$$u_i = \frac{z_i \mathcal{F} D_i}{RT} \quad [2.64.]$$

The simplified version of equation 2.63 is then:

$$J_i = -D_i \nabla c_i - u_i c_i \nabla \phi + c_i v \quad [2.65.]$$

When equation 2.65 is substituted into equation 2.62:

$$\begin{aligned} j &= \mathcal{F} \sum_i z_i (-D_i \nabla c_i - u_i c_i \nabla \phi + c_i v) \\ &= -\mathcal{F} \sum_i z_i D_i \nabla c_i - \mathcal{F} \sum_i z_i u_i c_i \nabla \phi + \mathcal{F} v \sum_i z_i c_i \end{aligned} \quad [2.66.]$$

The third term is equal to zero because we are considering a static system so the solution velocity is zero. As well,  $\sum z_i c_i$  is the solution's charge balance and assuming it is neutral would also make the third term equal to zero. To simplify the second term, the definition of fluid electrical conductivity ( $\sigma_f$ ) can be used (Bockris & Reddy, 1998, eq. 4.160):

$$\sigma_f = \mathcal{F} \sum_i z_i u_i c_i \quad [2.67.]$$

So equation 2.66 can be rewritten as:

$$j = -\mathcal{F} \sum_i z_i D_i \nabla c_i - \sigma_f \nabla \phi \quad [2.68.]$$

Since the fluxes occur in a porous medium, some changes must be made to equation 2.68. The conductivity calculated using equation 2.67 is the fluid conductivity ( $\sigma_f$ ) and it is necessary to use the bulk conductivity ( $\sigma_b$ ). For a non-conducting medium, this conversion can be made using the formation factor ( $F$ ) (Archie, 1942).

$$\sigma_b = \frac{\sigma_f}{F} \quad [2.69.]$$

The formation factor is dependant on the medium's water saturation following the relation:

$$F = \frac{F_0}{S_w^2} \quad [2.70.]$$

where  $F_0$  is the formation factor in a saturated medium and  $S_w$  is the fraction of pores filled with water (Archie, 1942).

As well, the diffusion flux must be corrected for the medium. This can be done by changing the diffusion coefficients ( $D_i$ ) to effective diffusion coefficients ( $D_i^*$ ). There are several methods to make the conversion, as discussed in Domenico (1977) and Shen & Chen (2007), and all are approximations. Following Marshall et al. (1996) and Hillel (1998):

$$D_i^* = \theta \xi D_i \quad [2.71.]$$

where  $\theta$  is the volumetric water content and  $\xi$  is a tortuosity factor. According to Bear (1972) the tortuosity factor can be estimated using:

$$\xi = \frac{1}{\phi F} \quad [2.72.]$$

where  $\phi$  is the medium's porosity. Equation 2.68 can be rewritten as

$$j = -\mathcal{F} \sum_i z_i D_i^* \nabla c_i - \sigma_b \nabla \phi \quad [2.73.]$$

In this formulation the first term on the right is the diffusion current and the second is the conduction current.

$$j = -j_{diffusion} - j_{conduction} \quad [2.74.]$$

#### 2.3.4 SUMMARY

Quantitative methods of spontaneous potential data analysis have been around for almost one hundred years and yet new methods are continually being developed. This is in part because SP surveys are being used in different settings, requiring new techniques. However it is mostly because there is no satisfactory method, though several are adequate for different purposes. The difficulty of the problem addressed explains this fact. It is not possible to know the underground distribution of the source of an SP anomaly given only the electrical potential data at the surface. More data of a different nature are required and

the various methods aim to optimise locating the SP source based on the minimum auxiliary data and assumptions required.

The first methods were analytical calculations of the potential due to a simple polarized body buried in a homogeneous half-space. These techniques were successful for finding buried ore bodies and they have not evolved much since the 1960s.

Anisotropy of the medium complicates things greatly. If the host medium is homogeneous and anisotropic it is possible to calculate how the SP signal from a known body will be altered. If the medium is heterogeneous, it is necessary to use numerical methods, which allow the space to be divided into the many nodes of a grid that can each be assigned a conductivity. This can be seen as a burden because though numerical methods might be able to account for varying conductivities and more complex source body shapes, they require more data: the conductivity of the subsurface.

Coupled fluxes can also be used to locate source bodies. It involves modelling a primary driving flux, calculating the induced current using cross-coupling coefficients and calculating the potential response due to the current. These problems are typically solved numerically and require a lot of additional data: the sources of the primary flux, the conductivity for the primary flux, the cross-coupling coefficient and the electrical conductivity at all grid nodes. There are three known causes: electrokinetic, due to the flow of solvent; thermoelectric, due to the flow of heat; and electrochemical, due to the flow of ions. All causes act simultaneously and are measured together. It is difficult to separate them, although at certain locations a single cause may generate most of the signal.

The focus of this work is spontaneous potentials of electrochemical origin, but field measurements will include thermoelectric and electrokinetic contributions. Thermoelectric potentials are negligible on contaminant sites and the effect of streaming potentials is explored in chapter 4. Calculations for both electrochemical and

electrokinetic sources are done using coupling with causes following the procedure developed by Sill (1983). The programme used is presented in chapter 3 and four types of current are calculated: conduction, convection, diffusion and redox. For any interpretation and inversion of SP measurements auxiliary data is necessary.

### 3 FINITE ELEMENT FORWARD MODEL

Quantitative analysis of spontaneous potential (SP) data typically requires numerical methods because most real world situations are too complex to be described by equations that can be solved analytically. For numerical analysis we chose to work with a 3D finite element MATLAB programme written by Kevin Hayley (2007) which he kindly provided. The programme was designed to solve electrical potential problems and could be modified to serve our purposes.

The three problems addressed; electrical potential, streaming potential and electrochemical SP, all have governing equations with the same formulation, as discussed in section 3.1. This means the same code can be used for all cases. The equations are expressed in the weak form, used for finite elements, and their implementation into a computer code is described in section 3.2. To demonstrate the programme's validity, results for two examples are shown. The first example, in section 3.3, is a comparison of numerical and analytical results of electrical potentials due to a simple electrical point source in an electrically anisotropic medium. In section 3.4 the finite element programme and SP3D, a finite volume software written by Sheffer & Oldenburg (2007), are compared using the theoretical example of a dam. This was possible with help from Oldenburg who gave us use of the software. A chapter summary is made in section 3.5.

The following notation is used for the variables in this chapter: italic upper and lower case for scalars, bold lower case for vectors, bold upper case for matrices, and double underline for tensors.

#### 3.1 Governing equations

Steady state field problems occur in many areas, including spontaneous potentials due to several causes. The problems deal with the diffusion or flux of a quantity ( $\mathbf{q}$ ), whose rate of diffusion is dependant on the sources and sinks ( $s$ ) in a volume. For steady state (Zienkiewicz & Taylor, 2000)

$$\nabla \cdot \mathbf{q} = s \quad [3.1.]$$

Generally the diffusion of the quantity is linearly related to the negative gradient of its potential field ( $\Phi$ ) by a constant ( $k$ ) representing the conductivity. Equation 3.1 can be rewritten as

$$-\nabla \cdot (k\nabla\Phi) = s \quad [3.2.]$$

All the problems with SP are due to coupled fluxes and these fluxes can be described by this diffusion equation. Since they are variations of the electrical potential problem, they can be expressed in terms of electrical current density ( $j$ ). The equivalencies are listed in Table 3.1.

**Table 3.1 Variables for the different SP problems. Abbreviations:  $\mathcal{F}$ –Faraday’s constant,  $z_i$ – valence of ion  $i$ ,  $D_i^*$ –effective diffusion coefficient of ion  $i$ .**

<b>problem type</b>	<b>potential</b>	<b><math>\Phi</math></b>	<b>conductivity</b>	<b><math>k</math></b>	<b>sources &amp; sinks <math>s</math></b>
electrical potential	electrical potential	$\phi$	electrical conductivity	$\sigma$	divergence of conduction current density $\nabla \cdot j_{conduction}$
streaming potential	head	$h$	streaming current coupling coefficient	$L'$	divergence of convection current density $\nabla \cdot j_{convection}$
diffusion electro-chemical SP	ionic concentration	$c_i$	ionic diffusion conductivity	$\mathcal{F} z_i D_i^*$	divergence of diffusion current density $\nabla \cdot j_{diffusion}$
redox electro-chemical SP	redox potential	Eh	electrical conductivity	$\sigma$	divergence of redox current density $\nabla \cdot j_{redox}$

When no external sources are imposed, the currents in a closed volume sum to zero. The conduction current is equal to different sources depending on the cause being studied. It can be equal to the negative of either the convection, diffusion or redox currents.

$$\begin{aligned}
\nabla \cdot \mathbf{j}_{conduction} &= -\nabla \cdot \mathbf{j}_{convection} & \nabla \cdot (\sigma \nabla \phi) &= -\nabla \cdot (L \nabla h) \\
\nabla \cdot \mathbf{j}_{conduction} &= -\nabla \cdot \mathbf{j}_{diffusion} & \nabla \cdot (\sigma \nabla \phi) &= -\nabla \cdot \left( \mathcal{F} \sum_i z_i D_i^* \nabla c_i \right) \\
\nabla \cdot \mathbf{j}_{conduction} &= -\nabla \cdot \mathbf{j}_{redox} & \nabla \cdot (\sigma \nabla \phi) &= -\nabla \cdot (\sigma \nabla E h)
\end{aligned} \tag{3.3.]$$

All the following developments will be done using conduction current, but they would be equivalent for the other types of current in Table 3.1.  $j_{conduction}$  is renamed as  $\mathbf{j}$  for the exercise and it is referred to a vector that represents the current at each node. A numerical model must include boundary conditions, and in the electrical case, since no current passes into the air because of its high resistivity, the current density flux normal to the ground surface is set to zero.

$$\mathbf{j} \cdot \mathbf{n} = 0 \tag{3.4.]$$

where  $\mathbf{n}$  is the normal to the surface. The underground boundaries can be set to fixed flux, fixed potential, or mixed conditions, but they should be far enough away from the area of interest so that they do not have an effect. The most general form is the mixed boundary condition (Rücker et al., 2006):

$$\sigma \left( \frac{\partial \phi}{\partial \mathbf{n}} + \alpha \phi \right) = \mathbf{j} \cdot \mathbf{n} \tag{3.5.]$$

In this programme  $\alpha$  is defined as  $\alpha = \mathbf{n} \cdot \frac{\mathbf{r}}{|\mathbf{r}|^2}$ , where  $\mathbf{r}$  is the distance between the surface and the point source (Rücker et al., 2006).

The equation

$$\nabla \cdot (\sigma \nabla \phi) = -\nabla \cdot \mathbf{j} \tag{3.6.]$$

is a strong formulation of the electrical potential problem and finite element methods use a weak formulation. The following equations are the steps taken to express equation 3.6 in a weak formulation and are modified from Hayley (2007).

- 1) Multiply equation by a perturbation  $\delta \phi$  and integrate over the domain  $\Omega$ .

$$\iiint_{\Omega} [\nabla \cdot (\sigma \nabla \phi) \delta \phi + \nabla \cdot (\mathbf{j}) \delta \phi] dv = 0 \tag{3.7.]$$

- 2) Using the vector identity  $\nabla \cdot (k \mathbf{f}) = k \nabla \cdot \mathbf{f} + \mathbf{f} \cdot \nabla k$ , where  $k$  is a scalar assigned to  $\delta \phi$  and  $\mathbf{f}$  a vector assigned to  $\sigma \nabla \phi$ , replace the first term.

$$\iiint_{\Omega} [\nabla \cdot (\sigma \nabla \phi \delta \phi) - \sigma \nabla \phi \cdot \nabla \delta \phi + \nabla \cdot (\mathbf{j}) \delta \phi] dv = 0 \quad [3.8.]$$

- 3) Apply the divergence theorem  $\iiint_{\Omega} \nabla \cdot \mathbf{f} dv = \iint_{\partial \Omega} \mathbf{f} \cdot \mathbf{n} dS$ , to replace the first term by assigning  $\mathbf{f} = \sigma \nabla \phi \delta \phi$ .

$$\iint_{\partial \Omega} (\sigma \nabla \phi \delta \phi) \cdot \mathbf{n} dS - \iiint_{\Omega} \sigma \nabla \phi \cdot \nabla \delta \phi dv + \iiint_{\Omega} \nabla \cdot (\mathbf{j}) \delta \phi dv = 0 \quad [3.9.]$$

- 4) Rearrange the general boundary condition (equation 3.5) to incorporate it into the first term.

$$\begin{aligned} (\sigma \nabla \phi \delta \phi) \cdot \mathbf{n} &= \sigma \delta \phi (\nabla \phi \cdot \mathbf{n}) \\ &= \sigma \delta \phi \left( \frac{1}{\sigma} (\mathbf{j} \cdot \mathbf{n} - \sigma \alpha \phi) \right) \\ &= \mathbf{j} \cdot \mathbf{n} \delta \phi - \sigma \alpha \phi \delta \phi \end{aligned}$$

$$\iint_{\partial \Omega} \mathbf{j} \cdot \mathbf{n} \delta \phi dS - \iint_{\partial \Omega} \sigma \alpha \phi \delta \phi dS - \iiint_{\Omega} \sigma \nabla \phi \cdot \nabla \delta \phi dv + \iiint_{\Omega} \nabla \cdot (\mathbf{j}) \delta \phi dv = 0 \quad [3.10.]$$

- 5) For the Galerkin method, the function  $\phi$  and its perturbation  $\delta \phi$  are approximated by linear combinations of shape functions

$$\delta \phi = \sum_i^N (\delta P_i) \psi_i, \quad \phi = \sum_j^N P_j \psi_j \quad [3.11.]$$

where  $N$  is the number of nodes.

- 6) Begin by replacing the  $\delta \phi$

$$\sum_i^N \delta P_i \left[ \iint_{\partial \Omega} \mathbf{j} \cdot \mathbf{n} \psi_i dS - \iint_{\partial \Omega} \sigma \alpha \phi \psi_i dS - \iiint_{\Omega} \sigma \nabla \phi \cdot \nabla \psi_i dv + \iiint_{\Omega} \nabla \cdot (\mathbf{j}) \psi_i dv \right] = 0 \quad [3.12.]$$

Since  $\delta P_i$  are independent coefficients, they can be set so that each of the integrals multiplied by  $\delta P_i$  yield zero.

- 7) Substitute the approximation of the function  $\phi$

$$\sum_j^N \sum_i^N P_j \left[ \iint_{\partial \Omega} \sigma \alpha \psi_j \psi_i dS + \iiint_{\Omega} \sigma \nabla \psi_j \cdot \nabla \psi_i dv \right] = \sum_i^N \left[ \iint_{\partial \Omega} \mathbf{j} \cdot \mathbf{n} \psi_i dS + \iiint_{\Omega} \nabla \cdot (\mathbf{j}) \psi_i dv \right] \quad [3.13.]$$

- 8) Express the solution in matrix notation

$$[\mathbf{M} + \mathbf{D}]\mathbf{p} = \mathbf{A}\mathbf{p} = \mathbf{s} \quad [3.14.]$$

where  $\mathbf{p}=P_j$ , a vector of the potential at each location;

$\mathbf{A} = \mathbf{M} + \mathbf{D}$ , the sum of the mass and diffusion matrices;

$\mathbf{M} = \oint\oint_{\partial\Omega} \sigma \alpha \psi_j \psi_i dS$ , the mass matrix;

$\mathbf{D} = \iiint_{\Omega} \sigma \nabla \psi_j \cdot \nabla \psi_i dv$ , the diffusion matrix;

$\mathbf{s} = \oint\oint_{\partial\Omega} \mathbf{j} \cdot \mathbf{n} \psi_i dS + \iiint_{\Omega} \nabla \cdot (\mathbf{j}) \psi_i dv$ , a vector with the source at each location.

The matrix equation has a vector  $\mathbf{p}$  of potentials (in volts) at each node and another vector  $\mathbf{s}$  of sources (in amperes) at each node. The matrix  $\mathbf{A}$  acts as an operator to transform the first vector into the second and it includes factors from the geometry connecting the nodes and the conductivity.

In the steps described conductivity appears as a scalar ( $\sigma$ ), which is only correct if the medium is isotropic. For an anisotropic medium conductivity is a tensor ( $\underline{\sigma}$ ), but this does not alter the procedure and the result is identical apart from the conductivity tensor.

### 3.2 Implementation

To transfer the governing equations presented in the previous section into a computer programme several issues have to be addressed. A mesh must be made to geometrically describe the model domain (sub-section 3.2.1), the matrix equation 3.14 has to be constructed (sub-section 3.2.2), the programme must be able to handle multiple sources (sub-section 3.2.3), methods of solving both the source and potential problems must be found (sub-section 3.2.4), and an estimation of error must be made (sub-section 3.2.5).

I increased the efficiency of subroutines in Kevin Hayley's (2007) code, including updating the mass matrix, and integrated them in a programme to calculate sources, as well as the potentials originally calculated in Hayley's programme.

### 3.2.1 MESHES

The equations were implemented in a finite element programme with tetrahedral elements. One of the strengths of the finite element method is that it does not require a structured grid, which is rectilinear with brick-shaped elements. An unstructured grid, where the domain is described by an irregular pattern of simple shapes, can be used instead. With an unstructured grid a site with steep topography can be described more precisely without an excessive number of elements. However, generating the mesh on an unstructured grid is more complicated.

The programme available for mesh generation, Tetgen (Si, 2003), was unable to generate adequate tetrahedral meshes for most geological models because the extents in x and y are so much greater than those in z. To bypass this problem I wrote a MATLAB routine to make a tetrahedral mesh from a structured grid by dividing each rectangular prism into six tetrahedra (Figure 3.1).

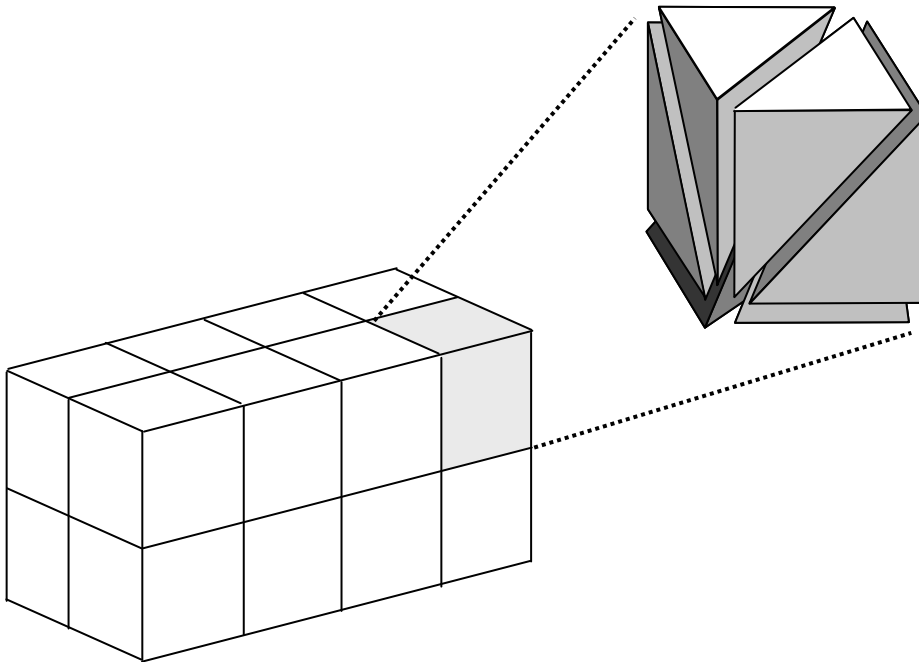


**Figure 3.1** Example of rectilinear structured grid. One element is divided into six tetrahedra, the shape used for finite element modelling.

### 3.2.2 CONSTRUCTION OF MATRIX EQUATION FROM GOVERNING EQUATIONS

The mesh provides a list of nodes, elements, each with four nodes, and outside faces, each with three nodes. Any point  $\mathbf{x}$  ( $x_i, y_i, z_i$ ) in the model domain can be described by interpolating the values at the nodes of the tetrahedron  $E$  ( $\mathbf{x}_1^E, \mathbf{x}_2^E, \mathbf{x}_3^E, \mathbf{x}_4^E$ ) which contain the point. In this programme the interpolation is linear and is done using shape functions that appear in equation 3.11. They can be thought of as mapping functions to transform a tetrahedron ( $E$ ) from global physical coordinates  $xyz$  to local parametric coordinates  $\xi\eta\zeta$  where the tetrahedron is orthogonal with three perpendicular faces of equal size and a fourth equilateral face (Pozrikidis, 2005).

$$\mathbf{x} = \mathbf{x}_1^E \psi_1 + \mathbf{x}_2^E \psi_2 + \mathbf{x}_3^E \psi_3 + \mathbf{x}_4^E \psi_4 \quad [3.15.]$$

The shape functions are given by

$$\psi_1 = 1 - \xi - \eta - \zeta, \quad \psi_2 = \xi, \quad \psi_3 = \eta, \quad \psi_4 = \zeta \quad [3.16.]$$

Substituting these functions into equation 3.15 yields

$$\mathbf{x} = \mathbf{x}_1^E + (\mathbf{x}_2^E - \mathbf{x}_1^E)\xi + (\mathbf{x}_3^E - \mathbf{x}_1^E)\eta + (\mathbf{x}_4^E - \mathbf{x}_1^E)\zeta \quad [3.17.]$$

The mapping is most easily described with a jacobian matrix

$$\mathbf{J} = \begin{bmatrix} \frac{\partial x}{\partial \xi} & \frac{\partial x}{\partial \eta} & \frac{\partial x}{\partial \zeta} \\ \frac{\partial y}{\partial \xi} & \frac{\partial y}{\partial \eta} & \frac{\partial y}{\partial \zeta} \\ \frac{\partial z}{\partial \xi} & \frac{\partial z}{\partial \eta} & \frac{\partial z}{\partial \zeta} \end{bmatrix} = \begin{bmatrix} x_2^E - x_1^E & x_3^E - x_1^E & x_4^E - x_1^E \\ y_2^E - y_1^E & y_3^E - y_1^E & y_4^E - y_1^E \\ z_2^E - z_1^E & z_3^E - z_1^E & z_4^E - z_1^E \end{bmatrix} \quad [3.18.]$$

and the determinant of the jacobian is equal to six times the tetrahedron volume, according to a geometrical interpretation of the outer vector product (Pozrikidis, 2005).

This mapping system is used to construct the mass and diffusion matrices in the equation 3.14. They are both symmetric square matrices with dimensions equal to the number of nodes. The diffusion matrix is constructed by visiting each element, making the appropriate calculations in local coordinates and assigning those values back to the global matrix at the correct node entry locations, where they are compiled. For the mass matrix,

it is each triangular face that is part of the model domain boundary that is visited. The appropriate calculations at each element are different for the mass and diffusion matrices.

The diffusion matrix,  $\mathbf{D} = \iiint_{\Omega} \sigma \nabla \psi_j \cdot \nabla \psi_i dv$ , includes gradients of shape functions. The

gradient  $\nabla \psi_i$  is originally in xyz coordinates,  $\nabla \psi_i = \left( \frac{\partial \psi_i}{\partial x}, \frac{\partial \psi_i}{\partial y}, \frac{\partial \psi_i}{\partial z} \right)$ , and in

parametric space this becomes  $\left( \frac{\partial \psi_i}{\partial \xi}, \frac{\partial \psi_i}{\partial \eta}, \frac{\partial \psi_i}{\partial \zeta} \right)$ , where

$$\begin{aligned} \frac{\partial \psi_i}{\partial \xi} &= (\mathbf{x}_2^E - \mathbf{x}_1^E) \cdot \nabla \psi_i \\ \frac{\partial \psi_i}{\partial \eta} &= (\mathbf{x}_3^E - \mathbf{x}_1^E) \cdot \nabla \psi_i \\ \frac{\partial \psi_i}{\partial \zeta} &= (\mathbf{x}_4^E - \mathbf{x}_1^E) \cdot \nabla \psi_i \end{aligned} \quad [3.19.]$$

Equations 3.19 above can be abbreviated as  $\mathbf{J}^T \cdot \nabla \psi_i$ , where  $\mathbf{J}^T$  is the transpose of the jacobian defined in equation 3.18. There are four shape functions as defined in equation 3.16 and if they are substituted into the previous equation, they produce the system of equations (Pozrikidis, 2005):

$$\mathbf{J}^T \cdot \nabla \psi_1 = - \begin{bmatrix} 1 \\ 1 \\ 1 \end{bmatrix}, \quad \mathbf{J}^T \cdot \nabla \psi_2 = \begin{bmatrix} 1 \\ 0 \\ 0 \end{bmatrix}, \quad \mathbf{J}^T \cdot \nabla \psi_3 = \begin{bmatrix} 0 \\ 1 \\ 0 \end{bmatrix}, \quad \mathbf{J}^T \cdot \nabla \psi_4 = \begin{bmatrix} 0 \\ 0 \\ 1 \end{bmatrix} \quad [3.20.]$$

If a matrix  $\mathbf{Q}$  is constructed by concatenating the four right hand sides, the system may be rewritten as

$$\mathbf{J}^T \cdot \nabla \psi_i = \begin{bmatrix} -1 & 1 & 0 & 0 \\ -1 & 0 & 1 & 0 \\ -1 & 0 & 0 & 1 \end{bmatrix} = \mathbf{Q} \quad [3.21.]$$

This can be solved for  $\nabla \psi_i$  by multiplying both sides by the inverse of  $\mathbf{J}^T$ ,  $(\mathbf{J}^T)^{-1}$ .

$$\nabla \psi_i = (\mathbf{J}^T)^{-1} \mathbf{Q} \quad [3.22.]$$

For each element

$$\mathbf{D}^E = \sigma \left( (\mathbf{J}^T)^{-1} \cdot \mathbf{Q} \right) \cdot \left( (\mathbf{J}^T)^{-1} \cdot \mathbf{Q} \right) \quad [3.23.]$$

If  $\underline{\sigma}$  is a tensor, then a dot product is used between the first two variables.

$$\mathbf{D}^E = \underline{\underline{\sigma}} \cdot \left( (\mathbf{J}^T)^{-1} \cdot \mathbf{Q} \right) \cdot \left( (\mathbf{J}^T)^{-1} \cdot \mathbf{Q} \right) \quad [3.24.]$$

To construct the global diffusion matrix  $\mathbf{D}$ , each model element is visited, its  $4 \times 4$  element diffusion matrix  $\mathbf{D}^E$  is calculated using equation 3.23 and included in the appropriate entries of the global diffusion matrix.

The formula  $\mathbf{M} = \iint_{\alpha\Omega} \sigma \alpha \psi_j \psi_i dS$  refers to a surface described by triangles that can be rotated so that it can be described in a 2D xy space. The xy surface can be further transformed into  $\xi\eta$  space by defining

$$\psi_1 = \zeta = 1 - \xi - \eta, \quad \psi_2 = \xi, \quad \psi_3 = \eta \quad [3.25.]$$

When the substitutions are made, for an outer face F of area A (Pozrikidis, 2005),

$$\mathbf{M}^F = \iint_F \sigma \alpha \psi_j \psi_i dx dy = 2A \iint_F \sigma \alpha \psi_j \psi_i d\xi d\eta = 2A \sigma \alpha \iint_F \begin{bmatrix} \zeta^2 & \zeta\xi & \zeta\eta \\ \xi\zeta & \xi^2 & \xi\eta \\ \eta\zeta & \eta\xi & \eta^2 \end{bmatrix} d\xi d\eta \quad [3.26.]$$

The double integration can be made using the integration formula

$$\iint \zeta^p \xi^q \eta^r d\xi d\eta = \frac{p!q!r!}{(p+q+r+2)!} \quad [3.27.]$$

and the result is a simple formula

$$\mathbf{M}^F = \sigma \alpha \frac{A}{12} \begin{bmatrix} 2 & 1 & 1 \\ 1 & 2 & 1 \\ 1 & 1 & 2 \end{bmatrix} \quad [3.28.]$$

assigned to the nodes of the outside face. The  $\alpha$  term is the dot product between the outer surface normal and the vector between the center of the outer surface and the location of the source. For the anisotropic case, the  $\sigma\alpha$  term is calculated together as:

$$\underline{\underline{\sigma}}\alpha = \frac{(\underline{\underline{\sigma}} \cdot \mathbf{n}) \cdot \mathbf{r}}{|\mathbf{r}|^2} \quad [3.29.]$$

In a manner identical to the global diffusion matrix, the global mass matrix  $\mathbf{M}$  is constructed by visiting each outer face, calculating its  $3 \times 3$  face mass matrix  $\mathbf{M}^F$  and adding them together at the correct nodes of the global mass matrix.

### 3.2.3 MULTIPLE SOURCES

When using the generalized boundary condition, each non-zero entry in the source term is used for the mass matrix calculations. For electrical resistivity surveys where there are typically two electrodes and therefore two sources, this is quite feasible. When calculating the potential due to electrokinetic or electrochemical sources, the sources occur on each node in the model domain. Even when considering only those nodes with sources greater than a cut-off amplitude, their number makes the mass matrix calculation prohibitive. In these cases a no flux boundary ( $\mathbf{j} \cdot \mathbf{n}=0$ ) is imposed everywhere and equation 3.14 can be simplified to

$$\mathbf{Dp} = \mathbf{s} \quad [3.30.]$$

For such calculations, two model domains are used. A smaller one covering the area of interest and serves for calculating sources whilst a larger second domain is used to calculate potentials and encompass the first, extending the boundaries at least one kilometre in each direction. The mesh of the extensions is coarse so that a large region can be added without increasing excessively the number of nodes.

Distant boundaries are necessary when calculating potentials using no flux boundaries because they imply no current is leaving the model domain and if the currents are not sufficiently small at the boundary, they cause edge effects on the calculated potentials. Edge effects are visible by erroneous potentials around the edge of the model domain or if the same problem calculated with two domain sizes produces different potentials. Imposing a no flux boundary condition absolutely everywhere requires the domain's sources to be exactly balanced. To avoid this problem, a single node in a corner at the surface is assigned a fixed potential of zero. This is done by setting the column of the  $\mathbf{D}$  matrix corresponding to the corner node to zero except at the row for the corner node, which is set to one.

### 3.2.4 SOURCE AND POTENTIAL SOLUTIONS

Sources can be calculated using a matrix-vector multiplication:  $\mathbf{s}=\mathbf{A}\mathbf{p}$ . To calculate potentials given  $\mathbf{s}$  requires the inverse of  $\mathbf{A}$ :  $\mathbf{p}=\mathbf{A}^{-1}\mathbf{s}$ . Calculations of both sources and potentials were made. For example, streaming potential can be calculated by first using streaming current coupling coefficients ( $L'$ ) and head ( $h$ ) to calculate a source term

$$\begin{aligned} \nabla \cdot (L' \nabla h) &= \nabla \cdot j_{convective} \\ \mathbf{A} = \nabla \cdot (L' \nabla *) \quad , \quad \mathbf{p} = h \quad , \quad \mathbf{s} = \nabla \cdot j_{convective} &= \mathbf{A}\mathbf{p} \end{aligned} \quad [3.31.]$$

The star (\*) in the expression of  $\mathbf{A}$  is a place holder to signify that the  $\mathbf{A}$  matrix, which incorporates information about the coefficients and the gradient between different nodes, must multiply the value at those nodes,  $\mathbf{p}$ . Since the divergences of the convective and conductive currents are equal but opposite in sign in the absence of imposed outside sources, the source term from equation 3.31 can be used with the electrical conductivity distribution ( $C$ ) to calculate electrical potentials ( $\phi$ )

$$\begin{aligned} \nabla \cdot j_{convective} &= -\nabla \cdot j_{conductive} \\ \mathbf{A} = \nabla \cdot (C \nabla *) \quad , \quad \mathbf{p} = \phi = \mathbf{A}^{-1}(-\mathbf{s}) \end{aligned} \quad [3.32.]$$

The  $\mathbf{A}$  matrices are very large and calculating their inverse can be time consuming so alternate methods are used. When solving a system with a limited number of sources the MATLAB matrix left divide function ( $\backslash$ ) was used. For symmetric matrices with real positive diagonal elements this function uses Cholesky factorization to approximate the inverse of  $\mathbf{A}$  and calculate  $\mathbf{p}$ . When the system of equations had many sources this method took longer and produced unphysical results with repeated variations in potential of 100s of millivolts over decimetres. An iterative method, the minimum residual method, was used to estimate  $\mathbf{p}$  instead.

### 3.2.5 ERROR

Errors in numerical modelling can arise from model discretisation. Using a refined mesh will produce more accurate results than a coarse mesh but the refinement also increases calculation requirements because it increases the size of the system of equations to be solved.

Hayley (2007) tested the accuracy of his code by comparing analytical and numerical solutions of a pole-pole electrical survey. He found that the error was within 5% with a mesh quality factor of 1.2 and within 2.5% with a mesh quality factor of 1.1. The quality factor is the circumsphere radius to the shortest length ratio of the mesh elements so that the ideal is roughly spherical elements. The meshes for geological domains typically have poor quality factors because they have larger x and y extents than z extents. This should not increase the error because property variations are usually not rapid in the x and y directions.

The largest source of error in numerical modelling is the uncertainty in the input data. It is necessary to populate the entire model domain with properties and since it is impossible to measure them everywhere in the field, interpolations and extrapolations are necessary and they introduce error. Minsley et al. (2007b) demonstrated how SP inversion results are sensitive to an unknown resistivity structure.

### 3.3 Electrical source in anisotropic medium

To validate the programme, it is easiest to compare its calculated results with analytical results for a simple problem. The problem chosen is a point electrical source in an anisotropic medium. The problem is solved for a whole space and would be equivalent to an electrode injecting current deep underground, with the second electrode located an infinite distance away.

The analytical solution for equation 3.6 when  $\mathbf{j}$  is a point source at  $\mathbf{r}_0$  of intensity  $I$  is (Telford et al., 1990)

$$\phi(p) = \frac{I\rho}{4\pi\mathbf{r}} \quad [3.33.]$$

where  $\mathbf{r} = \mathbf{r}_p - \mathbf{r}_0$ , the vector between observation point  $p$  and the source. It can be modified for an anisotropic medium by using a geometric mean of resistivity ( $\rho$ ) and multiplying the components of  $\mathbf{r}$  by the square root of resistivity in the appropriate direction (Parasnis, 1986):

$$\phi(p) = \frac{I\sqrt{\rho_x\rho_y\rho_z}}{4\pi\sqrt{\rho_x x^2 + \rho_y y^2 + \rho_z z^2}} \quad [3.34.]$$

The numerical solution was calculated in a model domain 4040 m cubed with the source located exactly in the middle. The analytical solution was calculated at the grid nodes. A first test was done with an isotropic 100  $\Omega\text{m}$  medium and a 1 ampere source. The second test introduced anisotropy with  $\rho_x=\rho_y=100 \Omega\text{m}$  and  $\rho_z=10 \Omega\text{m}$ .

A comparison of both analytical and numerical methods for both tests (Figure 3.2) shows good agreement between the methods. The figure presents electrical potential contours on different slices through the medium. The solid contours are the analytical solution and the dotted contours were calculated numerically. Figures for x or y anisotropy are not presented, but have similar precision.

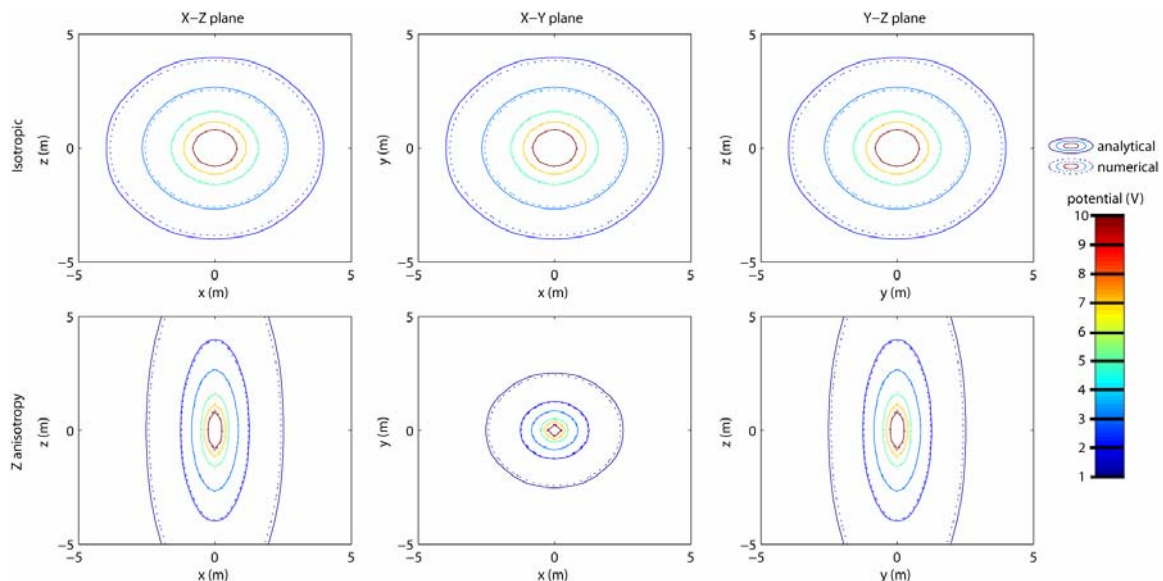


**Figure 3.2 Comparison of electrical potential calculated with analytical (solid line) and numerical (dotted line) methods. Different panels are sections through the centre of the model domain for the isotropic (TOP) and z anisotropy (BOTTOM) cases. The source is located at 0,0 in each panel.**

### 3.4 Streaming potential through a dam

For the next example, the finite element programme was compared to the SP3D programme developed by Megan Sheffer and described in the programme manual (UBC -

Geophysical Inversion Facility, 2005), an article (Sheffer & Oldenburg, 2007) and her Ph.D. dissertation (Sheffer, 2007). A comparison with a similar programme allows testing of models too complex to have analytical solutions.

The example is the calculation of streaming potential caused by a hydraulic gradient through a hypothetical dam. The dam problem is the example found in the SP3D programme manual. The dam is 350 m long by 100 m tall and 100 m wide, with a three part internal structure (Figure 3.3 TOP). The hydraulic conductivity ( $K$ ), streaming current coupling coefficient ( $L'$ ) and electric resistivity ( $\rho$ ) of each region are listed in Table 3.2.

**Table 3.2 Properties of different dam regions.**

	$K$ (m/s)	$L'$ (A/m <sup>2</sup> )	$\rho$ ( $\Omega\text{m}$ )	
			saturated	unsaturated
shell	$2 \cdot 10^{-4}$	$5 \cdot 10^{-5}$	350	800
transition	$5 \cdot 10^{-5}$	$2 \cdot 10^{-5}$	300	700
core	$10^{-8}$	$10^{-5}$	125	300

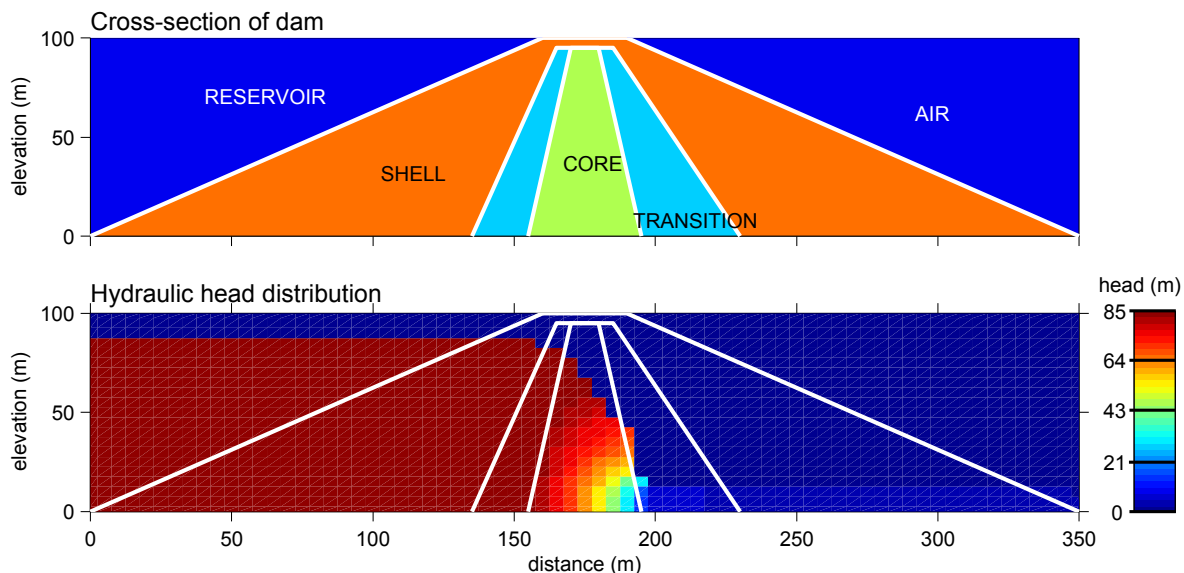


**Figure 3.3 TOP: Cross-section of dam with different regions for hypothetical problem. BOTTOM: hydraulic head distribution through dam.**

The unsaturated streaming current coupling coefficient is zero and the water resistivity 100  $\Omega\text{m}$ . The upstream reservoir on the left has a fixed water column height of 85 m and downstream the water level is fixed at 5m.

The hydraulic potential problem is solved using the software Visual MODFLOW (Waterloo Hydrogeologic Inc., 2002) and the resulting head distributions are shown in Figure 3.3 BOTTOM. Since MODFLOW uses a finite difference algorithm, the output is values at block centred nodes, which is represented by the blocky appearance of the picture.

Output from MODFLOW is used as input for the programme SP3D, which uses a finite volume algorithm. The SP model domain is extended by one times the initial hydraulic model length in each direction. The potentials calculated with SP3D for a cross-section through the dam (Figure 3.4 TOP) show a positive anomaly where the hydraulic head reaches its lower limit. There is also a negative anomaly in the transition zone of the dam. Two profiles were extracted, one at 5 m elevation, to pass through the anomalies (Figure 3.4 BOTTOM CENTRE), and a second at the downstream surface of the dam, where it would be possible to make SP measurements (Figure 3.4 BOTTOM).

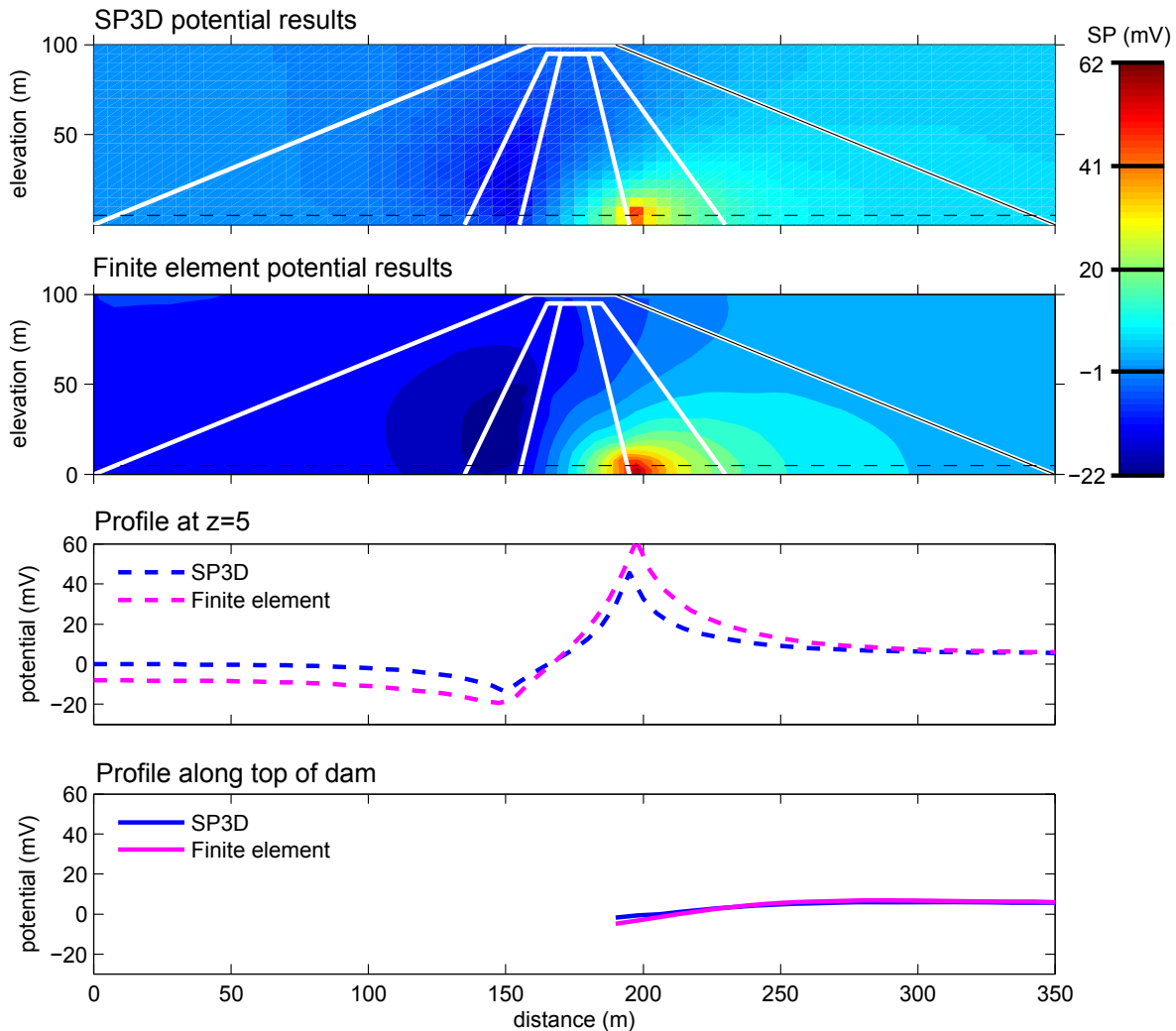


**Figure 3.4 Comparison of potentials calculated with two methods for the hypothetical dam model. All cross-sections and profiles are through the centre of the dam at  $y=50$  m. The solid and dashed black lines in the top two panels are the locations of the profiles found in the bottom two panels. TOP: Cross section of potentials calculated with SP3D. TOP CENTRE: Cross-section of potentials calculated with finite element programme. BOTTOM CENTRE: profile through cross-section at 5 m elevation. BOTTOM: profile along top of dam.**

Calculations using the finite element programme were made for the same model domain, but a different grid was used. It was possible to use an unstructured grid generated with Tetgen, which allowed refinement in the area around the water table. The hydraulic head values produced with MODFLOW were interpolated onto the mesh points using trilinear interpolation. The potentials calculated with the finite element model have the same pattern as those from SP3D, but the range of the anomalies is 37% greater (Figure 3.4

TOP CENTRE). This is to be expected because the coarseness of the mesh used in SP3D acts as a smoothing filter, reducing the anomaly amplitudes. The same two profiles were extracted from the finite element data and are presented with the SP3D data. The difference in anomaly amplitude between programmes is visible in Figure 3.4 BOTTOM CENTRE, whereas on the top of the dam, the potentials are almost identical (Figure 3.4 BOTTOM).

### 3.5 Summary

To better understand phenomena in the field it is helpful to model them. Their complexity often leaves numerical models as the only tool powerful enough to do so. This chapter introduced a finite element programme that will be used in the rest of this work to study spontaneous potentials.

When spontaneous potentials are described as being caused by coupled fluxes, the formulations due to different causes are identical, which means that the same code can work for several causes. The general formulation is  $\nabla \cdot (k \nabla \Phi) = -s$  and a finite element programme written by Hayley (2007) was used and modified for our purposes.

To demonstrate the validity of the programme, it was compared with other solutions for two examples. The first was an electric point source in an anisotropic medium and the potential contours calculated coincided with those found using an analytical solution. A hypothetical dam was used as the second example because it was more complex and included regions with different properties. In this case the finite element output was compared with that from the published programme SP3D and found to have the same pattern and similar amplitudes.



#### 4 LABORATORY MEASUREMENTS

The study of contaminant targets with spontaneous potential surveys is a recent development. Their application to such areas aims to map the redox degradation halos of organic groundwater plumes. Though the target is SP of electrochemical origin, part of the SP signal is due to streaming potential. It is therefore necessary to model streaming potential and subtract it from the total SP measurement.

To model streaming potentials it is necessary to know the streaming current coupling coefficient ( $L'$ ). The equation describing streaming potential is

$$j = -L'\nabla h - \sigma\nabla\phi \quad [4.1.]$$

where  $j$  is the current density,  $h$  is hydraulic head,  $\sigma$  is electrical conductivity and  $\phi$  is electrical potential. To obtain  $L'$  it may seem as that the simplest method would be to set

$\nabla\phi$  to zero to obtain  $L' = -\left(\frac{j}{\nabla h}\right)_{\nabla\phi=0}$ . However it is difficult to set  $\nabla\phi = 0$  because there is

an electrical potential as soon as there is a pressure gradient. Therefore the streaming potential coupling coefficient ( $C'$ ) is measured instead, because it is easy to set the current to zero by leaving the circuit open.

$$C' = -\frac{L'}{\sigma} = -\left(\frac{\nabla\phi}{\nabla h}\right)_{j=0} \quad [4.2.]$$

The streaming current coupling coefficient can then be calculated using equation 4.2. Since pressure ( $P$ ) is often easier to measure in the laboratory than hydraulic head, experiments are usually set up with horizontal flow and  $C$  ( $\Delta V/\Delta P$ ) is reported. When there is no elevation head it can be used to calculate  $L'$  using:

$$L' = -\sigma C \rho_w g \quad [4.3.]$$

where  $\rho_w$  is water density and  $g$  is the gravitational constant.  $L'$  is typically reported in units of  $A/m^2$  though a more accurate notation would be  $A/m \cdot m_{H_2O}$ .

Many laboratory studies have determined the streaming potential coupling coefficient, as described in section 2.1, but few of these have also measured the electrical resistivity or conductivity of the same sample. Sheffer (2005) noted this shortage.

Contaminants and their degradation can change sediment surface properties (Che-Alota et al., 2009), which will presumably change the streaming current coupling coefficient. The aim of this chapter is to test this hypothesis and determine what impact altered streaming current coupling coefficients could have on field studies. In order to do so, it is necessary to measure the streaming current coupling coefficient of both clean and contaminated sediment. The effect on  $L$  is potentially important information when trying to interpret an SP anomaly over a contaminant plume as it could help determine if part of the anomaly is due to special streaming potential effects or if the anomaly is of electrochemical origin. A laboratory apparatus was built to study the effect of hydrocarbon contamination on streaming potential in a controlled environment and the streaming current coupling coefficient of sediment and core samples from two sites was measured.

The apparatus was constructed following the plans found in Sheffer (2005) with some modifications and is described in section 4.1. The measurement procedures and calibration are presented in sections 4.2 and 4.3 respectively. Experimental results are reported in section 4.4, discussed in section 4.5 and summarized in section 4.6.

#### **4.1 Apparatus for measuring streaming current coupling coefficient**

In articles describing coupling coefficient measurements, a problem commonly mentioned is the lack of chemical equilibrium between the sample and the saturating solution (Guichet & Zuddas, 2003; Mainault et al., 2006). This causes chemical gradients which can contribute to the electrical potential measured and results in poor test reproducibility. To ensure sample-fluid equilibrium, groundwater was collected at the same sites as the sediment samples and used as saturating fluid.

A method of diminishing chemical disequilibrium is reducing the quantity of saturating fluid in contact with the sample. This can be done by using AC (alternating current) testing which has been shown to give results equivalent to the more common DC (direct current) method (Reppert & Morgan, 2001; Sheffer, 2005). The AC method was used

because the small volume of saturating fluid was also an advantage when dealing with hydrocarbon contaminated fluids.



**Figure 4.1 Apparatus consisting of a PVC cylinder and two end plates. The end plates are held in place by long bolts.**

The apparatus consists of a PVC cylinder and two end plates (Figure 4.1). The end plates are held in place by four bolts which go from one plate to the other along the length of the cylinder. The inside diameter of the cylinder is 5.85 cm and its length is 15 cm, which allows for a 0.4 L sample volume. Both ends are blocked with 100  $\mu\text{m}$  plastic mesh and a 2 mm plastic mesh. The finer mesh keeps the sample in the cylinder and the coarser mesh keeps the finer mesh from moving into the holes in the end plates. The face of the end plate against the cylinder has a 24 mm diameter hole through it. This hole is 21 mm deep and leads to a cylindrical chamber hollowed out in a block of PVC that is part of the end plate (Figure 4.2). A large diameter hole on the end plate between the sample and the sensors is necessary so that the entire drop in hydraulic head between the pressure sensors in either plate is through the sample and not due to a constricted flow path through the end plate.

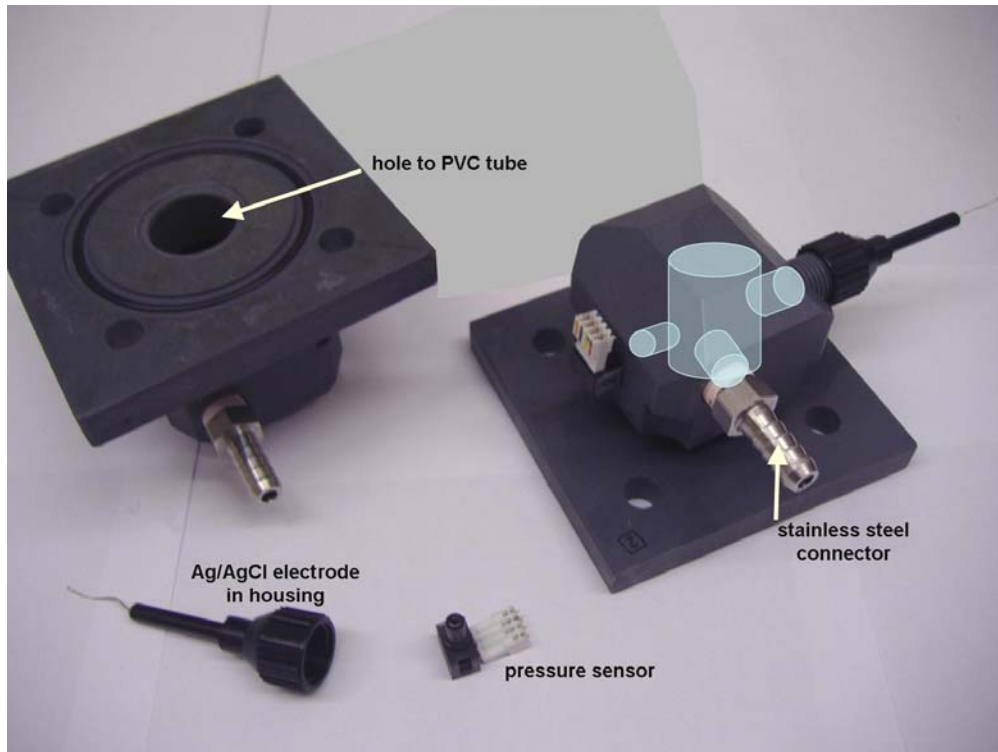


**Figure 4.2 End plates. On the right plate semi-transparent cylinders have been added to illustrate the hollow chamber and its three ports.**

The chamber has a 33.8 mm diameter, a 29 mm depth and is connected to three ports. Two ports are exactly opposite each other and house a pressure sensor and an electrode. The third port has a stainless steel connector to which an 8.5 mm diameter plastic tube can be attached to bring fluid in and out of the cylinder. The size of the chamber and ports is designed to fit the sensors. The tubes from each end plate lead to two cylindrical water reservoirs with an 8.6 cm diameter and 21.1 cm length, with capacities of 1.225 L. The sample holder was positioned for horizontal fluid flow so that hydraulic head is entirely described by pressure. This simplifies the calculations and the streaming potential coupling coefficient used is  $C$  in mV/MPa, and when necessary it is converted to the streaming current coupling coefficient  $L'$  in  $\mu\text{A}/\text{m}^2$  using equation 4.3.

The electrodes used are Warner Instrument Ag/AgCl flat tipped probes E208, chosen because of their small size and the AgCl was sintered on to prevent leakage. The electrical potential is measured through these electrodes using a National Instrument

USB-6215 data acquisition device (DAQ) with a  $10\text{ G}\Omega$  input impedance. The acquisition rates of this device are high enough to properly sample noise sources so they can be removed by filtering. The output of the pressure sensors is also measured with the DAQ.

The pressure sensors used are Omega PX26-005 GV gauge pressure transducers 0-5 PSIG range. Two separate pressure sensors are used to avoid the possibility of electrically connecting both sides of the sample. They require a 10 V input voltage which is provided using an Analog Devices 10V Precision Voltage Reference and two 9 V batteries. This ensures a constant and precise input voltage, which is necessary for an accurate pressure measurement since the output signal is dependant on the input voltage. The output signal is a voltage read by the DAQ.

For resistivity measurements the end plates are replaced with stainless steel discs (Figure 4.3). A wire is attached to each disc so that they can be hooked up into an electrical circuit.

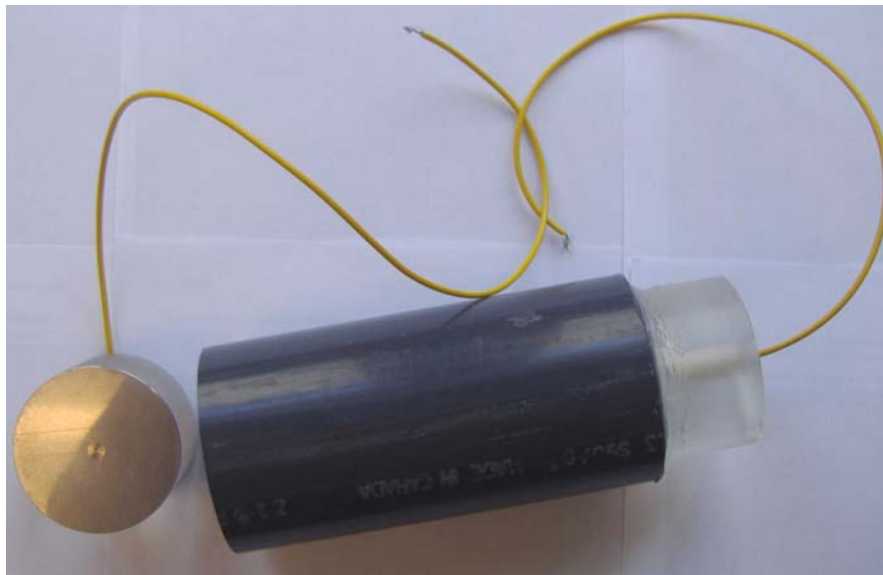


**Figure 4.3** PVC cylinder with stainless steel discs for resistivity measurements. Discs are held in place with silicone.

## **4.2 Measurement procedures**

Each sample was divided in two parts, one soaked in clean groundwater from the site and the other soaked in site groundwater polluted with hydrocarbons. The first samples tested were glass beads, to check that the apparatus worked properly and gave plausible results. The tests performed on each sample were streaming potential coupling coefficient, hydraulic conductivity, electrical resistivity and geochemical analyses, and the following four sub-sections describe how these experiments were done. Packing and measurements for each sub-sample took seven to eight days.

### *4.2.1 STREAMING POTENTIAL COUPLING COEFFICIENT*

Samples from two sites were analysed. The samples are described in sub-section 4.4.1 and the sites (RIVER and KNOLL) are the subject of chapter 5. Samples from the site RIVER are unconsolidated sediment and gravel larger than 1.5 cm was discarded because it would occupy too large a fraction of the sample-holder cross-section. Samples from the KNOLL site were consolidated material so the core was ground, first with a Jaw Crusher Mill by TM Engineering and then using a Swing Mill by Bleuler-Mill. To help with sample-solution equilibrium each sample was mixed with approximately 2 L of solution and kept in air tight plastic containers for periods varying from 12 days to 160 days before being measured.

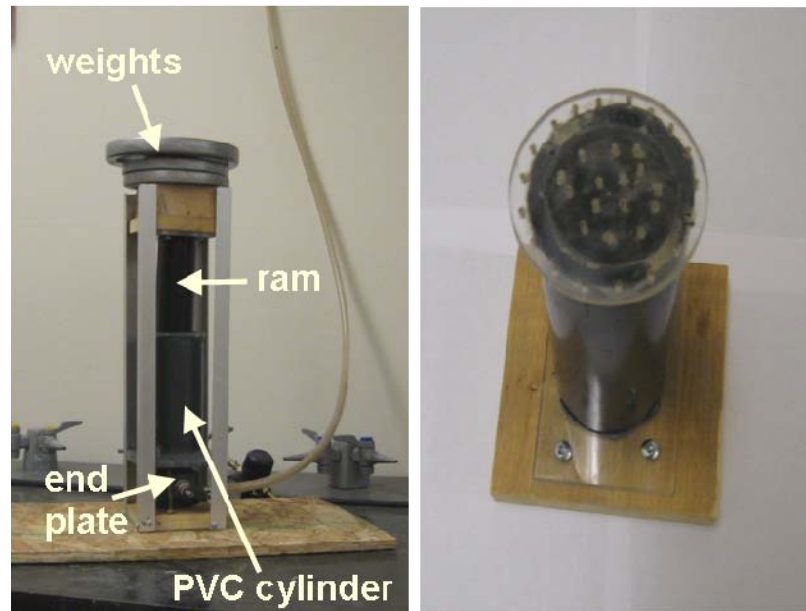


**Figure 4.4 Support for packing the sample with the ram. LEFT: Set up for packing the sample. RIGHT: Close-up of ram.**

The sample packing procedure involved the following steps:

- 1) An end plate with plastic mesh in place was fixed to the sample cylinder with silicone.
- 2) The sample holder was placed in a support to keep it vertical.
- 3) Solution was poured in to fill the end plate chamber and tubing.
- 4) The sediment was poured into the sample cylinder as a slurry
- 5) It was packed with a ram (Figure 4.4) and the weight on the ram was increased over the period of a day to a value similar to the in-situ overburden pressure for the samples. A weight equivalent to 2.5 m depth was used for RIVER samples and 3.8 m depth for KNOLL samples.
- 6) The samples were left a second day until they were no longer compacting.
- 7) The top end plate was attached with bolts and silicone.

Throughout the packing procedure the sediment was kept saturated since it is difficult to saturate once it is packed, and air bubbles were cited as a source of problems when making coupling coefficient measurements (Morgan et al., 1989). Once the top plate was well fixed, fluid was forced up through the cylinder that was kept vertical. This was done

by filling with water a long tube attached to the port of the bottom plate so that the water pressure was approximately 2 m of head. The fluid passed through the sample, filled the chamber in the top plate and came out of the tube attached to the top plate. For samples with low hydraulic conductivity it could take more than 24 hours to pass through.

Once the apparatus was packed with both end plates full of liquid, it could be set up to make streaming potential coupling coefficient measurements. The tubes from both end plates were attached to the reservoirs. At first compressed air was used to push the fluid from one reservoir to another, the flow being controlled by a valve (Figure 4.5 LEFT). Switching the valve created abrupt pressure changes that caused spikes in the electrical signal so this method was abandoned. The second method consisted of a see-saw holding both fluid reservoirs that could gently rock back and forth to change the relative reservoir heights (Figure 4.5 RIGHT). This produced smooth results when working with samples of high hydraulic conductivities. With low hydraulic conductivity samples, the fluid movement was so slow that the reservoirs did not drain. For these samples the tubes normally connected to the reservoirs were detached, filled with fluid, and alternately raised and lowered by hand.

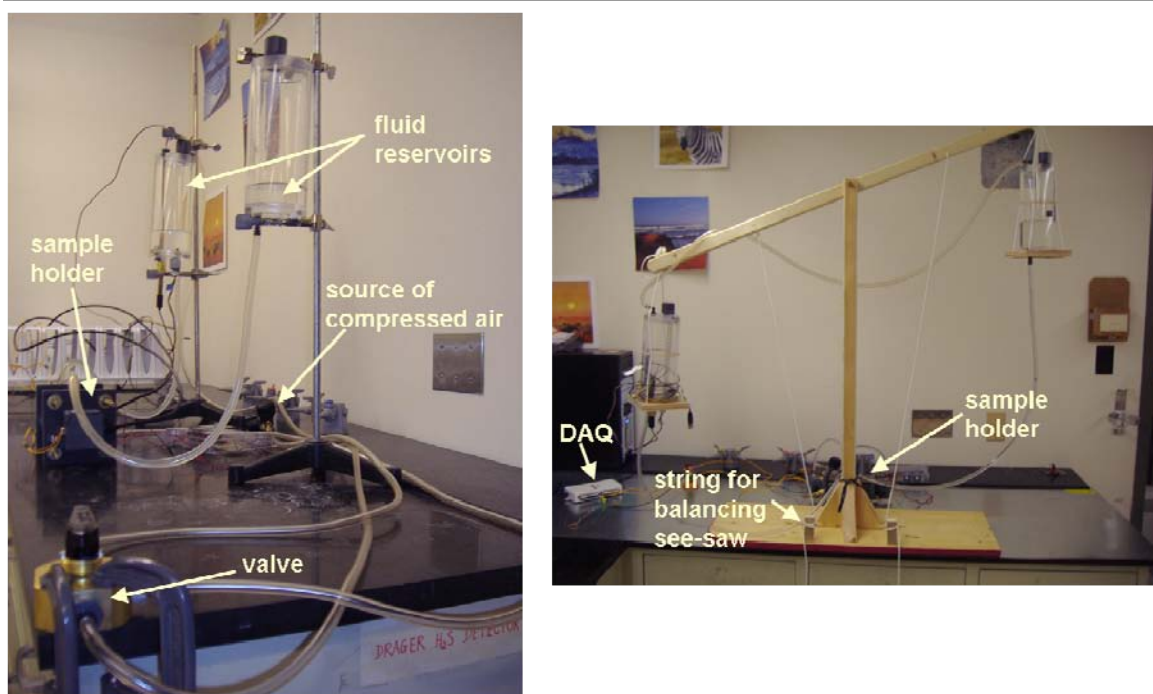


**Figure 4.5** Methods of pushing fluid through the sample. **LEFT:** Compressed air is brought from the bench to the valve, at the front of the image, which controls which reservoir the air is sent to. **RIGHT:** See-saw to balance the reservoirs, operated using a string attached to the cross bar in two places. Abbreviations: DAQ—data acquisition device.

When the system was first set up, the measured potential drifted significantly, up to several mV/min because the Ag/AgCl electrodes were not yet equilibrated with the system. After approximately 2 hours, this drift would be less than 0.05 mV/min at which point measurements could be made. Six minute tests were done by recording the electrical potential and pressure sensors signals with the DAQ for three phases: while the system was at rest for two minutes, while the fluid reservoirs or tubes were oscillated for two minutes and another two minutes of the system at rest. A computer displayed the DAQ data in real time which allowed the person moving the tubes to monitor progress.

Since the potential differences are on the order of tens to hundreds of microvolts, electrical noise from the environment poses a problem. Three measures were taken to reduce this noise. First, a galvanized steel sheet was used to cover the workbench on which the system was set up and the DAQ ground was connected to this sheet. Secondly,

bias resistors of  $100\text{ M}\Omega$  were installed as shown in Figure 4.6 when making the electrical potential measurements.

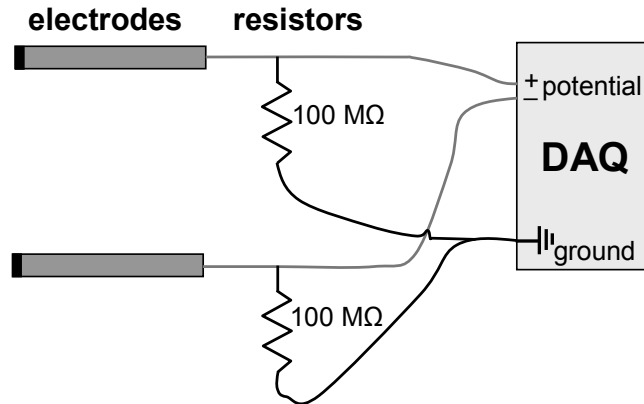


**Figure 4.6** Bias resistor set-up for reducing noise in potential measured between two electrodes. Abbreviations: DAQ—data acquisition device.

The third measure was filtering and averaging of the measurements made by the DAQ. National Instruments Labview software was used to create a programme to operate the DAQ. For streaming potential coupling coefficient measurements, 1200 readings were made per second, these data were filtered using a 4<sup>th</sup> order Butterworth low pass filter with a cut-off frequency of 10 Hz and the mean of 300 readings was recorded. This produced data at a 4 Hz rate which was clean and yet capable of accurately sampling the oscillations of the test which were at approximately 0.1 Hz. The signal from the electrodes and pressure sensors were both handled in the same way since the signals were going to be compared.

The first step in data analysis was the calculation of the difference in pressure. The voltage output signals from the pressure sensors were converted to pressure and the difference was taken. By convention the reference electrode (negative) is placed in the upstream reservoir, therefore the pressure from the endplate with the negative potential electrode was subtracted from that of the end plate with the positive electrode. The next step was to draw a scatter plot of difference in pressure ( $\Delta P$ ) vs. difference in potential ( $\Delta V$ ) and to do a regression as is discussed in section 4.3. The streaming potential coupling coefficient ( $C$ ) is the slope of this regression. For each measurement the 80

second period with the smallest signal drift was chosen for analysis. Each  $C$  was therefore determined from 321 values.

The temperature of the system was noted during each measurement. Work was done at room temperature, between 20 and 22 °C, but sometimes the sample holder was colder because when possible, it was kept in the fridge overnight for hydrocarbon samples.

#### 4.2.2 HYDRAULIC CONDUCTIVITY

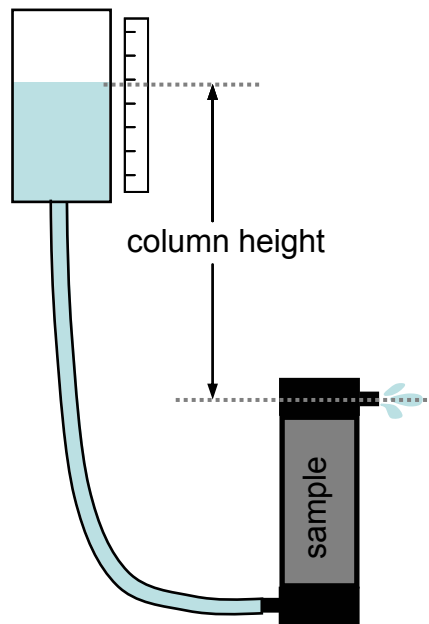


**Figure 4.7** Set-up for falling head hydraulic conductivity test.

While the sample was still in the apparatus for measuring coupling coefficient, it was relatively easy to measure its hydraulic conductivity. A falling head test was used for the measurements. The sample holder was placed upright with a tube and reservoir on the bottom port and the top port was left open (Figure 4.7). Fluid drained from the reservoir up through the sample and out the top. The fluid column height was measured between the top outlet and the fluid level in the reservoir. A ruler was pasted on the reservoir to note the level changes easily. For samples with low hydraulic conductivity it was necessary to use a long tube to generate ~1.5 m of head so that the levels changed perceptibly. The reservoir level was read at 30 s to 4 min intervals, using a stop watch for timing.

For the measurement of the glass bead samples, the hydraulic conductivity was much higher and the reservoir levels changed too rapidly to use the method described above. Instead the time interval necessary to drain 2 cm of fluid from the reservoir was measured.

The hydraulic conductivity ( $K$ ) was calculated using the formula (Domenico & Schwartz, 1998):

$$K = \frac{a\ell}{A} \frac{1}{t_1 - t_0} \ln \frac{h_0}{h_1} \quad [4.4.]$$

where  $a$  is the cross-sectional area of the fluid reservoir or tube,  $\ell$  is the length of the sample,  $A$  is the cross-sectional area of the sample,  $t_{0,1}$  are two times and  $h_{0,1}$  are the head or fluid column heights at times  $t_0$  and  $t_1$ .

#### 4.2.3 ELECTRICAL RESISTIVITY

Electrical resistivity was measured after the coupling coefficient and hydraulic conductivity had been measured. While keeping the sample holder vertical, the bolts, end plate and plastic mesh were removed from the top of the sample cylinder. A stainless steel disc was fixed to the end of the cylinder using silicone. When the silicone had solidified, the sample holder was flipped over and the remaining end plate and plastic mesh removed. The sediment plug was pushed down to the end of the sample cylinder with the fixed stainless steel disc using the ram. The sediment plug was  $\sim 3$  mm shorter than the PVC cylinder because of the space occupied by the plastic mesh. The space between the top of the sediment and the top of the sample cylinder was filled with fluid and the second stainless steel disc was placed on top of the cylinder.

The resistivity was measured by treating the sediment filled cylinder as a component in an electrical circuit. The software Labview was used to generate a sinusoidal voltage signal that was fed to the system through the DAQ. A sinusoid was used to avoid capacitance effects due to charge build up on the stainless steel discs, where current conduction switches from electronic to ionic. The signal was fed to the sample holder using the leads

connected to the discs. The potential was measured across the leads as well as across a resistor of known resistance in series in the circuit. Diagrams of the installation as well as an equivalent circuit diagram are illustrated in Figure 4.8.

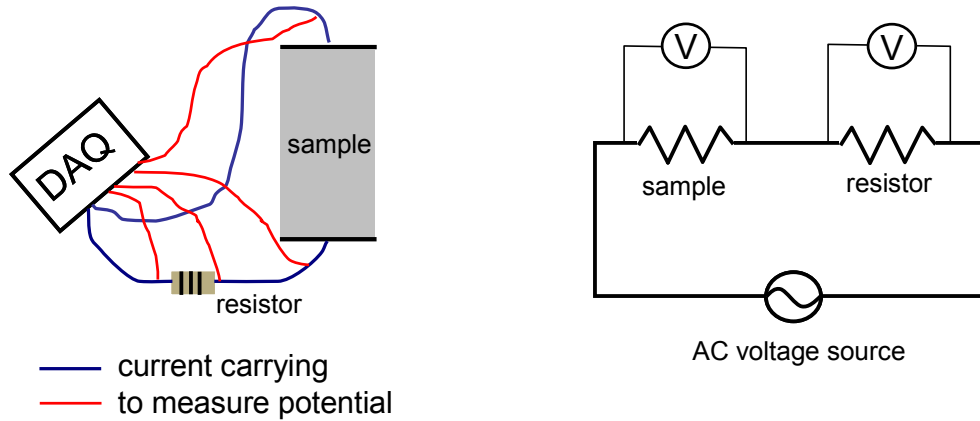


**Figure 4.8 LEFT: Sketch of set-up to measure sample resistivity. RIGHT: Equivalent circuit diagram. Abbreviations: DAQ—data acquisition device.**

The resistor included in the circuit was chosen to have a resistance similar to the sample, and this could be seen when the two measured potentials had similar amplitudes. The measurements were made at seven different frequencies (10, 100, 200, 400, 1000, 2000 and 4000 Hz) to find the frequency with the least capacitive effects.

The resistivity ( $\rho_S$ ) of the sample was determined by first calculating its resistance ( $R_S$ ) and multiplying this by the geometric factor ( $k$ ):  $\rho_S = R_S k$ . For a cylinder the geometric factor is  $k = \pi r^2 / \ell$  where  $r$  and  $\ell$  are the radius and length of the cylinder. The resistance of the sample is given by  $R_S = V_S / I$  where  $V_S$  is the potential measured across the sample and  $I$  is the current in the circuit. The current can be calculated using the potential across the resistor ( $V_R$ ) with  $I = V_R / R_R$  because  $R_R$ , the resistor resistance, has been independently measured using a Fluke 189 digital multimeter. The formulae in this paragraph can be combined to give

$$\rho_S = R_S k = R_S \frac{\pi r^2}{\ell} = \frac{V_S}{I} \frac{\pi r^2}{\ell} = \frac{V_S R_R}{V_R} \frac{\pi r^2}{\ell} \quad [4.5.]$$

Since electrical resistivity is temperature dependant, the measurement temperature was noted and values were corrected so that they could all be reported at 25 °C. The temperature correction used was (Hayashi, 2004)

$$\rho_{25^{\circ}\text{C}} = \rho_t \left( 1 + (t - 25^{\circ}) \cdot 0.0187^{\circ}\text{C}^{-1} \right) \quad [4.6.]$$

where  $t$  in the measurement temperature and  $\rho_{25^{\circ}\text{C},t}$  are the resistivities at 25 °C and at the measurement temperature  $t$ .

#### 4.2.4 GEOCHEMICAL MEASUREMENTS

Before any work was done on the samples, the unconsolidated RIVER sediment samples were classified using ASTM Standard Practise for Description and Identification of Soils (Visual-Manual Procedure) (ASTM International, 2007). Descriptions for the consolidated material KNOLL samples were available from well logs.

Once the coupling coefficient, hydraulic conductivity and electrical resistivity measurements were finished, the fluid and sediment were characterized. Fluid electrical conductivity was measured using a VWR Scientific Products EC Probe model 2052. Fluid pH was measured using a Barnant 20 Digital pH/mV/ORP meter and a VWR symphony 14002-764 pH probe.

For each sample, some fluid was filtered to remove any fine sediment and analysed for major cations ( $\text{Na}^+$ ,  $\text{K}^+$ ,  $\text{Mg}^{2+}$ ,  $\text{Ca}^{2+}$ ) and anions ( $\text{Cl}^-$ ,  $\text{NO}_3^-$ ,  $\text{SO}_4^{2-}$ ) using a Dionex CS-1000 liquid ion chromatography system. For the cations, the column used was an IonPac CS12A and the suppressor was a CSRS 300 4 mm. For the anions the column and suppressor were an IonPacAS12 and an ASRS 300 4 mm. Filtered fluid was also analysed for bicarbonate ( $\text{HCO}_3^-$ ) using titrations and the Gran curve method. For some samples this was done manually and for others it was done using an auto-titrator.

The hydrocarbon analyses were done by an outside laboratory. For the water sample F1 (C6-C10) and BTEX (benzene, toluene, ethylbenzene and xylene) analysis, the samples were run without extraction. Simultaneous runs measured headspace gas chromatography

(GC) using mass-spectrometric detection in selected ion monitoring for BTEX and using flame ionization detection (FID) for F1. For F2 (C10-C16) analysis, the water sample was extracted with hexane and measured using GC/FID with direct injection. Soil hydrocarbon analyses were not done for the KNOLL samples as the pollution source was lighter end hydrocarbons which were not expected to stay in the sediment. C11-C30 for the RIVER sediment were analysed using a GC/FID scan.

Additional soil analyses included measuring cation exchange capacity using the sodium acetate method (EPA method 9801) and mineralogical characterization of the samples using a petrographic microscope to examine thin sections of the samples solidified with epoxy.

### 4.3 Calibration of measurement procedures

Error in the streaming potential coupling coefficient and electrical resistivity are discussed together in the first sub-section because they are combined to give the streaming current coupling coefficient. The second sub-section discusses error in hydraulic conductivity measurements while the last sub-section addresses the geochemical measurements. The calibrations for geochemical measurements are not discussed in detail because they were not the main focus of this study.

Many of the values reported are calculated using several measured quantities. In these cases the error of a value  $y$  that is a function of  $(x_1, x_2, \dots, x_n)$  was calculated as (Bentley & Trenholm, 2002; Kirkup & Frenkel, 2006):

$$\Delta y = \sum_{i=1}^n \left( \frac{\partial y}{\partial x_i} \right)^2 (\Delta x_i)^2 \quad [4.7.]$$

where  $\Delta y$  and  $\Delta x_i$  are the errors associated with  $y$  and  $x_i$  respectively.

#### 4.3.1 CALIBRATION OF ELECTRICAL MEASUREMENTS

The streaming potential coupling coefficient is the ratio of  $\Delta V$  to  $\Delta P$ . The potential difference is measured with the DAQ using Ag/AgCl electrodes. The performance of the electrodes is not rated in their specifications so they were compared to copper wire

electrodes. A box waveform voltage was imposed across the ends of both the Ag/AgCl and copper wire electrodes and the potential was measured (Figure 4.9).

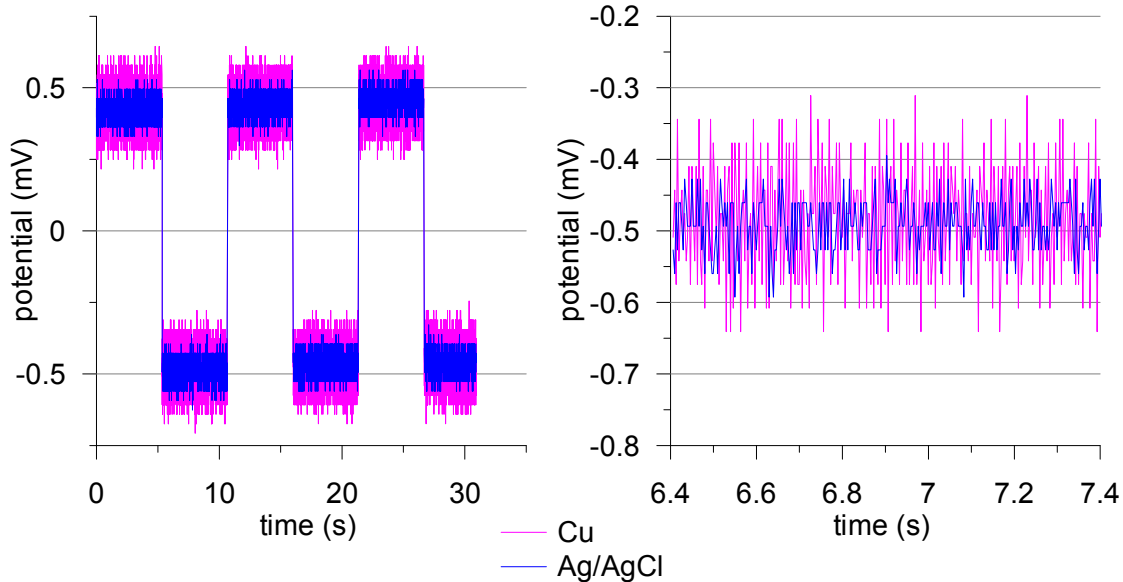


**Figure 4.9** Test comparing copper (Cu) and Ag/AgCl electrodes with a box waveform of 0.1 Hz frequency and 0.5 mV amplitude. LEFT: Entire test. RIGHT: Close up of one second during the test.

The Ag/AgCl electrodes are less noisy and the average is within 5  $\mu\text{V}$  of the average signal measured with the copper wires. Given that the absolute accuracy of the DAQ at the scale used ( $\pm 0.2$  V) is  $\pm 44$   $\mu\text{V}$ , these electrodes measure the same signal. The error in the potential measurements with the Ag/AgCl electrodes comes from the DAQ and is equal to the sensitivity of the DAQ since the measurements are differential. At the scale  $\pm 0.2$  V the sensitivity is 5  $\mu\text{V}$ . The range of potential measured typically ranges between  $\pm 0.2$  mV, so at the maximum values measured the error represents 2.5 %.

The electrical potential is measured by electrodes in recessed ports to protect them from motoelectric effects, but it also removes them from the ends of the sample. When the sample is much more resistive than the saturating fluid, one can assume that there is virtually no electrical potential drop between the end of the sample and the electrode. With the present experiments the saturating fluid resistivity is of the same order of

magnitude as the bulk sample resistivity so it is necessary to calculate the potential drop between the end of the sample and the electrode.

The end plates act as resistors in series in the measurement set-up (Figure 4.10 LEFT and MIDDLE).

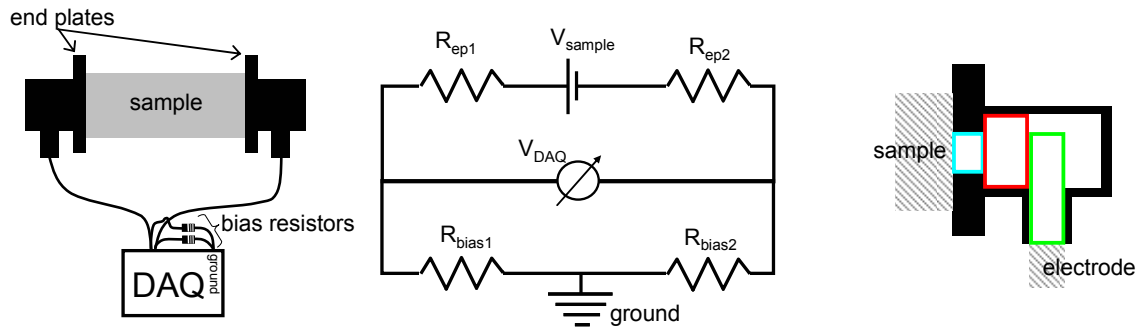


**Figure 4.10** Laboratory set-up used to measure voltages. **LEFT:** Cartoon sketch. **MIDDLE:** Equivalent circuit diagram. **RIGHT:** Cross-section of end plate. White areas are hollow and filled with fluid. Three coloured rectangles are drawn to show cylinders used for resistance calculations. Abbreviations: DAQ–data acquisition device.

The voltage drop ( $V_{eps}$ ) across the identical plates can be calculated as:

$$V_{eps} = I(R_{ep1} + R_{ep2}) = 2IR_{ep} \tag{4.8.}$$

The resistance of the end plates ( $R_{eps}$ ) can be calculated from the dimension of the current path and the conductivity of the fluid in this path. The flow path, as illustrated on a cross-section of the end-plate (Figure 4.10 RIGHT) is curved and complex. A conservative estimate can be made by using the resistance of three cylinders, with dimensions found in Table 4.1, put end to end.

**Table 4.1** Dimensions of three cylinders along flow path in end plates.

cylinder	length (m)	radius (m)
1	0.021	0.012
2	0.014	0.0169
3	0.031	0.005

The current ( $I$ ) in the circuit can be calculated by simplifying the two bottom branches of the circuit (Figure 4.10 MIDDLE) with an equivalent resistance and dividing the voltage

across the DAQ by this resistance. The equivalent resistance for the DAQ and two bias resistors that are in series is (Bogart, 1988):

$$R_{equiv} = \frac{R_{DAQ}(R_{bias1} + R_{bias2})}{R_{DAQ} + (R_{bias1} + R_{bias2})} \quad [4.9.]$$

For these calculations the fluid conductivity of sample RIVER1.C is used as an example.

$$V_{eps} = 2IR_{ep} \quad , \quad I = \frac{V_{DAQ}}{R_{equiv}} \quad , \quad R_{ep} = \frac{1}{\sigma_f} \left( \frac{\ell_1}{A_1} + \frac{\ell_2}{A_2} + \frac{\ell_3}{A_3} \right)$$

$$V_{eps} = 2V_{DAQ} \left( \frac{R_{DAQ} + (R_{bias1} + R_{bias2})}{R_{DAQ}(R_{bias1} + R_{bias2})} \right) \frac{1}{\sigma_f} \left( \frac{\ell_1}{A_1} + \frac{\ell_2}{A_2} + \frac{\ell_3}{A_3} \right)$$

$$V_{eps} = 2 \times 1.643 \cdot 10^{-4} \text{V} \frac{10^{10} \Omega + (2 \times 10^8 \Omega)}{(10^{10} \Omega)(2 \times 10^8 \Omega)} \frac{1}{0.218 \text{S/m}} \left( \frac{0.021 \text{m}}{\pi(0.012 \text{m})^2} + \frac{0.014 \text{m}}{\pi(0.0169 \text{m})^2} + \frac{0.031 \text{m}}{\pi(0.005 \text{m})^2} \right)$$

$$V_{eps} = 3.51 \cdot 10^{-9} \text{V}$$

The voltage drop in the end plates is  $3.51 \cdot 10^{-9}$  V and the voltages measured in the experiment are  $10^{-6}$  to  $10^{-4}$  V, so the effect of the end plates is negligible.

The pressure sensors were calibrated by attaching a tube filled with water to the end of the pressure sensor and changing the height of the water column in the tube. At each height pressure measurements were made during approximately one minute. The pressure was calculated by measuring the water column height with a ruler and converting the height, to pressure using 1 cm = 0.0981 kPa. The calibrations for both pressure sensors are shown in Figure 4.11 and include calibration tests from three different dates. The first test was done 194 days before the beginning of the experiments, the middle test 104 days into the experiments, and the last test after the last measurement had been completed. The measurements were made over a period of 315 days from 09.09.08 to 21.07.09. A linear regression was used to calculate the conversion factor from mV to kPa. The formulae are:

$$\begin{aligned} \text{sensor 1} & \quad \text{kPa} = (\text{mV} - 0.3465) / 1.4596 \\ \text{sensor 2} & \quad \text{kPa} = (\text{mV} - 0.5909) / 1.4883 \end{aligned}$$

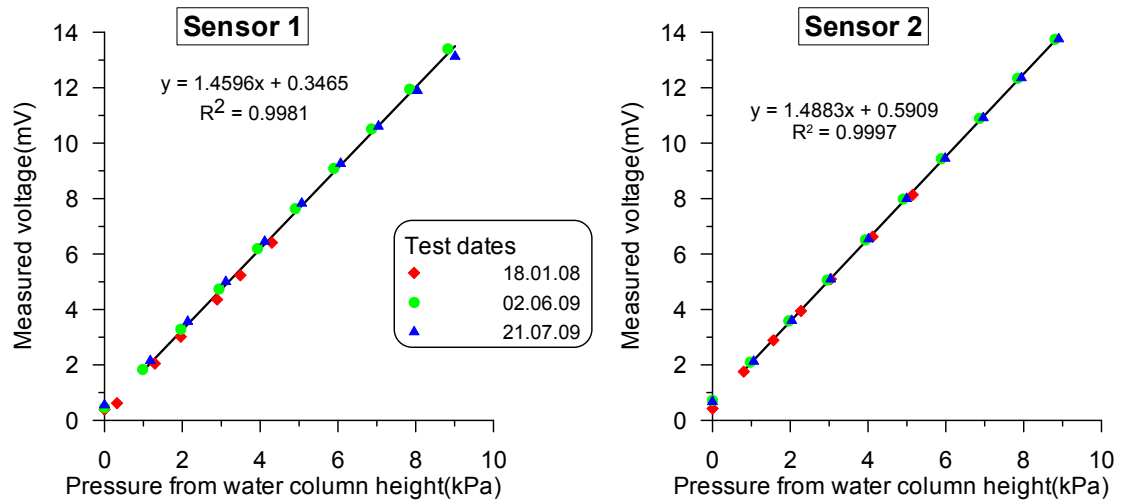


**Figure 4.11 Pressure sensor calibrations using water columns of known height. Linear regressions used for conversions are noted on the graphs.**

The error in the pressure sensor measurements was determined by taking the difference between the pressure calculated from the measured voltage using the calibration slope and the pressure calculated from the water column height. For sensor 1 the % relative error ranges from 0.1 to 11.0% with an average of 2.8%. For sensor 2 the range is 0.4 to 5.2% with an average of 1.5%. For both sensors the larger errors are associated with low pressures. The readings below 2 mV were not used to calculate the conversion factors and when running the experiments, an attempt was made to keep the pressures above 2 mV. Since the difference in pressure is used equation 4.7 can be applied to calculate an average error of 3.2%.

The streaming potential coupling coefficient ( $C$ ) is the ratio  $\Delta V/\Delta P$ . If the measurements were made using a DC method, the error calculated with equation 4.7 for an example where  $\Delta V = -0.171$  mV and  $\Delta P = 8.286$  kPa would be 4.3%. Since AC measurements were made many ratios are available to find  $C$ . If either  $\Delta V$  or  $\Delta P$  had an error much smaller than the other, it could be used as an independent variable for a linear regression, with  $C$  being the slope. Since the relative errors are of similar magnitude it is more appropriate to use a structural regression like the reduced major axis method which treats both variables equally (Swan & Sandilands, 1995). The slope ( $b_1$ ) is:

$$b_1 = \frac{s_x}{s_y} \quad [4.10.]$$

where  $s_{x,y}$  are the sample standard deviations of the variables  $x$  and  $y$ . The sample standard deviation can be calculated using

$$s_x = \sqrt{\frac{1}{n} \sum_{i=1}^n (x_i - \bar{x})^2} \quad [4.11.]$$

where  $n$  is the number of samples,  $x_i$  is an individual measurement of  $x$ ,  $\bar{x}$  is the average of all measured  $x$ . The standard error ( $s_e$ ) of  $b_1$  is given by

$$s_e = b_1 \sqrt{\frac{1-r^2}{n}} \quad [4.12.]$$

where  $r$  is the Pearson's product moment correlation coefficient.

$$r = \frac{\sum_{i=1}^n (x_i - \bar{x})(y_i - \bar{y})}{(n-1) \cdot s_x \cdot s_y} \quad [4.13.]$$

If the range  $b_1 + 1.96s_e$  to  $b_1 - 1.96s_e$  encloses zero, then the regression is not significant at the 95% level.

This method is valid if the data of both variables have normal distributions, which is the case for the data from these experiments. The standard error of the slope incorporates error from the two variables so it can be taken as the error in the calculated coupling coefficient.

As an example, the data from sample RIVER1.C are shown in Figure 4.12. The calculated coupling coefficient is  $-0.022$  mV/kPa with a standard error of  $0.001$  mV/kPa, or 5%. For each sample several coupling coefficient measurements were done, typically four measurements over a period of 12 to 24 hours. This was done to check the reproducibility of the tests and to monitor changes that might be occurring due to sample-liquid disequilibrium. Sheffer (2005) made repeated coupling coefficient measurements and her  $C$  vs. time data have a logarithmic trend, with the greatest changes occurring in the first five hours and values levelling off after 24 hours. In her study the sample and fluid were not equilibrated before starting the tests as they were in this study.

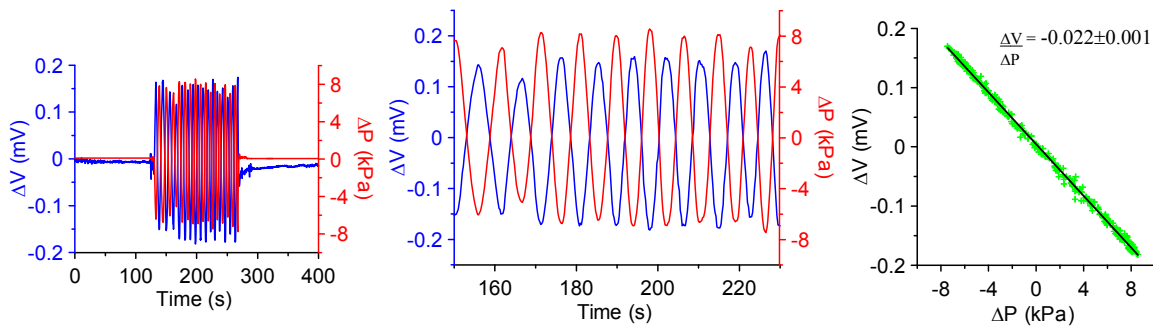


**Figure 4.12 Streaming potential coupling coefficient data for sample RIVER1.C. LEFT: Data for the whole test. MIDDLE: Close up of data used to determine  $C$ . RIGHT: Cross-plot of  $\Delta V$  vs.  $\Delta P$  from the middle panel, used to calculate the ratio.**

Of the twelve samples tested, the four  $C$  measurements for each sample were the same within error for 8 samples. Three more samples had one spurious reading due to electrode drift, but once the drift was corrected, the spurious reading concurred with the three others. There was only one sample with a spurious reading that could not be corrected, the data from this reading formed an oval rather than the typical line. The three other readings from this sample were standard.

To verify that there was no signal generated by the apparatus or plastic meshes, a test was performed with the apparatus set up with fluid but no sediment sample. The results did not show any coherent signal (Figure 4.13) which indicates that the coupling coefficients measured are generated by the samples.

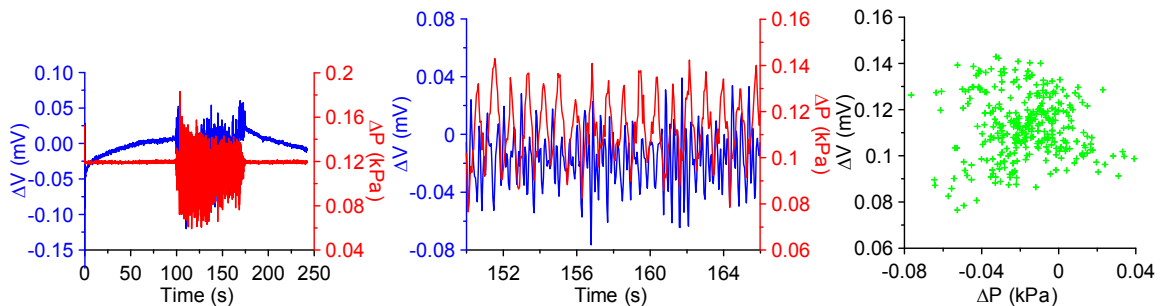


**Figure 4.13 Streaming potential coupling coefficient data for empty apparatus. The three panels are as described in Figure 4.12.**

Error in the electrical resistivity measurements comes from errors in measured potential, resistor resistance and sample holder dimension measurements. The error for the DAQ

potential measurements at the scale used ( $\pm 5$  V) is 525  $\mu$ V. However, since the generated signal is sinusoidal, a series of measurements are made so the standard deviation of these measurements can be used to estimate the error of  $V_S$  and  $V_R$ . These are typically on the order of 1 mV. The error in resistor resistance measured with the Fluke digital multimeter is  $\pm(0.05\% + 2$  digits). For most resistivity measurements a 1004.1  $\Omega$  resistor was used so the error is 0.7  $\Omega$  or 0.07%. The sample holder dimensions were measured with a ruler and the error in these measurements is estimated at 0.5 mm. Resistivity measurements are corrected for temperature differences and reported at 25  $^{\circ}$ C and this calculation also introduces error. The error in temperature measurements was estimated at 0.2  $^{\circ}$ C and the variability in the constant used for temperature corrections is 0.001 (Hayashi, 2004).

Sample RIVER1.C is used as an example again.

$$\rho_S = \frac{V_S R_R \pi r^2}{V_R \ell}$$

$$(\Delta\rho_S)^2 = \left(\frac{R_R \pi r^2}{V_R \ell}\right)^2 (\Delta V_S)^2 + \left(\frac{V_S \pi r^2}{V_R}\right)^2 (\Delta R_R)^2 + \left(-\frac{V_S R_R \pi r^2}{V_R^2 \ell}\right)^2 (\Delta V_R)^2$$

$$+ \left(2\frac{V_S R_R \pi r^2}{V_R \ell}\right)^2 (\Delta r)^2 + \left(-\frac{V_S R_R \pi r^2}{V_R \ell^2}\right)^2 (\Delta \ell)^2$$

$$(\Delta\rho_S)^2 = \left(\frac{1004.1 \pi \times 0.029^2}{3.889 \times 0.148}\right)^2 (0.0009)^2 + \left(\frac{4.055 \pi \times 0.029^2}{3.889 \times 0.148}\right)^2 (0.7)^2 +$$

$$\left(-\frac{4.055 \times 1004.1 \pi \times 0.029^2}{3.889^2 \times 0.148^2}\right)^2 (0.0008)^2 + \left(2\frac{4.055 \times 1004.1 \pi \times 0.029^2}{3.889 \times 0.148}\right)^2 (0.0005)^2 +$$

$$\left(-\frac{4.055 \times 1004.1 \pi \times 0.029^2}{3.889 \times 0.148^2}\right)^2 (0.0005)^2$$

$$\Delta\rho_S = 0.65\Omega\text{m}$$

$$\rho_{25^{\circ}\text{C}} = \rho_t (1 + k(t - 25))$$

$$(\Delta\rho_{25^{\circ}\text{C}})^2 = (1 + k(t - 25))^2 (\Delta\rho_t)^2 + (\rho_t k)^2 (\Delta t)^2 + (\rho_t (t - 25))^2 (\Delta k)^2$$

$$(\Delta\rho_{25^{\circ}\text{C}})^2 = (1 + 0.0187(20.0 - 25))^2 (0.65)^2 + (18.7 \times 0.0187)^2 (0.2)^2 + (18.7(20.0 - 25))^2 (0.001)^2$$

$$\Delta\rho_{25^{\circ}\text{C}} = 0.60\Omega\text{m}$$

The error as a percentage is 3.6%.

To verify the method for measuring electrical resistivity, a test was performed by measuring the sample cylinder filled with a fluid of known conductivity. Three solutions were prepared using tap water with different quantities of NaCl added. The solutions were made to have resistivities similar to those of the samples analysed. The fluid conductivities were measured with an EC probe calibrated with a standard solution before making measurements. The error in the probe is  $\pm(0.1\% + 1 \text{ digit})$ . The experimental results (Figure 4.14) show that at frequencies above 1 kHz the calculated resistivity is almost identical to that measured with the EC probe and that it is well within the error bounds.

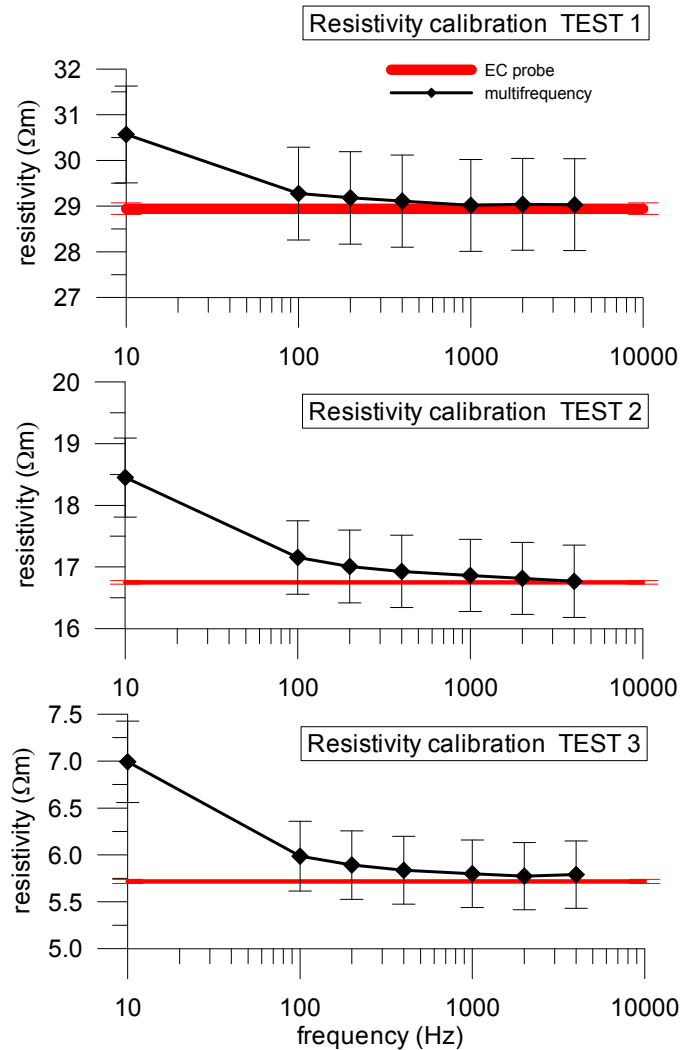


**Figure 4.14** Calibrating resistivity measurements with three solutions of known resistivity. The thickness of the 'EC probe' line encompasses the error in this measurement.

The error in streaming current coupling coefficient ( $L$ ) can also be calculated using equation 4.7. Once again, sample RIVER1.C is used as an example.

$$L = -\frac{C}{\rho}$$

$$(\Delta L)^2 = \left(-\frac{1}{\rho}\right)^2 (\Delta C)^2 + \left(\frac{C}{\rho^2}\right)^2 (\Delta \rho)^2$$

$$(\Delta L)^2 = \left(-\frac{1}{16.9}\right)^2 (0.001)^2 + \left(\frac{-0.022}{16.9^2}\right)^2 (0.6)^2$$

$$\Delta L = 7.51 \cdot 10^{-5} \text{ mV/kPa}\Omega\text{m}$$

The error as a percentage is 6%. We assume there is no error in the conversion from  $L$  to  $L'$  (kPa to  $m_{\text{H}_2\text{O}}$ ).

#### 4.3.2 CALIBRATION OF HYDRAULIC CONDUCTIVITY MEASUREMENTS

Given that the samples were disturbed, particularly the KNOLL core, the measured hydraulic conductivities are poor approximations of what the field values might be. They are interesting for comparison between samples and are used to determine if electro-osmotic effects can be neglected.

Most of the error in the hydraulic conductivity measurements came from the measurements made with a ruler. For dimensional measurements the error was estimated at  $\pm 0.5$  mm, while for the column height it was  $\pm 1$  mm. The error in the timing with the stopwatch was 0.5 s. For each sediment sample two tests were run with at least 7 column height readings in each test. The exception was a sample where the sample holder fell and broke after only three measurements. Several hydraulic conductivity calculations could be made, between each reading and the first as well as between successive readings. With over 20 calculated values it was possible to take the standard deviation as a measure of the error. Sample RIVER1.C is used as an example to compare the error of a single measurement and all measurements for one sample.

$$K = \frac{a\ell}{A} \frac{1}{t_{diff}} \ln \frac{h_0}{h_1}$$

$$(\Delta K)^2 = \left( 2 \frac{\pi r_a \ell}{A} \frac{1}{t_{diff}} \ln \frac{h_0}{h_1} \right)^2 (\Delta r_a)^2 + \left( \frac{a}{A} \frac{1}{t_{diff}} \ln \frac{h_0}{h_1} \right)^2 (\Delta L)^2 + \left( -2 \frac{a\ell}{\pi r_a^3} \frac{1}{t_{diff}} \ln \frac{h_0}{h_1} \right)^2 (\Delta r_A)^2 +$$

$$\left( -\frac{a\ell}{A} \frac{1}{t_{diff}^2} \ln \frac{h_0}{h_1} \right)^2 (\Delta t_{diff})^2 + \left( \frac{a\ell}{A} \frac{1}{t_{diff}} \frac{1}{h_0} \right)^2 (\Delta h_0)^2 + \left( -\frac{a\ell}{A} \frac{1}{t_{diff}} \frac{1}{h_1} \right)^2 (\Delta h_1)^2$$

$$(\Delta K)^2 = \left( 2 \frac{\pi \times 0.00425 \times 0.148}{2.688 \cdot 10^{-3}} \frac{1}{150} \times 2.057 \cdot 10^{-3} \right)^2 (0.0005)^2 + \left( \frac{5.675 \cdot 10^{-5}}{2.688 \cdot 10^{-3}} \frac{1}{150} \times 2.057 \cdot 10^{-3} \right)^2 (0.0005)^2 +$$

$$\left( -2 \frac{5.675 \cdot 10^{-5} \times 0.148}{\pi \times 0.0293^3} \frac{1}{150} \times 2.057 \cdot 10^{-3} \right)^2 (0.0005)^2 +$$

$$\left( -\frac{5.675 \cdot 10^{-5} \times 0.148}{2.688 \cdot 10^{-3}} \frac{1}{150^2} \times 2.057 \cdot 10^{-3} \right)^2 (0.5)^2 + \left( \frac{5.675 \cdot 10^{-5} \times 0.148}{2.688 \cdot 10^{-3}} \frac{1}{150} \frac{1}{1.460} \right)^2 (0.001)^2 +$$

$$\left( \frac{5.675 \cdot 10^{-5} \times 0.148}{2.688 \cdot 10^{-3}} \frac{1}{150} \frac{1}{1.457} \right)^2 (0.001)^2$$

$$\Delta K = 2.5 \cdot 10^{-8} \text{ m/s}$$

The error as a percentage is 130% whereas the standard deviation of all the measurements is  $3 \cdot 10^{-9}$  m/s or 6%.

### 4.3.3 CALIBRATION OF GEOCHEMICAL MEASUREMENTS

The EC probe and pH meter were calibrated using standard solutions before each measurement. A VWR Traceable Conductivity Standard was used for the EC probe and the temperature of the standard was measured to allow accurate calibration. As mentioned in the previous section, the error in the EC probe is  $\pm(0.1\% + 1 \text{ digit})$ . Fisher Scientific pH 4.00 and 7.00 Buffer Solutions were used to calibrate the pH meter. The specifications for the resolution and accuracy of the pH meter are  $\pm 0.01$  unit.

For the liquid chromatography system, standard solutions were prepared with the concentrations listed in Table 4.2. These standards were run to calibrate the machine before each set of measurements. Samples with concentrations higher than the range of the standards were reanalysed after doing a 1:10 dilution with de-ionized water so that the concentrations fell within the range of the standards. The error of the liquid ion chromatograph is 5% per analyte.

**Table 4.2 Concentrations of the standards used for the liquid ion chromatograph.**

	<b>Ions</b>	<b>Concentrations (mg/L)</b>
<b>Anions</b>	Cl <sup>-</sup> , SO <sub>4</sub> <sup>2-</sup>	1, 5, 10, 20, 40
	NO <sub>3</sub> <sup>-</sup> -as N	0.1, 0.2, 0.5, 1.0, 5.0
<b>Cations</b>	Na <sup>+</sup> , Mg <sup>2+</sup> , Ca <sup>2+</sup>	1, 5, 10, 20, 40
	K <sup>+</sup>	0.1, 0.5, 1.0, 5.0, 10

Charge balance for major ions, including carbonate, in each sample was calculated as a measure of the accuracy of the chemical analyses. In all but one sample, the sum of the anions and cations were within 10%.

The laboratory doing the hydrocarbon analyses used surrogates as one of their calibration procedures. The percent recovery indicates how well the systems were working and statistics for these values are listed in Table 4.3. The reportable detection limit was used as the error and it varies across analytes and even for the same analyte depending on the concentration.

**Table 4.3 Surrogates and their recovery for the hydrocarbon analyses.**

<b>Analysis</b>	<b>Surrogate</b>	<b>n</b>	<b>Recovery (%)</b>		
			<b>average</b>	<b>min.</b>	<b>max.</b>
Water F1	4-bromofluorobenzene	8	101	93	106
	D4-1,2-dichloroethane	8	95	89	102
	D8-toluene	8	100	95	108
Water F2	O-terphenyl	8	101	79	115
Soil C11-C30	O-terphenyl	4	84	76	90

The cation exchange capacity values reported have many potential error sources. The first is the small size of sample used, 4 to 6 g, which means that any heterogeneity in the sample would lead to different results. During the manipulations there were many volume measurements that would each have error associated with them. Finally, the sodium concentration in the resulting solution was measured using Perkin Elmer AAnalyst 100

flame atomic absorption spectrometer which has an error of less than 5%. Two samples were analysed in duplicate to verify the method's reproducibility. They gave 13.4 and 13.6 meq/100g and 37.3 and 33.4 meq/100g, which are errors of 1 and 11%. An average error of 6% is used for these measurements.

#### **4.4 Experimental results**

This section is organised in a similar manner to the previous one, with an additional subsection at the beginning to describe the samples. The results from electrical tests, hydraulic conductivity and geochemistry are presented.

##### *4.4.1 SAMPLE DESCRIPTIONS*

The apparatus calibration and first measurements were performed using glass beads (BEADS). They were chosen because of the many articles available describing streaming potential coupling coefficient measurements with other apparatus using glass beads as a porous medium (Schriever & Bleil, 1957; Ahmad, 1964; Sheffer, 2005). The glass beads used were perfectly spherical with diameters ranging from 250 – 500  $\mu\text{m}$  with most of them around 350  $\mu\text{m}$ . They were washed in de-ionized water before being used.

Samples from two sites were used, one site had unconsolidated sediment whereas the other had core. The core was from a site (KNOLL) with an operating gas plant where an unlined flare pit was in use from 1965 to 1997 (Matrix Solutions Inc., 2006). Condensate from this pit has leaked into the aquifer below. Samples KNOLL1 and KNOLL2 were taken within the hydrocarbon impacted area and sample KNOLL3 came from outside the delineated plume. The core from this site is from the Paskapoo Formation (Tertiary) which is made of non-marine sandstones, bentonitic shales, lignites and conglomerates (Carrigy, 1971). Two of the samples are sandstones (KNOLL2 and KNOLL3) and the third is a siltstone (KNOLL1) (Table 4.4).

The sandy sediment was from a site (RIVER) where an oil refinery operated from 1923 to the mid-1970s. The above ground infrastructure was removed, but immobile

hydrocarbons in the soil above the water table and liquid petroleum hydrocarbons on the surface of the water table remain (EBA Engineering Consultants Ltd., 2006). Both samples (RIVER1 and RIVER2) are from contaminated areas and were collected using a Becker hammer. They are also described in Table 4.4.

**Table 4.4 Sample descriptions including mineralogical composition.**  
**Composition found using thin sections (estimated %)**

Sample	Depth (m)	Visual-manual description	quartz	clay <sup>a</sup>	carbonates	opaques	biotite	muscovite	chlorite	plagioclase	garnet
KNOLL1	8.4 -9.0	light grey fine grained sandy siltstone	55	–	15	9 <sup>b</sup>	5	5	5	5	1
KNOLL2	4.9 -5.5	light brown fine grained sandstone, competent, iron stained fractures	45	20	5	13	7	5	3	2	–
KNOLL3	4.9 -5.5	light brown fine grained sandstone, weathered	55	15	5	5	10	2	5	2	1
RIVER1	1.8 -2.7	dark olive brown clayey sand	15	60	10	5	5	–	–	5	–
RIVER2	0.9 -1.8	greyish brown poorly graded sand with gravel	30	50	6	5	3	–	2	4	–

<sup>a</sup> The clays are clay sized particles of indeterminate mineralogy.

<sup>b</sup> This sample included one ribbon of pyrobitumen, probably related to coal seams nearby.

Groundwater from both sites was obtained in the autumn of 2006 and though it initially contained hydrocarbons, they were below detection limits two years later when the experiments were run. These waters were used for the experiments with clean water. For the KNOLL site condensate was obtained from the plant a few weeks before the experiments were run and was mixed into the stored water for experiments with polluted water. On the field site the condensate is degraded and therefore the fresh condensate used is not an exact reproduction of the polluted water. The KNOLL site clean and polluted groundwater was also used with the glass beads. A fresh polluted groundwater

sample from RIVER site was collected a couple of weeks before running the experiments. Each sample described in Table 4.4 was split in half, adding the suffix .C for clean water experiments and .P for hydrocarbon polluted water experiments.

#### 4.4.2 ELECTRICAL MEASUREMENTS

**Table 4.5 Measurements of sample electrical properties. The x.C sub-samples had clean water and x.P had hydrocarbon polluted water.**

<b>Sub-sample</b>	<b><math>C</math> (mV/MPa)</b>	<b><math>\rho@ 25^{\circ}\text{C}</math> (<math>\Omega\text{m}</math>)</b>	<b><math>L'</math> (<math>\mu\text{A}/\text{m}^2</math>)</b>
BEADS.C	$-280 \pm 20$	$55 \pm 2$	$50 \pm 4$
BEADS.P	$-240 \pm 10$	$63 \pm 2$	$37 \pm 2$
KNOLL1.C	$-15 \pm 1$	$8.8 \pm 0.3$	$16.7 \pm 1.3$
KNOLL1.P	$-10 \pm 1$	$19.6 \pm 0.7$	$5.0 \pm 0.5$
KNOLL2.C	$-17 \pm 1$	$15.6 \pm 0.5$	$10.7 \pm 0.7$
KNOLL2.P	$-23 \pm 1$	$25.4 \pm 0.9$	$8.9 \pm 0.5$
KNOLL3.C	$-30 \pm 2$	$20.0 \pm 0.7$	$14.7 \pm 1.1$
KNOLL3.P	$-38 \pm 2$	$20.5 \pm 0.7$	$18.2 \pm 1.2$
RIVER1.C	$-22 \pm 1$	$16.9 \pm 0.6$	$12.7 \pm 0.7$
RIVER1.P	$-21 \pm 1$	$19.2 \pm 0.7$	$10.7 \pm 0.6$
RIVER2.C	$-24 \pm 1$	$27.0 \pm 0.9$	$8.7 \pm 0.5$
RIVER2.P	$-18 \pm 1$	$23.1 \pm 0.8$	$7.6 \pm 0.5$

The streaming potential coupling coefficient ( $C$ ) and electrical resistivity ( $\rho$ ) measurements as well as the calculated streaming current coupling coefficient ( $L'$ ) are presented in Table 4.5. Streaming potential coupling coefficient data from each sample are plotted in Appendix A. The measured  $C$  has a smaller magnitude for three of the sub-samples to which hydrocarbons have been added. The two sandstone samples (KNOLL2 and KNOLL3) are the only ones where the polluted sub-sample  $C$  has a greater magnitude than for the clean sub-sample. In the clayey sand sample (RIVER1) the change is insignificant.

The  $C$  measured at different experimental temperatures for sample KNOLL1.P are shown in Table 4.6. No relationship between  $C$  and measurement temperature was found, which corresponds to the findings of most other research (Friborg, 1996; Pengra et al., 1999; Reppert & Morgan, 2003).

**Table 4.6  $C$  values measured for sample KNOLL1.P at different temperatures.**

<b>Test</b>	<b>Temperature (°C)</b>	<b><math>C</math> (mV/MPa)</b>
1	20.7	$-10 \pm 1$
2	21.2	$-9 \pm 1$
3	6.5	$-11 \pm 1$
4	10.6	$-10 \pm 1$

The resistivities measured are the same order of magnitude as those we measured on site using electrical resistivity tomography. On the KNOLL site, resistivity ranged from 5-70  $\Omega\text{m}$ , with most of the subsurface being around 20  $\Omega\text{m}$ , which concurs with the lab measurements of 9-25  $\Omega\text{m}$ . On the RIVER site resistivity ranged from 10-400  $\Omega\text{m}$ , with most of the subsurface around 60  $\Omega\text{m}$ . The lab measurements of RIVER sediment had resistivity values at the lower end of this range, around 20  $\Omega\text{m}$ .

## 4.4.3 HYDRAULIC CONDUCTIVITY MEASUREMENTS

Table 4.7 Measured hydraulic conductivities.

Sub-sample	$K$ (m/s)
BEADS.C	$(1.3 \pm 0.08) \cdot 10^{-3}$
BEADS.P	$(1.1 \pm 0.05) \cdot 10^{-3}$
KNOLL1.C	$(2.6 \pm 0.5) \cdot 10^{-8}$
KNOLL1.P	$(7.3 \pm 0.7) \cdot 10^{-8}$
KNOLL2.C	$(1.3 \pm 0.2) \cdot 10^{-6}$
KNOLL2.P	$(5.0 \pm 1) \cdot 10^{-7}$
KNOLL3.C	$(2.5 \pm 0.2) \cdot 10^{-6}$
KNOLL3.P	$(3.4 \pm 0.3) \cdot 10^{-6}$
RIVER1.C	$(4.3 \pm 0.3) \cdot 10^{-8}$
RIVER1.P	$(3.7 \pm 0.5) \cdot 10^{-8}$
RIVER2.C	$(5.8 \pm 3) \cdot 10^{-8}$
RIVER2.P	$(1.9 \pm 0.7) \cdot 10^{-8}$

The hydraulic conductivity ( $K$ ) values (Table 4.7) show that the C and P sub-samples of a single sample have the same conductivity within an order of magnitude. Given the error due to packing, these can be considered to be the same even though the calculated error margin usually indicates otherwise. The two sandstones from KNOLL have similar  $K$  whereas the siltstone has conductivities that resemble that of the RIVER sediment.

## 4.4.4 GEOCHEMICAL MEASUREMENTS

The fluids from each sample are characterised in Table 4.8 and Table 4.9. The water from the two different sites can be distinguished: RIVER groundwater has higher fluid conductivities and ion concentrations than KNOLL groundwater, but there is significant variability in the water from a single site. This variability is likely due to chemical interactions between water and sediment, and the differences between sub-samples are as great as the difference between samples.

**Table 4.8 Chemical characteristics of sample fluids measured during experiments.**  
**The error associated with pH measurements is 0.01 units. Abbreviations:**  
**symbol(–)–not measured.**

Sub-sample	Equilibration time (days)	pH	$\sigma_f @ 25C$ ( $\mu S/cm$ )
BEADS.C	79	–	$729 \pm 5$
BEADS.P	12	7.72	$615 \pm 5$
KNOLL1.C	153	7.81	$832 \pm 5$
KNOLL1.P	36	7.85	$714 \pm 9$
KNOLL2.C	160	8.09	$665 \pm 4$
KNOLL2.P	25	7.58	$832 \pm 3$
KNOLL3.C	148	8.16	$573 \pm 4$
KNOLL3.P	43	7.75	$652 \pm 6$
RIVER1.C	36	7.87	$2180 \pm 11$
RIVER1.P	26	7.55	$2668 \pm 63$
RIVER2.C	29	7.94	$1903 \pm 9$
RIVER2.P	17	7.70	$2382 \pm 30$

The addition of hydrocarbons to the saturating fluid decreases the fluid conductivity of the X.P sub-samples in three of the six samples and increases it in the remaining three sub-samples.

**Table 4.9 Results of chemical analyses of sample fluids. The error associated with the measurements is 5% Abbreviations: symbol(-)–not measured.**

Sub-sample	Ions (mg/L)								Charge balance (%)
	Na <sup>+</sup>	K <sup>+</sup>	Mg <sup>2+</sup>	Ca <sup>2+</sup>	Cl <sup>-</sup>	NO <sub>3</sub> <sup>-</sup> as N	SO <sub>4</sub> <sup>2-</sup>	HCO <sub>3</sub> <sup>-</sup>	
BEADS.C	-	-	-	-	-	-	-	-	-
BEADS.P	116.7	5.1	12.8	19.1	5.8	1.5	32.6	283	-12.7
KNOLL1.C	70.6	13.0	22.9	74.1	10.4	19.0	204.1	132	-5.4
KNOLL1.P	83.1	5.1	14.6	56.5	10.8	2.4	53.0	311	-7.5
KNOLL2.C	64.5	9.0	19.0	72.0	9.7	2.8	227.4	274	8.4
KNOLL2.P	85.3	5.4	5.7	48.7	18.8	8.2	39.2	311	2.0
KNOLL3.C	65.1	6.0	10.5	47.9	7.9	6.9	32.4	287	-1.2
KNOLL3.P	92.7	4.7	11.7	46.4	7.9	2.6	42.0	315	-7.0
RIVER1.C	163.5	46.9	140.0	242.0	198.1	1.6	592.8	516	-9.3
RIVER1.P	140.0	45.4	165.7	404.8	142.8	15.1	634.8	1128	-5.5
RIVER2.C	190.2	6.9	90.1	254.5	117.1	5.1	970.1	517	6.2
RIVER2.P	160.9	6.5	89.6	360.3	236.6	72.3	392.1	853	2.2

**Table 4.10 Hydrocarbon analyses of sample fluids and sediments. Abbreviations: symbol(–)–not measured, n.d.–concentrations below the detection limit.**

Sub-sample	Water (mg/L)			Sediment (mg/kg) C11-C30	Change in $L'$ (%)
	F1	BTEX	F2		
BEADS.C	–	–	–	–	
BEADS.P	46 ± 10	33.5 ± 0.2	0.4 ± 0.1	–	–25
KNOLL1.C	–	–	–	–	
KNOLL1.P	14 ± 10	15.4 ± 0.2	n.d.	–	–70
KNOLL2.C	–	–	–	–	
KNOLL2.P	7.1 ± 2	8.6 ± 0.04	n.d.	–	–17
KNOLL3.C	–	–	–	–	
KNOLL3.P	<10 ± 10	6.7 ± 0.2	n.d.	–	+24
RIVER1.C	n.d.	n.d.	n.d.	n.d.	
RIVER1.P	0.52 ± 0.1	0.002 ± 0.002	24 ± 0.1	110	–16
RIVER2.C	n.d.	n.d.	n.d.	n.d.	
RIVER2.P	1.3 ± 0.1	0.087 ± 0.002	75.4 ± 0.1	2100	–12

Soil and water hydrocarbon analyses were done on all the RIVER sub-samples, whereas for the KNOLL sub-samples, hydrocarbon analyses were only done on the water from polluted sub-samples (Table 4.10). The F1 results are supposed to include BTEX, but sometimes the sum of the individually measured benzene, toluene, ethyl benzene and xylene is greater than the total F1. This suggests inaccuracies in the measurements. The errors reported are minimum errors since they only include the analysis error reported by the outside laboratory. Hydrocarbon concentrations reported are likely low because the experimental set-up for the streaming current coupling coefficient tests exposed the fluids to air at room temperature for approximately one week, during which volatilization would have occurred.

Cation exchange capacities (CEC) of the sediment are listed in Table 4.11. The clay rich samples have higher CECs and the values for the glass beads are very small.

**Table 4.11 Cation exchange capacity of samples.**

<b>Sub-sample</b>	<b>CEC (meq/100 g)</b>
BEADS.C	1.2 ± 0.1
BEADS.P	1.0 ± 0.1
KNOLL1.C	33.8 ± 2.0
KNOLL1.P	33.4 ± 2.0
KNOLL2.C	22.7 ± 1.4
KNOLL2.P	21.8 ± 1.3
KNOLL3.C	18.1 ± 1.1
KNOLL3.P	17.8 ± 1.1
RIVER1.C	13.4 ± 0.8
RIVER1.P	13.4 ± 0.8
RIVER2.C	16.2 ± 1.0
RIVER2.P	15.9 ± 1.0

#### **4.5 Discussion**

To investigate the effect of hydrocarbon contamination on coupling coefficient, six samples were divided into sub-samples and tested with clean water and hydrocarbon contaminated water. This section reviews the results of the previous section to put them in the context of other work done in the field.

The electrical, hydraulic conductivity and geochemical results are examined in the first three sub-sections. The most important results are highlighted in sub-section 4.5.4. Sub-section 4.5.5 presents a numerical model used to study the impact on field measurements of the variations in  $L'$  caused by pollution, as measured in the laboratory.

## 4.5.1 ELECTRICAL RESULTS

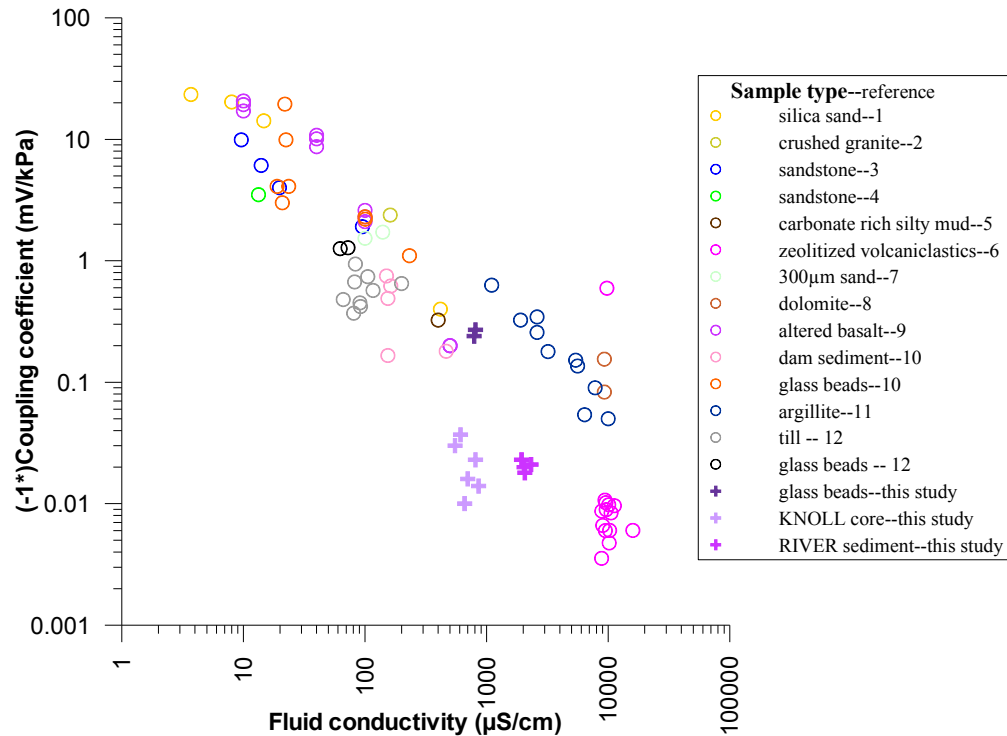


**Figure 4.15 Comparison of measured  $C$  values (+) with those from literature (o). The values are plotted against fluid conductivity since this is the most important controlling factor.**

**References: 1(Ahmad, 1964) 2(Morgan et al., 1989) 3(Jouniaux & Pozzi, 1995a)  
4(Lorne et al., 1999a) 5(Revil et al., 2002b) 6(Revil et al., 2002a)  
7(Guichet et al., 2003) 8(Revil & Cerepi, 2004) 9(Revil et al., 2004)  
10(Sheffer, 2005) 11(Revil et al., 2005b) 12(Friborg, 1996)**

The streaming potential coupling coefficients measured have small magnitudes. When compared with data in literature, the values for glass beads (BEADS) and RIVER sediment plot along the linear trend defined by reported measurements (Figure 4.15). The  $C$  of the KNOLL core are approximately an order of magnitude lower than this trend.

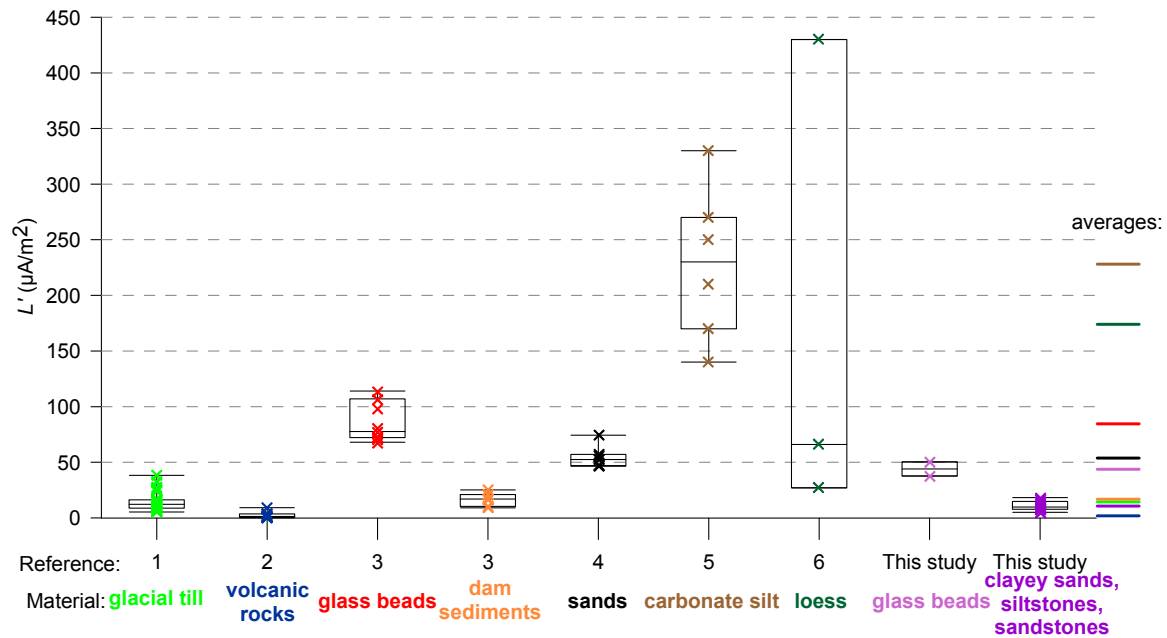


**Figure 4.16 Comparison of measured  $L'$  values with those from literature. The data are shown as crosses on box-and-whisker plots. The averages of each measurement series are shown as thick coloured lines at the right side of the plots so they can be compared.**

References: 1(Friborg, 1996) 2(Jouniaux et al., 2000b) 3(Sheffer, 2005)  
4(Revil et al., 2005a) 5(Suski et al., 2006) 6(Jardani et al., 2006)

The  $L'$  values calculated in this study are compared with those reported in literature (Figure 4.16). The glass beads and sediment are both in the tens of  $\mu\text{A}/\text{m}^2$ , matching what is most commonly reported. The  $L'$  measured on glass beads have higher values, consistent with the findings of Sheffer (2005) on glass beads and Revil et al. (2005a) on sands. The data of the various sediment types most closely resemble that of Friborg (1996), who studied glacial tills.

#### 4.5.2 HYDRAULIC CONDUCTIVITY RESULTS

The measurements indicate that the hydraulic conductivities are greater than  $10^{-9}$  m/s, which is the conductivity below which electro-osmosis and electrophoresis become non-negligible (Mitchell, 1991). Since the samples are disturbed, the measured hydraulic conductivities are not representative of in-situ values but can be used for comparison between samples.

#### 4.5.3 GEOCHEMICAL RESULTS

Addition of hydrocarbons does not produce a consistent effect on the fluid conductivity of the X.P sub-samples. A more regular change is the reduction of pH in polluted sub-samples for four of five cases, which can be explained by the degradation of hydrocarbons releasing  $H^+$  ions (Atekwana et al., 2006).

The water chemistry data are variable, with the only consistent trend being an increase in  $HCO_3^-$  in the polluted sub-samples. This fits well with the increase in pH, as hydrocarbon degradation releases carbon dioxide which reacts with water to form bicarbonate.

The hydrocarbon content measured was closely related to the equilibration time. With longer equilibration times there were less hydrocarbons, suggesting that they had degraded. The condensate used to pollute the KNOLL samples was very light hydrocarbons so it was particularly prone to volatilization and degradation.

Glass beads (CEC: 1 meq/100g) are not supposed to have any cation exchange sites and had CEC measurements lower than that of typical sandy soil (CEC: 3 meq/100g)(Coyne & Thompson, 2006). The siltstone (KNOLL1) had the highest CEC (33 meq/100g), close to that of a typical clay soil (CEC: 30 meq/100g). The remaining samples had CECs spanning 13 to 22 meq/100g, similar to what is measured for typical loam soils (CEC: 15 meq/100g)(Coyne & Thompson, 2006).

#### 4.5.4 SYNTHESIS

The most coherent results are compiled in Table 4.12. To facilitate the comparison of all these values, they are plotted in Figure 4.17 and the percentage difference between clean and contaminated sub-samples is displayed graphically in Figure 4.18.

Table 4.12 Compilation of test results for clean and polluted samples. Abbreviations: n.s.—not significant.

Sub-sample	Lithology	$C$ (mV/ MPa)	$\Delta C$ (%)	$\rho@ 25^\circ C$ ( $\Omega m$ )	$\Delta \rho$ (%)	$L'$ ( $\mu A/ m^2$ )	$\Delta L'$ (%)	$\rho_f@ 25^\circ C$ ( $\Omega m$ )	$\Delta \rho_f$ (%)	F1&F2 in fluid (mg/L)	pH	CEC (meq/ 100g)
BEADS.C	glass beads	$-280 \pm 20$		$55 \pm 2$		$50 \pm 4$		$13.7 \pm 0.1$			—	1.2
BEADS.P		$-240 \pm 10$	-14	$63 \pm 2$	+15	$37 \pm 2$	-25	$16.3 \pm 0.1$	+18	46.4	7.72	1.0
KNOLL1.C	siltstone	$-15 \pm 1$		$8.8 \pm 0.3$		$16.7 \pm 1.3$		$12.0 \pm 0.1$			7.81	34
KNOLL1.P		$-10 \pm 1$	-33	$20 \pm 1$	+123	$5.0 \pm 0.5$	-70	$14.0 \pm 0.2$	+17	15.4	7.85	33
KNOLL2.C	sandstone	$-17 \pm 1$		$16 \pm 1$		$10.7 \pm 0.7$		$13.3 \pm 0.1$			8.09	23
KNOLL2.P		$-23 \pm 1$	+35	$25 \pm 1$	+62	$8.9 \pm 0.5$	-17	$15.0 \pm 0.1$	+13	8.6	7.58	22
KNOLL3.C	sandstone	$-30 \pm 2$		$20 \pm 1$		$14.7 \pm 1.1$		$17.4 \pm 0.1$			8.16	19
KNOLL3.P		$-38 \pm 2$	+27	$21 \pm 1$	n.s.	$18.2 \pm 1.2$	+24	$15.3 \pm 0.1$	-12	6.7	7.75	18
RIVER1.C	clayey sand	$-22 \pm 1$		$16.9 \pm 0.6$		$12.7 \pm 0.7$		$4.6 \pm 0.02$			7.87	13
RIVER1.P		$-21 \pm 1$	n.s.	$19.2 \pm 0.7$	+13	$10.7 \pm 0.6$	-16	$3.8 \pm 0.09$	-18	24.5	7.55	13
RIVER2.C	sand	$-24 \pm 1$		$27 \pm 1$		$8.7 \pm 0.5$		$5.3 \pm 0.02$			7.94	16
RIVER2.C		$-18 \pm 1$	-25	$23 \pm 1$	-14	$7.6 \pm 0.5$	-12	$4.2 \pm 0.05$	-20	76.4	7.70	16

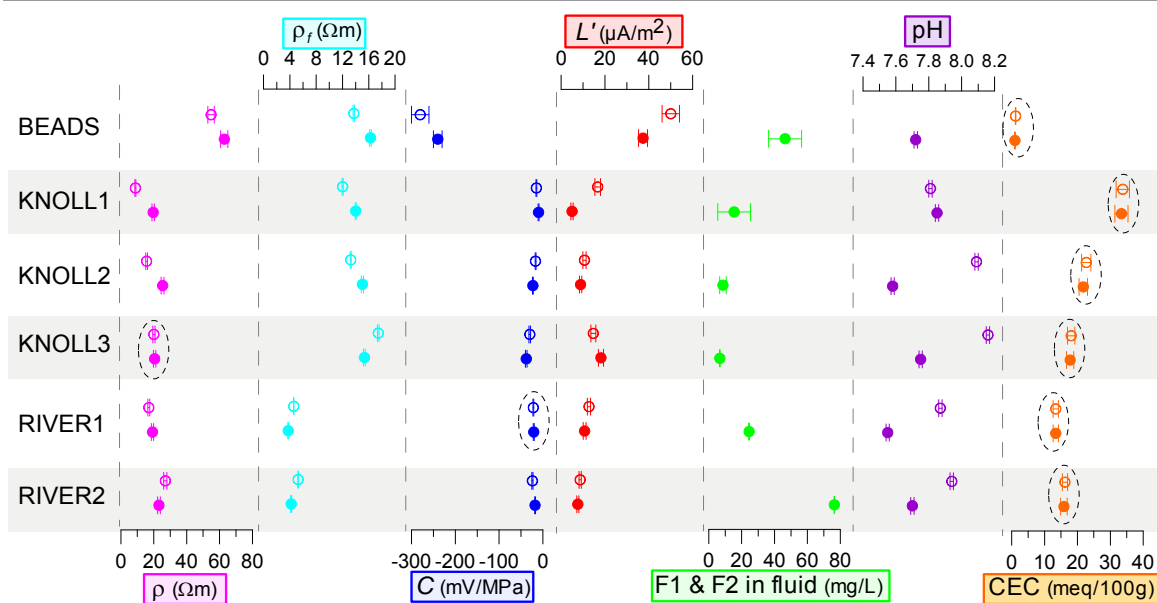


Figure 4.17 Compilation of most coherent lab results as compiled in Table 4.12 for six samples tested. Outlined circles ( $\circ$ ) are for clean sub-samples and filled circles ( $\bullet$ ) are for polluted sub-samples. Vertical bars indicate error associated with each measurement and pairs circled with dotted lines are clean and polluted sub-samples where measurements are the same within error.

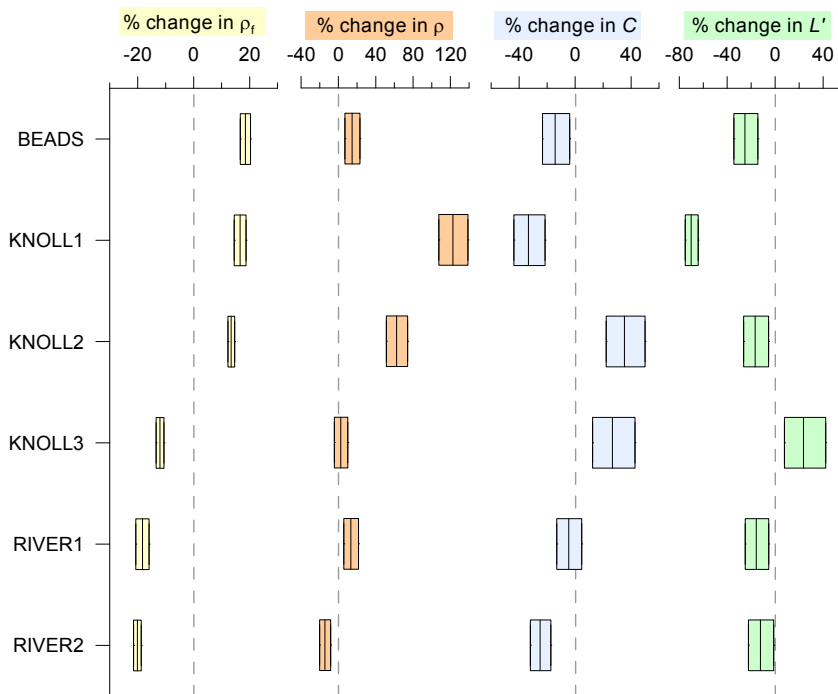


Figure 4.18 Change in electrical properties after addition of hydrocarbons. The bars represent the possible ranges given the errors and the black horizontal line at the centre of each bar is the percentage change using measured values.

Though the addition of hydrocarbons has a significant impact on the measured  $C$  and  $\rho$  and calculated  $L'$ , the effect is not consistent. Degradation of organic contaminants most often occurs through biodegradation, a process which changes many soil and fluid properties in a time varying manner (Atekwana et al., 2006; Che-Alota et al., 2009).

If the hydrocarbons are present in large concentrations and remain unaltered, it is possible to make precise statements about the effect on  $C$ . When experimenting with organic-aqueous solutions across a porous membrane, Zhang et al. (2007) found that  $C$  decreased as the weight percent of organic solvent in the solution increased and proposed two explanations. The first is that organic solvents lowered the solution's dielectric constant, lowering  $C$  according to the Helmholtz-Smoluchowski equation:

$$C = \frac{\varepsilon\zeta}{\eta\sigma_f} \quad [4.14.]$$

where  $\varepsilon$  is dielectric permittivity of the fluid,  $\zeta$  is zeta potential,  $\eta$  is dynamic viscosity and  $\sigma_f$  is fluid electrical conductivity. The second reason is that the organic solvents bind to charged sites on the media surface, decreasing  $\zeta$ , which also lowers  $C$  according to equation 4.14.

The two samples where the magnitude of  $C$  increased instead of decreasing or staying the same after the addition of hydrocarbons are sandstones (KNOLL2 and KNOLL3) and the only other property that distinguishes these two samples is that the clean sub-samples have the highest pHs. Streaming potential coupling coefficient displays a pH dependence in certain cases. In a laboratory experiment using quartz sand with 2% calcite, Guichet et al. (2006) found that the zeta potential, a factor in  $C$  (equation 4.14), decreased from  $-16$  to  $-27 \pm 4$  mV as pH increased from 4 to 7 and it remained constant at  $-25 \pm 1$  mV as the pH increased from 8 to 10.5. For the sandstones the clean sub-samples had a pH above 8 and the polluted ones had a pH below 8. This falls in the jump identified by Guichet et al. (2006), so the differing pH may explain why  $C$  responded differently to the addition of hydrocarbons for samples KNOLL2 and KNOLL3.

The streaming current coupling coefficient decreased in five of six samples. Most of the reductions in  $L'$  were from 12 to 25% (four samples). The two exceptions are a reduction of 70% (sample KNOLL1) and an increase of 24% (sample KNOLL3). The exceptionally large decrease occurs in the only siltstone and its large number of cation exchange sites may make it more susceptible to the effect of hydrocarbons, given that they will bind to the exchange sites. The only increase in  $L'$  is in a sandstone and it is from the only sediment sample that was collected outside a hydrocarbon impacted area. Yet the glass beads used had not been exposed to contamination before being used for the test and they showed a decrease in  $L'$ . KNOLL3 is also the sample with the lowest hydrocarbon content, though this is not sufficient to explain the rise in  $L'$  because no relationship was found between the quantity of hydrocarbons present and the proportion of the change.

The changes in electrical properties confirm the hypothesis that hydrocarbon contamination alters the streaming current coupling coefficient, even though it does not do so in a consistent direction, manner or amplitude. Perhaps variations of parameters which the experiments described did not account for, like the degree of degradation, might explain variations like the increase in  $L'$  of sample KNOLL3.

Estimating the impact in the field of the changes measured in these laboratory tests will help demonstrate that details like the degree of degradation are not likely to produce a measurable effect. This is the subject of the next sub-section.

#### 4.5.5 *STREAMING CURRENT MODELLING OVER CONTAMINANT SITES*

Numerical modelling can be used to isolate the effect of a change in the streaming current coupling coefficient as might be caused by a hydrocarbon contaminant plume. This exercise was undertaken to quantify the magnitude of the effect on field measurements. Calculations were made using a hypothetical site designed to have a large streaming potential signature. The model domain is a 4 by 4 km block with topography sloping towards the east and an 18 m total elevation change (Figure 4.19 LEFT). The model is invariant in the y direction. There are two layers, a sandy aquifer above and a sandstone bedrock 10-15 m below ground surface. A hydrocarbon contaminant plume was drawn in

the central portion of the aquifer (Figure 4.19 LEFT). Two scenarios with different bedrock structures were used to produce different hydraulic head gradient distributions. In scenario 1 the bedrock topography roughly follows the surface topography and the gradients are relatively constant (Figure 4.19 TOP RIGHT). The hydraulic head gradient is increased in the middle portion of the model in scenario 2 by making more pronounced steps in the bedrock and adding sections of weathered sandstone bedrock (Figure 4.19 BOTTOM RIGHT).

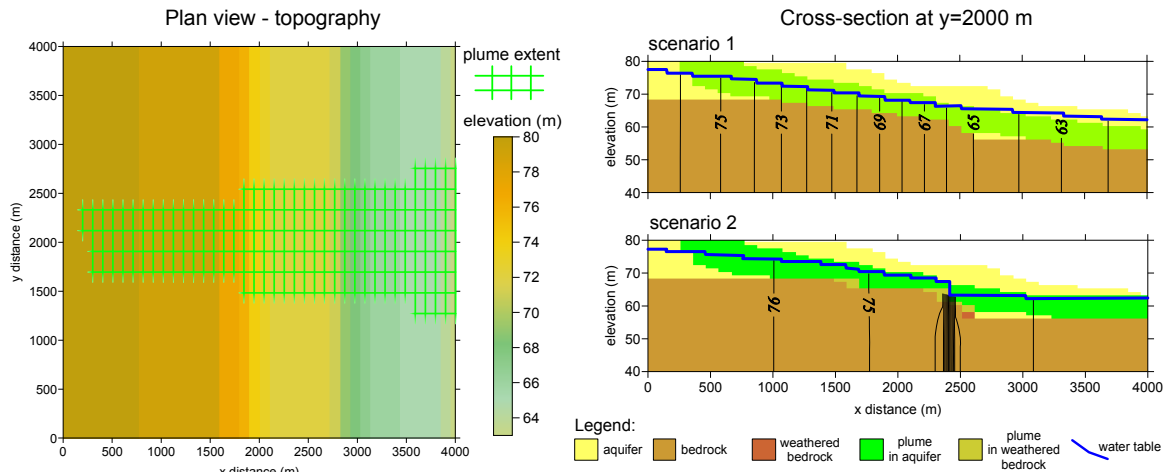


**Figure 4.19 Hypothetical model used for investigating the effect of contaminants on streaming potential. LEFT: Topography of model and extent of contaminant plume. RIGHT: Model cross-sections with different zones and hydraulic head contours (1 m spacing). Ten of the hydraulic head contours in scenario 2 are so close together that they appear as a thick black bar.**

Streaming potential can be modelled using the equation

$$\nabla \cdot (\sigma \nabla \phi) = \nabla \cdot (L' \nabla h) \tag{4.15.}$$

and this was done using the programme presented in chapter 3 with the properties of different zones are listed in Table 4.13. Each scenario was run twice, once over a clean site and a second time assuming there was a contaminant plume that changed the sediment properties.

Table 4.13 Properties used for numerical modelling.

Zone	K (m/s)	$L'$ ( $\mu\text{A}/\text{m}^2$ )		$\rho$ ( $\Omega\text{m}$ )	
		outside plume	within plume	outside plume	within plume
aquifer	$10^{-4}$	230	173	200	230
bedrock	$10^{-8}$	40	–	1000	–
weathered bedrock	$10^{-6}$	40	30	700	800
vadose	$10^{-4}$	0	0	300	300

The assignment of properties was based on literature values, chosen to produce a large streaming potential signature while remaining realistic. In order to have an impact measurable in the field where error in measurements is  $\pm 5$  mV, it is necessary to have a large initial streaming potential signature, so that a fractional reduction in  $L$  might produce a deviation larger than 20 mV. Hydraulic conductivity values were chosen from the ranges presented in Domenico & Schwartz (1998). For the streaming current coupling coefficient of the aquifer the average value measured by Suski et al. (2006) was used and for the bedrock, the median value of the averages in Figure 4.16 was used. Though most  $L'$  are tens of  $\mu\text{A}/\text{m}^2$  and these have been used in modelling (Wurmstich & Morgan, 1994), hundreds of  $\mu\text{A}/\text{m}^2$  have also been used (Titov et al., 2002). In the contaminant plume the  $L'$  values are decreased by 25%, which is at the high end of the data presented in this chapter.

To generate a large streaming potential a resistive aquifer was used over an even more resistive bedrock and values fall within the ranges listed in Telford et al. (1990). The vadose zone is a bit more resistive than the aquifer. Within the plume an increase of 15% over background resistivity was used, which is the median resistivity change of the laboratory results presented in this chapter.

The hydraulic head distributions were calculated using the software MODFLOW and imposing constant head boundaries of 76.7 and 61.2 m in the west and east respectively (Figure 4.19 RIGHT).

The streaming potentials calculated at the surface for scenario 1, where the hydraulic head gradients are relatively uniform across the site, have a 30 mV range (Figure 4.20 LEFT). The presence of the plume deflects the contours a bit and is most visible on the  $-8$  and  $+8$  mV contours (Figure 4.20 LEFT & MIDDLE). The difference between the two surface maps quantifies the change. It would not be measurable in the field since the range is only 1.6 mV, within the  $\pm 5$  mV error of field measurements (Figure 4.20 RIGHT).

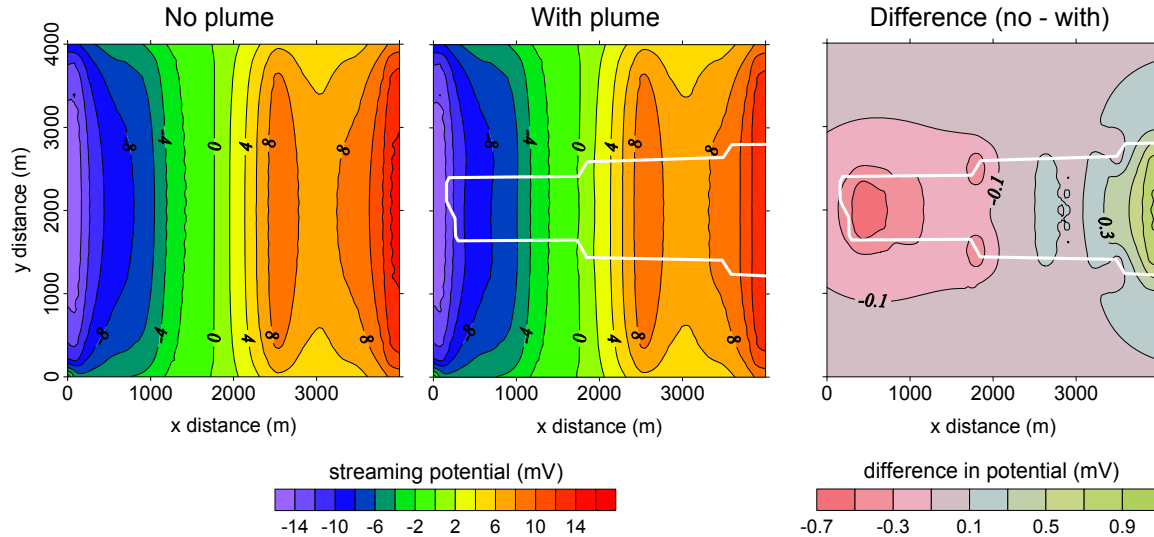


**Figure 4.20** Streaming potentials calculated at the surface of hypothetical model drawn in Figure 4.19 for scenario 1. **LEFT:** No plume. **MIDDLE:** With plume, thick white line outlines plume extent. **RIGHT:** Difference of left panel minus centre panel, thick white line outlines plume extent.

Scenario 2 generates much larger streaming potentials, with a range of 160 mV and a very strong dipolar anomaly in the centre of the domain (Figure 4.21 LEFT). A small deflection in the  $-10$  mV contour is visible in the map that includes the plume (Figure 4.21 MIDDLE). The effect of the plume seen in the difference panel (Figure 4.21 RIGHT) is twice that of the previous scenario, 4.5 mV, but still within the error of field measurements.

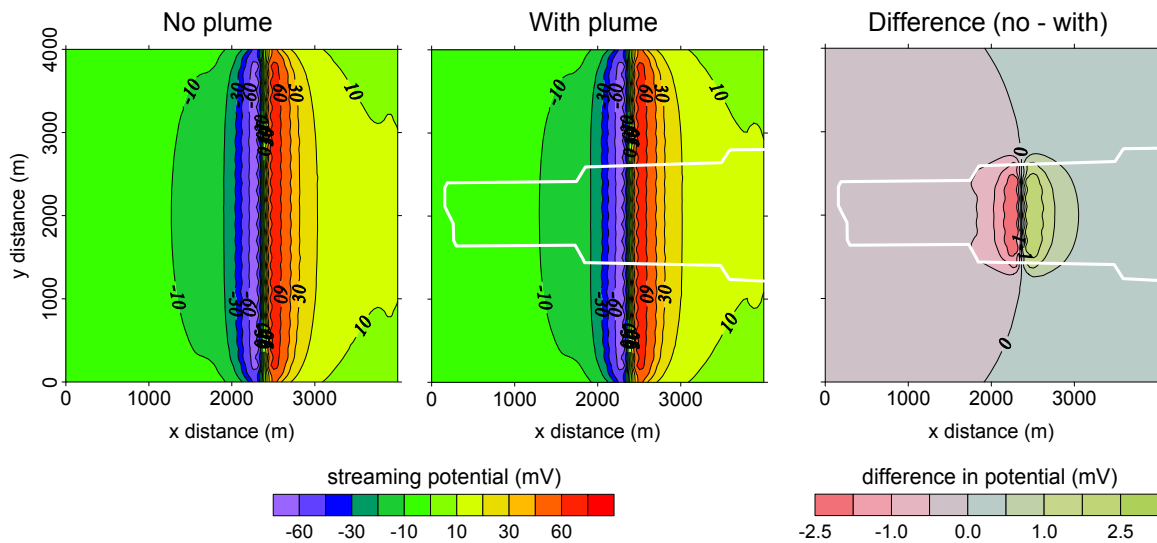


**Figure 4.21 Streaming potentials calculated at the surface of hypothetical model drawn in Figure 4.19 for scenario 2. LEFT: No plume. MIDDLE: With plume, thick white line outlines plume extent. RIGHT: Difference of left panel minus centre panel, thick white line outlines plume extent.**

In the two scenarios presented both  $L'$  and the conductivity were changed because both these properties were modified by the presence of hydrocarbons. Two more tests were run for the second scenario to isolate the effect of each property. The largest streaming potential anomaly occurs when just  $L'$  is modified, but the range is still below a  $\pm 5$  mV error (Table 4.14).

**Table 4.14 Range of differences in potential for different tests of scenario 2.**

<b>Property modifications in plume area</b>	<b>Range of difference in potential (mV)</b>
$L'$ reduced 25% $\rho$ increased 15%	-2.7 to 2.3
$L'$ reduced 25%	-4.0 to 3.0
$\rho$ increased 15%	-0.7 to 1.2

## 4.6 Summary

An apparatus capable of measuring streaming potential coupling coefficient, electrical resistivity and hydraulic conductivity of samples packed in a 15 cm long cylinder was

built and calibrated. The presence of an organic pollutant such as hydrocarbons in the sediment and saturating fluid has an effect on the coupling coefficient. It is not greater than the variability of  $L'$  between different samples from a same site. For the twelve subsamples tested,  $L'$  varies only over one order of magnitude, which suggests that this parameter can be safely estimated for modelling. The range goes from  $50 \mu\text{A}/\text{m}^2$  for glass beads with a CEC of 1.2 meq/100g and probably negligible surface conduction, to  $5 \mu\text{A}/\text{m}^2$  for a clay rich siltstone a CEC of 33.4 meq/100g which should have significant surface conduction. The average  $L'$  measured was  $16 \mu\text{A}/\text{m}^2$ . Although the contamination will have an impact of the streaming potential, subsurface heterogeneity may have a bigger effect on the reliability of modelling streaming potential. Contamination can cause a 25% reduction in  $L'$ , as measured in the laboratory. Though it is a significant change, it will not have a measurable impact on field measurements. As well, neither contamination nor heterogeneity can cause variations in  $L'$  that will alter the streaming potential component of SP enough to generate major anomalies in a field survey.

## **5 FIELD DATA**

Field data are critically important when trying to understand a natural phenomenon such as spontaneous potential (SP) of electrochemical origin. Few detailed survey results are published, yet they are important for developing hypotheses of mechanisms causing electrochemical SP and testing newly developed models. They are also essential for proving the practicality of proposed applications using electrochemical SP mapping. Based on the hypothesis that degrading organic contaminants generate SP anomalies measurable at the ground surface, spontaneous potential surveys were carried out on two impacted sites. Both sites that will be described have free phase hydrocarbon plumes floating on the water table from releases that occurred over several decades but are no longer ongoing. Groundwater geochemistry that includes reduced redox conditions and hydrocarbon chromatographs with humps from an unresolved mixture of compounds indicates active hydrocarbon degradation is occurring on both sites.

The aim of this chapter is to present detailed geochemical and SP data from two sites. This information can then be used to test hypotheses of mechanisms causing electrochemical SP. The first section (5.1) describes field and processing methods. Survey data from a site (RIVER) next to a river are presented in section 5.2. A survey conducted on a second site (KNOLL) in a field on a hill next to a gas plant is reported in section 5.3. Neither site can be located or named because the site owners have asked us to withhold this information, which is why geomorphologic names are used. A discussion is found in section 5.4 and a chapter summary in section 5.5.

### **5.1 Field and processing methods**

Several types of measurements were made on both sites and the field and processing methods for each type will be discussed successively. They are: spontaneous potential measurements (sub-section 5.1.1); electrical resistivity and induced polarization (IP) measurements (sub-section 5.1.2); and geochemical measurements and sediment sampling (sub-section 5.1.3).

### 5.1.1 SPONTANEOUS POTENTIAL MEASUREMENTS

Like other potential field methods, SP measurements are sensitive to noise and because the signal is natural, its intensity cannot be controlled. The basic survey consists of measuring the electrical potential difference between two electrodes at different locations in the ground by connecting them with a wire and a voltmeter. Data acquisition methods are important as they affect the data quality, but there is no widely accepted and practised field procedure. Corwin (1989; 1990; 2005) has several publications in which he tries to establish standard methods and carefully describes important aspects of SP surveying. Most of his recommendations were followed in the surveys described in this chapter. This sub-section is further subdivided to address in detail different aspects including electrodes, surveying, telluric monitoring, processing and error.

#### 5.1.1.1 Electrodes



**Figure 5.1** Copper-copper sulphate electrodes used for SP surveying. An assembled electrode is in the centre and the top and bottom are on either side. The ceramic on the bottom piece on the right is stained green by copper sulphate.

All surveying was done using copper-copper sulphate ( $\text{Cu}/\text{CuSO}_4$ ) electrodes (Figure 5.1). They are a plastic pot with a porous ceramic bottom that is filled with a saturated

copper sulphate solution. The lid screws on and has a copper wire which sits in the solution and is attached to a connector on the outside of the lid. Since the copper corrodes it is necessary to polish this portion of the electrode before each use.

Liquid junction electrodes, such as Cu/CuSO<sub>4</sub>, are recommended because they are considered non-polarizing (Corwin, 1990). Current in the ground is carried ionically and is measured with a voltmeter, where current passes electronically. There will be an accumulation of charge where the current type changes and these electrodes are designed to reduce this charge accumulation which falsifies the readings.

Non-polarizing electrodes are subject to drift because of temperature differences and polarization. The temperature response for Cu/CuSO<sub>4</sub> electrodes is ~0.3-0.5 mV/°C (Petiau & Dupis, 1980; Kassel et al., 1989), which means that if the two electrodes are at different temperatures, part of the potential measured will be produced by the electrodes themselves. Though the name suggests otherwise, electrode polarization will occur because of differing chemical reactions in the two electrodes as they are exposed to soils with different chemistry throughout the survey. Both these errors can be compensated if the drift is measured, either by repeating measurements at one location, which is called a tie point, or by measuring the potential between electrodes when they are both in a conductive medium, in our case a dish filled with CuSO<sub>4</sub> solution. Drift measurements were made at the beginning of the survey, at approximately two hour intervals during the survey and at the end so that corrections could be made.

#### *5.1.1.2 SP surveying*

The surveying method used was a fixed electrode spread (Telford et al., 1990), where one electrode is left stationary and used as a reference, and the second electrode, called the roving electrode, is moved from station to station. This method can require long lengths of wire if the stations are far removed from the reference, but this was not a problem because SP surveys for environmental applications cover relatively small areas.

At each station holes were dug with a 5 cm diameter auger to a depth of ~15 cm. This was done to remove the most active soil layer with vegetation and to try to reach a depth that would have uniform characteristics between stations (Fournier, 1989). As well, the deeper soil was moist which created good electrode contact. Spurious potentials can be caused by different moisture content at electrode locations. The response to changes is 0.3-1 mV/percent increase in the soil moisture content (Corwin, 1990). Certain sources (Perrier & Morat, 2000; Naudet, 2004) recommend putting salted clay in each hole to insure a better and more consistent contact with the ground, or watering the holes. Corwin & Hoover (1979) strongly discourage this practise because of the effect on the measured potential (Figure 5.2).

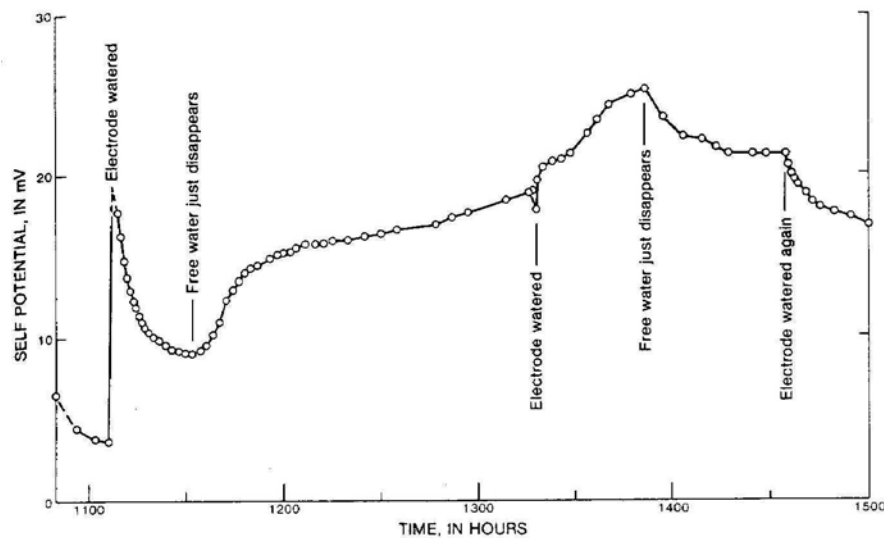


**Figure 5.2** Variation in electrode potential caused by watering of copper-copper sulphate electrodes, Raft River, Idaho. Electrode separation was 200 m. (Corwin & Hoover, 1979)

On the first field site, measurements were made both with the electrodes directly in contact with the ground and in a hole filled with salted bentonite. The results were equivalent (Figure 5.3) so the subsequent surveying was done without clay as it was easier.

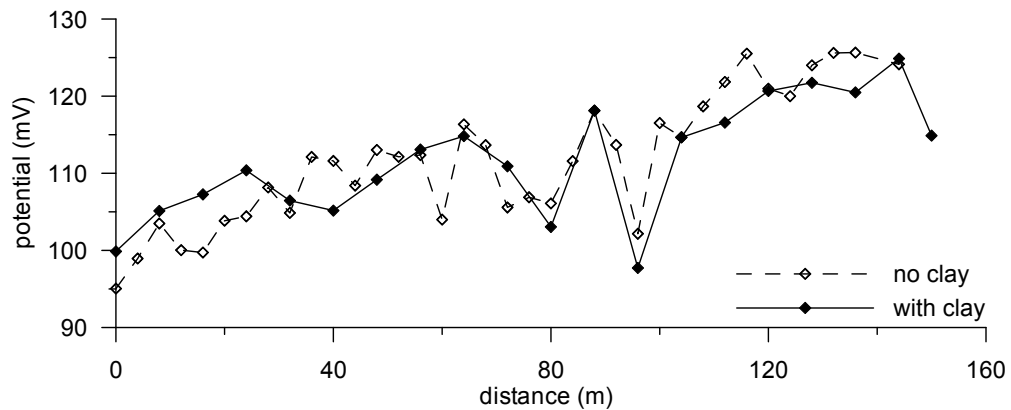


**Figure 5.3 Repeated SP measurements along a survey line. For “no clay” measurements the electrodes were directly in contact with the soil. For “with clay” measurements the electrodes were set in holes filled with salted bentonite. Measurements series were made 16 days apart.**

The two surveys presented in this chapter were on sites with electrically conductive ground that was moist to wet so that contact resistances were generally less than 5 k $\Omega$  (Figure 5.4, Table 5.1) and no action was taken to reduce it. The small proportion of measurements at the KNOLL site with very high contact resistances were in an area affected by anthropogenic noise.

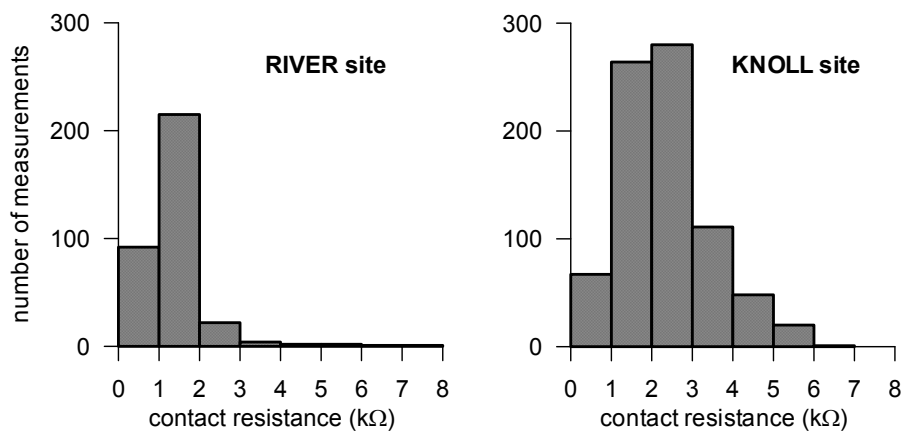


**Figure 5.4 Histograms of contact resistances for surveys on both sites.**

**Table 5.1 Statistics of contact resistances for surveys on both sites.**

Site	# measurements	Average (k $\Omega$ )	Maximum (k $\Omega$ )
RIVER	339	1.3	7.1
KNOLL	793 <10 k $\Omega$ 32 >10 k $\Omega$	2.4 <10 k $\Omega$	5600

At each station three holes were dug within a 0.5 m diameter circle so that repeat measurements could be made and averaged. For a reading, the roving electrode was placed in the hole and connected using a banana clip to the positive terminal of the multimeter. A Fluke model 189 multimeter with an input impedance of 100 M $\Omega$  and 0.025% accuracy (Fluke Corporation Inc., 2000) was used for the surveying. Its negative lead was connected to the reference electrode through a ~500 m long coil of insulated 20 gauge stranded stainless steel wire. The reading was made immediately after putting the electrode in the hole and included a 30 second average made using a built-in function of the multimeter as well as three instantaneous readings during these 30 seconds. Once an electrode is placed in contact with the ground it begins to equilibrate and the process can take more than an hour (Figure 5.5).

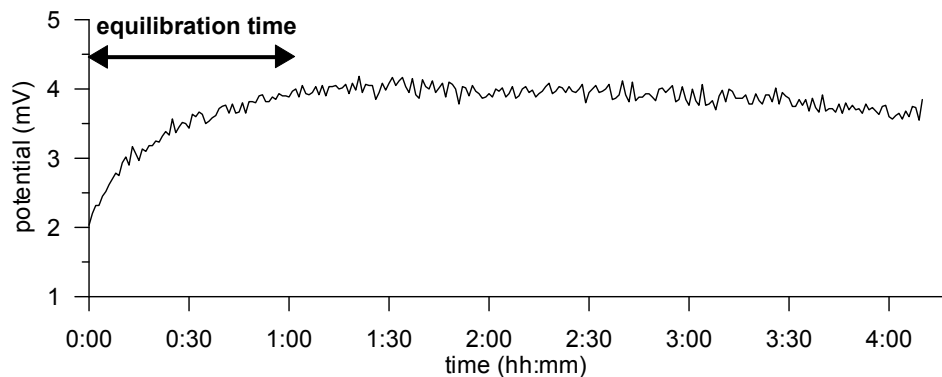


**Figure 5.5 Potential readings made after an electrode is set into the ground. The period of high drift during the first hour is due to the electrode equilibrating with the ground.**

There is controversy as to when the SP reading should be made, with some authors recommending waiting until the electrode equilibrates (Corwin, 1990). The time required for equilibration at each station would make a survey excessively lengthy. To avoid this

while remaining consistent, we tried to always make the measurements at the same place of the equilibration curve. Readings were made in the three holes at each station and if the difference between readings was greater than 2 mV, the hole with the spurious reading was revisited. This was only necessary 13% and 7% of the time at the RIVER and KNOLL sites respectively. Once all the potential readings had been made at a station, a single contact resistance was measured with the multimeter. The resistance measurements were made for less than 4 seconds because the process causes electrode polarization as current is forced to flow between the electrodes (Corwin, 2005). Only an approximate reading of contact resistance was needed as it was simply used to check if the values were relatively consistent between stations and to test the circuit integrity through the wire and reference electrode.

When set to read direct current (DC) voltages, the multimeter used a 60 Hz filter, which consisted of an integration over 16.66 ms (pers. comm. Smith, 2007). The time invariant voltages are the target for SP mapping, but high frequency measurements of transient voltages can hold interesting information about the electrical signal at a site. Transient voltage measurements were made at a limited number of stations on both sites using a National Instrument USB-6215 data acquisition device (DAQ) with an input impedance of 10 G $\Omega$  (National Instruments, 2007).

As with all types of surveying, it is necessary to determine the stations' locations to be able to plot them on a map. This was done using either a Leica total station or a real time differentially corrected Sokkia GSR2650LB GPS, which both provided coordinates with decimetre accuracy.

#### *5.1.1.3 Telluric monitoring*

One of the sources of noise in SP surveys is signals due to telluric currents: time varying electrical currents in the ground caused by activity in the ionosphere. Monitoring for these currents can be used to distinguish SP anomalies due to telluric currents from those due to other sources (Corwin, 2005). For the surveys described, monitoring was done using a base station where the electrical potential was measured between two perpendicular

electrode pairs (Figure 5.6). The measurements were made and recorded on a Campbell Scientific CR10X at a 2 second interval for the RIVER site and a 10 second interval for the KNOLL site. A lower frequency was used at the KNOLL site to reduce the quantity of data collected and it was sufficient to monitor telluric current variations.

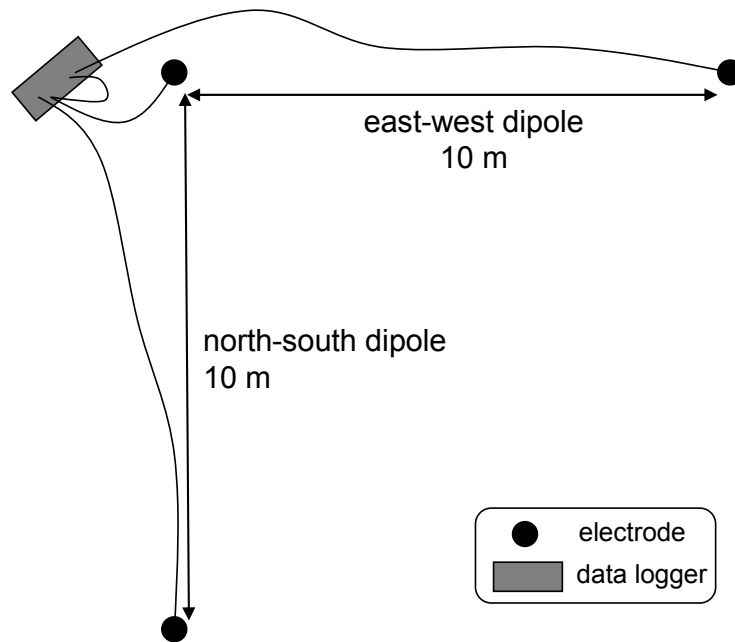


**Figure 5.6 Base station set-up for telluric monitoring. The electrode in the NW corner serves for both dipoles. This is done by using a jumper wire at the data logger.**

The data gathered are generally used only to determine if telluric activity could be a source of error, though it is possible to make corrections for the activity if it is deemed problematic. A typical potential profile for the day (Figure 5.7) has noise of  $\pm 0.5$  mV but the average remains relatively constant. The 2 mV variation in the north-south dipole is smaller than field measurement errors which are discussed in a following sub-section. The base station was set up at least half an hour before surveying to avoid the strongest signal changes due to electrode equilibration. Telluric activity was not a problem for the surveys presented because the variations observed were all very low frequency. The largest daily variation was of 3.3 mV and the average of 1.1 mV.

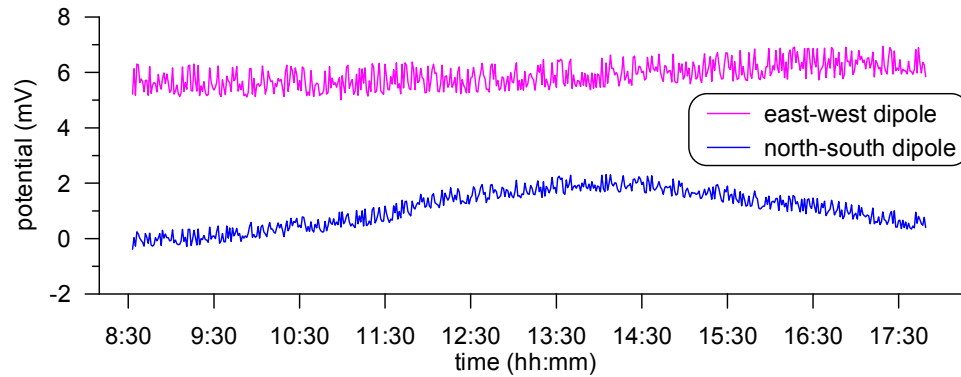


**Figure 5.7** Telluric monitoring record for October 2<sup>nd</sup>, 2006 at the KNOLL site. Each dipole has  $\pm 0.5$  mV high frequency chatter due to noise and a lower frequency signal from telluric current variations is visible as a trend. In the north-south dipole the variation is a 2 mV rise over the course of the day followed by a 1 mV decrease at the end of the afternoon.

#### 5.1.1.4 Processing

The processing involved making corrections for electrode drift. The differences between values measured at tie points or in the  $\text{CuSO}_4$  dish at different times were linearly interpolated and subtracted from the measurements (Figure 5.8).

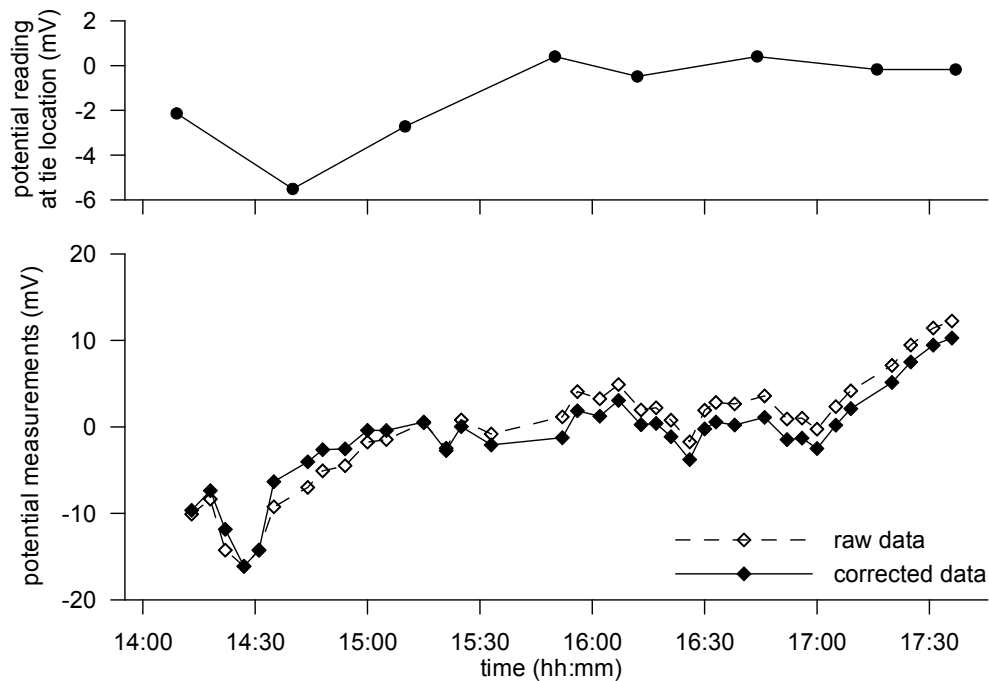


**Figure 5.8** Example of drift corrections applied to SP measurements. **TOP:** Potential measured at tie location at different times. **BOTTOM:** Raw measurements made between tie point readings and the same measurements with corrections applied.

At each station, the average of the 30 second average readings from the three holes was used to make maps or profiles. Two standard deviations were calculated: using the three instantaneous measurements in each hole and using the 30 second averages from the three holes at each station. The second standard deviation includes some spatial variability at each station so it is used when discussing error.

#### 5.1.1.5 Error

Most sources state that carefully conducted SP surveys typically have  $\pm 5$  mV error (Corwin, 1990; Friberg, 1996). During an extensive survey at the Entressen landfill, Naudet's (2004) measurements had a 20 mV standard deviation. Fournier (1989) also reports a 20 mV standard deviation, in this case the survey was over a volcanic aquifer. The standard deviation between the three measurements at each station for the surveys presented were typically  $\sim 2$  mV (Figure 5.9, Table 5.2). As with the resistance measurements, the small fraction of very large standard deviations at the KNOLL site were in an area affected by anthropogenic noise. The signal in this area had a very large amplitude so though the standard deviation absolute values were higher, the fractional standard deviations were not.

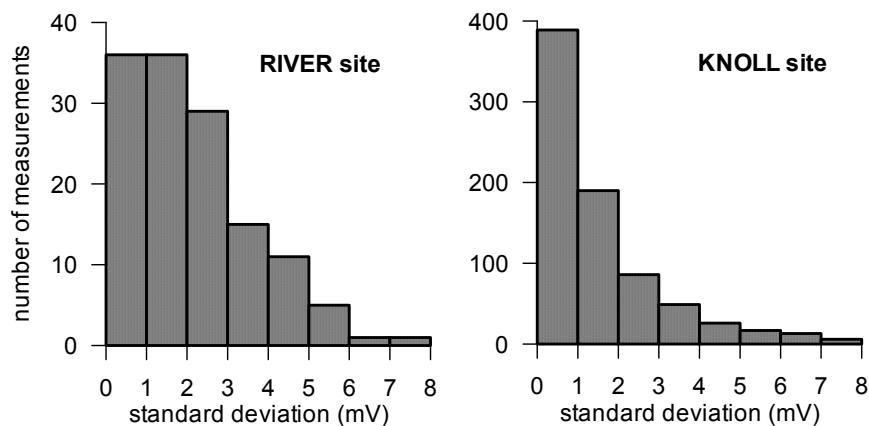


**Figure 5.9** Histograms of standard deviations of the readings at each station for surveys on both sites.

**Table 5.2 Statistics of standard deviations of the readings at each station for surveys on both sites.**

Site	# measurements	Average (mV)	Maximum (mV)
RIVER	134	2.1	7.2
KNOLL	785 <10 mV 53 >10 mV	1.6 <10 mV 3.4 all	127

Repeat readings were made at three stations on the KNOLL site, which were reoccupied at approximately every fortnight. The field conditions for the repeat measurements were extremely different, but spanned the range of what was encountered during the survey. The readings varied more than by the typical standard deviations. If  $\pm 5$  mV error bars are added to the readings, the measurements at two of the three stations are the same within error (Figure 5.10).

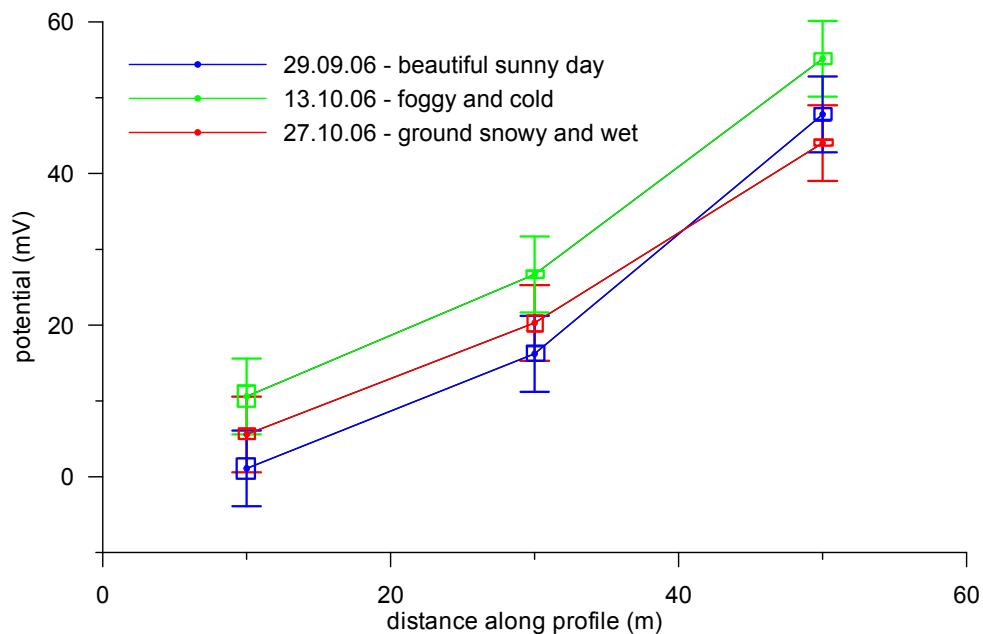


**Figure 5.10 Repeat measurements at three stations every fortnight. The boxes around the central points are the standard deviation of the readings and the error bars are  $\pm 5$  mV. The readings at the 10 and 30 m stations are the same within error whereas at the 50 m station the measurements from 13.10.06 and 27.10.06 do not overlap.**

### 5.1.2 RESISTIVITY AND INDUCED POLARIZATION MEASUREMENTS

Ground resistivity affects the strength of a spontaneous potential signal and a change in resistivity, such as might be found across a fault zone, can create SP anomalies in the presence of a source of current (Cull, 1985). Equations used for modelling, as presented in chapter 3, show that it is necessary to know the ground resistivity distribution in order to model an SP signature. This motivated the resistivity surveys on the sites along with induced polarization measurements, which can also provide helpful geological information.

The resistivity and IP surveys were done using an IRIS Syscal Pro resistivity meter with an internal transmitter, an external switch box and cables with take-outs for 72 electrodes. The surveys consist of injecting electrical current into the ground through an electrode pair and reading the electrical potential generated between another electrode pair. Resistivity readings are made as the current is being injected and IP readings are made after the current stops, while the voltage is decaying (Figure 5.11).

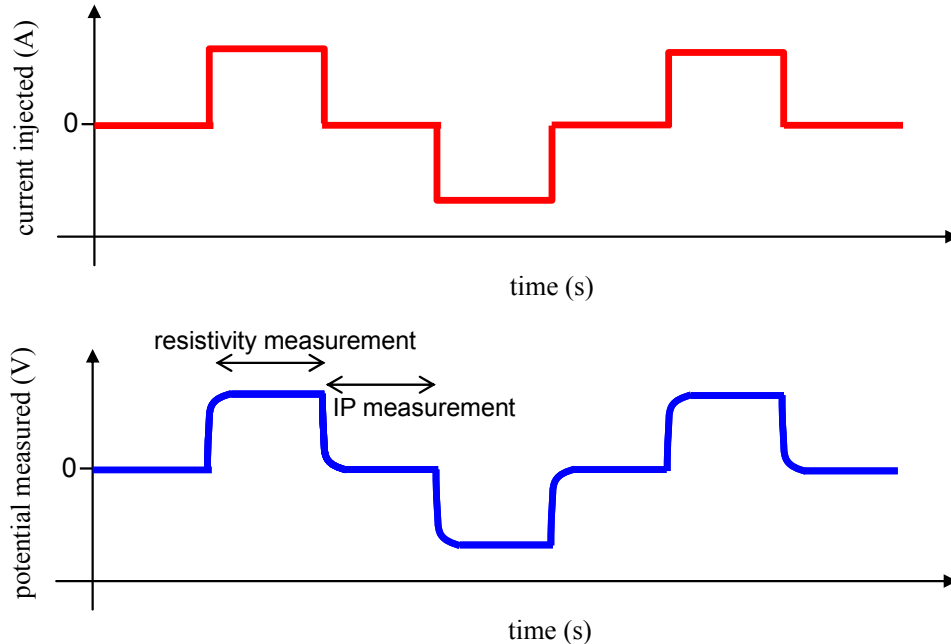


**Figure 5.11** Timing of resistivity and induced polarization (IP) measurements with respect to current injection and potential produced.

Most of the surveys were done with stainless steel electrodes and resistivity was measured, though one line at the RIVER site was done measuring IP as well. The survey configurations will be described in each site section since they were varied to explore which ones were optimal.

The first processing step was rejecting bad data points. A first criterion was exclusion of data points that produced negative apparent resistivities. Next, points with a standard deviation between repeat measurements above 1% were rejected. The final criterion was the similarity of reciprocal readings, though these were not made for all surveys. When reciprocal measurements were made, only readings that were within 10% of the reciprocal value were kept. The second and final processing step was data inversion, done using the commercial software RES2DINV (Loke & Barker, 1996) which applies a non-linear least squares technique. The model cell size was set to one half the electrode spacing. The inversion calculates 2D resistivity profiles of the subsurface from the data gathered with electrodes at the surface.

### 5.1.3 GEOCHEMICAL MEASUREMENTS AND SEDIMENT SAMPLING

Both sites have ongoing environmental monitoring programmes, mainly concerned with plume delineation. Most of the geochemical and geological site descriptions come from reports produced for these programmes. The sites were chosen because they had been well characterized, which allowed us to focus geophysical field work in areas of interest.

RIVER was the only site where we did additional work, measuring groundwater field parameters in monitoring wells that did not have free phase hydrocarbons. This was done using a hand-held YSI multi-probe meter, calibrated before use. It measured temperature, pH, electrical conductivity ( $\sigma_f$ ), dissolved oxygen (DO) and redox potential (Eh). Measurements were made once the probe was immersed in water and repeated at 50 cm intervals while the probe was being lowered to the bottom of the well. Generally the temperature, pH, DO and Eh decreased with depth whereas  $\sigma_f$  increased (Figure 5.12).

Only the first reading in each well was used for the maps because the probe mixed the water column as it was lowered, its diameter being just under that of the well.

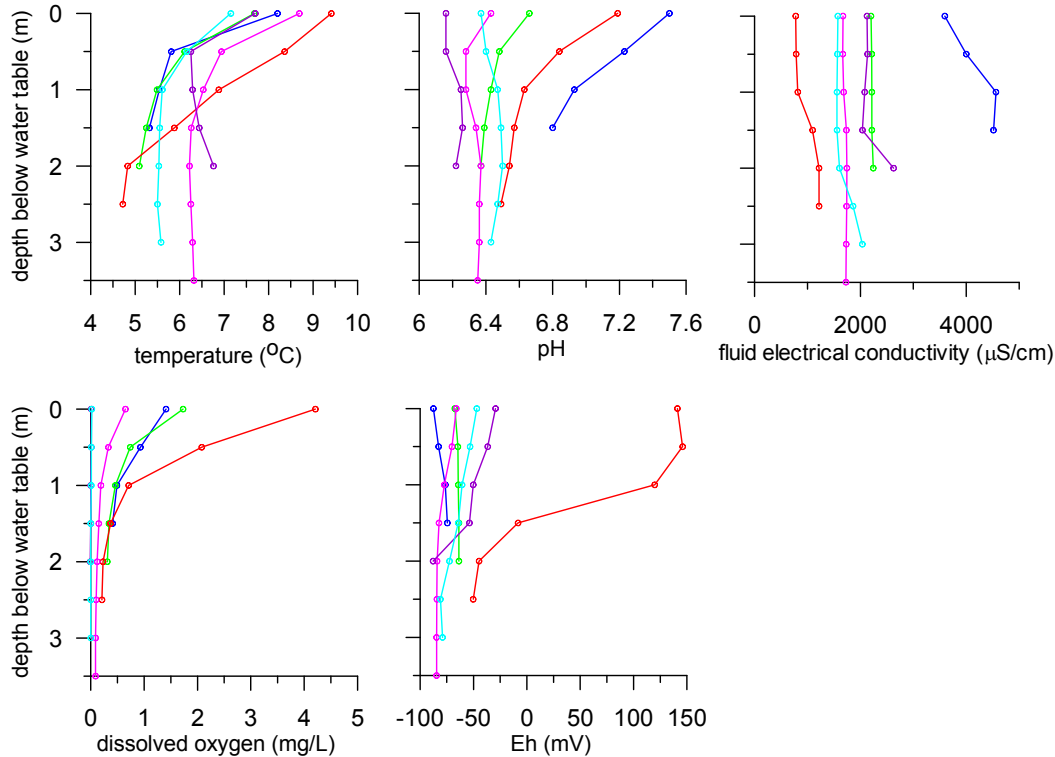


**Figure 5.12 Variations of groundwater field parameters with depth for six wells at the RIVER site. The different colours for the profiles represent different wells.**

Two water samples were collected from the RIVER site with a Waterra pump. One water sample was collected for us by the consulting company doing monitoring at the KNOLL site. The water was used for streaming current coupling coefficient measurements and the analyses of these samples are found in chapter 4.

At the RIVER site, we also sampled unconsolidated sediment using a Becker hammer drill to investigate targets found with the resistivity surveys. This method of drilling is appropriate for the coarse grained sediment found on the site and consists of a steel drill stem driven into the ground by a double acting diesel hammer while an air-injection/cyclone system removes the cuttings (Sy & Campanella, 1992). The cuttings collected with this method are very disturbed and it is not possible to know their exact depth of origin. During the drilling, the cuttings from approximately every metre were put

into separate rubber buckets for identification and sampling. Eight holes were dug in different locations and sediment samples were collected in zip-lock bags every time the lithology changed. At the KNOLL site core with a 3.75 cm diameter obtained using a hollow stemmed auger was provided by the consulting company doing the monitoring.

## **5.2 RIVER site**

The RIVER site is located on a riverbank in central Alberta. Although the river is dammed and the flow is controlled, it is still very dynamic with an average base flow of 55 m<sup>3</sup>/s and a peak of ~190 m<sup>3</sup>/s usually in June (Bow River Basin Council, 2005). The geology in the river valley is an interfingering of sands and gravels from old river channels within silty to sandy overbank deposits. Bedrock is 5 to 12 m below surface and is the Paskapoo Fm. (Tertiary), primarily siltstones with some sandstone channels (Carrigy, 1971).

An oil refinery operated on the site from 1923 to 1977 and when it was decommissioned the above ground infrastructure, which included large above ground tanks and a hydrocarbon sludge weathering area, was removed (Alberta Environmental Appeal Board, 2002). Some of the structures were buried on site and fill was brought in to level the site.

The hydrogeological and geochemical data are presented in sub-section 5.2.1 and were used to delineate targets for the geophysical work described in sub-section 5.2.2. Both the geophysical data and information from the drillings were then used to develop a site model (sub-section 5.2.3).

## 5.2.1 HYDROGEOLOGICAL AND GEOCHEMICAL DATA

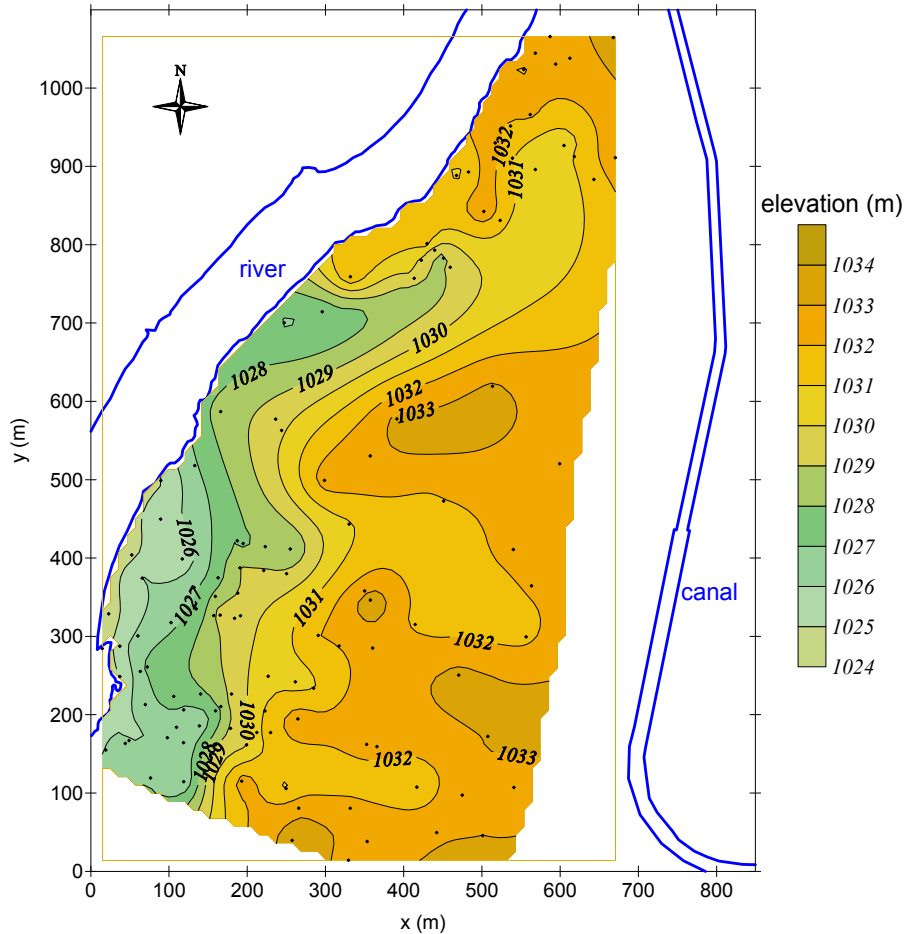


**Figure 5.13** Topographical map of the RIVER site. Elevation contours are every metre. The black dots are data locations used to make the contour map.

The RIVER site is on the east bank of a river and there is a canal used to divert irrigation water a couple of hundreds of metres to the east (Figure 5.13). The ground surface slopes towards the river and the difference in elevation is  $\sim 5$  m. Contour maps of the water levels over the seasons (Figure 5.14) show that the hydrologic system is variable. Flow directions are principally parallel to the river most of the year, whereas in the fall there is also a component perpendicular to the river.

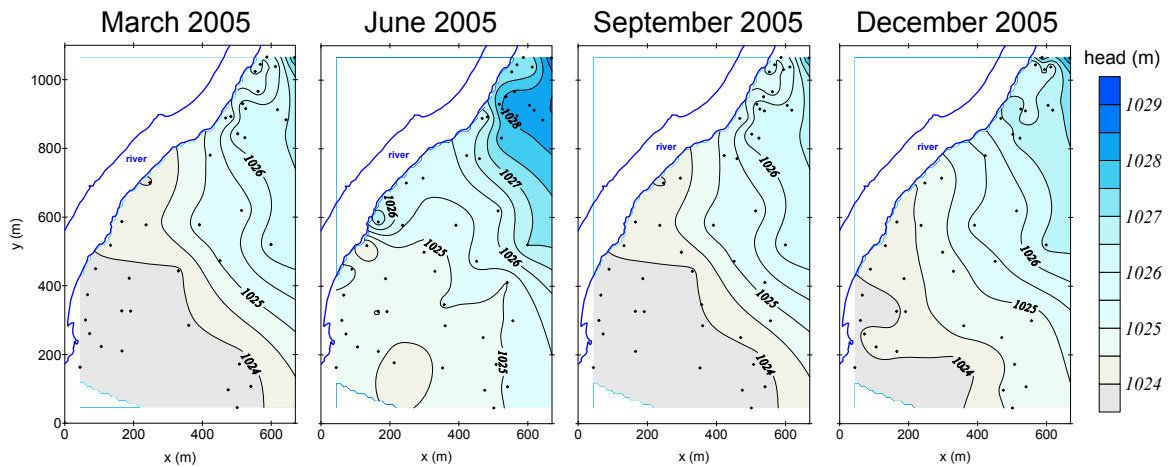


**Figure 5.14 Groundwater elevation maps for four seasons of 2005. Elevation contours are every half metre. The black dots are data locations used to make the contour maps.**

There are a wide variety of hydrocarbons on this site including tar seeping to the surface, immobile hydrocarbons in the soil, free phase liquid petroleum hydrocarbons on the water table surface and a dissolved phase (EBA Engineering Consultants Ltd., 2006). Both hydrocarbon chromatographs (Figure 5.15) show humps caused by an unresolved mixture of compounds, indicating that the hydrocarbons have been degraded. The chromatograph of a sample from the free phase (Figure 5.15 LEFT) shows that most of the hydrocarbons are at the heavy end, between C15 and C40. The chromatograph for the dissolved phase (Figure 5.15 RIGHT) shows lower concentrations of lighter hydrocarbons, principally C15 to C25. The dissolved phase is likely less degraded because there are still some distinct compound peaks above C25 that may be longer chain alkanes.

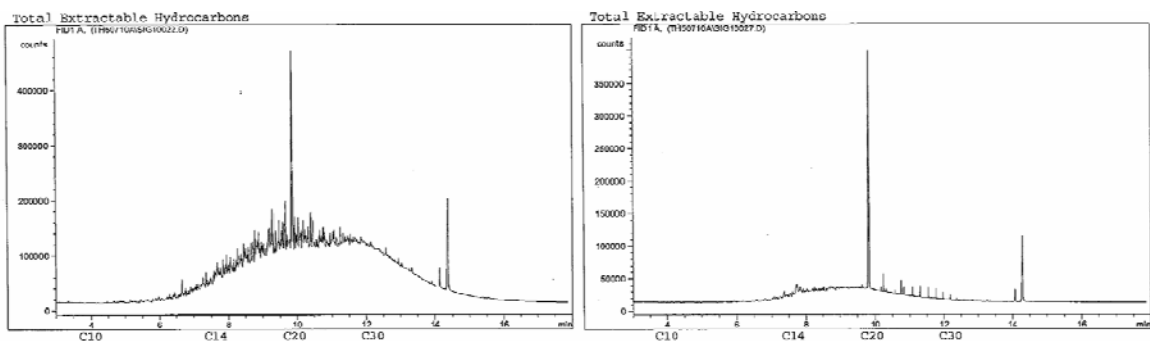


**Figure 5.15 Chromatographs of hydrocarbons found on the RIVER site. LEFT: Free phase. RIGHT: Dissolved phase. The distinct peaks at 9.5 and 14.5 are surrogates used for quality control. (EBA Engineering Consultants Ltd., 2006)**

The dynamic water flow regime moves the free phase hydrocarbon plumes around the site (Figure 5.16). The location and thickness of the plume varies with the seasons but it does not generally reach the river. The water flow parallel to the river keeps the plume running north-south and there may also be preferential flow in this direction along abandoned river channels. The large lobe in the south-eastern plume extent in March 2005 is probably due to insufficient data as many wells were dry in this area during the survey.

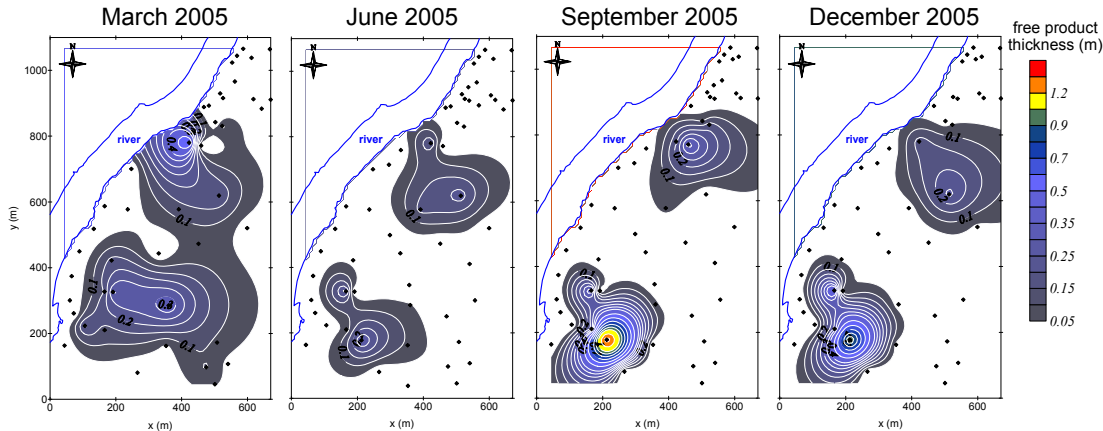


**Figure 5.16 Free phase petroleum hydrocarbon thickness maps for four seasons of 2005. The black dots are data locations used to make the contour map.**

Two weeks prior to the principal geophysical surveys, many of the wells on the site were monitored to determine the location of the free phase hydrocarbons. Groundwater parameters were measured in wells where there was no free product. Low redox potentials near the plume were expected because of the hydrocarbon degradation, with values increasing with distance from the plume edge. There is no such pattern in the data (Figure 5.17) although the Eh values are generally low. The river water is fully oxygenated so it limits the western extent of the reduced plume. The free phase hydrocarbons are found in a band roughly parallel to the river.

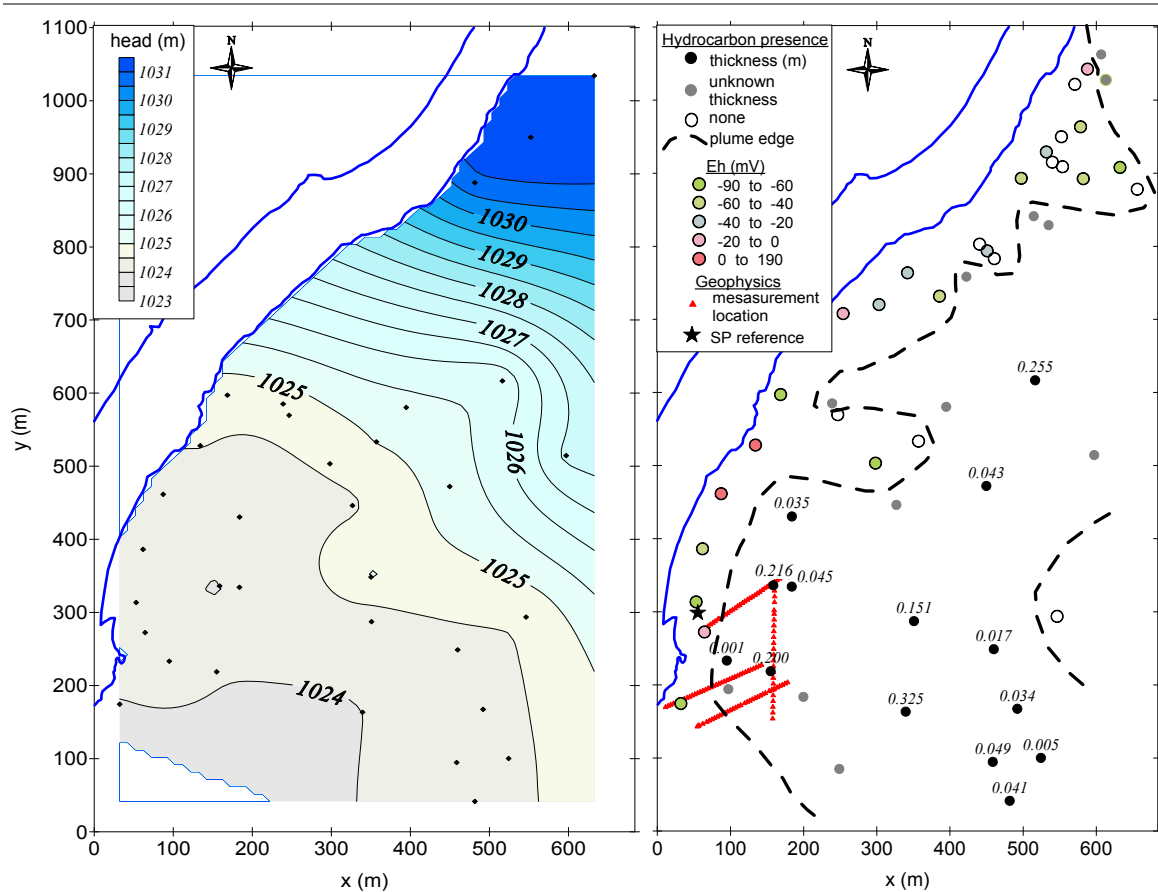


**Figure 5.17 June 2006 data for RIVER site. LEFT: Groundwater elevation map with contours are every half metre. The black dots are data locations used to make the contour map. RIGHT: Hydrocarbon distribution and redox potentials measured in wells. A dashed line is drawn around the edge of the plume. The red markers indicate where our geophysical work was done.**

### 5.2.2 GEOPHYSICAL DATA

Geophysical surveys were restricted to the south west corner of the site. SP and resistivity were gathered on three roughly parallel 142 m long lines located to straddle the plume edge near monitoring wells (L1-L3) (Figure 5.17 RIGHT, Figure 5.18). IP was collected on L2 and SP data were also collected on a fourth line (L4), 184 m in length, perpendicular to the first three. Transient voltage measurements were made in seven locations (Figure 5.18).

The spontaneous potentials do not show great variations, with a range of 39 mV. Although there is noise in the data, the general trend is for the values to decrease to the southwest (Figure 5.18).

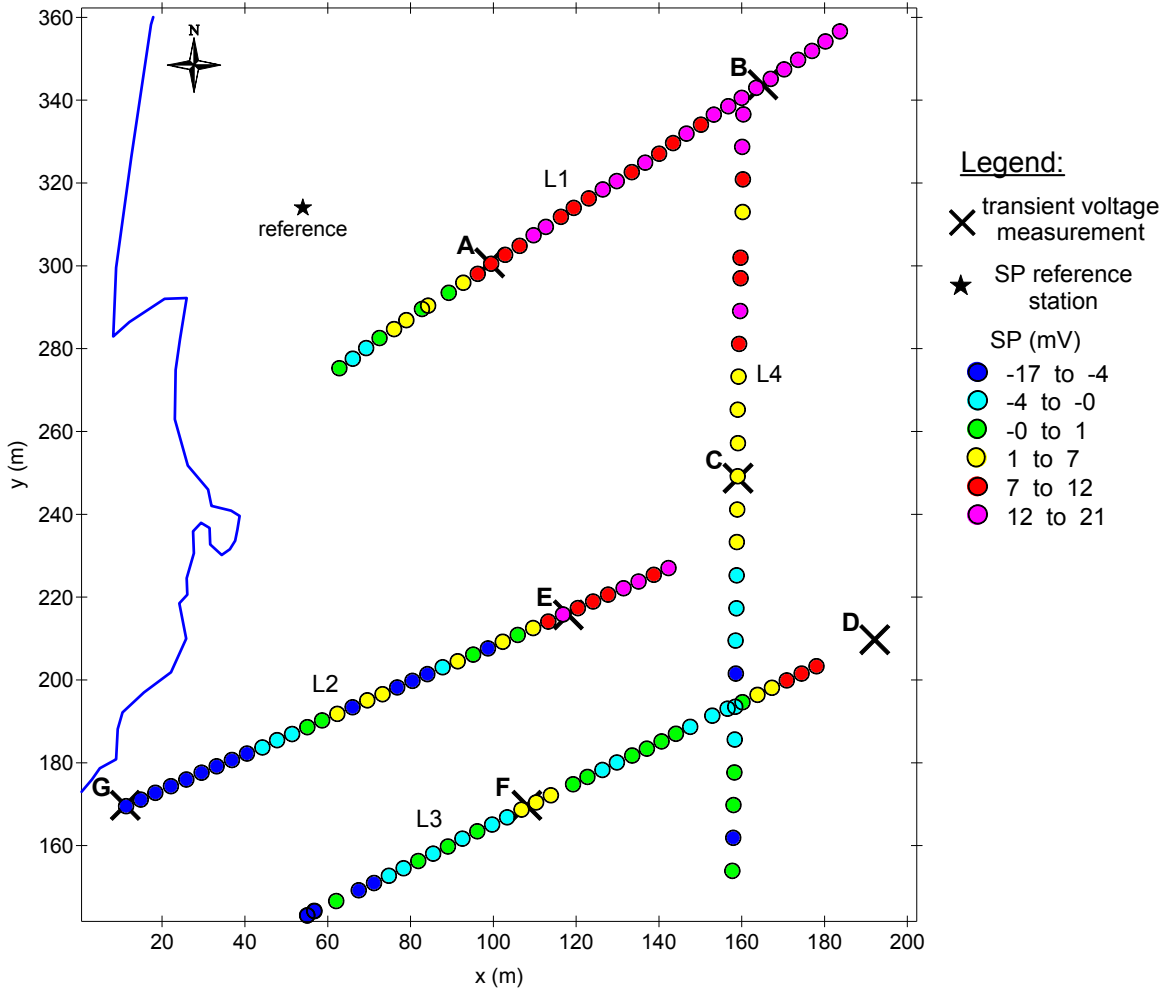
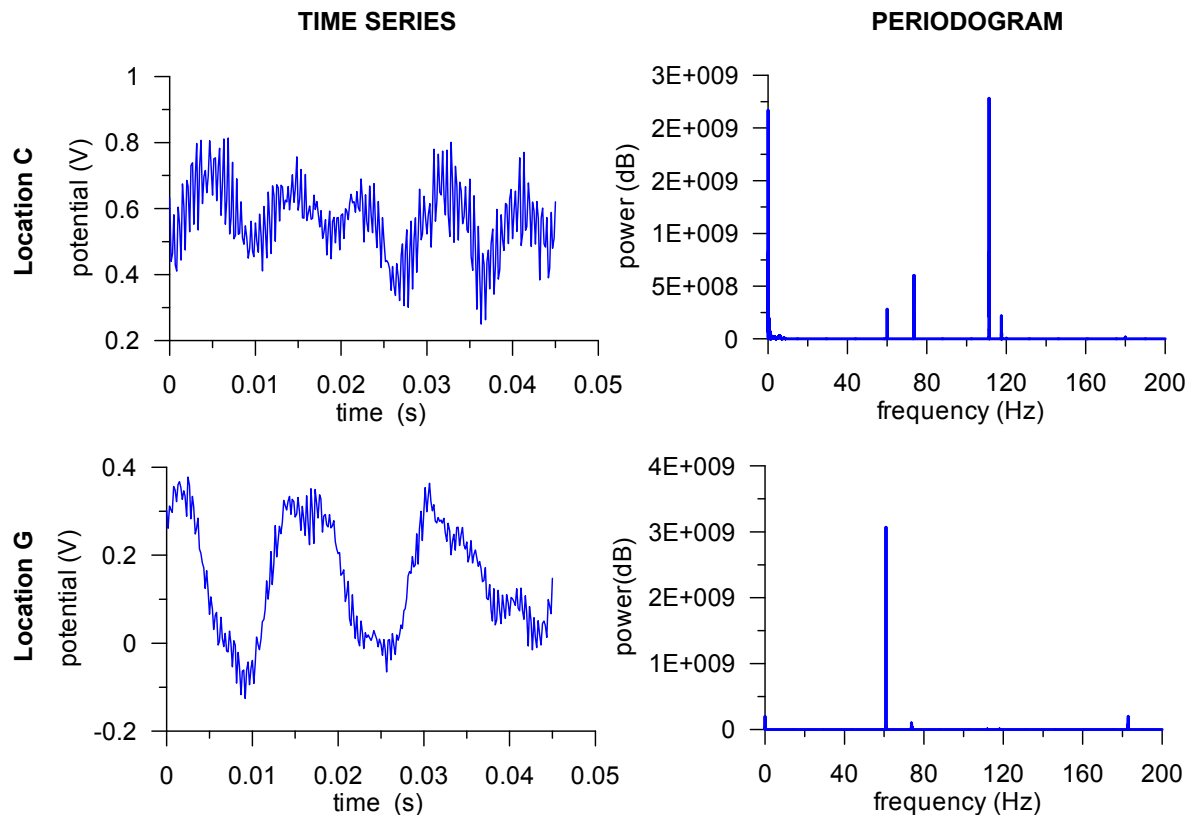


Figure 5.18 Spontaneous potential measurements at RIVER site.

The transient voltages indicate that there could be several sources of anthropogenic noise. Locations A, B and C have an important source with a 110 Hz signal, whereas at locations E, F and G the strongest signal has 60 Hz, which is the frequency of power in North America (Figure 5.19). Potential sources of anthropogenic noise include power lines, grounded generators, pipelines, buried utilities, electric fences and any other infrastructure that is electrically charged or carries current.



**Figure 5.19 High frequency (6000 Hz) measurements of transient voltages and spectral analyses for locations C (TOP) and G (BOTTOM). LEFT: Time series data showing the sum of a high frequency signal and a lower frequency one. RIGHT: Periodograms to show the dominant signal frequencies.**

The resistivity surveys were done using a 2 m electrode spacing and a Wenner array for L1 and L3, and a gradient array for L2. IP was collected on L2 where the survey installation involved two adjacent lines of electrodes 10 cm apart. One line had stainless steel stakes and was used for current injection. The second line had Cu/CuSO<sub>4</sub> electrodes like those used for SP surveying and was used for measuring potentials. Contact resistances between the ground and electrodes were less than 2 k $\Omega$  and the data acquired were of good quality. Processing and inversion statistics are found in Table 5.3.

**Table 5.3 Statistics of electrical resistivity and IP surveys at RIVER site.**  
**Abbreviations: res.—resistivity.**

<b>Line</b>	<b>array type</b>	<b>total # data points</b>	<b># points after processing</b>	<b>% rms error in inversion</b>
L1	Wenner	916	808 (88.2%)	2.53
L2	Gradient	6129	5904 (96.3%)	res.:2.40 IP:0.49
L3	Wenner	825	821 (99.5%)	1.13

The highest resistivities at the site are 460  $\Omega\text{m}$  with most of the values between 30 and 150  $\Omega\text{m}$  (Figure 5.20). Although the range is limited, all three profiles have similar ranges and there are coherent bodies underground. The chargeability measured with IP is generally low with an exception at ~115 m where the values reach 23 mV/V.

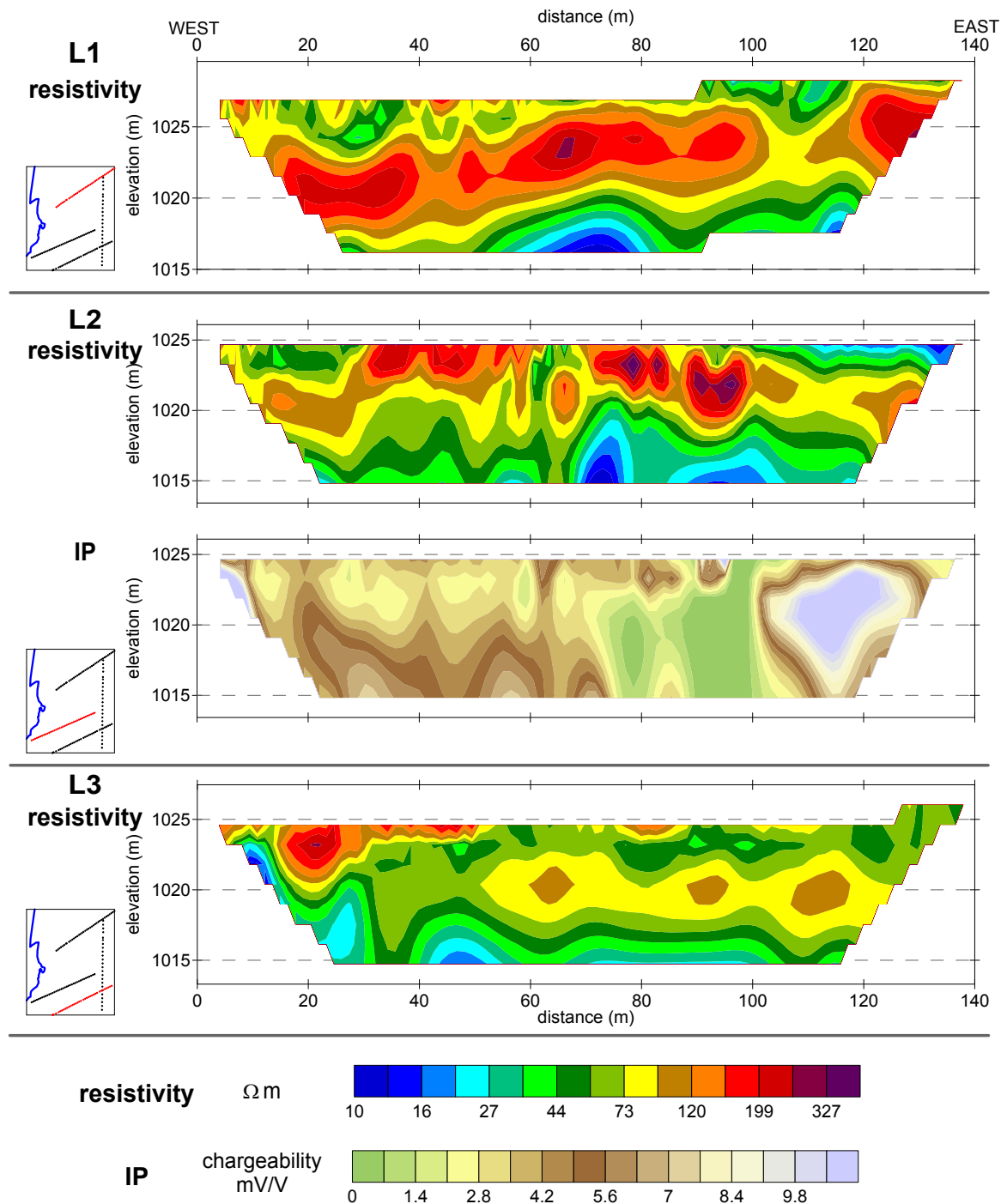


**Figure 5.20** Electrical resistivity and IP inversion results for three of the lines at the RIVER site. The warm coloured bodies on the resistivity profiles are continuous and coherent within each profile but cannot be mapped between profiles. The chargeability values are generally low with an exception at 115 m and possibly something at 10 m though the second anomaly is poorly constrained because of sparse data. The small location maps on the left highlight the line corresponding to the presented data.

### *5.2.3 RIVER SITE MODEL*

The groundwater table was within 2 m of the ground surface during the survey, which contributed to lowering the resistivities since almost all the sediments were saturated. Eight drilling targets were chosen using the resistivity data with the aim of better defining the lithologies. The logs of the boreholes near the lines are included as the BH logs of Figure 5.21. Other logs available included those from test pits dug in the late 1980s, and they appear as the TP logs on the same figure. Though the stratigraphies in the test pits are more accurate than what was gathered from the Becker hammer cuttings, the height at which the profiles are drawn are less certain because the land may have been levelled with fill added or removed since they were logged.

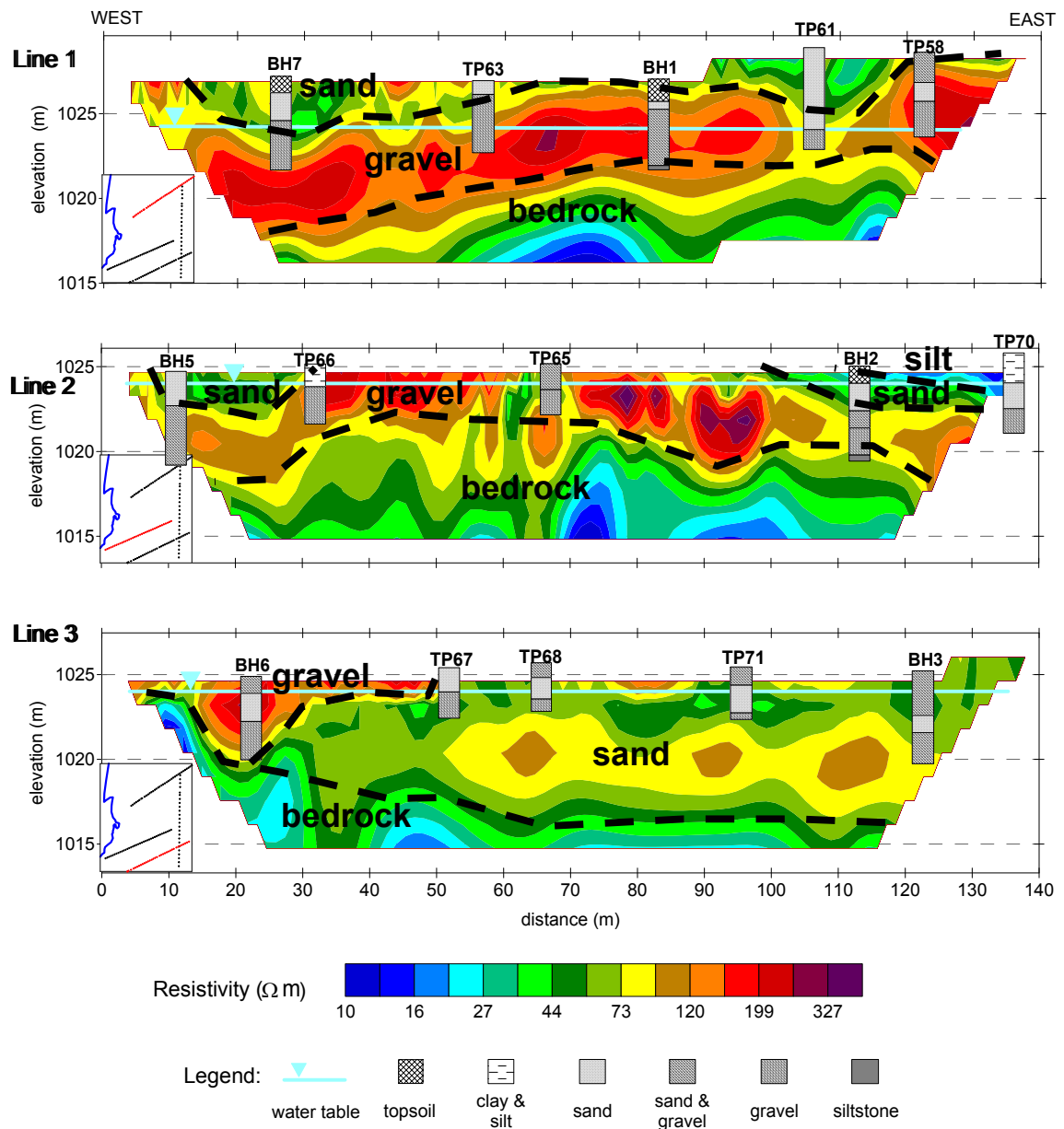


**Figure 5.21** Interpreted resistivity sections for the RIVER site with the water table and well logs. The small location maps on the left highlight the line corresponding to the presented data.

It is possible to map the top of bedrock, which is a siltstone with resistivities of 10-30  $\Omega$ m. Gravel bands appear as relatively continuous horizontal bodies with resistivities of 120-400  $\Omega$ m. There is always sand mixed in with the gravel, and likewise the sand bodies with resistivities of 50-100  $\Omega$ m usually include gravel. Dashed lines on Figure 5.21 outline the lithologies. In the field, the boundary with bedrock is sharp but it does not

appear this way on the figure because the inversion process smoothes the data. The boundaries above the bedrock seemed more gradual, although it was hard to tell precisely with the Becker hammer drill cuttings. The resistivity profiles are not close enough to form a 3D picture of the subsurface which seems heterogeneous since the bodies cannot be mapped between the different profiles.

The RIVER site is hydrologically active because its lithology includes many hydraulically conductive sands and gravels that are connected to a river with fluctuating flows. This has led to an irregular distribution of hydrocarbons and the mixing may prevent the formation of a stable redox zonation typically seen downstream of organic contaminants (Christensen et al., 2000). It is sometimes possible to image hydrocarbon contaminants either as resistive zones when the spill is recent (Mazáč et al., 1990) or conductive zones once degradation has begun (Werkema et al., 2003; Atekwana et al., 2005). The data from this site do not show a difference between the east, where hydrocarbons are known to occur, and the west, where there are none; therefore resistivity cannot be used to delineate hydrocarbons. With the induced polarization survey, hydrocarbons are expected to show up as areas with high chargeability because hydrocarbon saturated ground will interrupt ionic current flow, causing a charge build up (Vanhala, 1997). The IP anomaly on line 2 could be interpreted as such an anomaly and was targeted with BH2. We found hydrocarbon odour and staining in this borehole and in all other boreholes as well. The IP information is not conclusive because though a high chargeability indicated hydrocarbons in BH2, there is no equivalent signature at a well at 93 m on line 2 where free phase hydrocarbons were detected.

When looking at the spontaneous potential data, it is necessary to consider the portion of the signal due to streaming potential. The SP measured does not have a significant Pearson correlation with the water elevation contours, even though the typical relationship is for SP to increase with decreasing water levels (Revil et al., 2004). The streaming current coupling coefficient was measured for two samples from this site as described in chapter 4. With clean groundwater, these values were 9 and 13  $\mu\text{A}/\text{m}^2$  and

using polluted groundwater they were 5 and 8  $\mu\text{A}/\text{m}^2$ . In the section where the SP surveys were done the range of the water table elevations is 2 m and if an average ground resistivity of 75  $\Omega\text{m}$  is used, the expected streaming potential signal can be estimated

$$\Delta V = \Delta h \cdot L' \cdot \rho = (2 \text{ m})(13 \cdot 10^{-6} \text{ A}/\text{m}^2)(75 \Omega\text{m}) = 0.002 \text{ V} \quad [5.1.]$$

where  $\Delta V$  is the difference in potential,  $\Delta h$  is the difference in hydraulic head,  $L'$  is the streaming current coupling coefficient and  $\rho$  is the resistivity. This is the maximum possible streaming potential as the calculations assumes convection and conduction currents are occupying the same volume, when in fact the conduction current occurs in a larger volume (Ishido & Pritchett, 1999). The streaming potential is only two millivolts, which is within the error of measurements in field conditions. Its contribution can therefore be neglected.

There are no important thermal gradients on site which means the two remaining sources of SP signal are electrochemical and anthropogenic. Electrochemical SP caused by the redox halo of degrading organic contaminants would be expected to generate negative anomalies greater than 100 mV downstream from the plume (Revil et al., 2010). The signal measured at the RIVER site has a much smaller amplitude and increases in the downstream direction. This leaves anthropogenic sources as the probable cause of the measured signal. There is likely more than one source of noise, because the transient voltage measurements show distinct spectral signatures for the south east (60 Hz) and north west (110 Hz).

### 5.3 KNOLL site

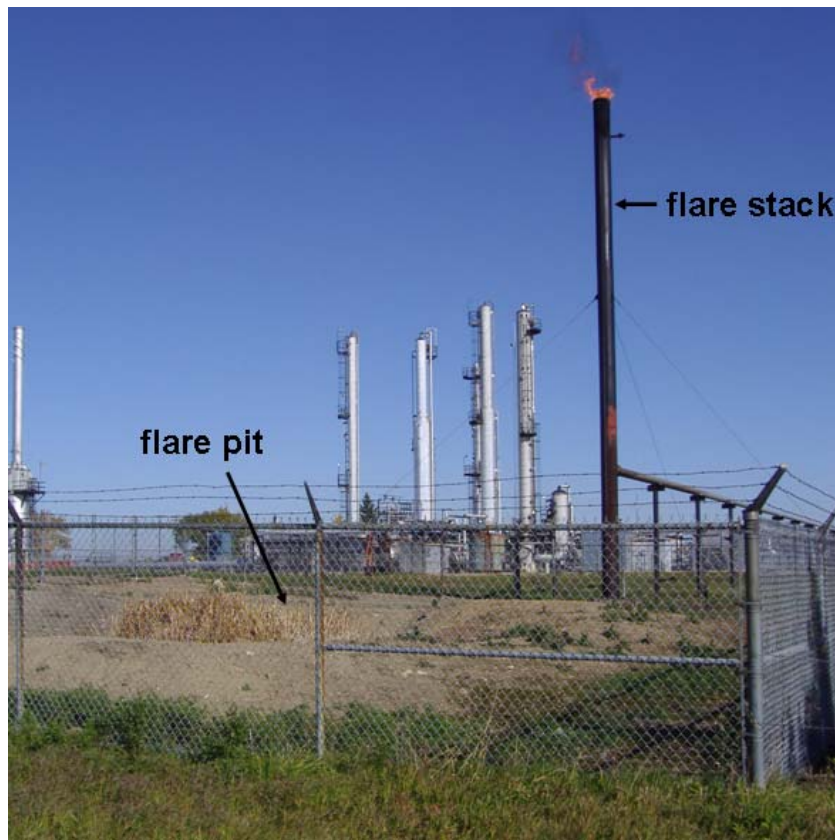


**Figure 5.22** Picture of flare stack and pit at KNOLL site.

The KNOLL site is located on rolling land east of the Foothills in central Alberta. It has an operating gas plant constructed in 1965 that processes sweet gas. The plant used an unlined flare pit from 1965 to 1997 and this is the source of pollution (Matrix Solutions Inc., 2006). The plant has a flare stack to which it diverts any unexpected increase in production to be burned. At the base of the stack is a flare pit which collects any liquid that does not burn (Figure 5.22). This liquid is called condensate and consists mostly of light end hydrocarbons: C7-C12, and a tiny fraction of asphaltenes.

The hydrogeological and geochemical data are presented in sub-section 5.3.1. The geophysical survey data are shown in sub-section 5.3.2 and correction made to the SP measurements is described in sub-section 5.3.3. A site model is developed in sub-section 5.3.4.

### 5.3.1 HYDROGEOLOGICAL AND GEOCHEMICAL DATA

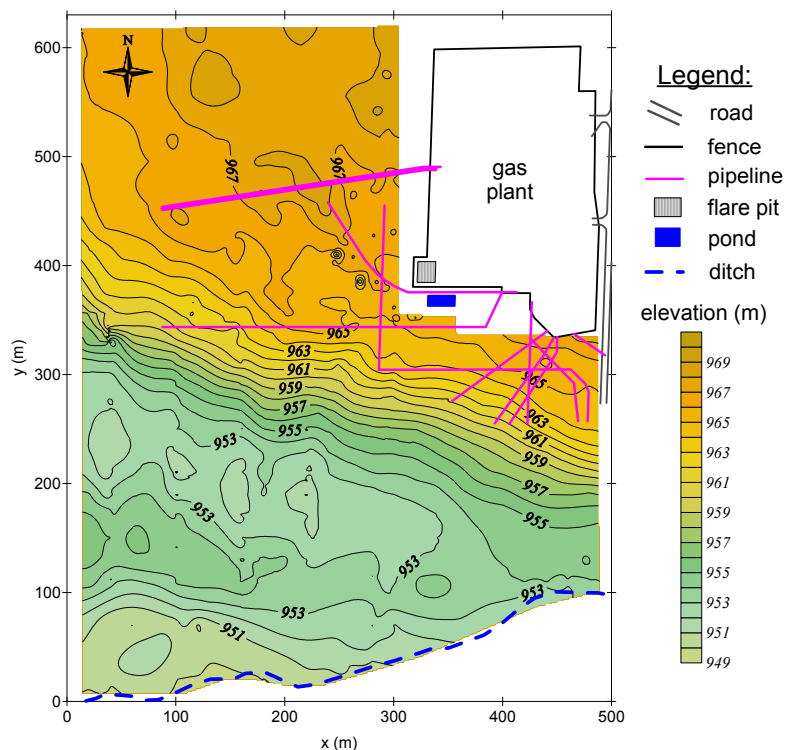


**Figure 5.23 Topography and infrastructure at the KNOLL site. Elevation contours are every metre. Only the portions of the pipelines nearest to the plant are drawn though they extend across the whole site.**

The KNOLL site is on the top and south flank of a small hill (Figure 5.23). The gas plant is in the northeast corner of the site and we did not survey within its limits. There are many pipelines throughout the survey area that are buried 0.6 to 1.2 m below ground. The two surface water bodies are a pond, located just to the south of the plant fence line and a ditch at the bottom of the hill in the south of the survey area. The ditch was dry unless there was a lot of rain or snow. The areas around the gas plant are cultivated fields. In 2006, when we did the survey, the area to the west of the plant was in canola, harvested during the survey, and the large field to the south had a grain crop harvested before the survey.

The water level map for November 2006 (Figure 5.24) shows a mound below the pond and flare pit and the contours mirror topography, decreasing towards the ditch in the south.

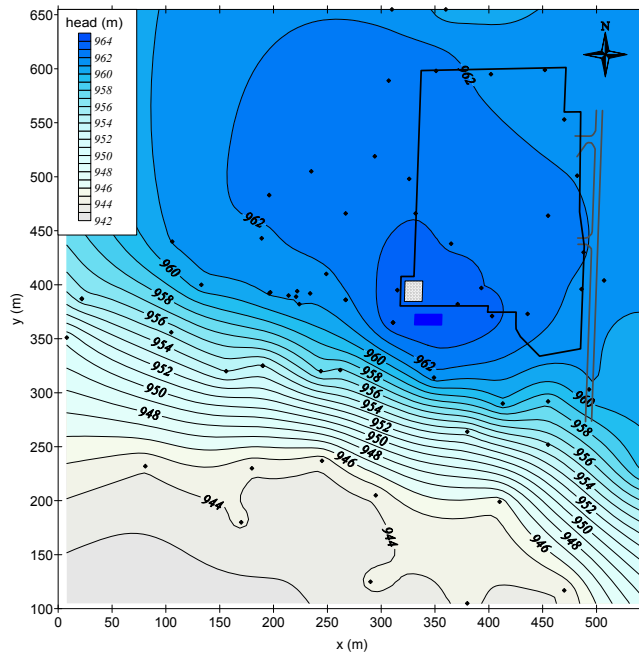


**Figure 5.24 November 2006 groundwater elevation map with contours every metre for the KNOLL site.**

The hydrocarbon plume does not follow the water level contours, but instead has a NW-SE trend around the flare pit (Figure 5.25). Redox potential was not measured on this site so dissolved oxygen (DO) is used as a surrogate. When organic contaminants are degraded the first electron acceptor to be reduced is oxygen, so lowered DO concentrations can be a sign of organic contaminants. Other factors such as temperature and nitrate contamination can also affect dissolved oxygen levels, so some variation is natural. A background dissolved oxygen concentration greater than 10 mg/L was expected based on measurements made in a groundwater monitoring well (Matrix Solutions Inc., 2006). Though DO concentrations generally increase with distance from the hydrocarbons, the pattern is not entirely consistent.

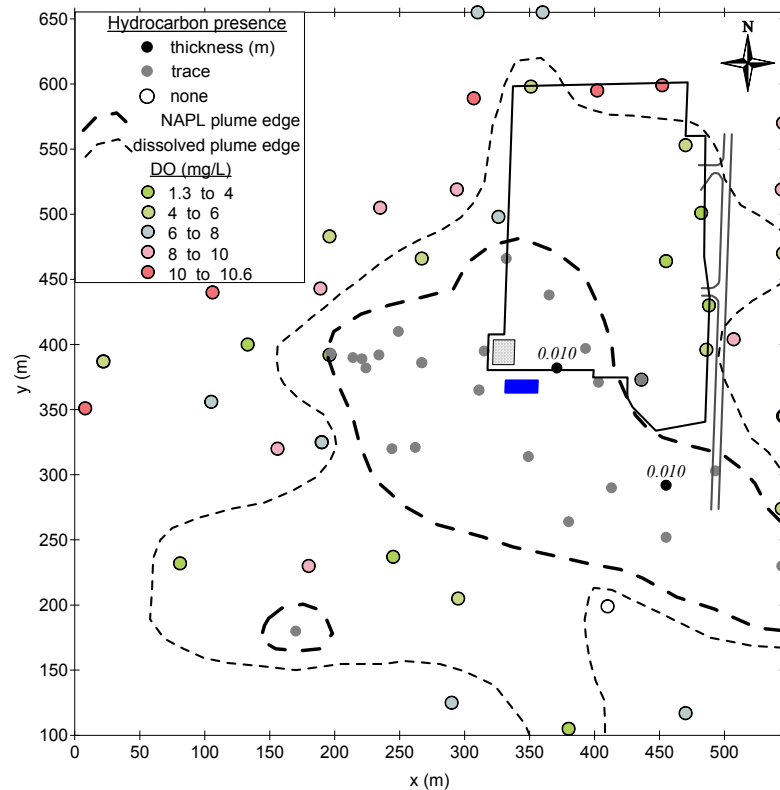


**Figure 5.25 November 2006 hydrocarbon distribution with dissolved oxygen (DO) concentrations measured in wells at the KNOLL site. A thick dashed line is drawn around the edge of the free phase plume and a thin dashed line delineates the dissolved phase plume.**

As mentioned before, the condensate is light and the chromatograph of a sample from the well nearest to the flare pit shows hydrocarbons from the C6 to C16 range (Figure 5.26). A hump characteristic of degradation is visible on the chromatograph even though several compound peaks still show up distinctly.

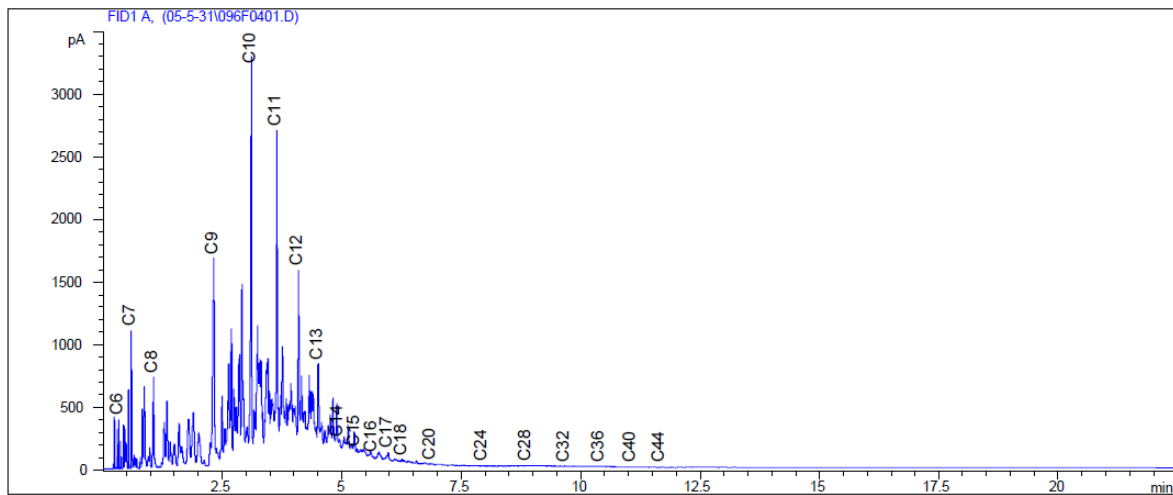


Figure 5.26 Chromatograph of hydrocarbons found at the KNOLL site. (Matrix Solutions Inc., 2006)

5.3.2 GEOPHYSICAL DATA

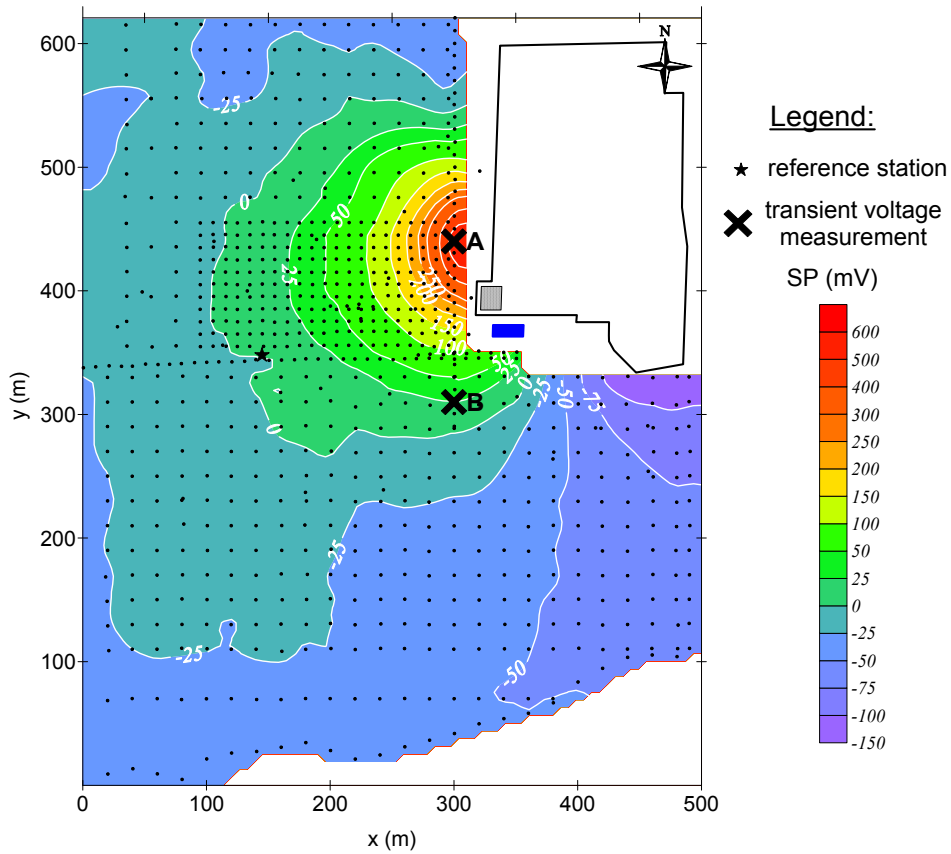
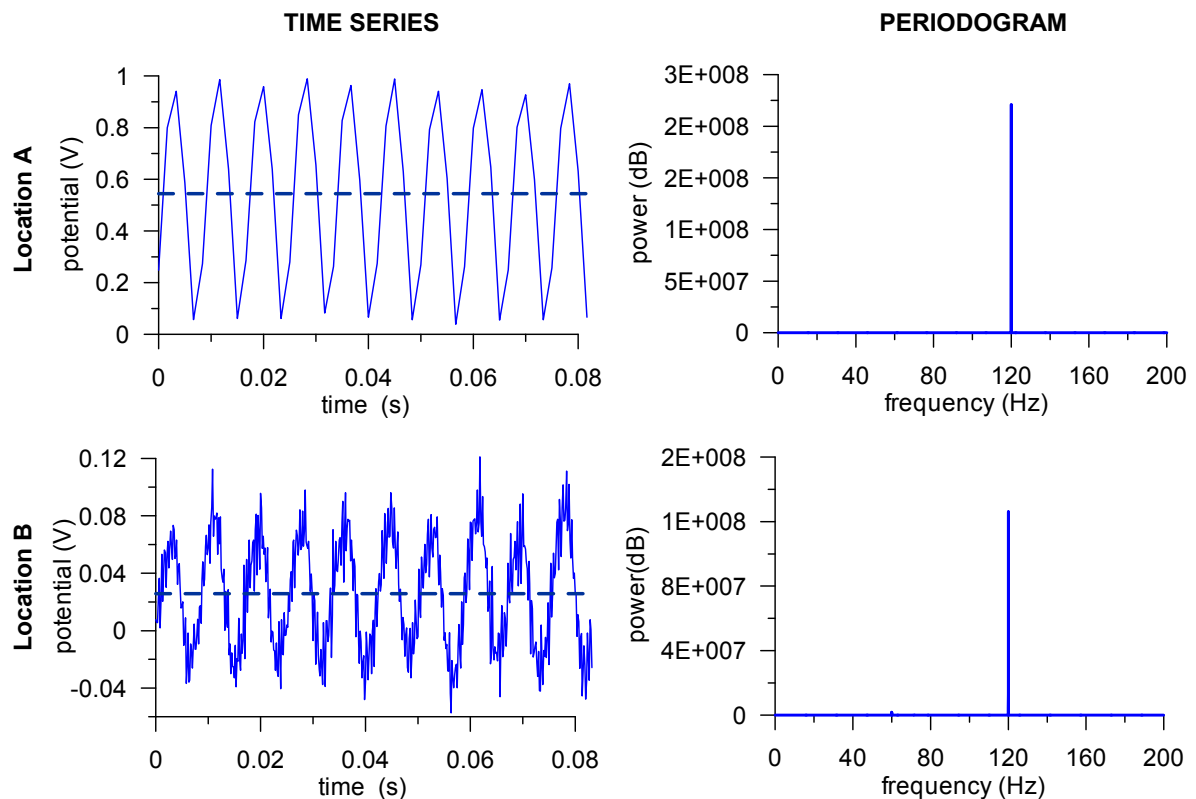


Figure 5.27 Spontaneous potential measurements at the KNOLL site. Small black dots are measurement locations.

Spontaneous potential data were measured on a 20 m grid throughout most of the area with a detailed area on a 10 m grid and some more widely spaced measurements around the edges. The gridded SP map show a 560 mV positive anomaly on the eastern edge of the survey, to the north of the flare pit (Figure 5.27). The data are very smooth so the contour map produced has few irregularities. The transient voltage measurements made in two locations have DC offsets equal to the SP measured at those locations with the multimeter (Figure 5.28). The dominant frequency is 120 Hz, or twice the power frequency in North America, and this signal could be obtained from a rectified voltage source.



**Figure 5.28** Transient voltage measurements and spectral analyses for locations A (TOP) and B (BOTTOM). They were acquired at frequencies of 600 Hz for A and 6000 Hz for B. LEFT: Time series data showing a sinusoidal signal. The dashed lines are drawn at the average potential, which is equal to the DC values measured in the field. RIGHT: Periodograms to show the dominant signal frequency, 120 Hz.

Twelve resistivity lines (R01-R12) were surveyed. All lines were oriented N-S apart from R12, which was E-W (Figure 5.29). The lines are 213 m long, with the exception of R09

which is 429 m long. Lines R01 to R08 will be referred to as the lines in the south and lines R09 to R12 are referred to as the resistivity lines in the north. Resistivity surveys were made using a 3 m electrode spacing so that the region with the highest resolution is at the water table, between 3 and 10 m depth. A dipole-dipole configuration was used for the survey as it offers a good coverage on the ends of the lines and it is sensitive to horizontal changes in resistivity, which can be helpful for imaging vertical structures. As well, it is simple to do a reciprocal dipole-dipole survey and this was done to allow better data quality control. Reciprocal measurements are made by switching the current injecting and potential reading electrode pairs and should theoretically produce identical results. For R12 we did not have the time needed to make reciprocal measurements.

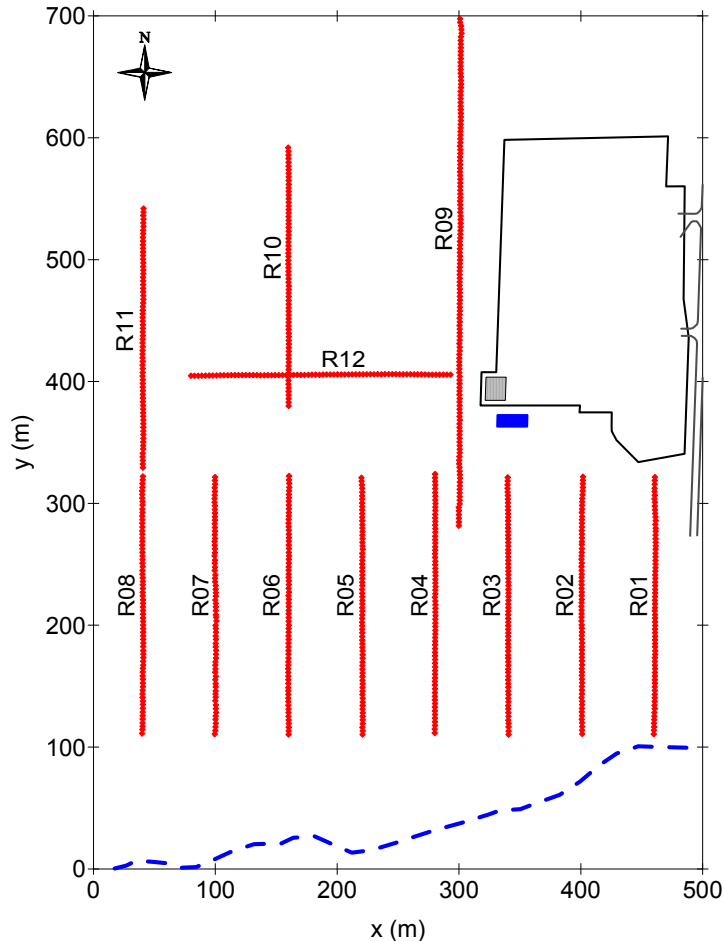


**Figure 5.29** Location of resistivity lines surveyed at the KNOLL site. Small red diamonds are electrode locations.

Processing and inversion statistics are found in Table 5.4. The data from the last four lines are of lower quality, as measured by the percentage of data rejected. Data from R09 are not used because many measurement points were rejected and the remaining data do not form a coherent image on inversion.

**Table 5.4 Statistics of electrical resistivity surveys at KNOLL site. Abbreviations:  $\rho_a$ —apparent resistivity, Q—quality factor: standard deviation between measurements.**

<b>Line</b>	<b>total # data points</b>	<b># points with <math>\rho_a &gt; 0</math> and Q &lt; 1%</b>	<b>total # reciprocals</b>	<b># points with reciprocals &lt; 10%</b>	<b>% rms error in inversion</b>
R01	2142	2132 (99.5%)	1660	1613 (97.2%)	2.0
R02	2142	1909 (89.1%)	1399	1393 (99.6%)	1.3
R03	2142	2134 (99.5%)	1667	1610 (96.6%)	2.3
R04	2142	2135 (99.5%)	1665	1597 (95.9%)	2.1
R05	2142	2134 (99.5%)	1663	1604 (96.5%)	2.1
R06	2142	2134 (99.6%)	1662	1583 (95.2%)	2.2
R07	2142	2133 (99.6%)	1659	1620 (97.6%)	2.3
R08	2142	2127 (99.0%)	1659	1591 (95.9%)	1.9
R09	4995	4846 (97.0%)	3161	1864 (59.0%)	8.3
R10	2142	2132 (99.2%)	1662	1363 (82.0%)	1.9
R11	2142	2126 (98.8%)	1654	1308 (79.1%)	2.4
R12	2142	2130 (99.0%)	—	—	2.7

Data from the first eight lines (R01-R08) are presented together as they are parallel with a 60 m spacing in the E-W direction (Figure 5.30). The two N-S lines in the north (R10 & R11) are shown with the continuation of the data in the south (Figure 5.31). The last line (R12) crosses R10 so they are presented together to allow comparison of their intersection (Figure 5.32). The range in resistivities, 12-84  $\Omega\text{m}$ , is small with the lowest values around

y=260-300 m on lines R01-R05 from the ground surface to depths of ~945 m. The highest resistivities are found in the south below depths of ~940 m on line R03.

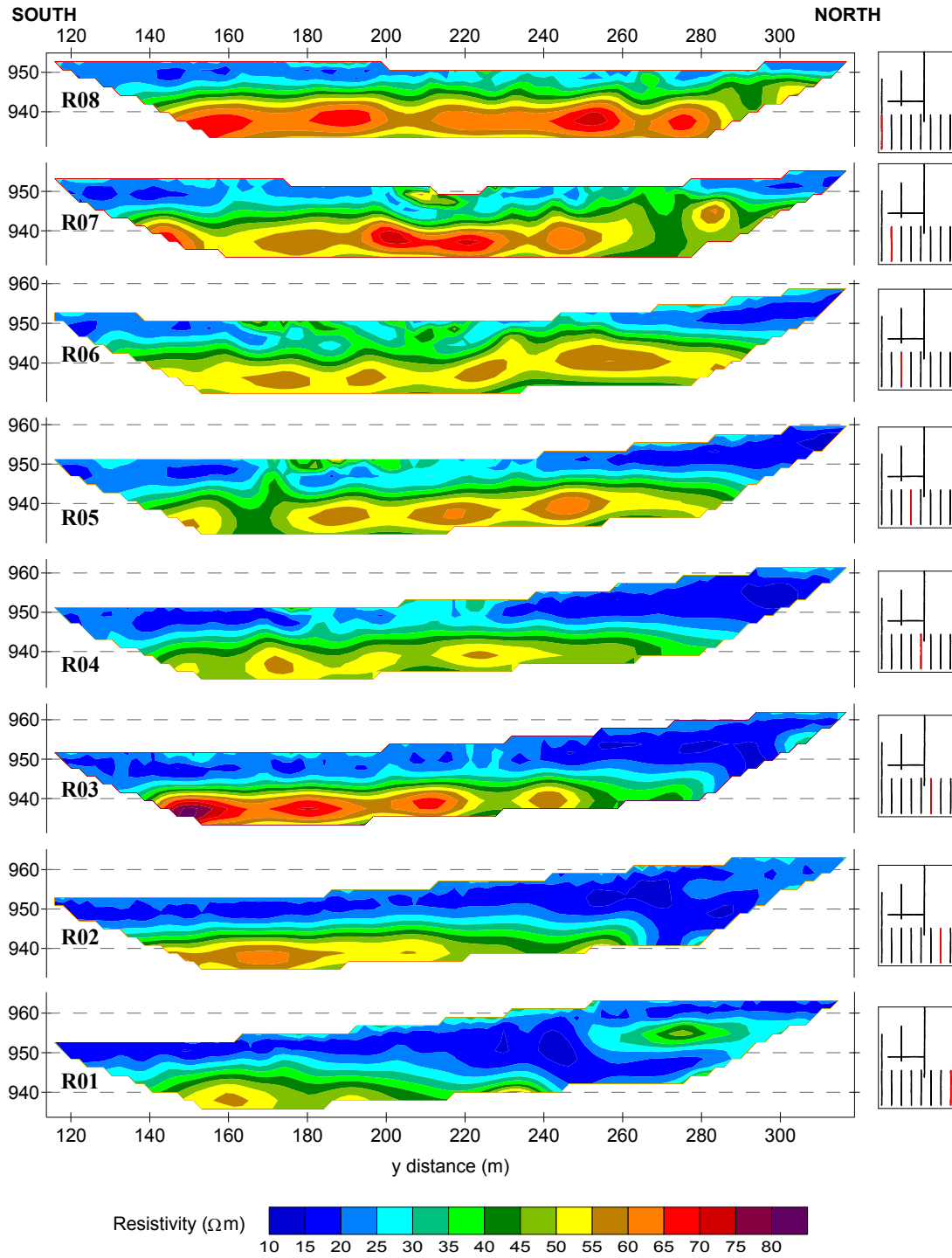
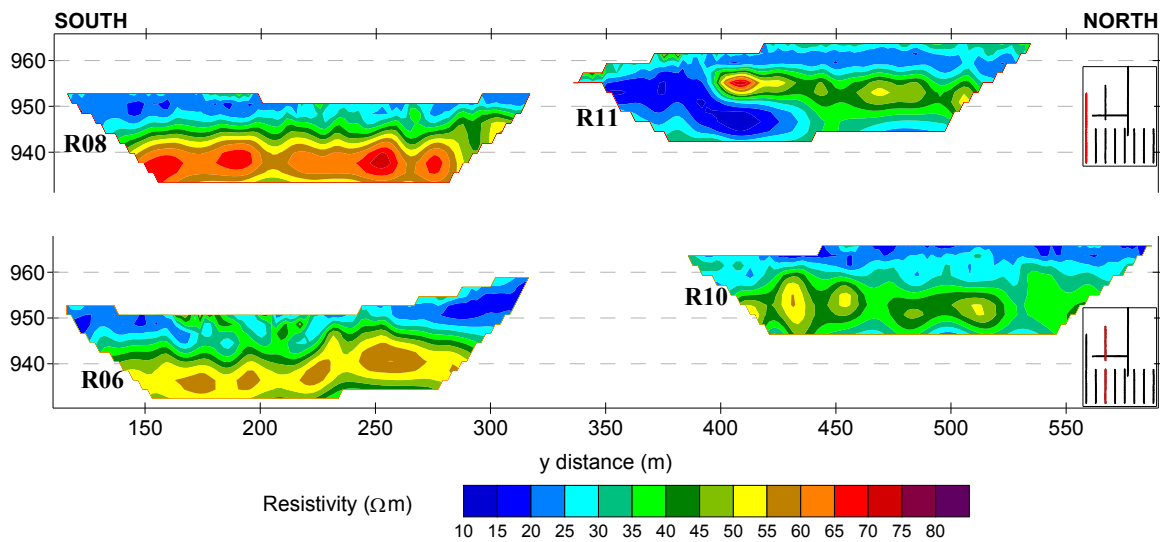
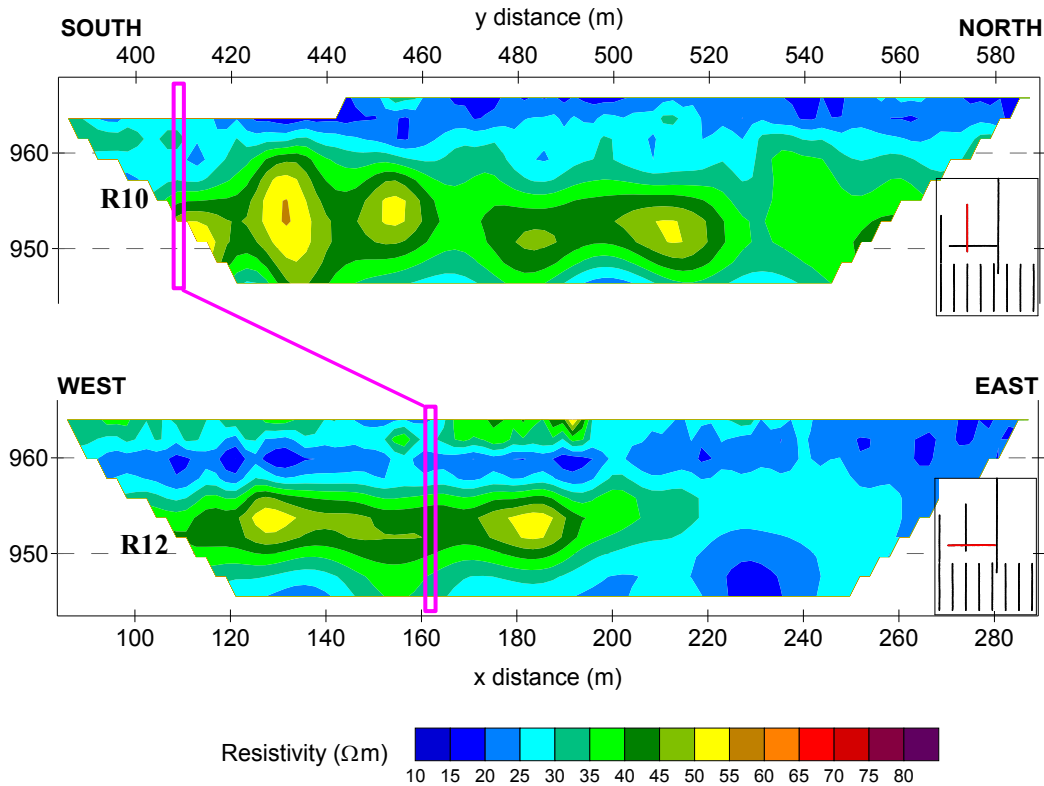


Figure 5.30 Electrical resistivity inversion results for lines R01-R08 at the KNOLL site. The warm and green coloured shapes form a continuous body between the profiles with the top at ~945 m. This is overlain by blue coloured material which

thickens towards the east (decreasing R numbers) as the ground surface elevation increases. The small location maps on the right highlight the line corresponding to the presented data.



**Figure 5.31** Electrical resistivity inversion results for lines R06, R08, R10 and R11 at the KNOLL site. Both R10 and R11 have green coloured bodies with a top ~957 m. The inversion profiles are not deep enough to map bodies from the south lines to the north ones but the dark blue wedge at  $y = 400$  to  $425$  m on R11 below a warm coloured zone indicates the green and warm coloured bodies in the north are likely distinct from those in the south. The small location maps on the right highlight the line corresponding to the presented data.



**Figure 5.32** Electrical resistivity inversion results for line R12 and the line it intersects, R10. The pink rectangles are drawn at the intersection. On both lines there is a green coloured body with a top at ~958 m. The small location maps on the right highlight the line corresponding to the presented data.

### 5.3.3 CORRECTIONS TO SPONTANEOUS POTENTIAL DATA

Buried pipelines are typically cathodically protected, so we thought we might see a signature from the many pipelines on site. We did not see such a signal but chose to confirm this by doing a detailed survey over and beside a pipeline (Figure 5.33). In a three metre square we made measurements every 30 cm and in this case the measurements reported are those of a single hole, rather than the average of three. If the pipeline was an SP source, potentials should increase or decrease perpendicular to it. This is not the case and instead the contours have a N-S trend apart from two bull's eyes at (231.8, 459.4) and (232.1, 457.6). Pipeline signatures reported by Naudet et al. (2004) were sharp negative excursions of 150-300 mV in SP profiles.

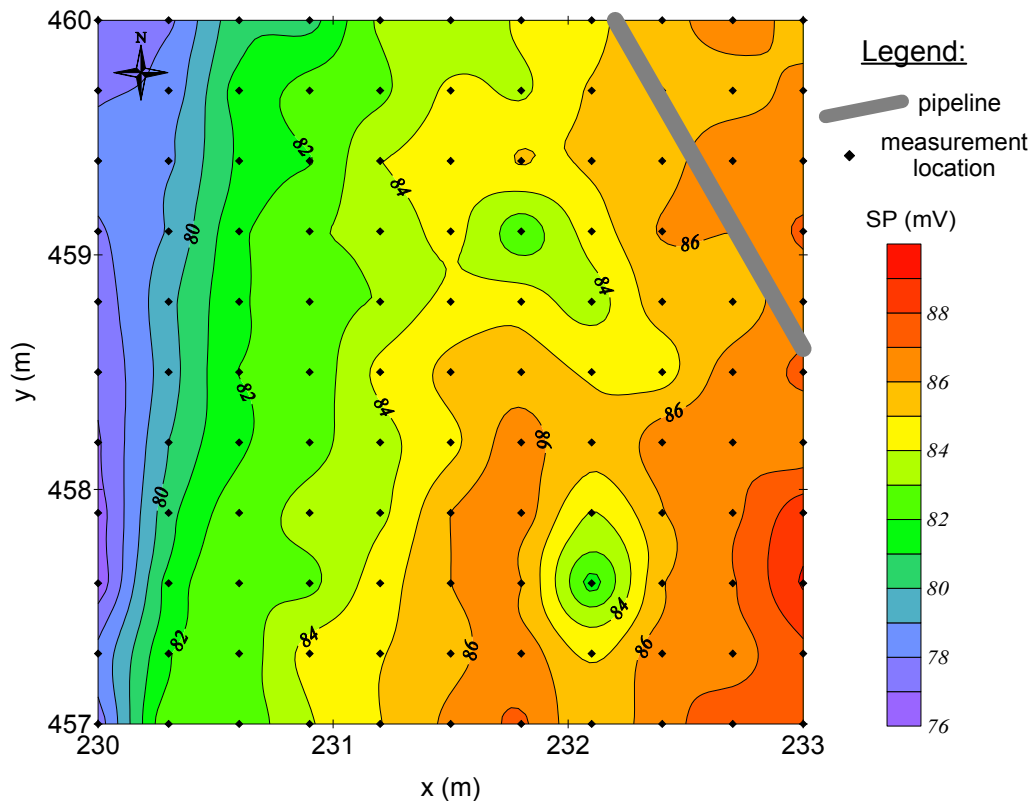


**Figure 5.33 Detailed SP survey over and next to a pipeline. If anthropogenic noise from the pipeline was contributing to the measured spontaneous potential, contours would have a NW-SE trend parallel to the pipeline. Instead the contours are N-S, mapping a more regional trend.**

Although we could not see a signature from the pipelines, we learned that part of the pipeline protection system was an anode bed along the western fence line of the plant. This is the source of the large positive anomaly we measured and is presumably the cause of the large amplitude 120 Hz sinusoid seen with the high frequency measurements. The anode bed is fed 7.25 A of current at 20.5 V but the details of its geometry are not known. Typically anode beds are a series of vertical zinc rods placed at 30 to 90 m depths that are positively charged so that they will corrode preferentially over the steel pipelines (pers. comm., Shaw, 2008). Along the road in the east at (500, 330) there are cathodic cable ties. These are places where there are wires connected to the pipeline that reach the surface and that are used to test the voltages on the pipeline. They show up as negative anomalies on the SP map.

The signals from the pipeline protection system are considered as noise on this survey. They were therefore modelled and subtracted from the measured data. The location or size of the anode bed was not known precisely so it was modelled using two methods which provided similar results.

The first method is a charge occurrence probability tomogram developed by Patella (1997a; b). His algorithm was implemented and run in MATLAB and since it required a square data grid, SP contours were extrapolated into the north-east corner of the map where the plant is. The tomogram incorporates topography and locates areas where if charges occurred, they would be most likely to produce the measured signal. The charges can be either positive or negative. On the KNOLL site the highest charge probability occurrence (0.929) is at (310, 440, 935) and the lowest (-0.165) is at (470, 340, 930) (not shown) (Figure 5.34).

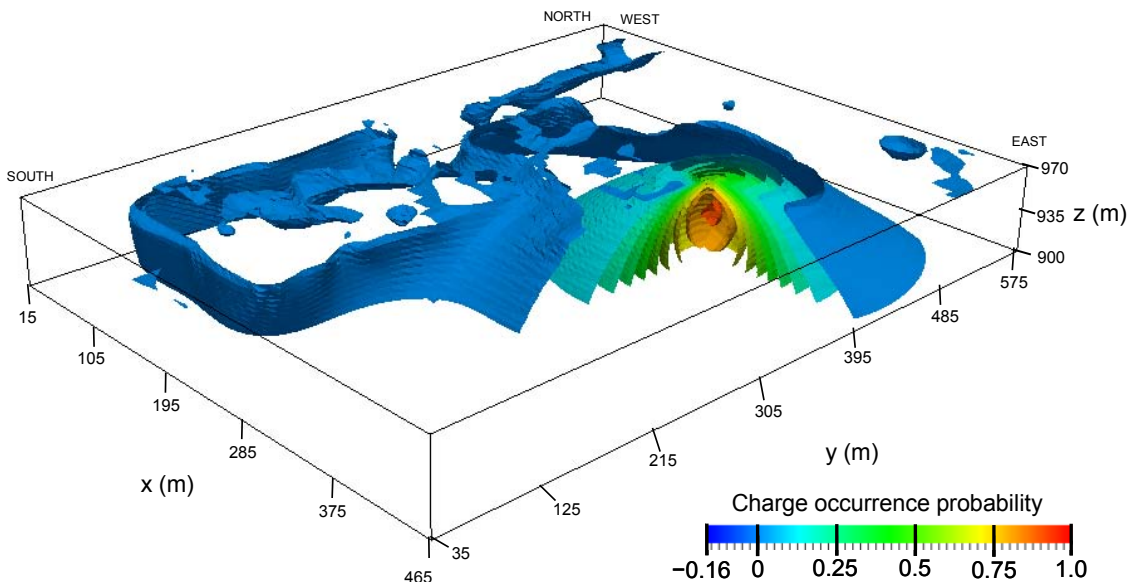


**Figure 5.34** Isosurface contours of charge occurrence probability tomogram at the KNOLL site. The south-east corner has been cut out to show the maximum and (310, 440, 935), which has removed the contours of the minimum just east of the map at (470,340,930).

The second method is a three dimensional source inversion. The code was developed by Minsley (2007) and he kindly ran the inversion presented in Figure 5.35. The inversion

produces sources of specified currents at precise locations underground. Though the inversion does not incorporate topography, it was not necessary to extrapolate measurements into the north-east corner and it includes resistivity, which was set to 20  $\Omega\text{m}$ . The N-S slice presented is drawn through the maximum which is at (294, 428, 937). On this slice the dipole visible at the north end seems to be an artefact, perhaps due to edge effects. The E-W slice at 330 m shows negative sources at depths of 17.5 m which correspond to the cathodic cable ties. The sum of source currents greater than 10 mA is 3.5 A which compares well with the 7.25 A of current fed to the anode bed since the inversion produces smooth results that underestimate actual values.

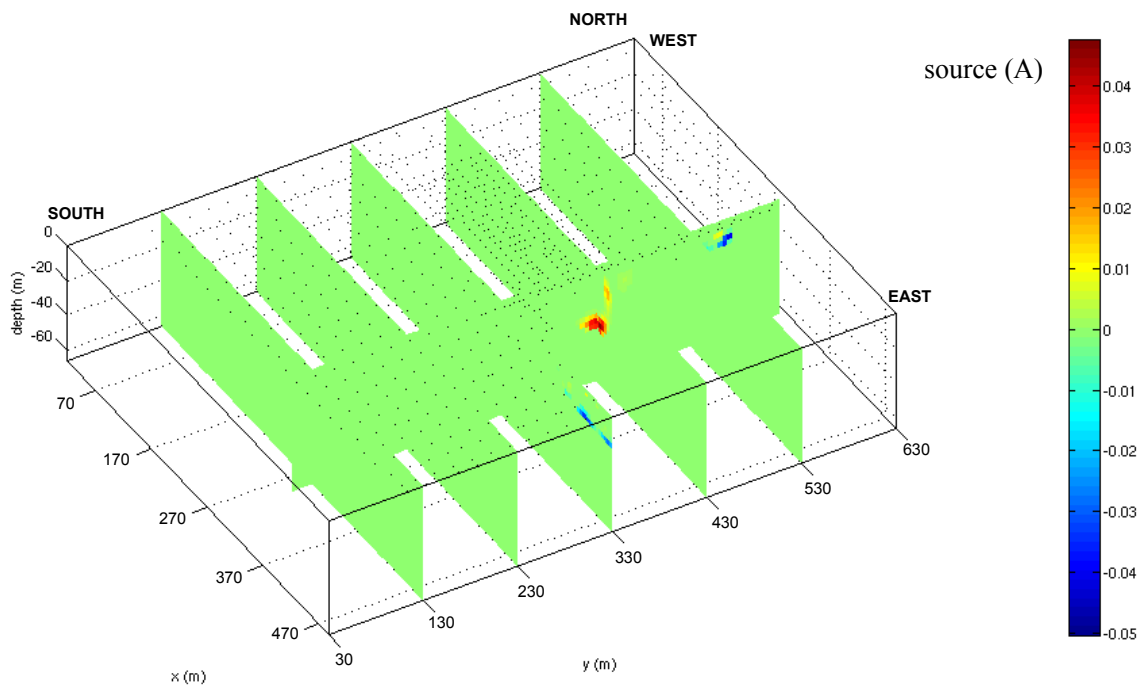


**Figure 5.35 Slices through the source inversion results for the KNOLL site. The N-S slice is drawn through the maximum. The small black dots on the surface of the cube are locations of data points used in inversion.**

These source location estimates were used to simulate an anode bed by inserting sources at those locations in a model for the site. The forward calculations were done using the finite element code described in chapter 3. The exact locations and strengths of the sources (Figure 5.36) were adjusted to produce the best possible fit between measured and modelled potentials near the anode bed (Figure 5.37). The positive sources of the

anode bed sum to 7.25 A and the negative sources at the cathodic cable ties have a total intensity of  $-0.825$  A. The SP near the anode bed is likely dominated by this source, so the profile of the 75 m nearest to the bed were fit while keeping the sources close to the locations of sources found with the three-dimensional source inversion, which is consistent with the tomogram probability distribution.

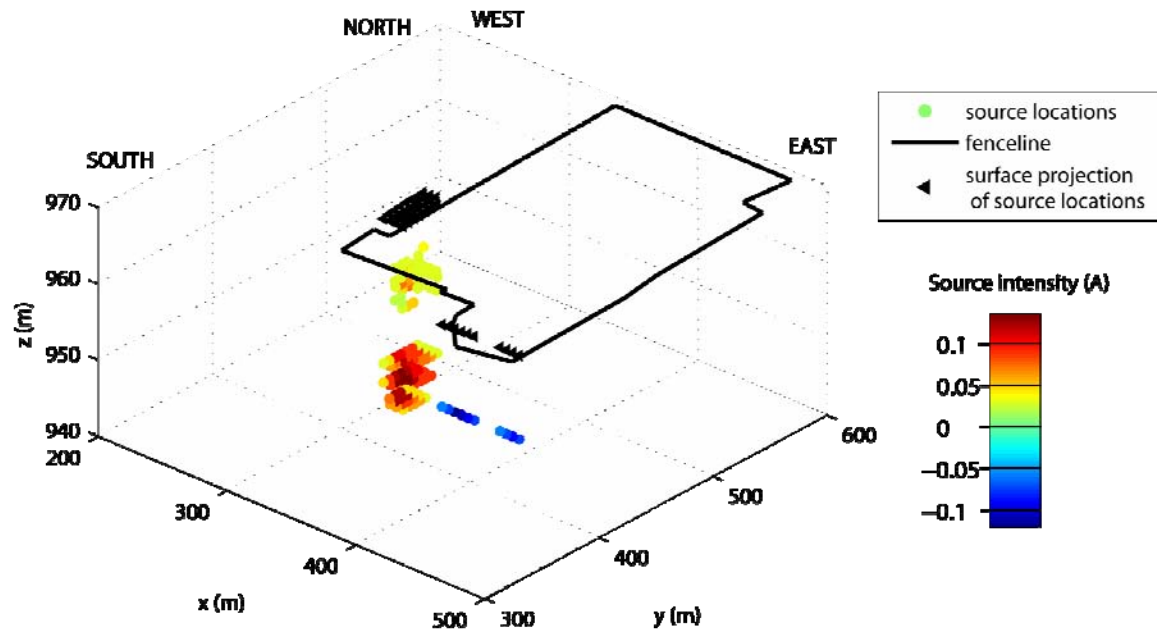
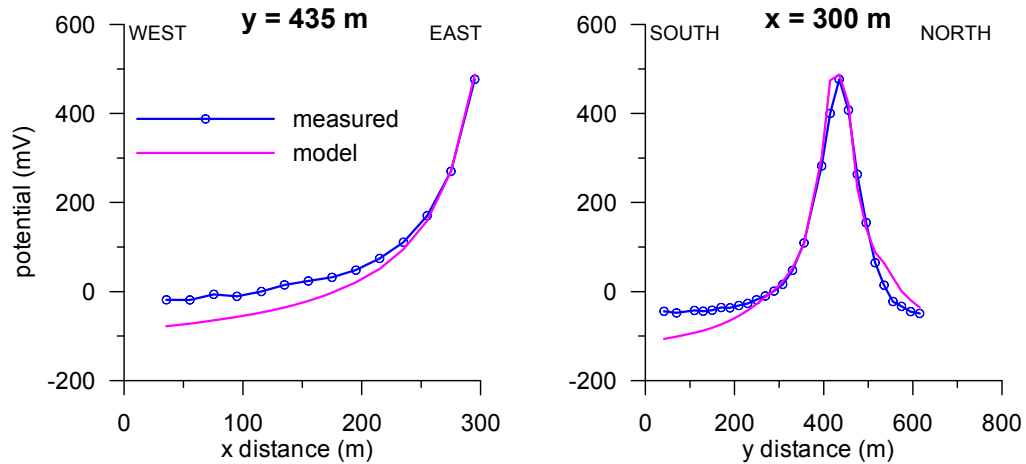
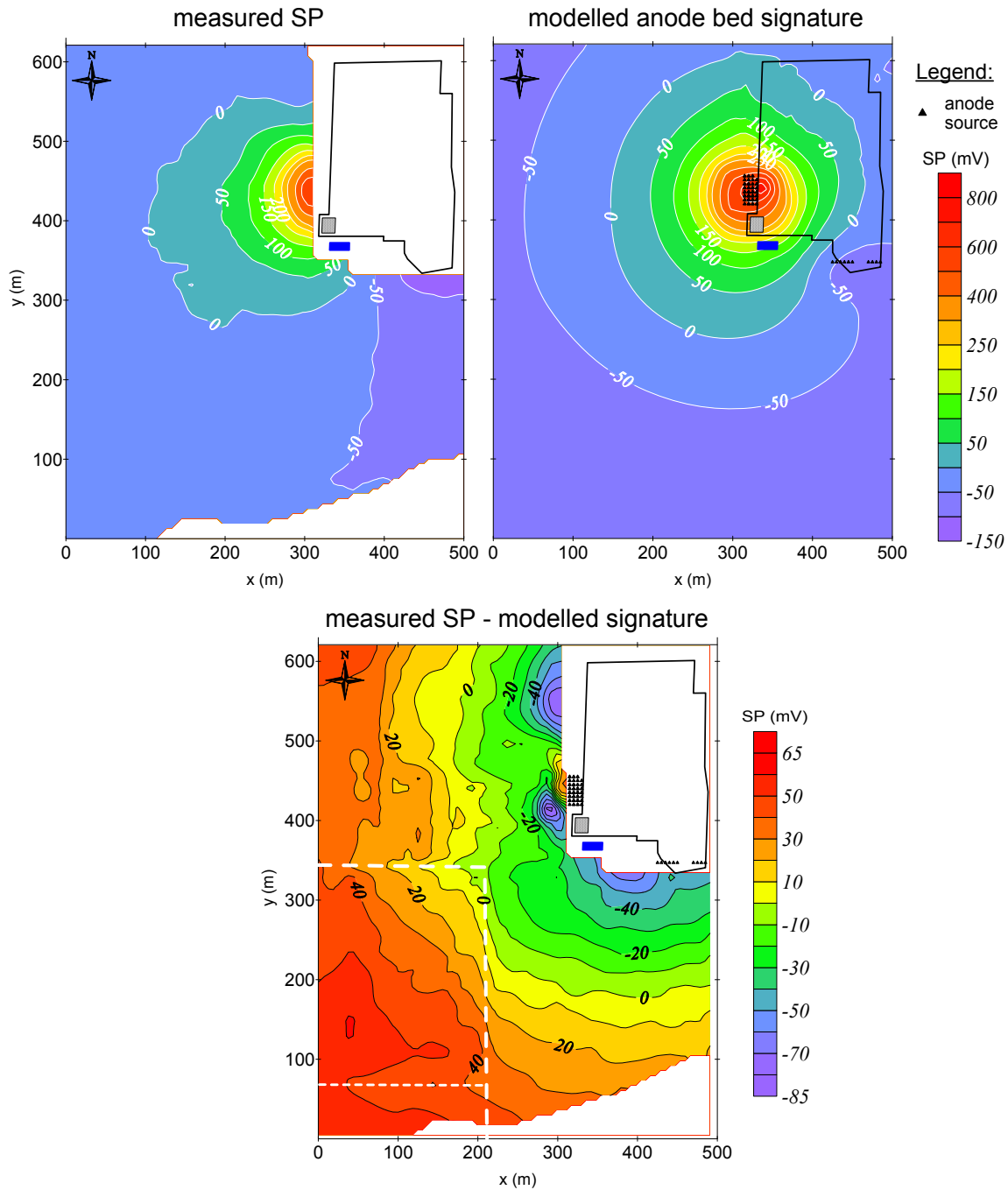


Figure 5.36 Location and intensity of the sources used to model the anode bed. The sources are 10–23 m below ground and their surface projections have been included to help locate them relative to the plant fence line.



**Figure 5.37 Profiles to demonstrate fit between anode model potential signal and measured SP at the KNOLL site. There is a close fit between measured and modelled SP for the 75 m on either side of the anomaly. SP measured further from the anomaly could have contributions from sources other than the anode bed so a close fit with the model is not necessary.**

The residual, which is the measured minus the modelled SP, can be considered as the signal that one might see without the anode bed (Figure 5.38). The correction is not perfect as there is a sharp negative anomaly to the south of the bed and the residual map contours are roughly centered on the anode bed location. No data are available above or to the east of the anode bed which makes it difficult to produce an accurate model.



**Figure 5.38** Corrections to the spontaneous potential data for the anode bed at the KNOLL site. Locations of sources for corrections are represented by black triangles. **TOP LEFT:** SP data measured in the field. **TOP RIGHT:** SP signature of anode bed created with finite element code. **BOTTOM:** Residual SP (measured – modelled SP).

The dashed lines emphasize inflections in the contour lines that demark the SW corner where data were gathered under wetter field conditions. The dotted line at  $y=75$  m delimits data gathered under colder field conditions, visible by an excursion in the 50 m contour.

After the correction, a block appears in the southwest of the residual map where contour lines have an inflection at  $x=225$  m and  $y=340$  m. This demarks data gathered on different days. The southeast portion was surveyed in sunny weather and the southwest was surveyed four days later, in wet conditions after lots of rain. Two lines were added at the end of the survey in the very south and were measured 22 days later in wet conditions following snow. These data are visible by the excursion to the west of the 50 mV contour. These details are masked on the measured SP map because of the size of the anode bed anomaly.

#### 5.3.4 *KNOLL SITE MODEL*

The water table at the KNOLL site is 4-7 m below ground and its location is noted on the resistivity inversion profiles (Figure 5.39, Figure 5.40). The vadose zone is expected to be more resistive because of lower water saturation. Effectively, on many inversion profiles the top couple of metres are 5 to 10  $\Omega\text{m}$  more resistive; between 160-200 m on R03, 170-250 m on R01 and along most of R11.

Well logs were available for monitoring wells drilled on site and their profiles are drawn over the resistivity sections when they were located nearby (Figure 5.39, Figure 5.40). In order of increasing resistivity, the units mapped in the logs were clay, clay till, mudstone, siltstone, shale and sandstone. The inversion process smoothes the data so that all contacts appear gradational and thin layers cannot be discerned. As well, resistivity measurements can contain off-line effects, where a body of contrasting resistivity located beside the survey line is projected onto the profile.

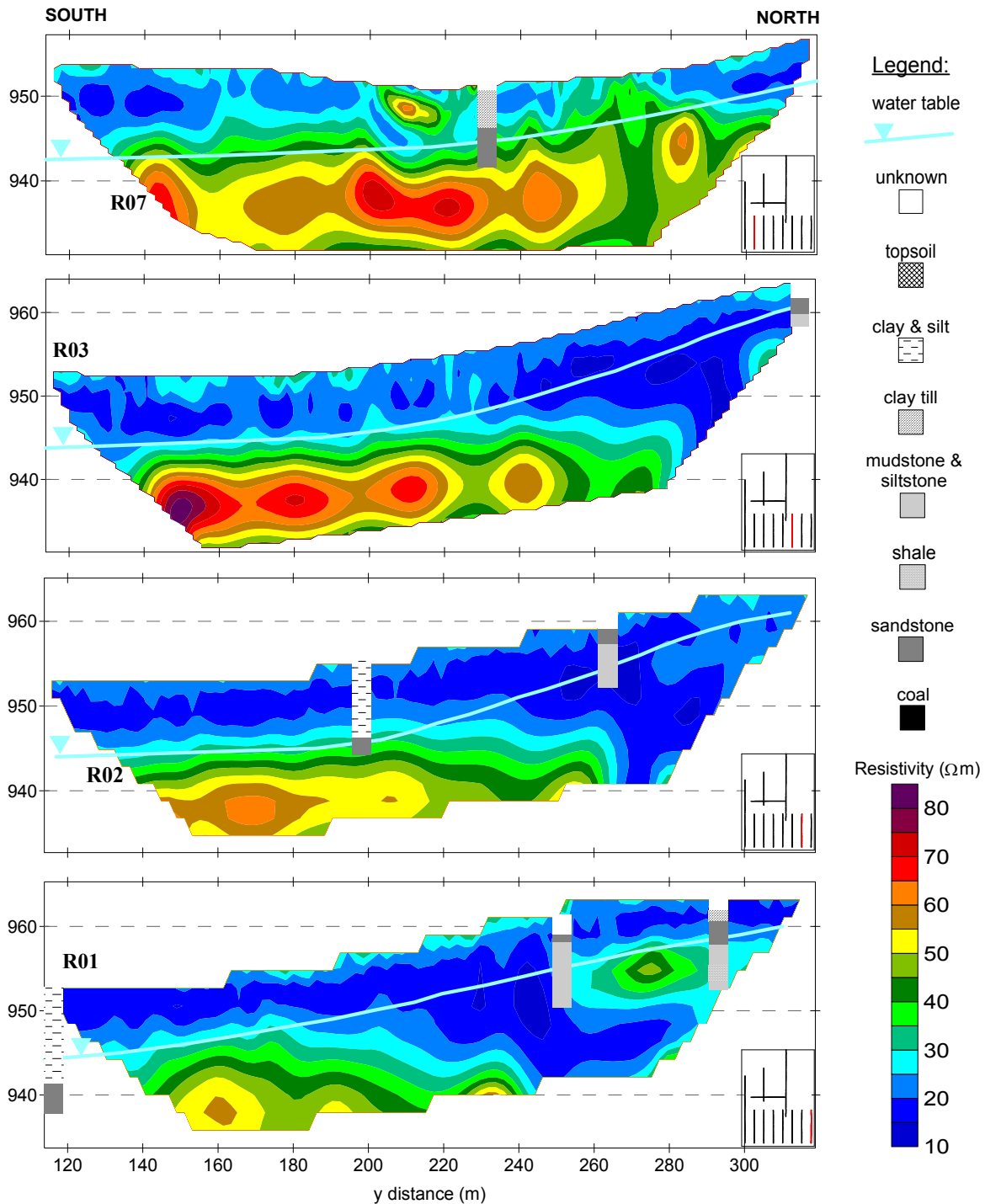
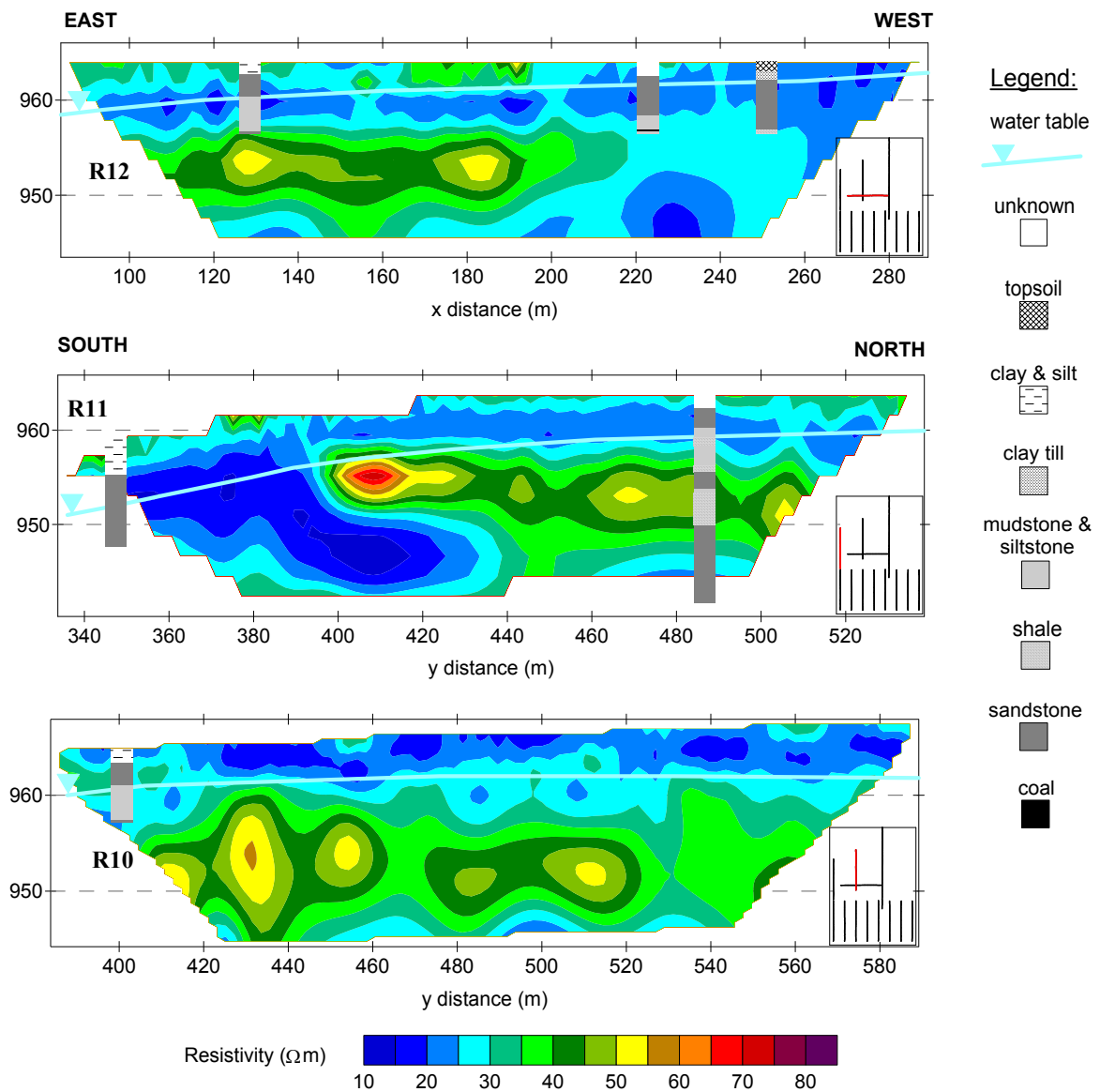


Figure 5.39 Electrical resistivity inversion images for four lines in the south with water table and lithologies from logs of nearby wells. The small location maps on the right highlight the line corresponding to the presented data.



**Figure 5.40** Electrical resistivity inversion images for three lines in the north with water table and lithologies from logs of nearby wells. The small location maps on the right highlight the line corresponding to the presented data.

The correspondence between different lithologies and resistivity values is not always consistent, particularly for the sections with many lithologies. The green and warm colours ( $>35 \Omega\text{m}$ ) generally correspond to sandstone, but it is not possible to distinguish clay, clay till, mudstone, siltstone or shale by the resistivity alone. There is no boundary visible between unconsolidated and consolidated sediment, as might be expected if it corresponded to a large change in porosity.

When all the profiles are shown in three dimensional space (Figure 5.41) a high resistivity body with a top at ~943 m in the east and that rises slightly to ~946 m in the west can be seen in the south. The bottom of this body was not imaged and must be below 930 m. The body is persistent between profiles so it is likely one continuous body that can be interpreted as a sandstone channel. The two lines in the north also show a high resistivity body, but this one is at a higher elevation, bounded between 948 and 957 m. This is likely also a sandstone channel, and based on profile R11, it seems to be distinct from the first body. The E-W profile on R12 shows the eastern limit of the second high resistivity body at  $x = 220$  m.

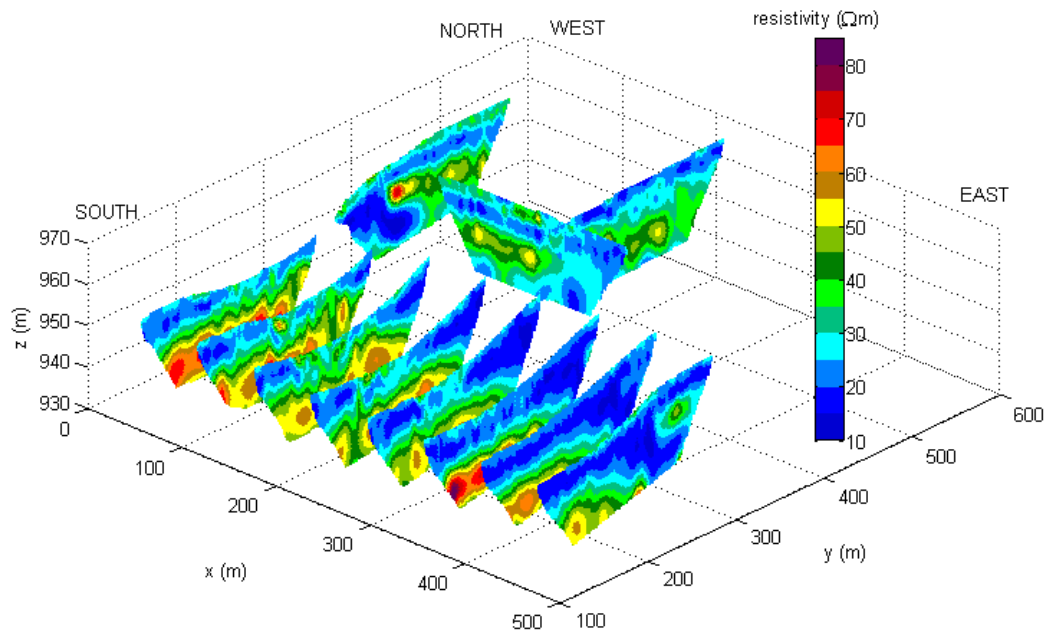


**Figure 5.41** Three dimensional drawing of all the electrical resistivity inversions at the KNOLL site.

Many of the profiles also have small high resistivity spots within 5-10 m of the surface. According to the well logs these are sandstone, but they seem scattered and are likely poorly connected. If these units are sandstone, they could represent rock that has been gouged or rafted during glaciation. Another possibility is that these spots are sand lenses misidentified during drilling.

The lithological logs show that there is usually clay or clay till above the sandstone, and any mudstone, siltstone or shale is generally found beneath a layer of sandstone. This suggests that where there are scattered high resistivity spots near the surface, such as at  $y = 180$  m on R04 and R06 and at  $y = 390$  m on R10 and R11, the blues below are likely mudstone, siltstone or shale. The blues above any sandstone, such as at  $y = 130$  m on R01 and R08, are likely clay or clay till.

In summary, there seems to be both thick laterally extensive sandstone bodies that are interpreted as bedrock sand channels and small patches of sandstone or sand lenses near the surface. It is not possible to differentiate clay, clay till, mudstone, siltstone or shale, other than by making assumptions about their position relative to the sandstone.

The resistivity survey line R09 passed very near the anode bed and this is likely the reason why the data were of poor quality. The spontaneous potential values in this area are as high as the potentials induced by current injection, so it was difficult to distinguish between the two, even though a correction for SP was made. Since the SP are time invariant, the number of data points rejected for the forward measurements on R09 was only 3%, but it was not possible to make accurate reciprocal measurements. When the similarity of reciprocal measurements was used as a processing criterion it was necessary to reject 41% of the data and what remained was insufficient for a proper inversion.

The spontaneous potential data have been corrected for the effect of the anode bed in the previous sub-section. It is also necessary to consider streaming potentials. A cross-plot of hydraulic head vs. SP corrected for the anode bed shows a significant Pearson correlation at the 95% level. However, the variance of a linear regression is only 0.34 so the changes in head account for less than half the variations in SP.

Since a more detailed subsurface model was developed for this site, the streaming potential signature was calculated using the finite element code described in chapter 3. A

site model was first constructed and adjusted in the MODFLOW software so that the calculated hydraulic head distribution resembled that measured in the field. The MODFLOW output was used as input for the hydraulic head values necessary for the finite element model. Streaming current coupling coefficients are necessary for the calculations and were measured on three samples from this site as described in chapter 4. The median values were used;  $15 \mu\text{A}/\text{m}^2$  for areas with clean groundwater and  $9 \mu\text{A}/\text{m}^2$  for areas where there was hydrocarbon contamination. At the surface, the calculated streaming potential signature has a 1.1 mV range (Figure 5.42), which is within the  $\pm 5$  mV error of field readings. It would not mask any signal due to redox gradients from the contaminant plume.

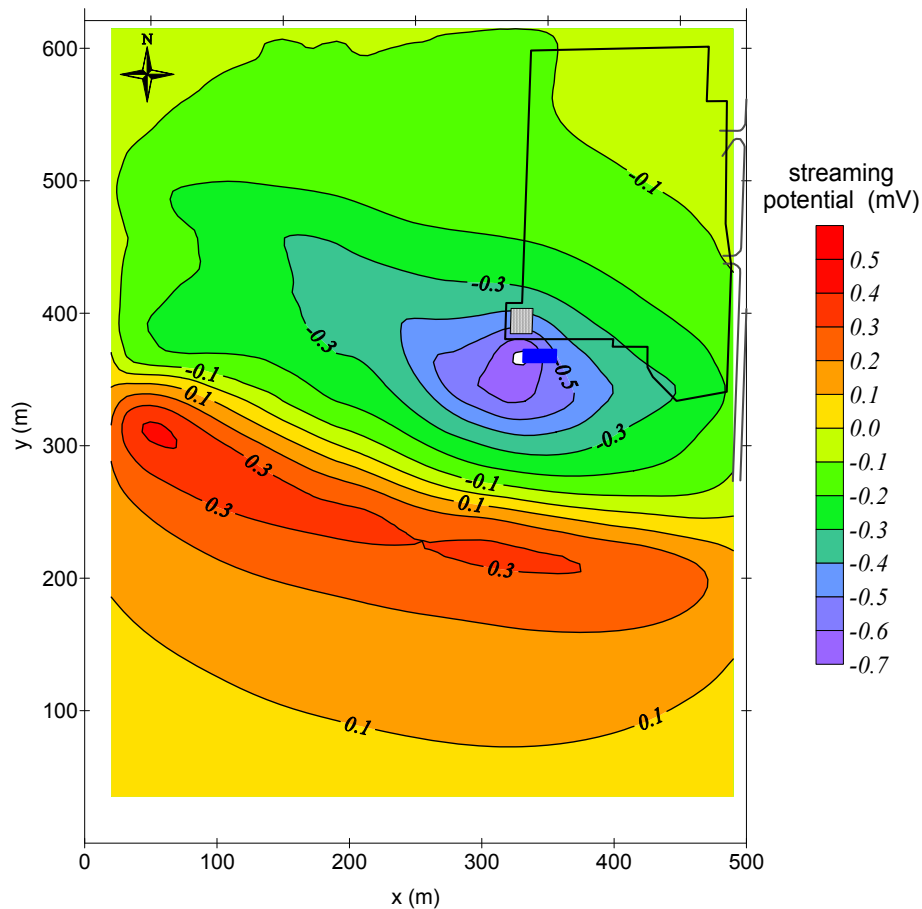


**Figure 5.42 Streaming potential signature at the KNOLL site, calculated with the finite element code.**

To investigate the relationship between SP and redox potential variations caused by the hydrocarbon plume degradation, the residual SP contours were drawn with the plume extent and dissolved oxygen concentrations (Figure 5.43).

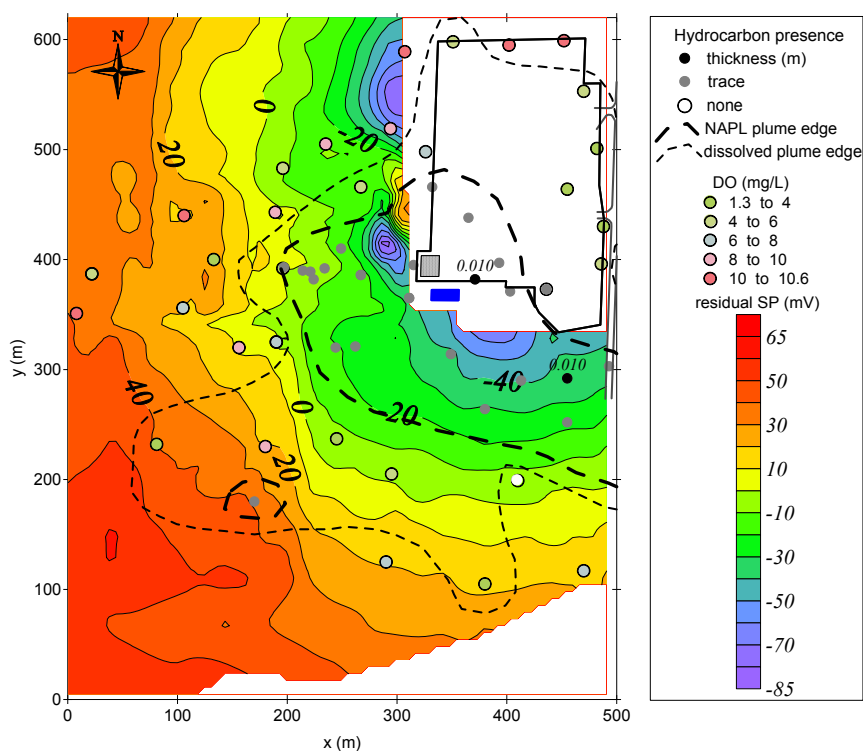


**Figure 5.43** Chemical data overlay on the residual SP map at the KNOLL site.

Unfortunately the anode bed and flare pit are located next to each other so uncertainty with corrections complicate the signal around the flare pit. However, there is no large negative anomaly close to the edge of the plume, as should be seen according to the redox SP model of Revil et al. (2010).

#### 5.4 Discussion

The aim of the two spontaneous potential surveys described was to investigate SP of electrochemical origin from degrading organic contaminant plumes in groundwater. Before electrochemical SP could be investigated it was necessary to account for SP from other sources. Thermoelectric sources are only significant in geothermal areas and were deemed unimportant. Streaming potential signals were calculated and were negligible on

both sites. Anthropogenic noise was the principle source of the SP measured at the KNOLL site. The source of noise, an anode bed, was modelled so that its contribution to the total signal could be removed.

Contaminated sites will almost always occur where there is infrastructure, as it is human activities that cause the contamination. Anthropogenic noise will almost always be a confounding factor so if SP is to be used as a method for delineating degrading contaminant plumes, we must be able to identify and model these sources. High frequency measurements of transient voltages and their spectral analysis can be helpful for identifying and locating noise sources (Figure 5.19, Figure 5.28).

Based on the literature examples presented in chapter 2, a negative SP anomaly with amplitudes of 50 mV or more over the plume or its margins was expected. Revil et al. (2010) propose that there might be something equivalent to an electronic conductor, in which case the anomalies would have magnitudes larger than 100 mV. Profiles from each site are drawn with redox information to show that the surveys did not produce the anticipated results (Figure 5.44, Figure 5.45).

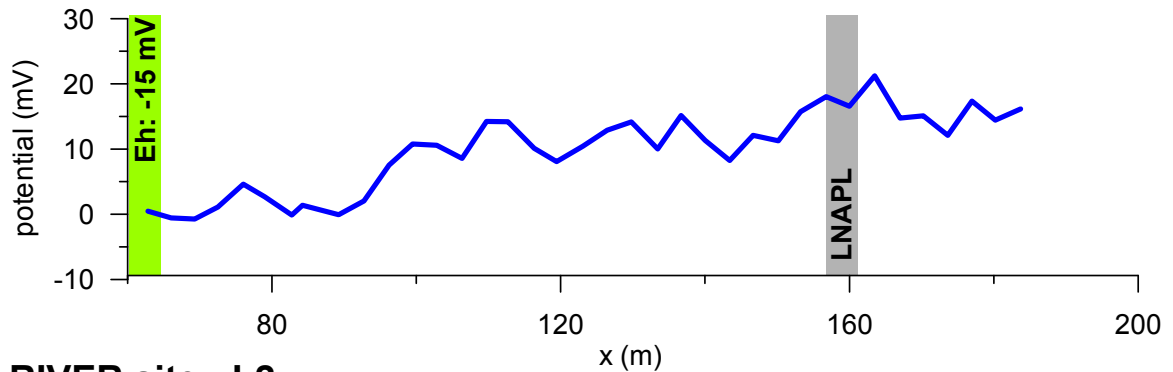
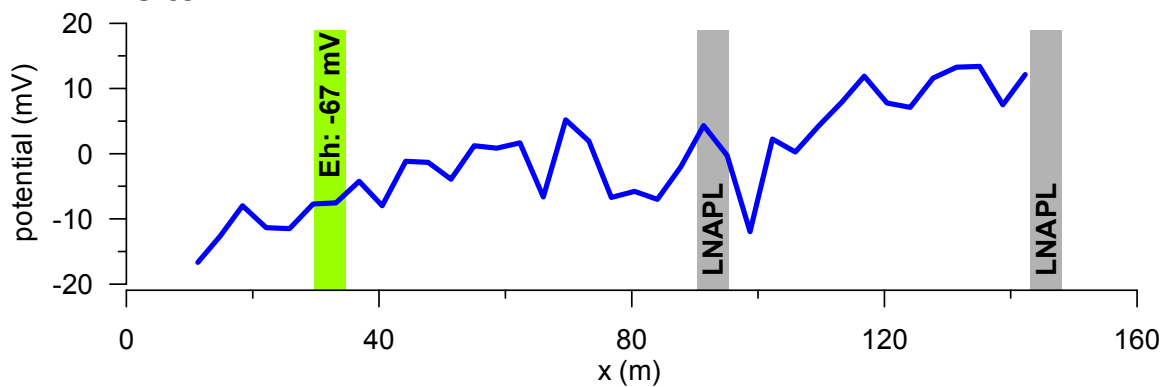
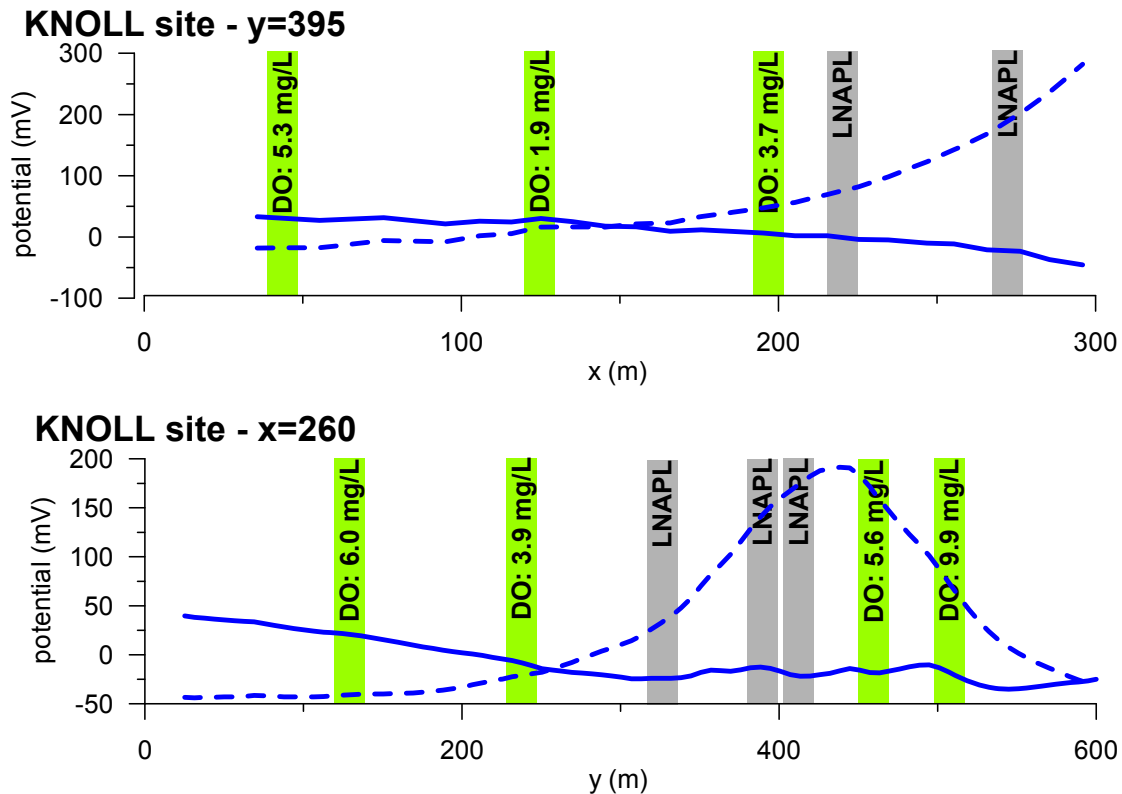
**RIVER site - L1****RIVER site - L2**

Figure 5.44 SP profiles at the RIVER site with information on the contaminants. The vertical rectangles are wells on or near the survey line. The wells drawn in grey had hydrocarbons above the water so redox parameters could not be measured. SP decreases slightly away from the plume. Abbreviations: LNAPL—light non-aqueous phase liquid.



**Figure 5.45** SP profiles at the KNOLL site with information on the contaminants. The vertical rectangles are wells on or near the survey line. The wells drawn in grey had hydrocarbons above the water so redox parameters could not be measured. Dashed line is measured SP and solid line is SP corrected for the effect of the anode bed. SP increases with distance from the pollutants but as a trend rather than a sharp anomaly. Abbreviations: LNAPL—light non-aqueous phase liquid, DO—dissolved oxygen.

On both sites the signal has a much smaller amplitude than expected. At the RIVER site SP decreases slightly away from the contaminants, contrary to examples found in the literature. The corrected signal at the KNOLL site does increase with distance from the pollution source, but the increase is a trend without any excursion that might indicate a plume edge.

The two hypotheses in sub-section 2.2.5 can be revisited in the light of findings at these two sites. The first hypothesis, which was based on galvanic voltages, is not applicable at these sites because all the measurements were made at the surface where redox conditions are relatively uniform. The modification of this hypothesis proposed by Naudet et al.

(2003) linked the difference in redox potential to spontaneous potential using  $C_H$  as a proportionality constant. As in sub-section 2.2.6, cross-plots can be drawn to compare spontaneous and redox potentials. In this case dissolved oxygen is used as a surrogate for Eh. Only three wells where SP measurements were made at the RIVER site did not have LNAPL and have dissolved oxygen measurements that can be used for comparison (Figure 5.46 LEFT). At the KNOLL site data from nineteen wells are available (Figure 5.46 RIGHT). Neither site has significant Pearson correlation at the 95% level, which indicates that this hypothesis is not consistent with the results obtained at these sites.

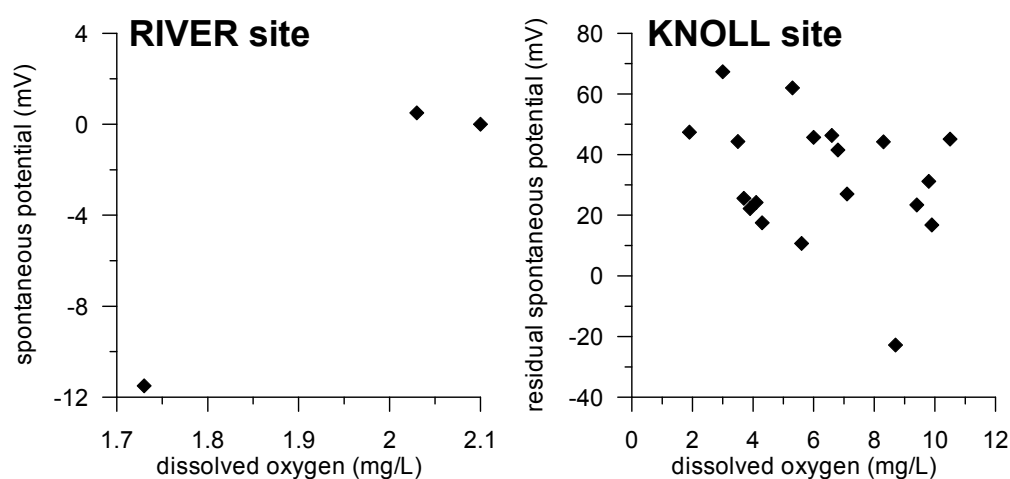


**Figure 5.46** Cross-plots of dissolved oxygen in groundwater measured in wells and SP measured next to the wells for both sites studied.

The second hypothesis necessitates an electronic conductor, perhaps microbial mats, to produce anomalies larger than 100 mV (Revil et al., 2009; Revil et al., 2010). Since these sites do not show such anomalies, this hypothesis implies that electronic conductor did not develop in a transition zone located at the capillary fringe. On the RIVER site it is conceivable that no microbial mats could set up a transition zone because the hydraulic system is so dynamic; the water levels, flow directions and plume location change throughout the year. The hydraulic regime is less variable at the KNOLL site yet no transition zone seems to have developed there either. This may be because the clays and silts present in the till and sandstone create a thick capillary fringe that is wider than can be bridged by bacteria with their pili. Alternatively, the plume may be deeper in the

groundwater so that the strongest redox gradients are below the water table and not accessible to bacteria in a transition zone restricted to the capillary fringe.

Neither hypothesis for SP of electrochemical origin over contaminants explains the measurements made at the RIVER and KNOLL sites. It is possible that there were no measurable SP anomalies because the current sources were only due to diffusion potentials. The magnitude of the SP signal due to diffusion potentials can be calculated using numerical modelling. Modelling can also be used to explore under what conditions the electronically conductive transition zone hypothesis would produce measurable anomalies at the surface. Both these modelling exercises are the subject of chapter 6 and contribute to further discussion on electrochemical SP over contaminants.

### **5.5 Summary**

Spontaneous potential surveys were done on two sites with well characterized degrading hydrocarbon plumes in the groundwater. At the RIVER site the total variation was only 39 mV. The SP signal produced a coherent map, where the potentials increased to the north-east. No correlation was found between the measured signal and electrokinetic or electrochemical sources.

The SP signal at the KNOLL site had a 560 mV positive anomaly generated by an anode bed. A residual SP map was produced by subtracting the modelled signature of the anode bed from the measured SP. No correlation was found between the residual SP and electrokinetic or electrochemical sources.

Neither survey presented an electrochemical SP anomaly similar to those reported over contaminant plumes in literature.

## **6 NUMERICAL MODELLING OF ELECTROCHEMICAL SP OVER CONTAMINANT PLUMES**

Interpreting field work is challenging because many potentially important parameters are uncontrolled, possibly variable and sometimes difficult to measure. Numerical modelling can be used to test the influence of different parameters, but it must be done within a theoretical model.

The field results presented in chapter 5 did not show the negative spontaneous potential anomaly we expected to see over degrading organic contaminant plumes. In this chapter the finite element programme presented in chapter 3 is used to make numerical models that explore the influence of different parameters, such as ground resistivity, placement of the source zone and location of the plume on the SP measured at the ground surface. The aim is twofold: to see if the field results of this research can be modelled and to understand what conditions are necessary to generate large SP anomalies at the surface.

The two theoretical models used are reviewed in section 6.1. There is insufficient geochemical data from the field sites described in chapter 5 for numerical modelling so an alternate data set is used and it is presented in section 6.2. Calculation results are shown in section 6.3 which is divided into several sub-sections, one for each scenario tested. The discussion in section 6.4 puts the results in context of the field work presented here and elsewhere. A chapter summary is made in section 6.5.

### **6.1 Theoretical models**

Two theoretical models will be used: the diffusion and Eh models. These were presented in detail in sub-section 2.3.3.3. The Eh model is a special case of the diffusion model.

#### *6.1.1 DIFFUSION MODEL*

In a porous medium electric current density is due to ionic fluxes which can be described by the Nernst-Planck equation. This leads to the formulation:

$$\nabla \cdot (\sigma_b \nabla \phi) = -\nabla \cdot \left( \mathcal{F} \sum_i z_i D_i^* \nabla c_i \right) \quad [6.1.]$$

where  $\sigma_b$  is bulk conductivity,  $\phi$  is electrical potential,  $\mathcal{F}$  is Faraday's constant, and  $z_i$ ,  $D_i^*$  and  $c_i$  are the valence, effective diffusion coefficient and concentration of ion  $i$ . In most circumstances the concentration gradients are small and the resulting potentials are small as well. They are often termed shale, liquid junction or diffusion potentials (Telford et al., 1990). In a degrading contaminant plume there is the possibility of larger concentration gradients because ions can be consumed or produced by redox reactions. To calculate an expected potential, the concentrations of all ions and the resistivity are needed throughout the model domain. This means that it is only possible to calculate potentials. The calculation of sources would involve determining the concentration distributions for all ions from electrical potentials, and it is too underdetermined to be feasible.

The derivation of equation 6.1 used concentrations which is appropriate for solutions with ionic strengths less than 0.001 mol/L (Krauskopf & Bird, 1995). A more theoretically rigorous approach uses activities ( $a_i$ ) instead of concentrations following (Bockris & Reddy, 1998, eq. 3.55):

$$a_i = \gamma_i c_i \quad [6.2.]$$

where  $\gamma_i$  is the activity coefficient of ion  $i$ . In ideal dilute solution  $\gamma$  is one, but for more concentrated solutions and bulky ions or those with large valence,  $\gamma$  is considerably less than one. For the calculations presented in this chapter, activities are used instead of concentrations.

### 6.1.2 EH MODEL

Revil and co-workers (Naudet, 2004; Naudet et al., 2004; Arora et al., 2007; Linde & Revil, 2007; Castermant et al., 2008; Revil et al., 2009; Revil et al., 2010) present a model linking SP to Eh with the formula:

$$\nabla \cdot (\sigma \nabla \phi) = -\nabla \cdot (\sigma \nabla Eh) \quad [6.3.]$$

The formula is applied in three articles: Arora et al. (2007), Linde & Revil (2007) and Castermant et al. (2008); and developed in two other articles: Revil et al. (2009) and Revil et al. (2010). The formulation is derived from the formula for electric current density due to diffusion controlled ionic fluxes.

$$j_s = -k_b T \sum_{i=1}^N \frac{t_i \sigma}{q_i} \nabla \ln a_i \quad [6.4.]$$

where  $j_s$  is the source current density,  $k_b$  is Boltzmann's constant,  $T$  is temperature,  $\sigma$  is electrical conductivity,  $t_i$ ,  $q_i$  and  $a_i$  are the Hittorf number, charge and ionic activity of species  $i$ . They make the summation over all charge carriers so they include electrons and make the summation over  $N+1$ . Finally, they assume that in some zones there are biotic electronic conductors, perhaps bacterial pili, giving electrons a much higher mobility. The electrons' Hittorf transport number is almost one and the contribution from all other ions becomes negligible. The activity of electrons is used in the definition of Eh and the source current density can be expressed as:

$$j_s = -\sigma \nabla \text{Eh} \quad [6.5.]$$

The authors call the zone in which there is source current the transition zone (T-zone). They locate it at the water table, stating that it acts as an interface between the oxidized vadose zone and the reduced aquifer. Presumably the sources due to diffusion continue to act in the rest of the domain, so an explicit formulation of equation 6.3 would be:

$$[\nabla \cdot (\sigma \nabla \phi)]_{\Omega_{all}} = -[\nabla \cdot (\sigma \nabla \text{Eh})]_{\Omega_{T\_zone}} - \left[ \nabla \cdot \left( \mathcal{F} \sum_i z_i D_i \nabla a_i \right) \right]_{\Omega_{all-T\_zone}} \quad [6.6.]$$

The simplified version of this equation,

$$[\nabla \cdot (\sigma \nabla \phi)]_{\Omega_{all}} = -[\nabla \cdot (\sigma \nabla \text{Eh})]_{\Omega_{T\_zone}} \quad [6.7.]$$

where the contribution of diffusion sources is assumed to be negligible, is used by Arora et al. (2007) to calculate the SP signature over a redox distribution similar to what was found at the Entressen site (Naudet et al., 2003). They use redox potential and resistivity distributions interpolated from values measured in the field and the calculated SP anomaly is  $-250$  mV, which is approximately half of the magnitude measured in the field.

An apparent inconsistency in the application of this model is that the transition zone Arora et al. (2007) use is not very conductive, they did not alter the background conductivity. If a conductive transition zone (10 S/m) is included in their model, the calculated SP anomaly drops to  $-10$  mV.

Theoretically, if charge transfer in the transition zone is electronic, the conductivity should be larger than the solely ionic conductivity in the rest of the domain. The conductivity of the transition zone would be that of microbial mats serving as biotic conductors and it is not known. The effect of biofilms on electrical conductivity is dependent on the species of bacteria in the biofilm. Several species form biofilms that do not significantly change the conductivity of a medium other than changes to the fluid conductivity (Davis et al., 2006; Abdel Aal et al., 2010) and other species act as insulators (Lovley, 2008b). Those species reported to form conductive biofilms are studied for microbial fuel cells and the two species mentioned the most are *Geobacter sulfurreducens* and *Shewanella oneidensis*.

Three estimates of biofilm conductivity reported in literature were found. Torres et al. (2008) modelled measured electron transfer rates for *G. sulfurreducens* with the Nernst-Monod model using biofilm conductivity as a fitting parameter to estimate its value. The minimum conductivity required was 0.05 S/m but there were no significant potential losses across their 79  $\mu\text{m}$  biofilm which indicated that the film was highly conductive. El-Naggar et al. (2010) report measurements of electrical conductivity along pili of *S. oneidensis* MR-1 which are believed to participate in electron transfer. With both of the methods they used, the pili conductivities were on the order of 100 S/m. The third estimate comes from a study of iron reduction by a mixed microbial inoculum in a sand column where biofilm distribution is being numerically modelled to explain the bulk electrical conductivities measured (Regberg et al., 2011, in prep.). The results are preliminary and have bounded the biofilm conductivity between 10 and 55 S/m (pers. comm., Cockett, 2011).

For some of the scenarios tested in this chapter, the conductivity of the transition zone was increased to 10 S/m. The conductivity is very high because it is necessary for electrons to dominate as charge carriers in this zone, while remaining well below values for known electronic conductors such as metals ( $10^8$  S/m)(Keller & Frischknecht, 1966). This value was also chosen because 10 S/m is on the order of conductivities of certain ore bodies like haematite or chalcopyrite or graphitic slate (Telford et al., 1990), over which SP anomalies have been measured.

An advantage of the Eh model is that it requires less input than the diffusion model: only the resistivity and Eh distributions throughout the model domain are necessary. It is therefore possible to make both potential and source calculations. A map of SP, which is relatively easy to measure, could be used to estimate the redox distribution, which is notoriously difficult to measure.

## **6.2 Data set used**

A disadvantage of numerical modelling is the quantity of data necessary. Unfortunately, for neither field site studied do we have sufficient data for this exercise. On both the RIVER and KNOLL sites water chemistry data from wells is available, but they are not from multi-level samplers and there are no data for the vadose zone.

For a realistic numerical model of a contaminant plume, data at a density high enough to capture the concentration changes is necessary. This will mean data on a decimetre scale and is critical because if the available data is sparser, it must be interpolated. The concentration distributions created this way are smoother and their smaller gradients reduce calculated SP signal strength. It is also necessary to have concentration distributions and redox conditions throughout the model domain, which includes both the vadose and phreatic zones. Species concentrations are rarely measured in the vadose zone and it is very difficult to determine redox conditions in this zone. These requirements mean that no field site will have sufficient data for a proper numerical model. We have chosen to use the output of another numerical model as input for the numerical modelling

in this chapter. This other model is the programme MIN3P, a kinetic reactive transport model (Mayer, 1999). If the initial conditions and chemical reactions at a field site are characterized, MIN3P can be used to calculate the species distributions throughout the model domain at any level of detail.

As a surrogate for the field sites presented in chapter 5, results from a MIN3P simulation of toluene biodegradation were used. These results were kindly provided by Uli Mayer and are described and published in the article: “Multicomponent reactive transport modeling in variably saturated porous media using a generalized formulation for kinetically controlled reactions” (Mayer et al., 2002). The lithology does not correspond to that at the field sites presented but, like the RIVER and KNOLL site, it is a shallow unconfined setting and the contaminants are hydrocarbons. Mayer said his simulation was similar to what was occurring at the Bemidji crude-oil spill site (Cozzarelli et al., 1994).

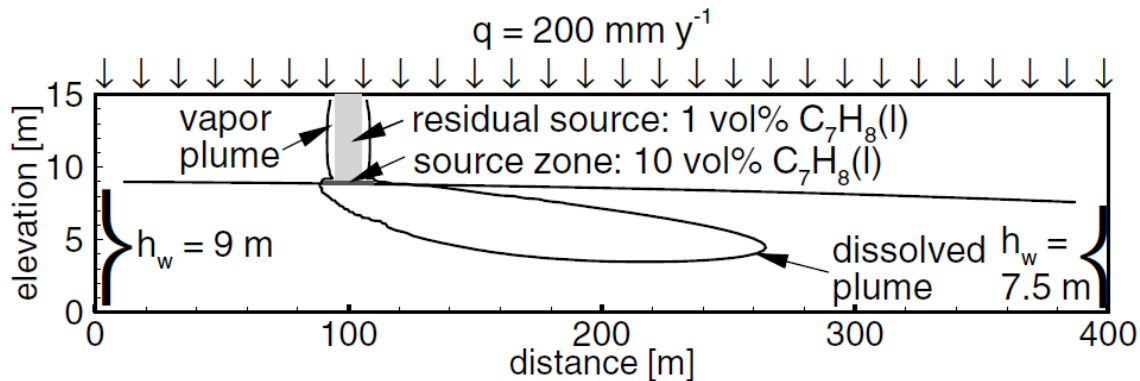


**Figure 6.1 Problem definition for biodegradation problem showing location of contaminant source and flow boundary conditions. (Mayer et al., 2002) This sketch is a cross-section parallel to the groundwater flow direction in the centre of the plume. The horizontal line in the centre of the rectangle represents the water table. Abbreviations:  $q$ —surface recharge,  $h_w$ —height of the water table.**

The hypothetical problem is a spill of light petroleum hydrocarbon in a shallow sandy carbonate unconfined aquifer as shown in Figure 6.1. The contaminants are degraded by aerobic and anaerobic processes involving the reductive dissolution of iron oxides and methanogenesis (Mayer et al., 2002). The model was run for 300 years and we used simulated data from two time steps: 10 and 20 years.

Two model zones were used for the calculations; an interior zone where there is chemical data for source calculations, and an exterior zone that extends 1 km further (Table 6.1). Distant boundaries are used because they are assumed to be no-flux during the potential calculations. The interior model zone used was the same as for the MIN3P model and since the simulated data are only two dimensional (x-z) it was extended into three dimensions by making plume concentrations fall to background concentrations within 10 m in the y-direction. The high data density available made interpolations unnecessary, so the same grid nodes were used as for the MIN3P model. The charges were balanced to within 6% in the simulated data, but to avoid any potential sources we balanced them to within  $10^{-12}$  percent by adjusting the  $\text{Ca}^{2+}$ ,  $\text{CaHCO}_3^+$  and  $\text{HCO}_3^-$  concentrations.

**Table 6.1 Toluene biodegradation model domain dimensions.**

zone	x extent (m)	y extent (m)	z extent (m)	# nodes	# elements
interior	0 to 400	-10 to 10	0 to 15	144 430	784 800
exterior	-1000 to 1400	-1010 to 1010	-1000 to 15	398 286	2 268 000

A list of ions included in the data and used for the model is found in Table 6.2 and the distribution profile of 5 ions;  $\text{CO}_3^{2-}$ ,  $\text{HCO}_3^-$ ,  $\text{Ca}^{2+}$ ,  $\text{Fe}^{2+}$  and  $\text{FeOH}^+$ , are shown for the 10 year time step in Figure 6.2 and the 20 year time step in Figure 6.3. All data are presented as cross-sections through the centre of the plume, parallel to the groundwater flow direction, at  $y=0$  m. The ions that are listed in Table 6.2 but are not among the five displayed have distributions similar to those presented; they outline the plume.

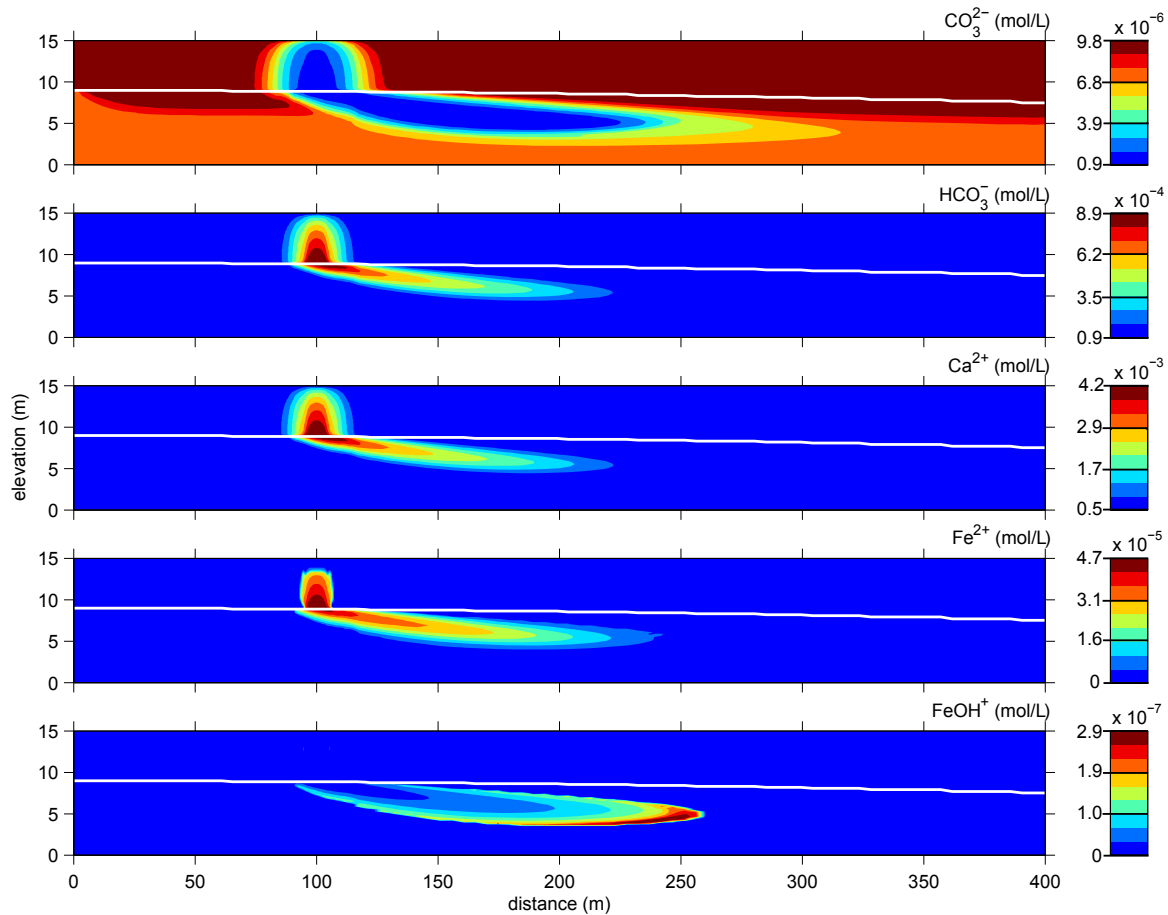


**Figure 6.2** MIN3P simulation data from the 10 year time step of toluene biodegradation. These are cross-sections parallel to the groundwater flow direction through the centre of the plume. The white line is the water table. Above the water table the concentration contours mark an area through which the toluene is percolating below the spill site at a distance of 100 m. Below the water table the concentration contours outline the plume. In the vadose zone all the species apart from carbonate ( $\text{CO}_3^{2-}$ ) have elevated concentrations below the spill site and the contours are stretched to the bottom right under the influence of advection. The carbonate distribution is the opposite with the lowest values at the centre of the plume because initially it is present everywhere and the low pH in the plume transforms it into bicarbonate. The iron hydroxide ( $\text{FeOH}^+$ ) has highest concentrations at the toe of the plume in the bottom right because it is produced by secondary reactions, which are reactions of species such as  $\text{Fe}^{2+}$  produced during the toluene biodegradation.

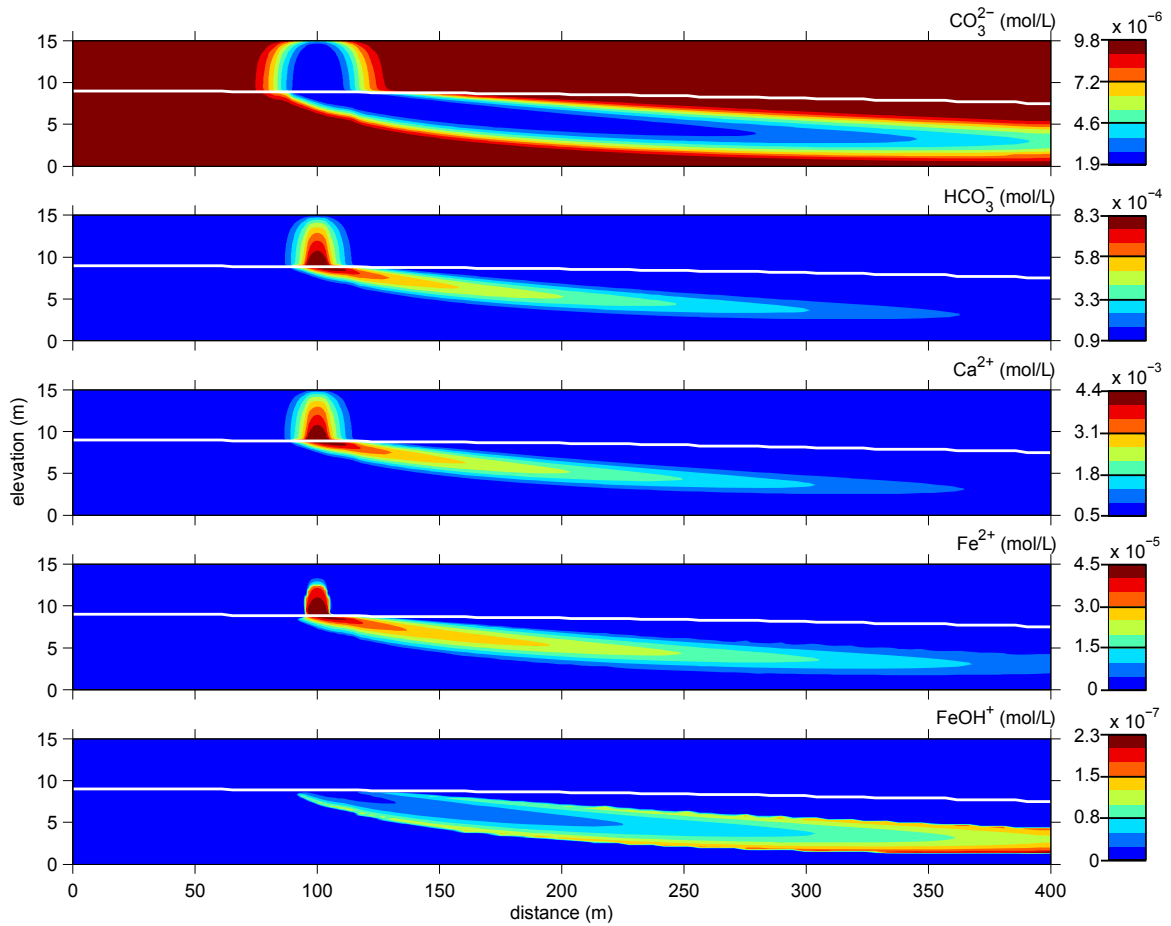


**Figure 6.3** MIN3P simulation data from the 20 year time step of toluene biodegradation. The white line is the water table. For a detailed description of the plume see caption from Figure 6.2. This plume stretches further to the right because the longer period of time has allowed further transport.

The diffusion coefficients at infinite dilution are also listed in Table 6.2. Tabulated diffusion coefficients were not available for all ions, and for these ions, a coefficient was estimated following the methods described by Nigrini (1970) using thermodynamic data from Bard et al. (1985) and Naumov et al. (1974). The activity coefficients ( $\gamma$ ) listed in Table 6.2 are those calculated by MIN3P for the aquifer. They are accurate outside the plume but will change due to high ionic concentrations inside the plume. Therefore activities were calculated everywhere using the formula of Davies (1962):

$$-\log \gamma = 0.5z^2 \left( \frac{\sqrt{I}}{1 + \sqrt{I}} - 0.2I \right) \quad [6.8.]$$

where  $I$  is the ionic strength of the solution and  $z$  is the ion valence. This equation is appropriate for solutions in water at 25 °C. The ionic strength of a solution is defined as (Krauskopf & Bird, 1995):

$$I = \frac{1}{2} \sum_i c_i z_i^2 \quad [6.9.]$$

where  $c_i$  and  $z_i$  are the concentration and valence of ion  $i$ .

**Table 6.2 Ionic diffusion coefficients at infinite dilution at 25°C. Values are from Li & Gregory (1974), unless followed by an asterisk, in which case they were estimated from thermodynamic data. Activity coefficients are those calculated by MIN3P for the aquifer.**

Ions	Diffusion coefficient (m <sup>2</sup> /s)	Activity coefficient
CO <sub>3</sub> <sup>2-</sup>	9.55×10 <sup>-10</sup>	0.8455
OH <sup>-</sup>	52.7×10 <sup>-10</sup>	0.9580
HCO <sub>3</sub> <sup>-</sup>	11.8×10 <sup>-10</sup>	0.9589
FeOH <sub>3</sub> <sup>-</sup>	9.1×10 <sup>-10</sup> *	0.9587
FeOH <sub>4</sub> <sup>-</sup>	8.9×10 <sup>-10</sup> *	0.9589
H <sup>+</sup>	93.1×10 <sup>-10</sup>	0.9605
Fe <sup>3+</sup>	6.07×10 <sup>-10</sup>	0.6961
Fe <sup>2+</sup>	7.19×10 <sup>-10</sup>	0.8465
Ca <sup>2+</sup>	7.93×10 <sup>-10</sup>	0.8470
FeCO <sub>3</sub> <sup>+</sup>	2.9×10 <sup>-10</sup> *	0.9581
CaOH <sup>+</sup>	11.5×10 <sup>-10</sup> *	0.9592
CaHCO <sub>3</sub> <sup>+</sup>	12.0×10 <sup>-10</sup> *	0.9592
FeOH <sup>+</sup>	6.0×10 <sup>-10</sup> *	0.9587
FeHCO <sub>3</sub> <sup>+</sup>	12.3×10 <sup>-10</sup> *	0.9581
FeOH <sup>2+</sup>	7.2×10 <sup>-10</sup> *	0.8448
Fe(OH) <sub>2</sub> <sup>+</sup>	6.0×10 <sup>-10</sup> *	0.9589
Fe <sub>2</sub> (OH) <sub>2</sub> <sup>4+</sup>	5.0×10 <sup>-10</sup> *	0.5043
Fe <sub>3</sub> (OH) <sub>4</sub> <sup>5+</sup>	4.5×10 <sup>-10</sup> *	0.3431

Resistivity is necessary for numerical modelling and the simplest method of calculating it is using Archie's law (1942):

$$\sigma_b = \frac{\sigma_f}{F} \quad [6.10.]$$

where  $\sigma_{b,f}$  are the bulk and fluid conductivities and  $F$  is the formation factor. For sandy aquifers with porosities of 0.2 to 0.3, formation factors are typically 4-8 (Kirsch, 2009). Archie's law assumes that the matrix is non-conducting, however in cases when the fluid conductivity is low (<1 S/m), surface conductivity ( $\sigma_s$ ) along mineral grain faces is not negligible (Wildenschild et al., 2000). Waxman & Smits (1968) proposed a formula to incorporate surface conductivity as a parallel conductor:

$$\sigma_b = \frac{\sigma_f + \sigma_s}{F_a} \quad [6.11.]$$

where  $F_a$  is the apparent formation factor. For the model calculations presented in this chapter, the conductivity is calculated using the Waxman-Smits model. Fluid conductivity is calculated from ionic concentrations and mobilities with (Keller & Frischknecht, 1966):

$$\sigma_f = \mathcal{F} \sum_i |z_i| u_i c_i \quad [6.12.]$$

where  $\mathcal{F}$  is Faraday's constant,  $z_i$ ,  $u_i$  and  $c_i$  are the valence, mobility and concentration of ion  $i$ . Mobilities are calculated with the Einstein-Smoluchowski equation (Bard & Faulkner, 2001, eq. 4.2.2):

$$u_i = \frac{z_i \mathcal{F} D_i}{RT} \quad [6.13.]$$

where  $D_i$  is the diffusion coefficient of ion  $i$ ,  $R$  is the universal gas constant and  $T$  is temperature.

In the vadose zone, conductivity will be lower because there is less fluid, and it is the fluid that carries most of the current. Down to water saturations ( $S_w$ ) of 0.15 to 0.2 the conductivity can be modified using (Archie, 1942):

$$\sigma = \sigma_0 S_w^2 \quad [6.14.]$$

where  $\sigma_0$  is the conductivity at saturation. The soil moisture content was available in the MIN3P data and was used to calculate the water saturation.

The surface conductivity and apparent formation factor were approximated as 0.0055 S/m and 5 respectively, using values measured for clean Ottawa silica sands (Wildenschild et al., 2000). The calculated resistivity profile (Figure 6.4) outlines the plume as the concentration profiles did.

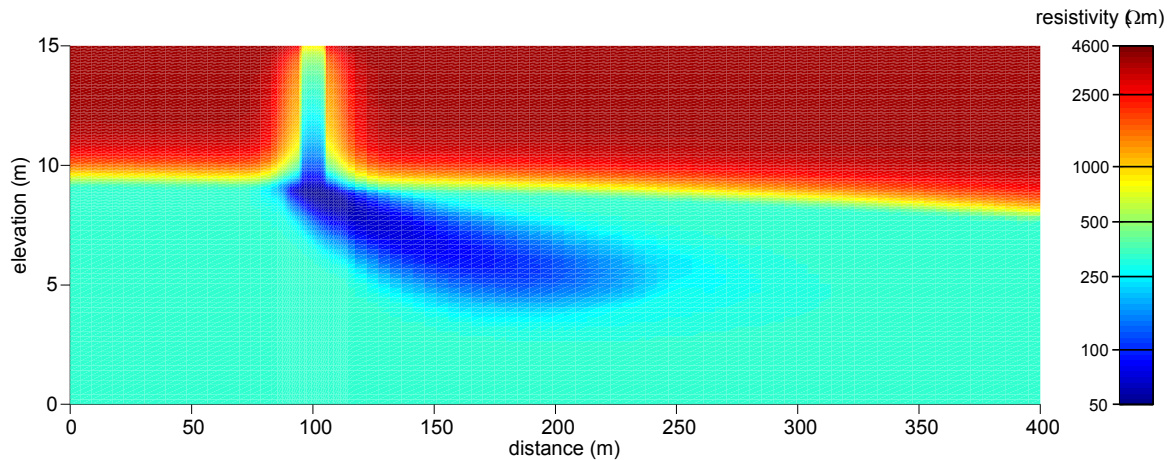


**Figure 6.4 Resistivity profile for the 10 year time step calculated using Waxman-Smits equation. The vadose zone appears with resistivities above 700  $\Omega\text{m}$  (yellow to red colours). The exception is below the spill site at a distance of 100 m where the resistivity is reduced by the high ionic concentrations. In the groundwater the plume is defined by resistivities below 250  $\Omega\text{m}$  (blue colours).**

The redox potential cannot be correctly defined for this data set because it is not in chemical equilibrium since the reactions are kinetically controlled. Eh can be approximated using redox couple concentrations and the Nernst equation. Three couples are available in the data:  $\text{Fe}^{2+}/\text{Fe}^{3+}$ ,  $\text{O}_2/\text{H}_2\text{O}$  and  $\text{CH}_4/\text{CO}_2$ . Each couple is sensitive to redox in different ranges (Table 6.3). For example, the oxygen couple is sensitive to changes in the most oxic environments, but once oxygen has been consumed, such as in the centre of a plume, it no longer describes further changes.

**Table 6.3 Redox potential ranges of different redox couples calculated using the Nernst equation and the 10 year time step data.**

Redox couple	Eh range (mV)
$O_2/H_2O$	+200 to +410
$Fe^{2+}/Fe^{3+}$	-290 to +440
$CH_4/CO_2$	-740 to -600

The highest Eh values measured in the field are typically  $\sim +370$  mV whereas the lowest values are  $-200$  to  $-150$ , depending on the field site (Chapelle et al., 1996; Christensen et al., 2000; Lee et al., 2001; Naudet et al., 2003). The iron couple has the range that most resembles typical field values (Figure 6.5 TOP). The oxygen and methane couples can be used to produce a combined map, where Eh is calculated using oxygen outside the plume (Eh over  $+300$  mV) and using methane inside the plume. The methane values are scaled so that they are not too low, but instead reach  $-320$  mV, the lowest field value reported in literature for leachate plumes (Anneser et al., 2008) (Figure 6.5 BOTTOM).

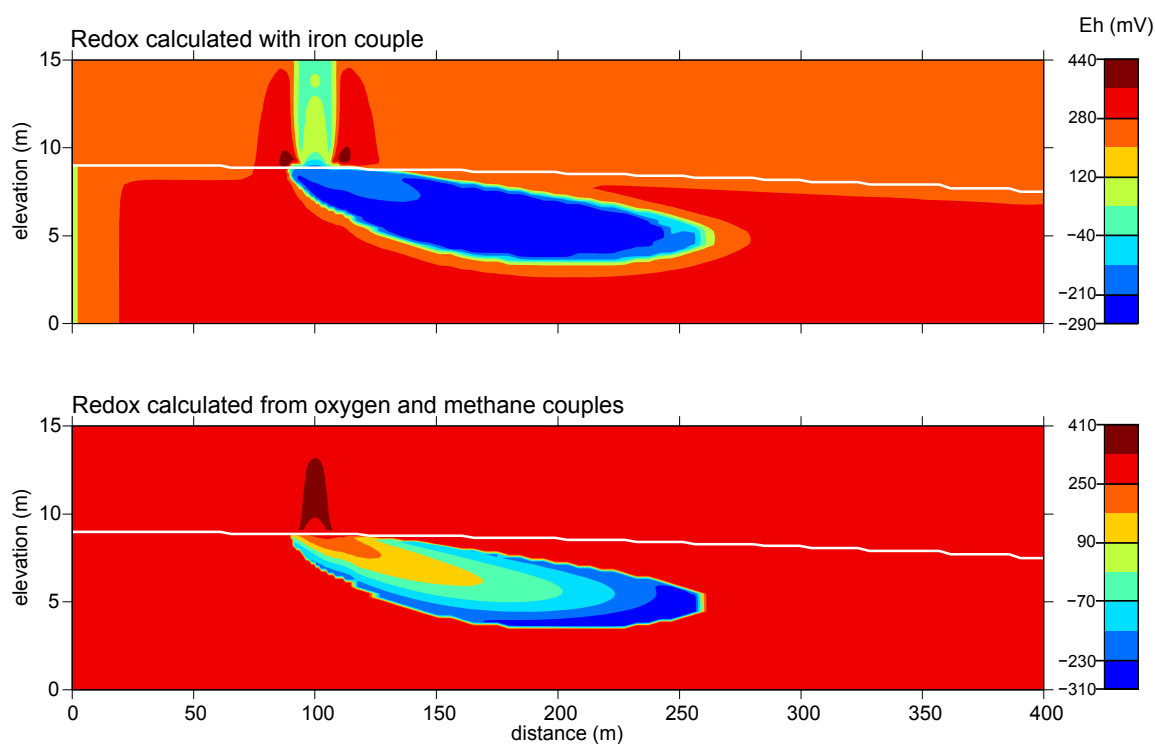


**Figure 6.5 Estimation of redox potential distribution using 10 year time step data of simulated toluene biodegradation. The white line is the water table. The cool colours represent low Eh and reduced redox conditions. TOP: With  $Fe^{2+}/Fe^{3+}$  redox couple.**

The redox calculated with iron has lower Eh values (orange colour) above the water table outside the area impacted by toluene. This is an artefact caused by differences in iron ion concentrations that are on the order of  $10^{-13}$  mol/L. **BOTTOM:** Combination of  $O_2/H_2O$  couple outside the plume and  $CH_4/CO_2$  couple inside the plume.

The two calculated Eh profiles (Figure 6.5) are different. Redox calculated with the iron couple produces a plume with the lowest values in the centre and a reduced zone where there are residual hydrocarbons above the water table, at a distance of 100 m. In contrast, redox calculated with the oxygen and methane couples places the most oxidized zone in the residual hydrocarbons above the water table and the most reduced zone is at the toe of the plume. These profiles can be compared with profiles reported in literature as summarised in a cartoon by Christensen et al. (2001) (Figure 6.6). The most reduced zone is in the centre of the plume, right next to the source. Neither redox potential distributions calculated for the simulated data follows the same pattern. Since the iron couple Eh resemble field distributions more closely than the oxygen and methane Eh, it will be used for modelling calculations. It has an additional advantage of less uncertainty in the transition between inside and outside the plume than the oxygen and methane Eh.

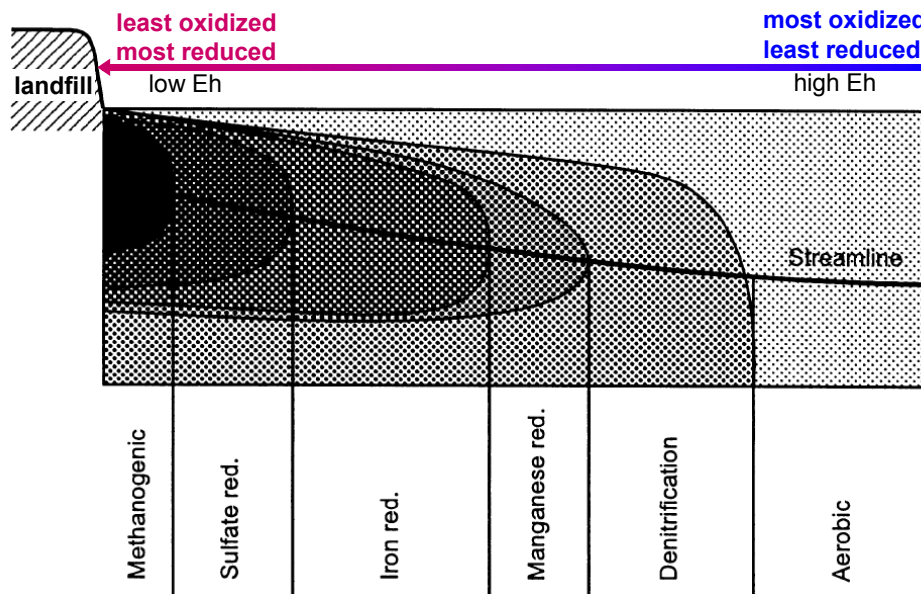


Figure 6.6 Schematic redox zonation in an originally aerobic aquifer down gradient from a landfill. (Christensen et al., 2001) The zones are defined by the predominant redox reactions. The most reduced zone is to the left (lowest Eh) and it becomes progressively more oxidized to the right.

### **6.3 Calculation results**

Eight tests will be presented, each with slightly different parameters. The first five tests were run three times using: (1) the diffusion model, (2) the Eh model with resistive transition zone and (3) the Eh model with a conductive transition zone. For the last three test only the Eh models were run. The tests differ by the age of the plume, plume location, transition zone location, model resistivity and Eh distribution. To isolate the effect of different parameters, only one is changed at a time which is why so many tests are necessary (Table 6.4).

**Table 6.4 Description of eight numerical modelling tests to explain motivations for each modification. Abbreviations: T-zone—transition zone, Res.—resistivity, vad.—vadose zone, sat.—saturated zone.**

Test	Data	T-zone location	Plume location	Res. ( $\Omega\text{m}$ )	Motivation
1	10 year	water table	water table	vad.:4600 sat.:500	To reproduce plume distribution used by Arora et al. (2007)
2	10 year	water table	normal	vad.:4600 sat.:500	More realistic plume distribution that includes surface recharge
3	10 year	plume edge	normal	vad.:4600 sat.:500	Transition zone moved to area with strongest redox gradients
4	20 year	plume edge	normal	vad.:4600 sat.:500	To look at the effect of a plume with a larger distribution
5	10 year	plume edge	normal	vad.:30 sat.:27	To look at the effect of reduced background resistivity
6	10 year	plume edge	normal	vad.:4600 sat.:500	To look at the effect of anisotropic resistivity in the transition zone
7	10 year	plume edge	normal	vad.:4600 sat.:500	To determine the sensitivity to the method used to calculate Eh
8	10 year	encircling plume	normal	vad.:4600 sat.:500	To look at the effect of a transition at all plume boundaries

The Eh models are tested with estimated Eh distributions. The transition zone qualifications are relative. It is called resistive if its conductivity is calculated using the Waxman-Smits equation and conductive when it is uniformly  $0.1 \Omega\text{m}$ . Each sub-section describes the results of one test and the final sub-section is a summary.

6.3.1 TEN YEAR DATA WITH PLUME AND TRANSITION ZONE AT WATER TABLE

In the numerical model of Arora et al. (2007) large Eh contrasts are present at the water table. This might require a site where there was negligible surface recharge except over the contaminant zone and a strong horizontal hydraulic flux in the aquifer, which is uncommon. To test a scenario with large redox gradients at the water table similar to that of Arora et al. (2007), a triangular slice of data between the water table and the centre of the plume was removed from the MIN3P data to bring the centre of the contaminant plume to the level of the water table (Figure 6.7).

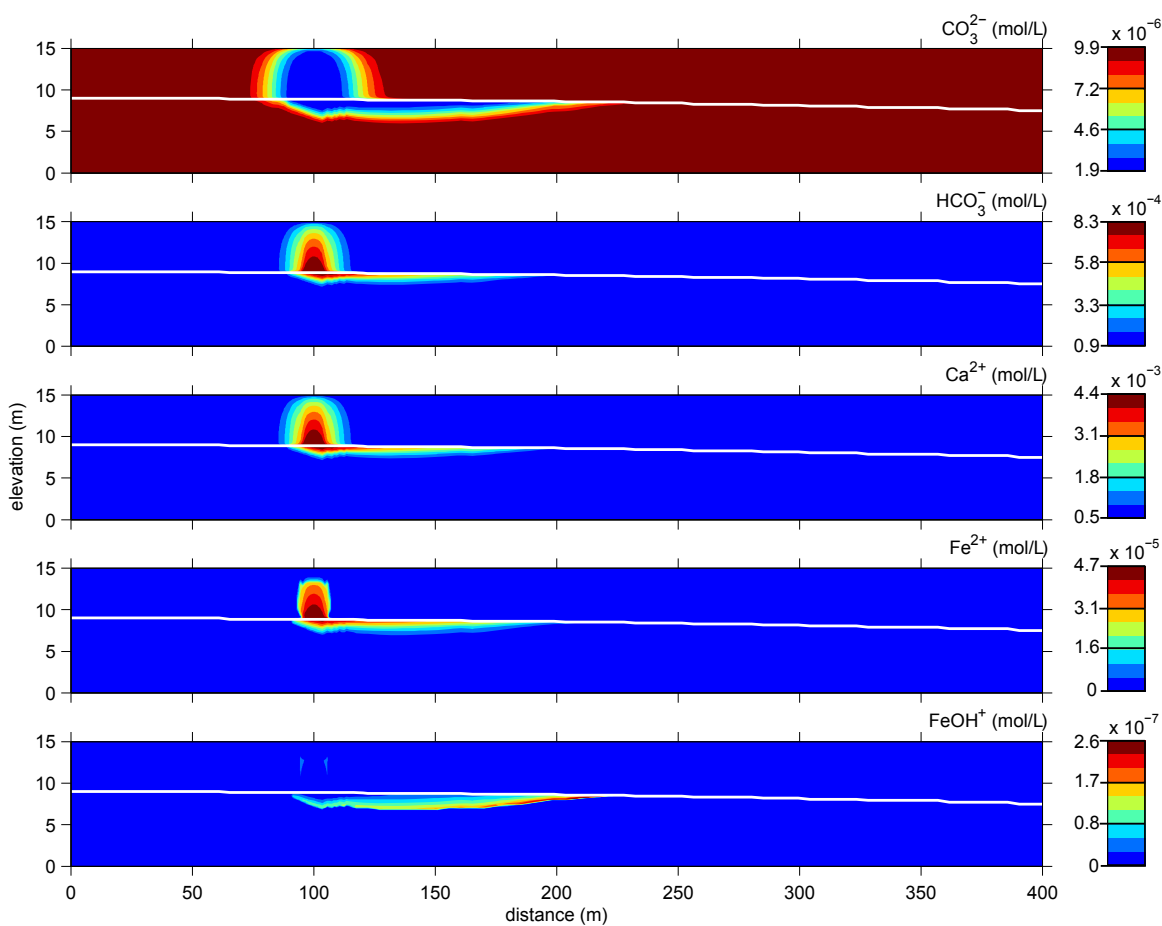
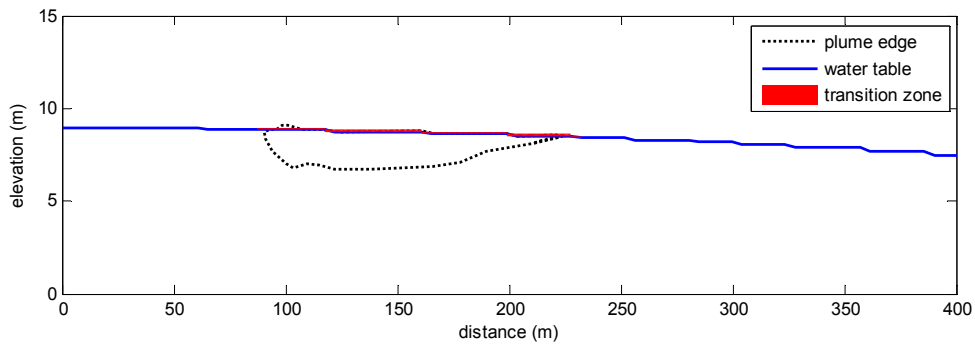


Figure 6.7 Simulation data from the 10 year time step modified so that the centre of the plume is at the water table. The white line is the water table. For a detailed explanation see caption from Figure 6.2.

The finite element model used calculates a current in amperes for each node and its electrical potential. The transition zone was located at the water table and its thickness is one element, 12 cm (Figure 6.8).



**Figure 6.8 Position of transition zone for Eh model relative to the plume outline and water table for the modified 10 year data.**

The variation in source magnitude depending on the model used is striking (Figure 6.9). The magnitude of the sources for the Eh model with a conductive transition zone are huge (Figure 6.9 BOTTOM). The values are given at nodes used to describe the upper and lower surfaces of the transition zone. On the profiles pictured, most nodes have an area of  $4.4 \text{ m}^2$  associated with them. Between distances of 78 and 122 m the area per node is only  $1 \text{ m}^2$ , which is why the source magnitudes are lower in this section. The diffusion model has sources throughout the model domain though most are located in the plume and along the water table, because this is where the strongest concentration gradients occur. Both Eh models have sources restricted to the transition zone, which in this case is at the water table above the plume.

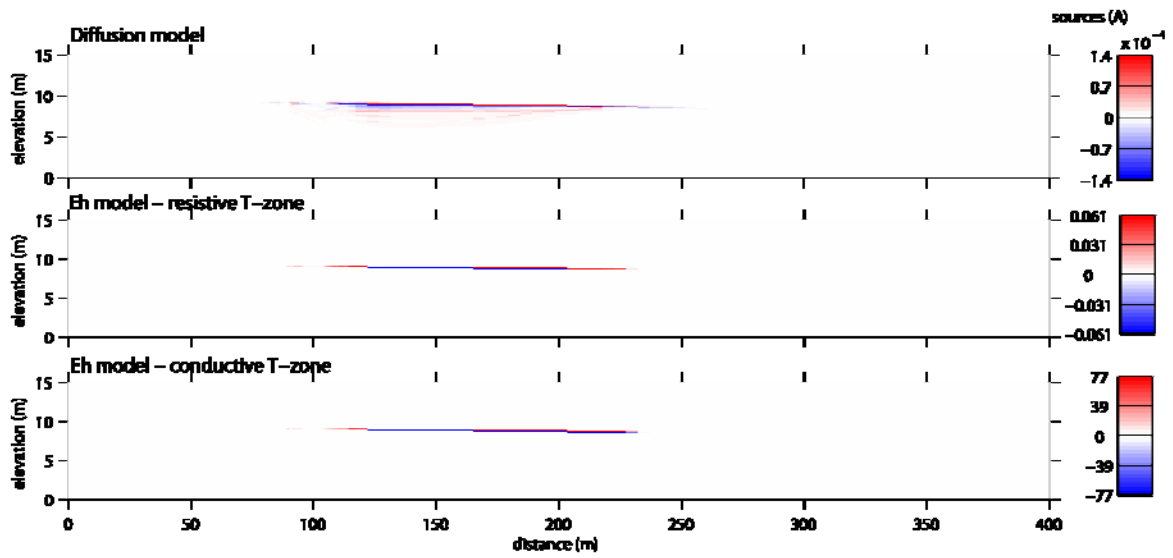
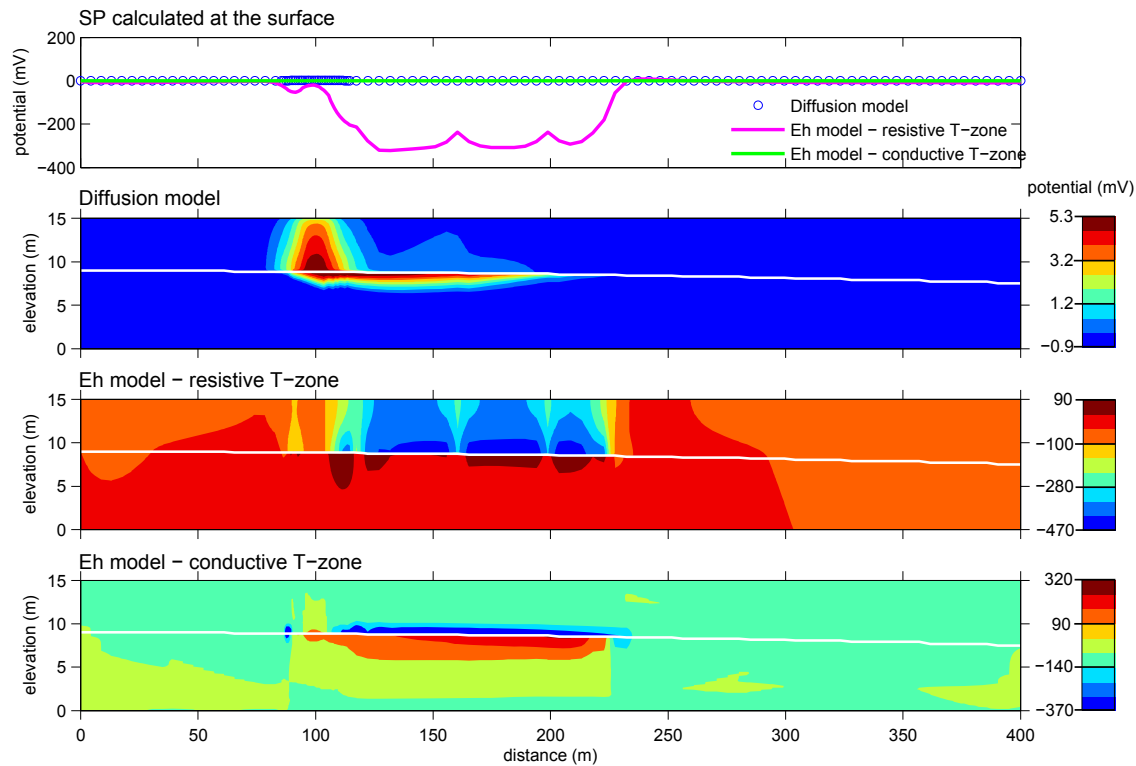


Figure 6.9 Source currents calculated with the modified 10 year data. The profiles are maps of the current source in amperes at each node. Both the centre of the plume and the transition zone are at the water table. The sources of the diffusion model (TOP) are throughout the plume where there are strong concentration gradients. The two Eh models (CENTRE and BOTTOM) have sources restricted to the transition zone, which was defined as the elements spanning the water table above the plume.

The potentials produced by the sources shown above have magnitudes consistent with the size of the sources (Figure 6.10). The three bottom panels present cross-sections of the potential distribution, whereas the top panel has SP profiles as they would be measured at the surface for the three models. For the diffusion model and Eh model with conductive transition zone, the potentials are restricted to areas immediately around the sources and there is little surface SP expression. However, the Eh model with resistive transition zone produces a  $-320$  mV anomaly at the surface and the potential signal extends further away from the sources.



**Figure 6.10 Potentials calculated using the modified 10 year data with the plume centre and transition zone at the water table. The profiles are contour maps of the potential at each node generated by the source currents in Figure 6.9 given a resistivity distribution calculated with the Waxman-Smits equation. The top panel is SP as it would be measured at the surface of the model domain, at 15 m elevation. The three bottom profiles are contour maps of the electrical potential in millivolts at each node. The strongest potentials are found where the sources are. In the diffusion (TOP CENTRE) and Eh model with conductive transition zone (BOTTOM) the potential anomaly is restricted to the area immediately adjacent to the sources. In the Eh model with resistive transition zone (BOTTOM CENTRE) the potential anomaly spreads further.**

### 6.3.2 TEN YEAR DATA WITH TRANSITION ZONE AT WATER TABLE

Since most dissolved phase plumes are below the water table down gradient from the contaminant source, a second test was run with the concentrations as shown in Figure 6.2. These are the original results of MIN3P and have more typical concentration distributions than those used for the first test. The redox transition zone was located at the water table because Arora et al. (2007) suggested this is where it would occur (Figure 6.11) and in contrast with test 1, the strongest redox gradients are below the zone rather than in it. Calculated source amplitudes are smaller than for test 1 (Figure 6.12).

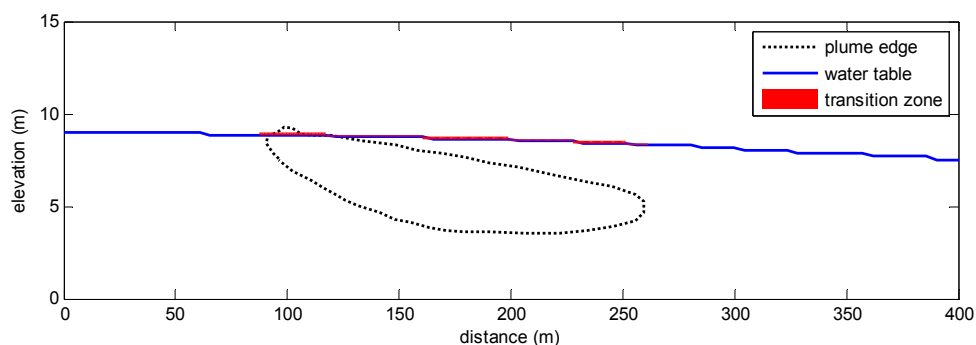


Figure 6.11 Position of transition zone for Eh model relative to the plume outline and water table with sources at the water table and normal 10 year data.

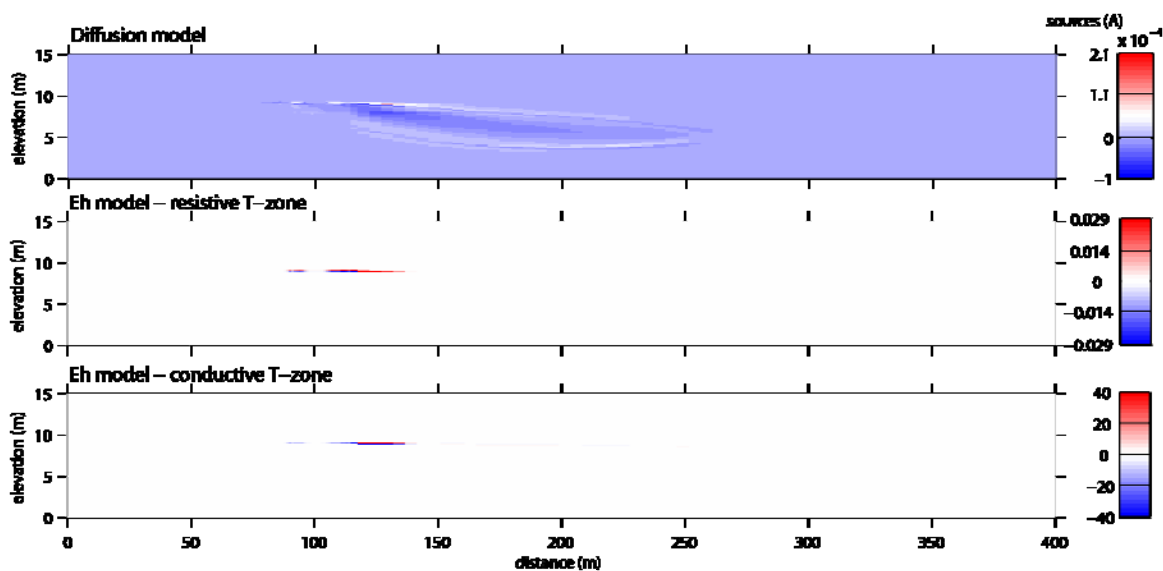
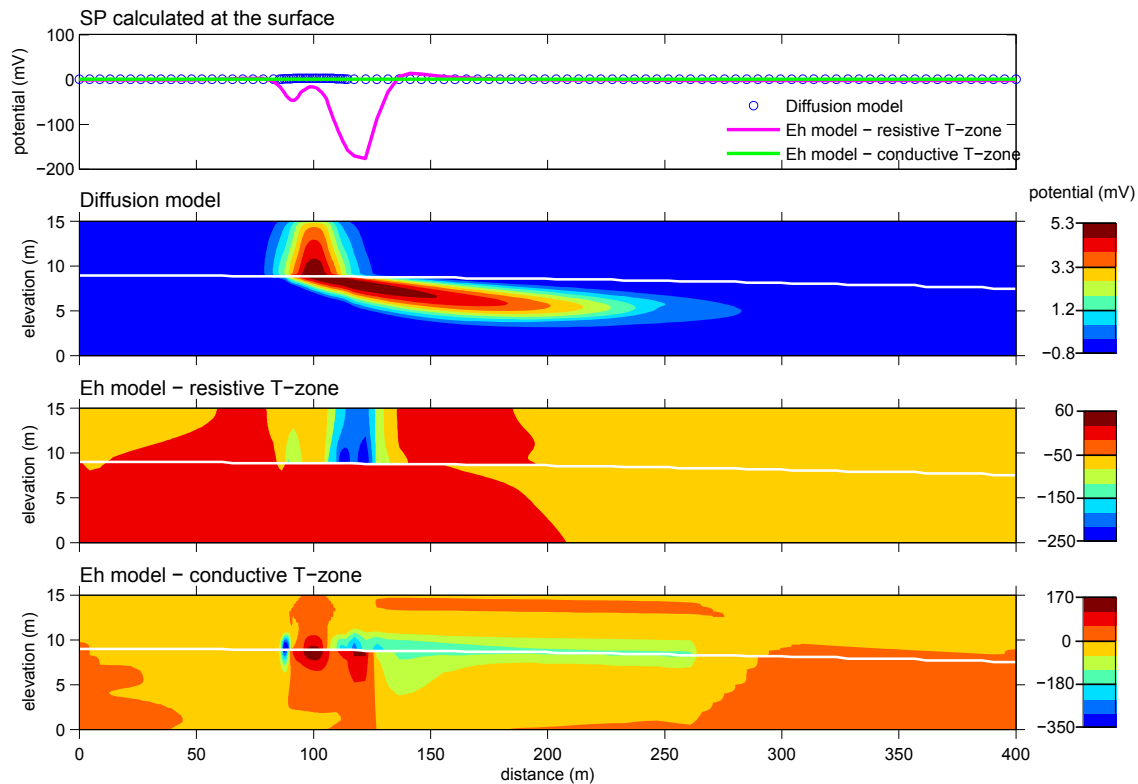


Figure 6.12 Source currents calculated with the 10 year data and sources at the water table for the three models.

The potentials generated by these sources are shown in Figure 6.13. The diffusion model potential anomaly reaches +5.4 mV and at the surface the signal is only +2.7 mV. The Eh model with resistive transition zone has the largest surface expression with an anomaly of -176 mV. The Eh model with conductive transition zone produces the largest SP anomaly, but it remains channelled in the conductive transition zone and there is little surface expression.



**Figure 6.13** Potential generated by the source currents in Figure 6.12, calculated with the 10 year data and sources at the water table for the three models. The top panel is SP as it would be measured at the surface of the model domain.

### 6.3.3 TEN YEAR DATA WITH TRANSITION ZONE AT PLUME EDGE

Since surface recharge is incorporated in the MIN3P toluene biodegradation simulated data, the plume is not at the water table, but rather below it. The edge of the plume is presumably where microbes are most active in its degradation. The Eh models rely on a transition zone where current is carried electronically and it may be comprised of microbial mats that would likely be at the plume edge. The transition zone in the next test was displaced to the location where the Eh gradient was strongest at the top of the plume (Figure 6.14). It is still 12 cm thick.

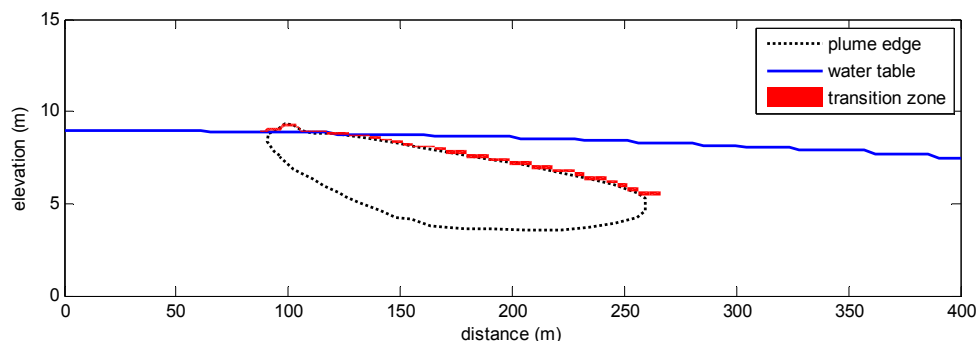


**Figure 6.14** Position of transition zone for Eh model relative to the plume outline and water table with sources at plume edge and normal 10 year data.

The diffusion model for this test is identical to that in test 2 and the resulting sources (Figure 6.15) have the same amplitudes. The largest difference is that in the Eh model with resistive transition zone, the SP anomaly at the surface spans 175 m instead of only 50 m in test 2 (Figure 6.16). Neither the diffusion model nor the Eh model with conductive transition zone produce significant surface anomalies.

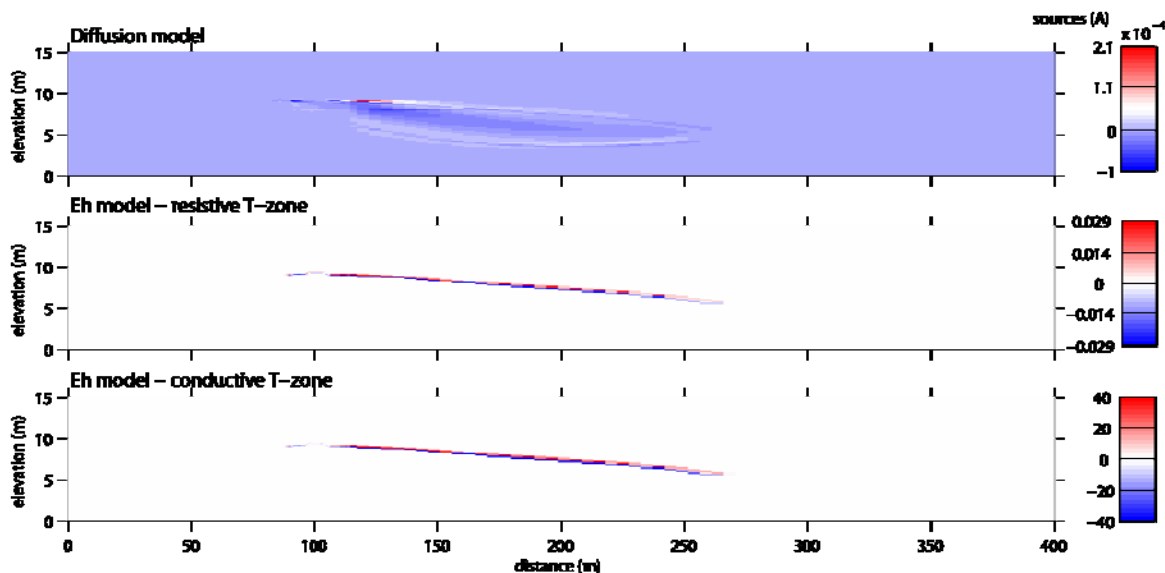


**Figure 6.15** Source currents calculated with the 10 year data and sources at the plume edge for the three models.

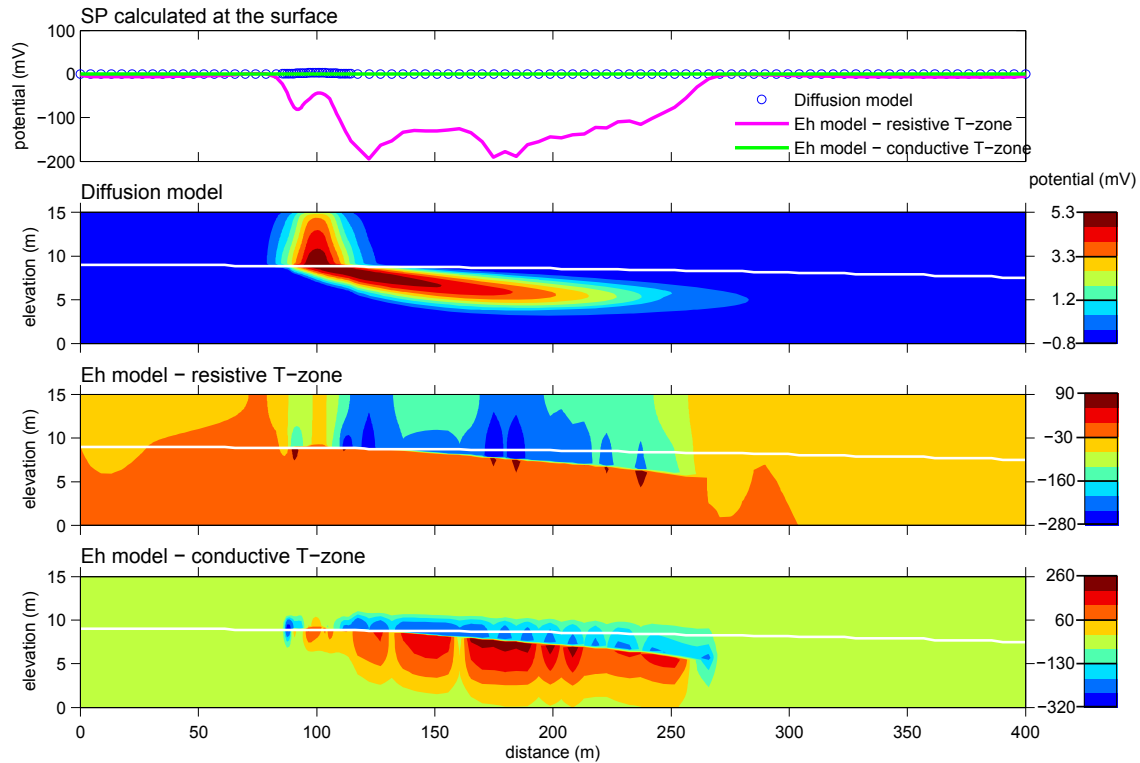


**Figure 6.16** Potential generated by the source currents in Figure 6.15, calculated with the 10 year data and sources at the plume edge for the three models. The top panel is SP as it would be measured at the surface of the model domain.

#### 6.3.4 TWENTY YEAR DATA WITH TRANSITION ZONE AT PLUME EDGE

The fourth test has a transition zone at the plume edge, like the third test. The difference between the two tests is that the simulated data from the 20 year time step were used instead of the 10 year time step. After 20 years, the plume has travelled further and the chemistry has changed. The sources have the same magnitudes, but they are distributed over a larger area since the plume has a greater extent (Figure 6.17).

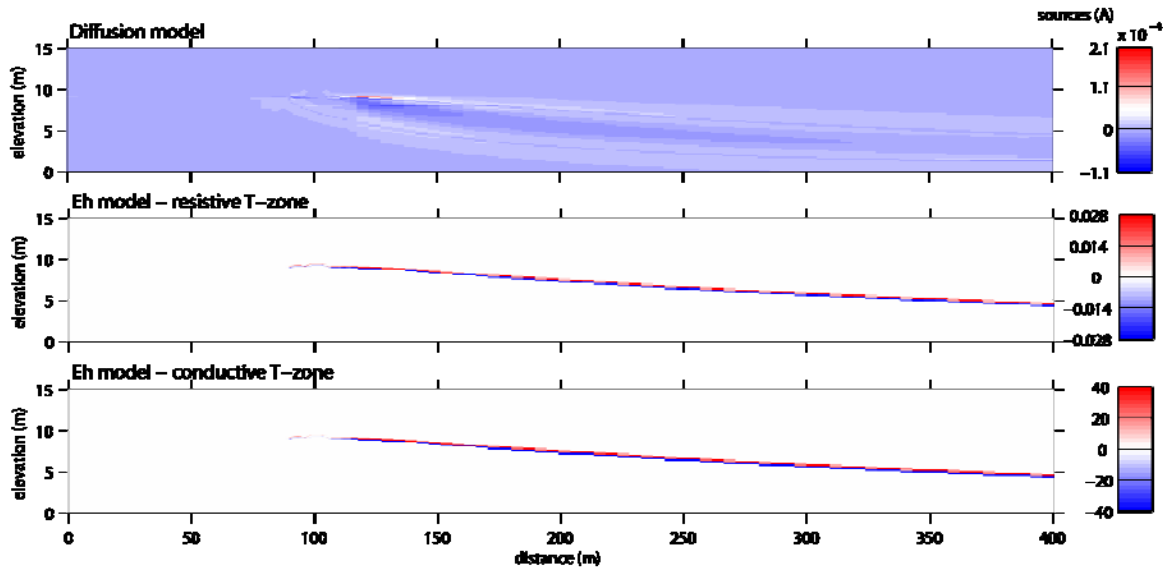


**Figure 6.17 Source currents calculated with the 20 year data and sources at the plume edge for the three models.**

There is no measurable surface SP anomaly for the diffusion and Eh with conductive transition zone (Figure 6.18). The Eh with resistive transition zone produces a negative surface anomaly of similar magnitude to the previous tests, but its extent is greater. It could be used to map the approximate extent of the plume.

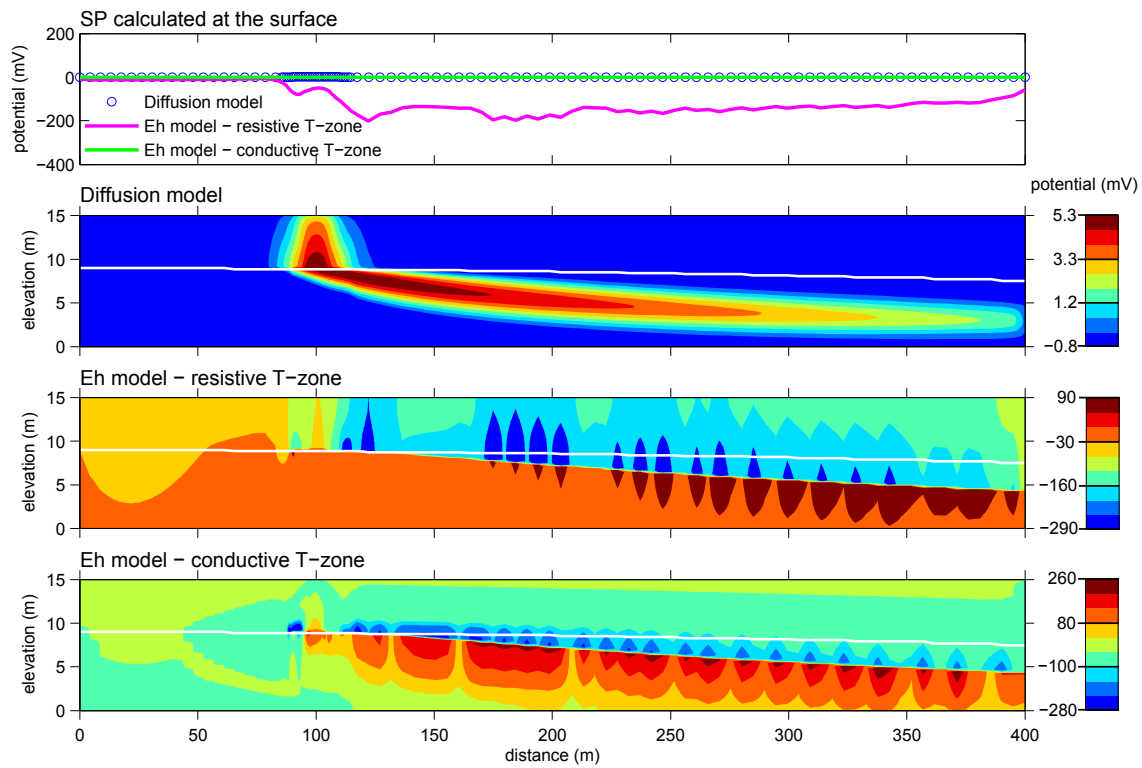


Figure 6.18 Potential generated by the source currents in Figure 6.17, calculated with the 20 year data and sources at the plume edge for the three models. The top panel is SP as it would be measured at the surface of the model domain.

6.3.5 TEN YEAR DATA WITH TRANSITION ZONE AT PLUME EDGE AND REDUCED MODEL RESISTIVITY

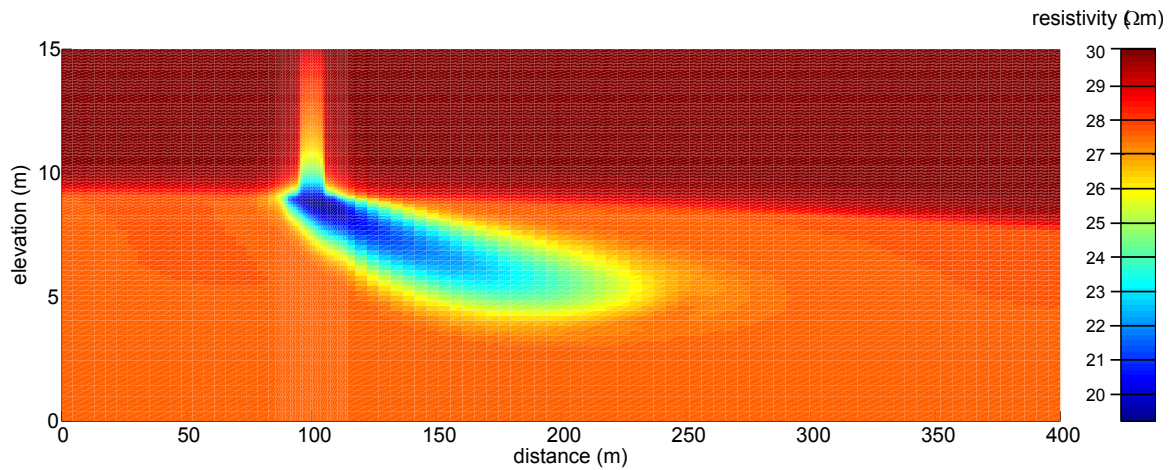


Figure 6.19 Resistivity profile for the 10 year time step calculated by adding a conductivity of 0.033 S/m to the conductivity calculated using the Waxman-Smiths equation.

At the two field sites presented in this work the ground was more conductive than the 4600  $\Omega\text{m}$  vadose zone and 500  $\Omega\text{m}$  saturated zone of the previous tests. The KNOLL site was the most conductive due to tills and siltstones with resistivities of 15-20  $\Omega\text{m}$  when saturated and 25-35  $\Omega\text{m}$  in the vadose zone. To observe the effect of ground resistivity, it was reduced for the fifth test. To approximate conditions at the KNOLL site, a target vadose zone resistivity of 30  $\Omega\text{m}$  was set. To reach this resistivity with the Waxman-Smits equation (6.11), it was necessary to increase the surface conductivity so much that it dominated and the plume was no longer visible. To remedy this, instead of using only Waxman-Smits, a second surface conductivity, of 0.033 S/m was added to the previously calculated conductivities (Figure 6.19).

$$\sigma_b = \frac{\sigma_f + \sigma_{s1}}{F_a} + \sigma_{s2} \quad [6.15.]$$

where  $\sigma_{b,f,s1,s2}$  are the bulk, fluid, Waxman-Smits surface, and second surface conductivities, and  $F_a$  is the apparent formation factor.

A different lithology changes resistivity but will also alter chemical compositions. This means that the fifth test is a rather crude approximation because the simulated data were not modified, but it is nevertheless helpful to explore the influence of ground resistivity. The sources of the diffusion model and Eh model with conductive transition zone are identical to those of the third test. In this test, the Eh model with resistive transition zone produces sources that are seven times greater in magnitude than for the third test. This is because even though the Eh gradient remains unchanged, the resistivity of the zone over which it is calculated is reduced. The diffusion model produces an even smaller SP anomaly than in the previous tests (Figure 6.20). Both Eh models have significant surface SP expression and they are of the same magnitude. This is the first test where the potential anomaly of the Eh model with conductive transition zone reaches the surface, because the conductivity contrast between the transition zone and surrounding is smaller and the currents do not stay channelled in this zone.

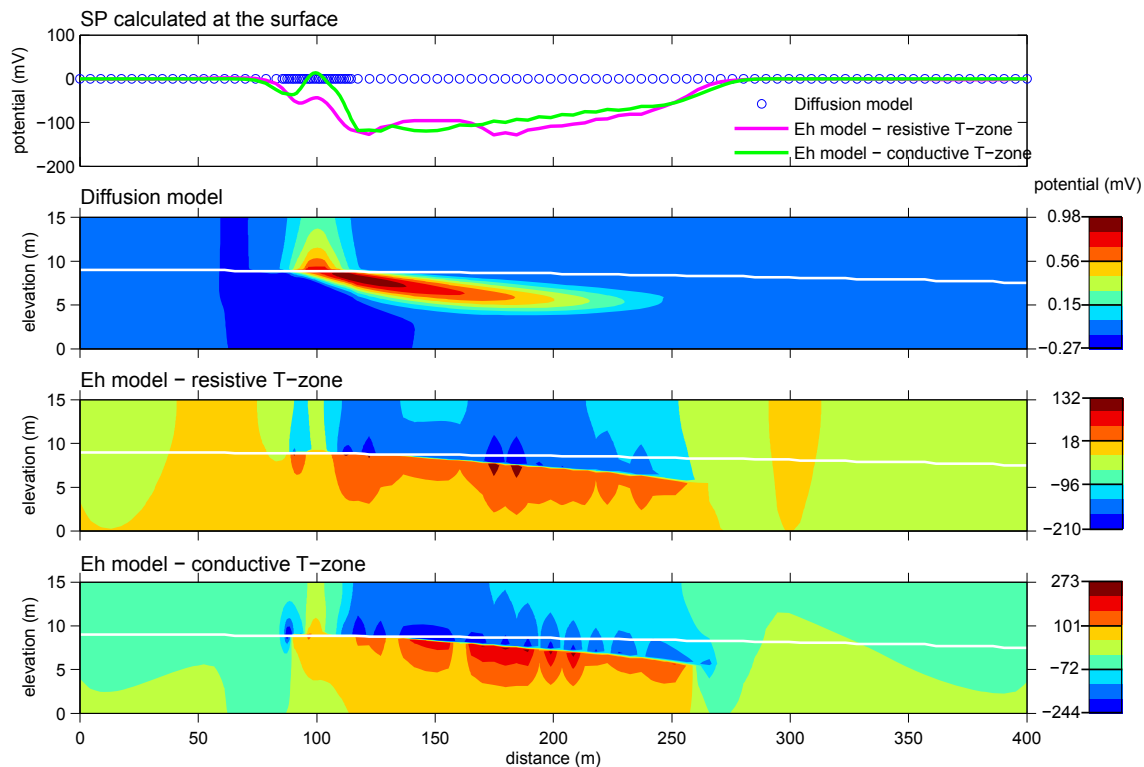


**Figure 6.20** Potential generated by the source currents calculated with the 10 year data with reduced resistivity and sources at the plume edge for the three models. The top panel is SP as it would be measured at the surface of the model domain.

### 6.3.6 TEN YEAR DATA WITH TRANSITION ZONE AT PLUME EDGE AND ANISOTROPIC TRANSITION ZONE RESISTIVITY

The previous test demonstrates the importance of the resistivity distribution on the SP signatures at the surface when using the Eh theoretical model. According to the Eh model theory, conduction in the transition zone is microbially mediated (Revil et al., 2009) and it is conceivable that this could produce anisotropic conductivity. If something like microbial pili are conducting current to bridge two redox zones, they would be preferentially oriented perpendicular to the redox gradient. This test investigates the effect of anisotropic resistivity in the transition zone. The ten year data are used with a normal plume distribution and a transition zone at the plume edge (Figure 6.14). The resistivity in the x and y directions is that presented in Figure 6.4 whereas in the z direction, the resistivity includes a conductive transition zone (Figure 6.21). The diffusion model does not include a transition zone and was not run in this test that investigates transition zone properties.

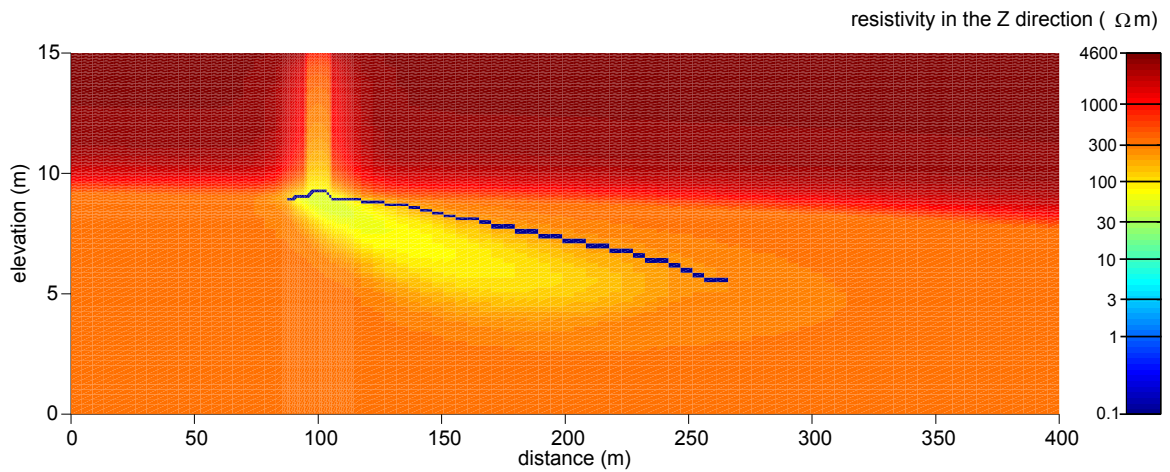


**Figure 6.21 Resistivity distribution in the z direction for the 10 year time step calculated from using Waxman-Smits equation with a  $0.1 \Omega\text{m}$  transition zone added.**

The results are presented with those from test 3 so that they can be compared with the isotropic results. The magnitude of the sources in the anisotropic model is the same magnitude as for the conductive transition zone. The potentials generated by the anisotropic model have a range in between the resistive and conductive transition zone models (Figure 6.22). However the expression at the surface is like that of the conductive transition zone in that no signature is visible.

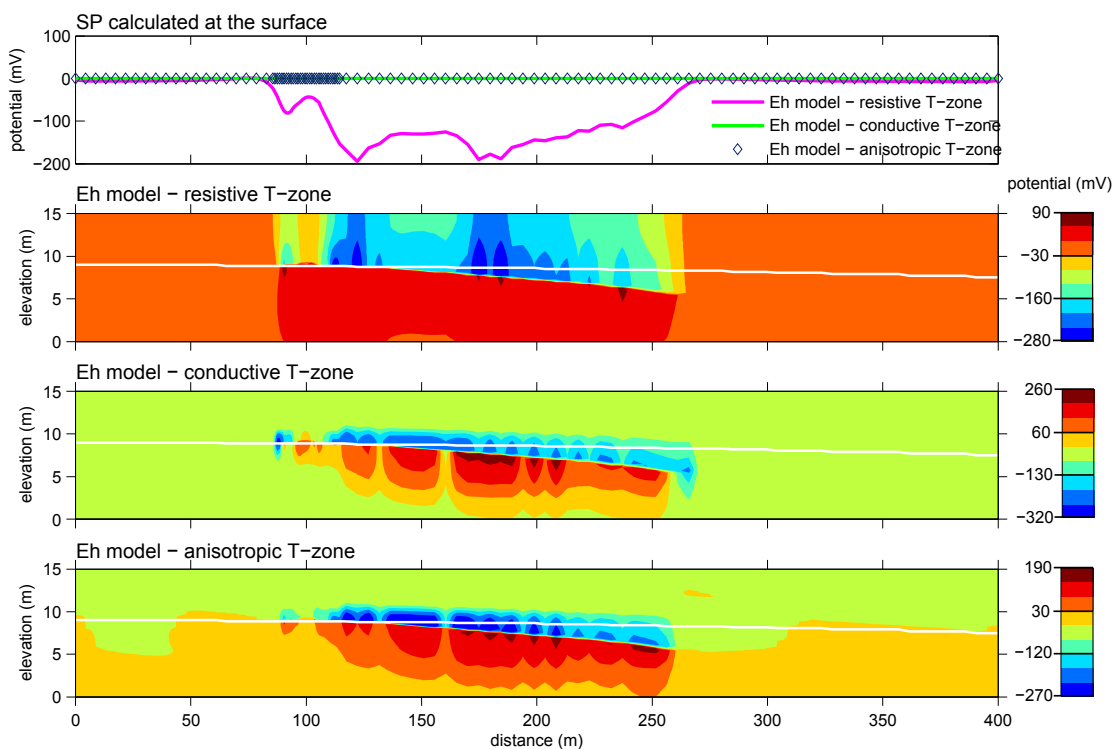


**Figure 6.22** Potential generated by the source currents calculated with the 10 year data with sources at the plume edge. The top panel is SP as it would be measured at the surface of the model domain. **CENTRE TOP: Resistive transition zone. CENTRE BOTTOM: Conductive transition zone ( $0.1 \Omega\text{m}$ ) BOTTOM: Anisotropic resistivity in transition zone (resistive in x and y,  $0.1 \Omega\text{m}$  in z).**

### 6.3.7 TEN YEAR DATA WITH TRANSITION ZONE AT PLUME EDGE AND EH CALCULATED DIFFERENTLY

This test uses the Eh distribution calculated using a combination of the oxygen and methane couples (Figure 6.5 BOTTOM). Eh calculated with the iron redox couple was used in all tests described above because it was deemed more similar to field measurements over contaminant plumes. Combining Eh from the oxygen and methane couples may be a more theoretically sound calculation method, therefore this test was run using the Eh model with a resistive transition zone and combined Eh data. The results are presented with those from test 3 to aid comparison. Neither the diffusion model nor the Eh model with conductive transition zone were run, because the first does not incorporate Eh and the second had no surface SP expression in the initial test.

The source magnitudes are larger with the combined Eh than the iron couple Eh because the gradients at the top of the plume are larger. The resulting potentials for the combined Eh are higher than for the iron couple Eh, which is expected as the sources have larger magnitudes (Figure 6.23). Surprisingly, the surface expression of the combined Eh as a smaller magnitude. There are two causes: (1) The combined Eh transition zone is in a more conductive part of the plume so the currents stay channelled in the plume to a greater degree. (2) The highest redox gradients are further downstream in the combined Eh and these sources have less impact on the surface because they are deeper.

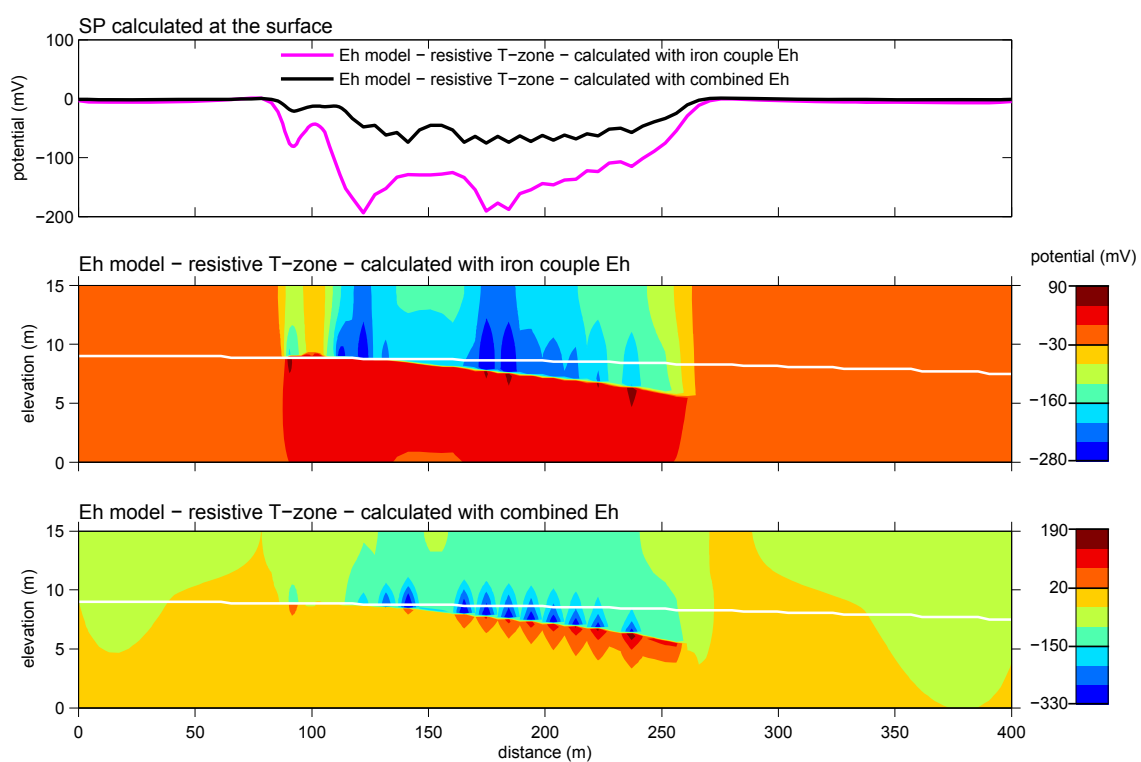


**Figure 6.23** Potential generated by the source currents calculated with the 10 year data with sources at the plume edge. The top panel is SP as it would be measured at the surface of the model domain. CENTRE Modelled using Eh calculated with the iron couple. BOTTOM: Modelled using Eh distribution made from a combination of those calculated with oxygen and methane couples.

### 6.3.8 TEN YEAR DATA WITH TRANSITION ZONE ALL AROUND PLUME

The Eh model of Arora et al. (2007) had a transition zone at the water table. In the third test the zone was moved to the edge of the plume where redox gradients were strongest. Only the top edge of the plume was considered as it was nearest to the water table and the

ground surface, where measurements would be made. In this test the transition zone is extended to encircle the plume (Figure 6.24) because presumably there would be microbes on the bottom edge of the plume as well.

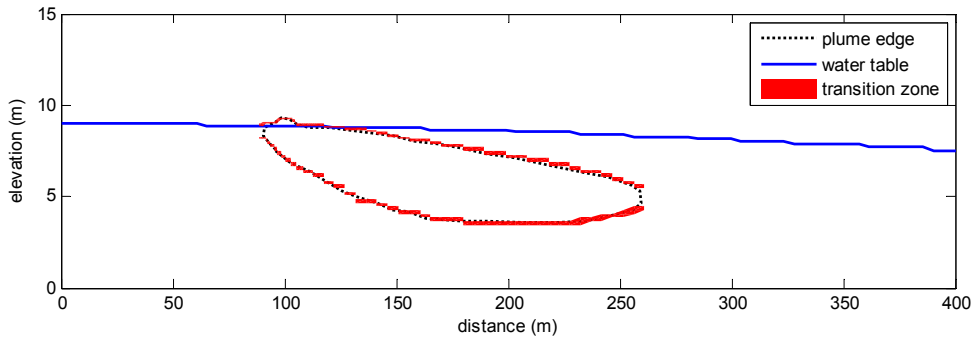


**Figure 6.24** Position of transition zone for Eh model relative to the plume outline and water table with sources all around the plume and normal 10 year data.

For this test only the resistive transition zone was used because the diffusion model has no transition zone and the conductive transition zone model produced no surface SP anomaly. The test results are shown with those from test 3 to aid in comparison. The sources have the same magnitudes and show the extension of the transition zone (Figure 6.25).

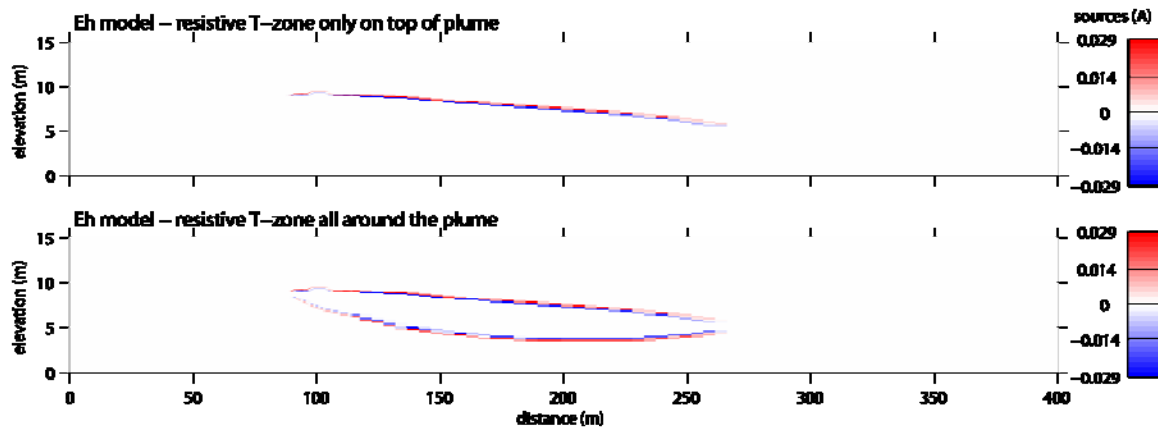


**Figure 6.25** Source currents calculated with the 10 year data with sources at the plume edge and a resistive transition zone. **TOP:** Modelled using sources just at the top of the plume. **BOTTOM:** Modelled using sources all around the plume.

The plume location is easier to identify on the potential map when the transition zone encircles the plume as opposed to when it is only at the top edge (Figure 6.26). The surface SP expression for the Eh model with resistive transition zone encircling the plume

shows a dipolar anomaly; above the spill zone the potentials reach  $\sim +80$  mV while downstream magnitudes of the negative anomaly are reduced,  $\sim -90$  mV.

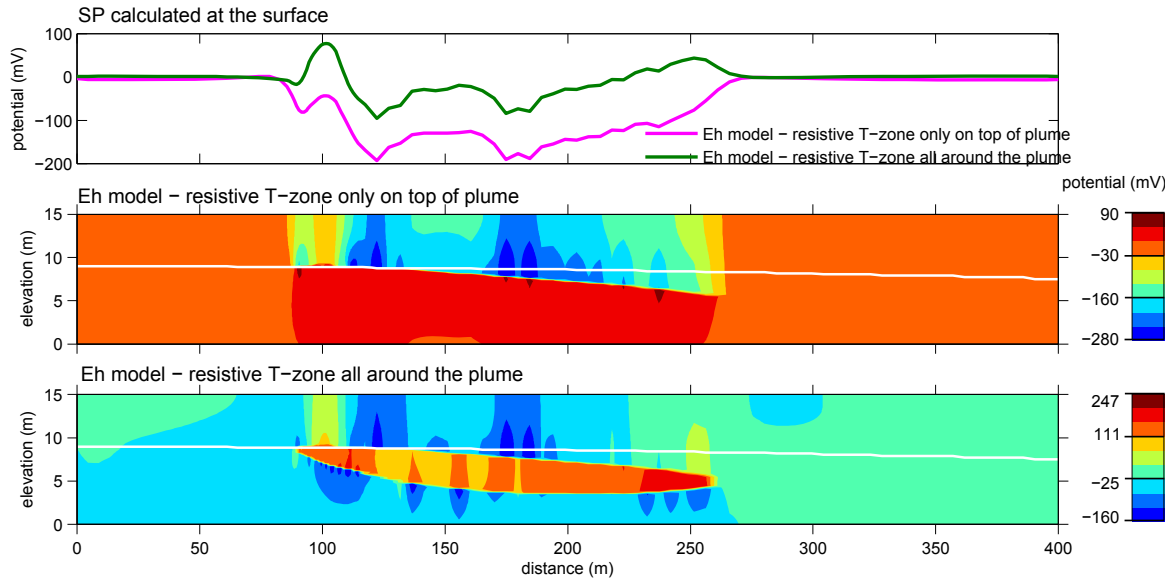


**Figure 6.26 Potential generated by the source currents in Figure 6.25, calculated with the 10 year data with sources at the plume edge. The top panel is SP as it would be measured at the surface of the model domain. CENTRE Modelled using sources just at the top of the plume. BOTTOM: Modelled using sources all around the plume.**

### 6.3.9 SYNTHESIS

All the test results are compiled in Table 6.5.

**Table 6.5 Amplitude of sources and potentials for different tests with toluene biodegradation data. The resistive and conductive qualifiers for the Eh models refer to the relative resistivity of the transition zone. Abbreviations: T-zone—transition zone, Res.—resistivity, Surf. SP—SP anomaly at the ground surface, vad.—vadose zone, sat.—saturated zone, D—dipole.**

Test	Data	T-zone location	Plume location	Res. ( $\Omega\text{m}$ )	Theoretical model	Range of sources (A)	Surf. SP (mV)
1	10 year	water table	water table	vad.:4600 sat.:500	diffusion	+ 0.001	+2.9
					Eh-resistive	$\pm 0.184$	-330
					Eh-conductive	$\pm 232$	0
2	10 year	water table	normal	vad.:4600 sat.:500	diffusion	+ $2 \cdot 10^{-4}$	+2.9
					Eh-resistive	$\pm 0.087$	-190
					Eh-conductive	$\pm 119$	0
3	10 year	plume edge	normal	vad.:4600 sat.:500	diffusion	+ $2 \cdot 10^{-4}$	+2.9
					Eh-resistive	$\pm 0.087$	-195
					Eh-conductive	$\pm 119$	0
4	20 year	plume edge	normal	vad.:4600 sat.:500	diffusion	+ $2 \cdot 10^{-4}$	+2.9
					Eh-resistive	$\pm 0.084$	-195
					Eh-conductive	$\pm 119$	0
5	10 year	plume edge	normal	vad.:30 sat.:27	diffusion	+ $2 \cdot 10^{-4}$	+0.3
					Eh-resistive	$\pm 0.480$	-130
					Eh-conductive	$\pm 119$	-134
6	10 year	plume edge	normal	vad.:4600 sat.:500	Eh-resistive	$\pm 0.087$	-195
					Eh-conductive	$\pm 119$	0
					Eh-anisotropic	$\pm 119$	0
7	10 year	plume edge	normal	vad.:4600 sat.:500	Eh-resistive iron couple Eh	$\pm 0.087$	-195
					Eh-resistive combined Eh	$\pm 0.091$	-76
					Eh-resistive	$\pm 0.087$	-195
8	10 year	plume edge	normal	vad.:4600 sat.:500	Eh-resistive	$\pm 0.087$	-195
		encircling plume			Eh-resistive	$\pm 0.087$	173 D

Using the diffusion model, the first three tests (Figure 6.27) produce almost identical SP anomalies at the surface: +2.9 mV. This amplitude is below detection limit in the field and it is of opposite polarity of field examples in literature (Shi, 1998; Nyquist & Corry, 2002; Naudet et al., 2003). The source terms are smaller than 1 mA and those contributing the most to the SP anomaly at the surface are the ones in the vadose zone directly at the spill site. When the plume is right at the water table (test 1) there is a small signal of +0.5 mV downstream from the spill site. In the fifth test, where the ground is more conductive, the SP anomaly is only +0.3 mV because the sources are the same but the signal dissipates more quickly in a conductive medium.

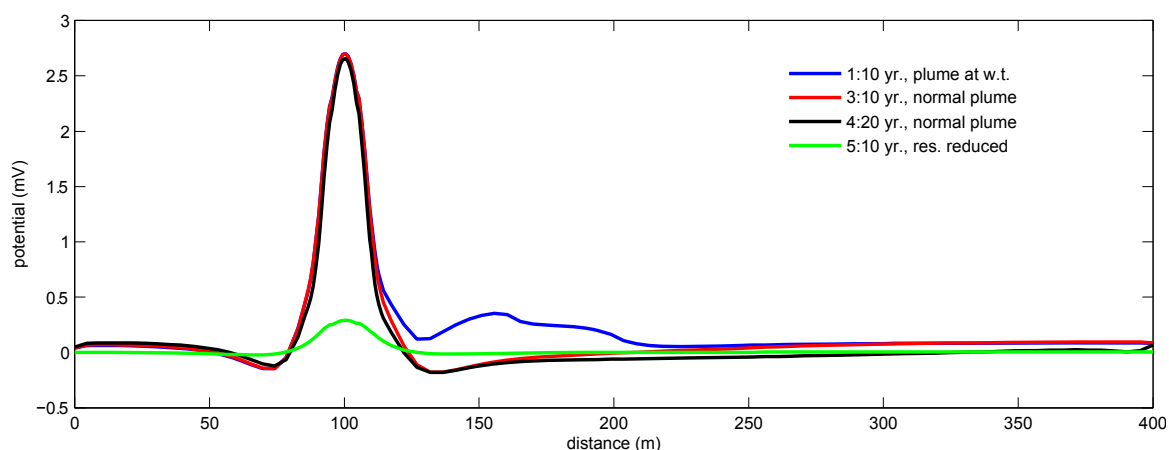


**Figure 6.27** SP calculated at the surface for the four tests using the diffusion model. Abbreviations : yr.–year, w.t.–water table, res.–resistivity.

Using the Eh model with a resistive transition zone, all tests produced SP anomalies greater than 100 mV at the surface and showed the largest variation between tests (Figure 6.28). Test 1 creates very large redox gradients at a sharp boundary, the water table. Since the gradients across the transition zone are the greatest in this test, so are the source terms and spontaneous potential generated. When the plume is deeper in the aquifer, displacing the transition zone from the water table (test 2), to the plume edge (test 3) increased the amplitude of the anomaly seen at the surface because the transition zone was moved to the area of highest redox gradients. Placing the transition zone along the plume edge also allows definition of the plume extent, as can be seen by comparing tests 3 and 4. In test 5 the ground resistivity is reduced everywhere, which means the source terms are larger but the electric signal dissipates faster so the SP at the surface is of smaller magnitude than

the previous tests. Test 7 can be compared with test 3 as the only difference between them is the method used for calculating Eh. The combined Eh calculated using the oxygen and methane couples has larger gradients but they are deeper and in a more conductive area so they produce a signal smaller than that of test 3. The last test, 8, can also be compared with test 3 as the only difference in this case is that the transition zone encircles the plume. It produces a dipolar anomaly with a positive peak above the spill zone (100 m).

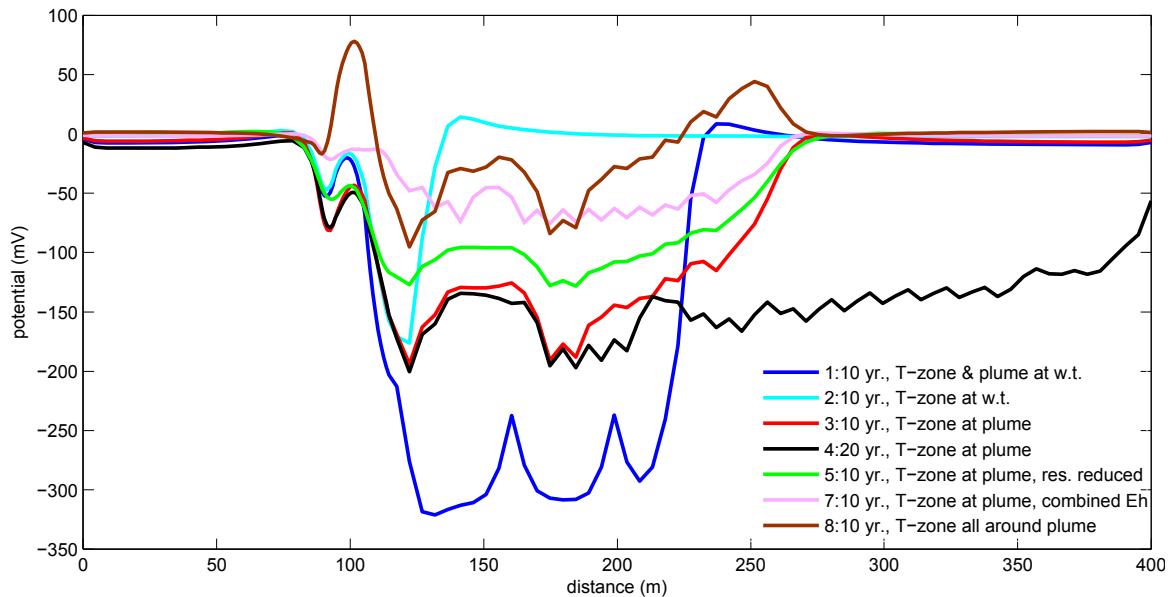


**Figure 6.28** SP calculated at the surface for the seven tests using the Eh model with resistive transition zone. Abbreviations :T-zone–transition zone, yr.–year, w.t.–water table, res.–resistivity.

The test results using the Eh model with conductive transition zone (Figure 6.29) are similar to the diffusion results for the tests 1, 2, 3, 4 and 6 in that there are no measurable SP anomalies at the surface. Below ground the results are different because the source terms are six orders of magnitude larger and the potentials two orders of magnitude greater. As mentioned before (sub-section 6.3.1), the source magnitudes up to several hundreds of amperes are huge and they will be compared with experimental data in the discussion (sub-section 6.4.2). The resistivity contrast between the ground and transition zone causes the current to stay channelled in the conductive transition zone and there is no surface expression of surprisingly large potential anomalies 6 m below the ground surface. Test 5 is the exception because the ground resistivity is reduced everywhere, the

contrast with the transition zone resistivity is smaller and the current travels more freely throughout the model domain. In this case the SP anomaly at the surface is almost the same as if the transition zone were resistive. When an anisotropic transition zone is used (test 6) the sources generated are a bit smaller than for a uniformly conductive transition zone but the currents still stay channelled in the zone so that there is no surface expression.

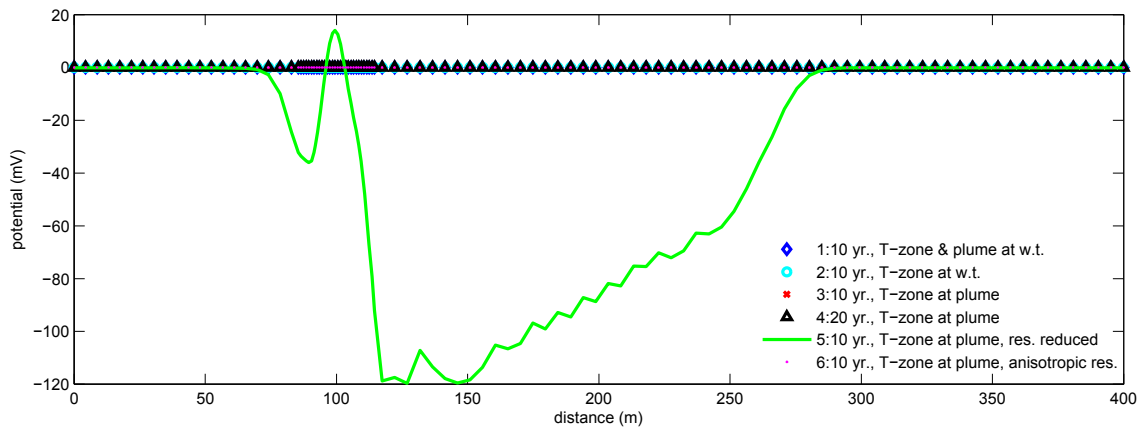


**Figure 6.29** SP calculated at the surface for the six tests using the Eh model with conductive transition zone. Abbreviations: T-zone—transition zone, yr.—year, w.t.—water table, res.—resistivity.

The conductivities of the transition zone and background are important in determining the magnitude of the surface signal. The conductivity contrast can be altered in two ways; by changing the background conductivity or by changing the transition zone conductivity. The first method is relevant if the transition zone conductivity is known and kept constant while the model is tested for various environments with different conductivities. If the transition zone conductivity is unknown, the second method can be used to explore the sensitivity of potentials generated. Trials run with both methods (Figure 6.30 LEFT & MIDDLE) produced resistivity contrast-vs.-surface SP anomaly curves with the same shape (Figure 6.30 RIGHT). For these graphs, since the background conductivity is not uniform, the mean conductivity of elements in the transition zone was used to represent bulk conductivity.

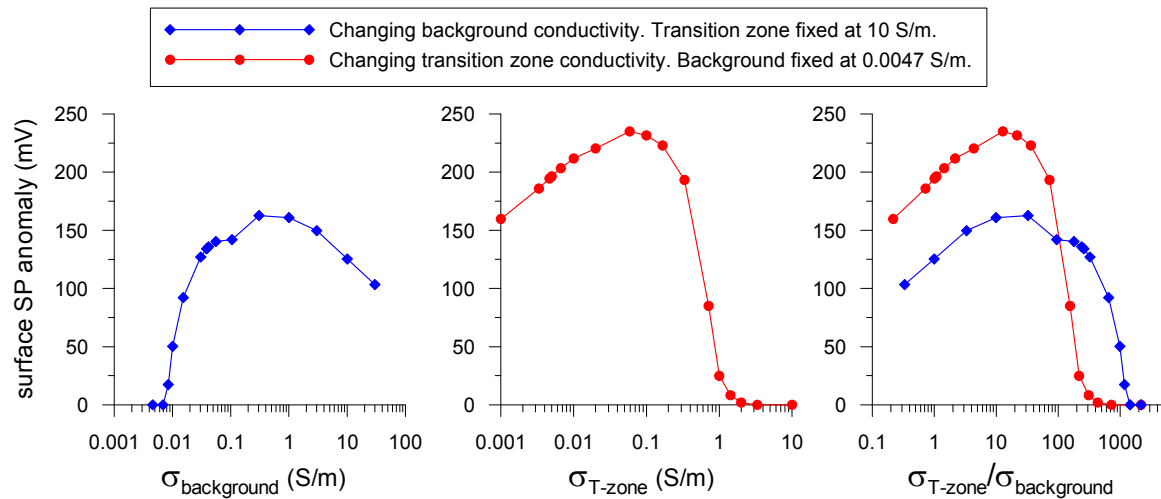


**Figure 6.30** Effect of changing the model resistivity on the SP anomaly measured at the surface. **LEFT:** Background conductivity is varied while transition zone is fixed at 10 S/m. The mean conductivity of elements in the transition zone is used as background. **MIDDLE:** Transition zone conductivity is varied while the background is fixed at 0.0046 S/m. **RIGHT:** The data of the first two graphs plotted against the transition zone to background conductivity ratio.

There are three factors related to conductivity affecting the magnitude of the surface SP anomaly generated by the Eh model:

- 1) Background conductivity: The potential at the surface decreases as background conductivity increases because at very high conductivities the signal dissipates as the effect of positive and negative sources cancel each other.
- 2) Conductivity of the transition zone: Since the source generating mechanism, the redox potential gradient, does not change, the magnitude of the sources increase linearly with transition zone conductivity, causing an increase in potentials at the surface.
- 3) Conductivity contrast between the transition zone and background: The larger the contrast between the conductivity of the transition zone and the background, the more current will stay channelled in the transition zone, reducing surface SP anomalies.

The curves in Figure 6.30 show a combination of influences. When the transition zone conductivity is kept constant (Figure 6.30 LEFT & RIGHT), at first the surface signal increases as the background conductivity is increased because less current is channelled in the transition zone. However, as the background conductivity rises past 1 S/m to unrealistically high values, the whole medium is so conductive the potentials reaching the surface are reduced. If the background conductivity is kept constant (Figure 6.30 MIDDLE & RIGHT), at first the potentials at the surface increase as the increasing transition zone conductivity causes the source magnitudes to increase. Yet as the transition zone conductivity increases further, current channelling in this zone arises, which reduces the surface SP signal.

As discussed in section 6.1.2, 10 S/m is a plausible biofilm conductivity and if this value is assigned to the transition zone, surface SP anomalies are only produced if the background conductivity is more than 0.0073 S/m (136  $\Omega\text{m}$ ) based on the linear relation in Figure 6.30 LEFT. To generate a 20 mV anomaly that might be measured with a field survey, the background conductivity must be more than 0.0084 S/m (120  $\Omega\text{m}$ ).

## 6.4 Discussion

This discussion will integrate the work from chapters 4, 5 and 6 with literature examples presented in chapter 2 to explore which theoretical models best describe field data. Separate sub-sections discuss different elements. The field results from chapter 5 are interpreted in light of the modelling results in sub-section 6.4.1. The huge source magnitudes of the conductive transition zone Eh models are so large they seem unrealistic so they are compared with experimental data in sub-section 6.4.2. A critical review of mechanisms that could cause large surface SP anomalies present in literature is found in sub-section 6.4.3.

### 6.4.1 INTERPRETATION OF RIVER AND KNOLL SITE DATA

The aim of the previous section's calculations was to test different theoretical models on a data set that served as a surrogate for the RIVER and KNOLL field sites presented in

chapter 5. The diffusion model does not generate potentials larger than a few millivolts, even with high concentration gradients caused by redox reactions in a contaminant plume. Since the Eh model with resistive transition zone generates surface SP anomalies, it could not be used to explain the data measured at the RIVER and KNOLL sites. The Eh model with conductive transition zone could be used if the resistivity contrast between transition zone and background were greater than approximately three orders of magnitude. The diffusion model is preferred for interpretation of the RIVER and KNOLL data because it does not require the invoking of electronic conductors in the ground.

A comparison of tests 3 and 5, where only the ground resistivity changes, demonstrates the SP signal sensitivity to resistivity. The low ground resistivities at both field sites studied will dissipate the current from any possible sources, causing the potential anomalies associated with the sources to be extremely localized, and it might contribute to the fact no electrochemical SP anomaly was measured at the surface.

#### 6.4.2 CURRENT DENSITY AND REACTION RATE CONSIDERATIONS FOR EH MODEL

To evaluate the values calculated with the Eh model in the previous section it is necessary to compare them with experimental data. This can be done using two related metrics: current density and reaction rates. Current densities are reported in  $A/m^2$  where the total current is normalized by the electrode surface area. For the results of section 6.3, the normalization area is the surface area of the transition zone ( $2 \times 178.4 \text{ m} \times 20 \text{ m}$ ) since current values are calculated for the entire zone.

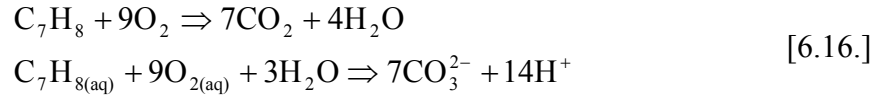
These results are compared with values reported in literature in Table 6.6. Current density from the Eh model with resistive transition zone is approximately the same as that measured over a sulphide conductor. Current density for the Eh model with a conductive transition zone is higher than that of any experimental data, even microbial fuel cells.

**Table 6.6 Compilation of experiments with instances of electrochemical SP where current densities and power densities were reported. Abbreviations: med.–median.**

<b>experiment</b>	<b>authors</b>	<b>maximum current density (mA/m<sup>2</sup>)</b>
field measurements over sulphide conductor	Lile (1996)	6.2
laboratory experiment with sulphate reducing bacteria in a sand column	Williams et al. (2007)	275
compilation of data from 10 microbial fuel cells	Nevin et al. (2008)	44-6000 med. 783
Eh model with resistive transition zone (~0.0046 S/m) using simulated toluene biodegradation data	sub-section 6.3.3	4.0
Eh model with conductive transition zone (10 S/m) using simulated toluene biodegradation data	sub-section 6.3.3	8800

The second metric, reaction rates, is more complex so it involves assumptions and simplifications. Current is a measure of the flux of charge and for the Eh model the charge is electrons produced by redox reactions. Therefore it is possible to calculate the reaction rates necessary to sustain a given current production and this rate can be compared with measured values. Measuring biodegradation reaction rates can be done *in situ* using respiration rates or pollutant mass depletion rates. Field and microcosm measurements agree within error, which can be as high as  $\pm 50\%$  (Baker et al., 2000; Cozzarelli et al., 2010). The rates typically follow first order models, where the rate is dependant on the concentration of compound to be degraded down to a threshold concentration below which degradation does not occur (Cozzarelli et al., 2010). In the field, the reaction rates are also depth dependent because the environments change (Baker et al., 2000). Baker et al. (2000) report a values of hydrocarbon degradation of 1.522 kg/m<sup>2</sup>-year in a gasoline contaminated aquifer by adding the degradation rates measured for zones at different depths multiplied by the thickness of those zones.

To compare the currents calculated in section 6.3 with the values reported by Baker et al. (2000), the biodegradation reaction considered will be the complete mineralization of toluene:



Both the aerobic and aqueous reactions (equation 6.16) involve a transfer of 36 electrons. The current density can be divided by this number and Faraday's constant and multiplied by the number of seconds in a year to find the toluene degradation rate.

$$\frac{8.8\text{A}}{\text{m}^2} \times \frac{\text{mol C}_7\text{H}_8}{36 \text{ mol e}^-} \times \frac{\text{mol e}^-}{96485.31 \text{ C}} \times \frac{\text{C/s}}{\text{A}} \times \frac{3.1536 \cdot 10^7 \text{ s}}{\text{year}} = 79.9 \frac{\text{mol C}_7\text{H}_8}{\text{m}^2 \cdot \text{year}} \quad [6.17.]$$

The toluene degradation rates for the Eh model are 79.9 mol C<sub>7</sub>H<sub>8</sub>/m<sup>2</sup>·year with an conductive transition zone (10 S/m) and 0.0363 mol C<sub>7</sub>H<sub>8</sub>/m<sup>2</sup>·year with a resistive zone (~0.0046 S/m). The value reported by Baker et al. (2000) was for weathered gasoline degradation, which has a biodegradation rate within an order of magnitude of that of toluene. If the respiration rates estimated by Baker et al. (2000) are converted to toluene mineralization, it yields 15.8 mol C<sub>7</sub>H<sub>8</sub>/m<sup>2</sup>·year. This falls between the values calculated with the Eh model.

Reported current densities and degradation rates can be used to bound possible conditions under which the Eh model could occur. With the Eh model, the current density and reaction rate are directly dependent on the transition zone conductivity. For the toluene biodegradation example presented in section 6.3, the transition zone conductivity was varied while the background conductivity remained as in Figure 6.4. Resulting variations of current density-vs.-surface SP anomaly and degradation rate-vs.-surface SP anomaly are scaled versions of Figure 6.30 MIDDLE. These are plotted with the limits from available data (Figure 6.31). The current density range is that of the data compiled in Table 6.6 and includes the density generating the largest surface SP anomaly (235 mV)(Figure 6.31 LEFT). The toluene degradation rate is bounded one order of magnitude

above and below the value reported by Baker et al. (2000) and limits the maximum surface SP anomaly (219 mV)(Figure 6.31 MIDDLE).

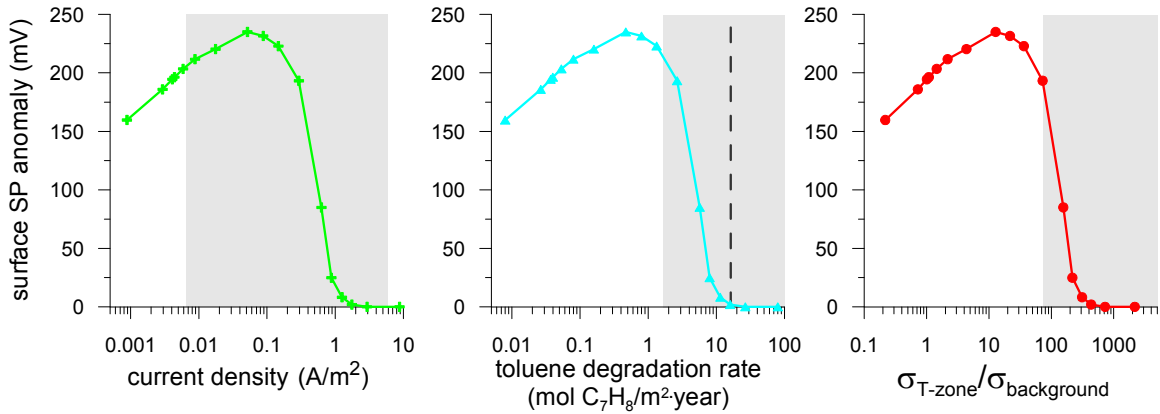


**Figure 6.31 Magnitude of surface SP anomaly associated with varying current density (LEFT), toluene degradation rate (MIDDLE) and transition zone to background conductivity ratio (RIGHT). The gray boxes are plausible limits from: compiled data (LEFT), an order of magnitude either side of the value reported by Baker et al. (2000) (dashed line) (MIDDLE), and implications of model assumptions (RIGHT).**

Another factor limiting the surface SP anomaly magnitude is the Eh model assumption that most of the redox current is carried by electrons. Revil et al. (2009) implement this by setting the Hittorf transport number of electrons to one and that of all other charge carriers (ions) to zero. The definition of the Hittorf transport number ( $t_i$ ) is (Bard & Faulkner, 2001, eq. 2.3.11):

$$t_i = \frac{|z_i|u_i c_i}{\sum_i |z_i|u_i c_i} \quad [6.18.]$$

where  $z_i$ ,  $u_i$  and  $c_i$  are the valence, mobility and concentration of species  $i$ . Revil et al. (2009) include electrons as a species so that the denominator of equation 6.18 could be written explicitly as:

$$\sum_i |z_i|u_i c_i + |-1|u_{e^-} c_{e^-} \quad [6.19.]$$

To safely assign a Hittorf transport number of zero to all ions, one could assume that their contribution to equation 6.19 is 100 times smaller than the contribution of electrons, which allows the quantification of the electron contribution:

$$\sum_i |z_i|u_i c_i + 100 \sum_i |z_i|u_i c_i \quad [6.20.]$$

The expression in the denominator of equation 6.18 is exactly that found multiplied by Faraday's constant ( $\mathcal{F}$ ) in the calculation of fluid conductivity ( $\sigma_f$ )(equation 6.12):

$$\sigma_f = \mathcal{F} \sum_i |z_i| u_i c_i \quad [6.21.]$$

Therefore, the minimum transition zone conductivity ( $\sigma_{T\_zone}$ ) necessary for the Eh model is:

$$\sigma_{T\_zone} = \frac{(\sigma_f + 100\sigma_f) + \sigma_s}{F_a} \quad [6.22.]$$

where  $\sigma_s$  is the surface conductivity and  $F_a$  is the apparent formation factor. For the toluene degradation model tested, this is equivalent to a transition zone 76 times more conductive than background and it limits the maximum surface SP anomaly (182 mV)(Figure 6.31 RIGHT).

The calculations in this sub-section demonstrate that the Eh model can generate large surface SP anomalies (>100 mV) under specific circumstances. Counter-intuitively, these conditions are when the transition zone is inefficient; it is not very conductive, few electrons are being transferred and biodegradation rates are low. This brings to light the fact that the Eh gradients were held constant during the calculations while in reality they would vary. Slow biodegradation rates would not produce the strong Eh gradients present in the MIN3P simulation data.

When modelling the degradation of toluene with MIN3P, Mayer et al. (2002) used an aerobic toluene mineralization rate of  $2.0 \cdot 10^{-10}$  mol/L·s, based on laboratory experiments reported by Baker et al. (2000). Based on these and other laboratory experiments, Baker et al. (2000) integrated degradation rates at different depths to estimate an average rate in the field, 15.8 mol/m<sup>2</sup>·year, which is the rate used earlier in this discussion. The MIN3P simulation involved many other reactions, including other toluene mineralization pathways, but their rates are all at least one order of magnitude smaller than aerobic degradation, so the total toluene mineralization rate can be approximated as 15.8 mol/m<sup>2</sup>·year. This is the rate that produced the Eh distribution used for modelling and the

calculated surface SP anomaly for this rate is only 2 mV (Figure 6.31 MIDDLE, dashed line).

A positive aspect of the Eh model is that it underlines the link between reaction rates and source currents. Though the link appears to be more complex than this model proposes, redox reactions involve an exchange of charge so their rates will necessarily control the magnitude of redox currents. Other factors would also exert controls on the cumulative redox current magnitude, such as the diffusion rate of reactants and products to and from the reaction site, pH, temperature and the extent of alignment of reaction dipoles on a reaction front.

#### 6.4.3 *MECHANISMS CAUSING LARGE SP ANOMALIES OVER CONTAMINANT PLUMES*

Some studies presented in chapter 2 reported negative anomalies greater than 50 mV measured over contaminant targets (Perry, 1997; Shi, 1998; Vichabian et al., 1999; Nyquist & Corry, 2002; Naudet et al., 2003) and it would be nice to understand the mechanisms producing large SP anomalies only on certain sites. SP measurements will delineate areas with anomalously high current densities. These can be due to either anomalously high electric fields or conductivities (Hamilton, 2000). Electric field anomalies are discussed in a first sub-section (6.4.3.1). Mechanisms involving high conductivity have been the focus of most explanations of electrochemical SP. Conductivity quantifies the ease with which electrical charge moves through a medium and it can be carried either by electrons or ions. The two charge carriers will be discussed in turn in sub-sections 6.4.3.2 and 6.4.3.3

##### 6.4.3.1 *Electric field anomalies*

According to Hamilton (2000) an electrochemical gradient represents a field of electrical potential in an electrolyte. As principal electrochemical gradient he used the redox potential gradient in the ground due to oxygen diffusion. Presumably, this would also apply to redox gradients present in a degrading contaminant plume. Hamilton's (2000) proposition is disproven by Revil et al. (2009) who demonstrate in a laboratory

experiment that in the presence of exceedingly large Eh anomalies (1100 mV), the resulting SP anomaly is modest (36 mV). No other source generating anomalous electric fields has been proposed to explain SP anomalies.

#### 6.4.3.2 *Current anomalies with electrons as charge carriers*

Revil and co-workers (Revil et al., 2009; Revil et al., 2010) focus on electrons as charge carriers and postulate a transition zone where current is carried electronically by microbial mats of organisms degrading organic contaminants in a plume, citing work by Ntarlagiannis et al. (2007) and Gorby et al. (2006). The research of these authors is part of a bigger body of work done on microbial fuel cells. In the past five years researchers have learned some of the mechanisms microorganisms use to transfer electrons during the oxidation and reduction reactions they mediate. Two of these mechanisms are: (1) direct contact, sometimes through pili also named ‘nanowires’, and (2) redox shuttles, soluble components produced by the bacteria (Rabaey et al., 2007). In microbial fuel cells the microbial mats that form on the anode are efficient conductors (Torres et al., 2008). Lovley (2008a) cautions against applying these ideas directly to field cases:

*“...even when carbon sources are being added to sedimentary environments, such as during in-situ bioremediation, the density of cells is relatively low and therefore, organised confluent biofilms are not expected.”*

Given that only a few microbial species have been found to form conductive mats and they would not likely form continuous zones in natural environments, electron transferring transition zones might only occur under very special circumstances. Nevertheless, if one adopts the Eh model, it can generate surface SP anomalies of an appropriate magnitude and polarity under specific circumstances (sub-section 6.4.2). The conditions necessary are strong Eh gradients and a relatively resistive transition zone, which for the toluene biodegradation simulation data modelled was a transition zone to background conductivity ratio between 80 and 200. The resistive transition zone implies

reaction rates are relatively low and it is not known if it would be possible to set up strong Eh gradients in a groundwater plume under these conditions.

Another possibility for electronic conduction is proposed by Nyquist & Corry (2002), who believe that the SP survey equipment is the electronic conductor and that SP anomalies are created by galvanic currents. When two electrodes connected by a wire are placed in areas with different redox potentials, electrical current will flow as described by the Nernst equation (2.18). Most field surveys are done with both electrodes located in the vadose zone, which has relatively uniform redox potentials. These surveys would not produce SP anomalies, but surveys where one electrode is placed directly in the reduced zone could measure significant SP anomalies.

This hypothesis is supported by measurements reported by Greenhouse & Harris (1983) over a landfill in Borden, Ontario. The SP data measured at the ground surface are not presented, but are described: “ a self potential survey was used unsuccessfully in an attempt to map the contaminants through variations in the streaming potential across the plume” (Greenhouse & Harris, 1983). Any anomaly present was likely smaller than 20 mV given the typical noise associated with SP surveys. However, SP measured in wells drilled for monitoring showed a positive anomaly through the plume (Figure 6.32)

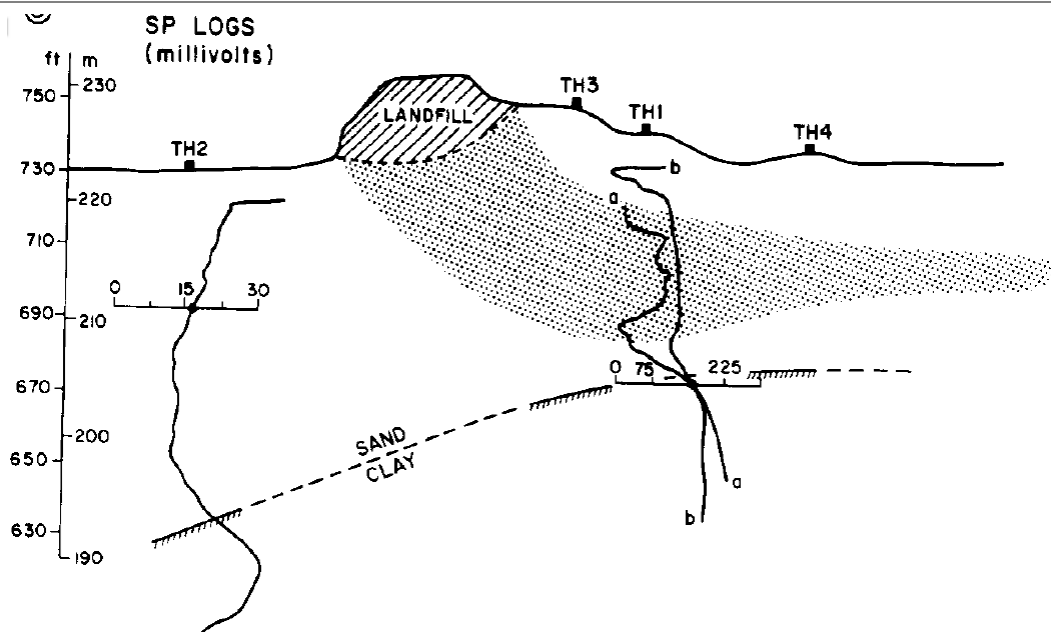


Figure 6.32 SP logs with units of millivolts. The gradual decrease in the response with depth at TH2 from 220 to 200 m is not thought to represent lithological change. The sand-clay boundary is seen as a gradual transition in all cases. Curve a at TH1, measured immediately after drilling was complete, appears to respond to the contaminant plume. Curve b, measured 2 days later, may also respond to the plume but more weakly and over a broader zone. This change in response probably reflects borehole mixing during the intervening time. (Greenhouse & Harris, 1983) This figure is a cross-section through the centre of the plume parallel to the direction of groundwater flow. The stippled area is the contaminant plume, defined as the area enclosed by the  $1000 \mu\text{S}/\text{cm}$  conductivity contour.

#### 6.4.3.3 Current anomalies with ions as charge carriers

The second type of charge carrier is ions. They migrate in response to forces described by the phenomenological equations. Mass transfer will not occur in response to redox gradients alone (Hamilton, 1998; Timm & Möller, 2001) but an ion flux will be produced by gradients in electrical potential, pressure, temperature, and concentration. An anomalously high electrical current due to ions in a contaminant plume must be explained by these forces when only abiotic forces are considered. The gradient of the electrical field was discussed in sub-section 6.4.3.1 and it will not be considered further as it is thought to be an effect and not a cause. The other forces will be discussed in turn.

Gradients in pressure create a flux in the ion-carrying liquid and generate streaming potentials. According to the results presented in chapter 4, the presence of a contaminant plume will alter the streaming current coupling coefficient but will not have a significant impact on the signatures measured in the field. An exception may be a site with an exceedingly high streaming potential signature such as Entressen (Naudet et al., 2004).

Gradients in temperature have not been considered to date as this phenomenon is generally considered very minor. Nourbehecht (1963) calculated that the thermoelectric response of a nuclear blast 30 m underground would produce a maximum potential of 24 mV with a 2.6 mV SP signature at the surface. His calculation method requires a difference in temperature and a difference in thermal coupling coefficients. Reactions in a contaminant plume can increase the temperature either through abiotic exothermic reactions or heat generated by metabolic activity. The temperature contrast between the inside of the plume and background values is typically 2-5 °C (MacFarlane et al., 1983; Sogade et al., 2006). Values for thermal coupling coefficients ( $CC$ ) range from 0 to 1.4 mV/°C with typical values of 0.2 to 0.5 mV/°C, so the difference in coefficients might be 0.2 to 0.3 mV/°C (Nourbehecht, 1963). The maximum potential anomaly can be calculated and with the typical values this gives:

$$\Delta V = \Delta T \cdot CC = (5^\circ\text{C})(0.3\text{mV}/^\circ\text{C}) = 1.5\text{ mV} \quad [6.23.]$$

The surface SP anomaly would be even smaller than the maximum value of 1.5 mV and this source can also be safely neglected. It is interesting to note that the 1.5 mV thermoelectric SP is only three times smaller than the magnitude of diffusion SP calculated as ~5 mV in the previous section (ex. sub-section 6.3.3).

The redox reactions occurring in a contaminant plume create very strong concentration gradients. The ion fluxes generated are not enough to create large SP anomalies according to the calculations made with the diffusion model in section 6.3. An uncertainty in these calculations is the diffusion coefficients used, which were those at infinite dilution. Within a degrading plume, ionic concentrations are relatively high, which could alter the

diffusion coefficients. Activities were used in the calculations instead of concentrations to account for the varying ionic concentrations, but it is not known if this properly describes changes in the diffusion coefficient.

None of the forces discussed seems capable of generating potential anomalies at the surface with magnitudes of tens of millivolts. A caveat was included in the discussion of forces causing ion fluxes which was that they were abiotic. If biotic processes are considered there are perhaps additional forces at play.

In the presence of an organic contaminant, bacterial cell populations increase exponentially after an acclimation period and remain high as long as the source of carbon persists (Alexander, 1999). It is conceivable that the micro-organisms have a significant impact on the movement of charged species. The Eh model attempts to quantify this impact using electronic conductors. This model has weaknesses discussed in sub-section 6.4.2 and perhaps another model might be more appropriate. The high bacterial populations will have an effect on the distribution and movement of elements that make up bacterial cells. For example, calcium is a component of bacterial cells where it acts as a major cation in cell processes and enzyme cofactor (Eweis et al., 1998) and perhaps its movement in a contaminant plume is not adequately described by abiotic diffusion processes.

### **6.5 Summary**

The aims of this chapter were to model something similar to the field data presented in chapter 5 and identify conditions necessary to produce large surface SP anomalies. Based on calculations using toluene biodegradation simulation data, the diffusion model explains why no SP signature was visible at the RIVER and KNOLL sites since the surface SP anomaly expected is below measurement noise levels.

To produce large surface SP anomalies with the models tested using toluene degradation simulation data, it is necessary to apply the Eh model with a transition zone that is

between 80 to 200 times more conductive than the background. The reaction rates implied by these conductivities are lower than those used in the toluene degradation simulation, which would likely reduce the Eh gradients and consequently the surface SP anomaly magnitude. As well, these transition zone conductivities are lower than those measured for biofilms, which are postulated to conduct electrons in this zone. Biotic mechanisms might generate large SP anomalies but if and how they do so under field conditions remains speculative.



## 7 CLOSING REMARKS

Spontaneous potential surveys have been used for over 100 years and yet their interpretation remains largely qualitative. To further the development of this geophysical method it is necessary to move towards quantitative interpretation, which requires a detailed understanding of the mechanisms generating spontaneous potentials. This challenge has yet to be met though there are interesting possibilities such as the overpotential model of Stoll et al. (1995) and the redox potential model of Arora et al. (2007)

This work focused on SP over contaminant plumes because it appeared to be a promising and simple method of delineating degrading organic contaminant plumes in groundwater from the ground surface. The redox gradients present in such plumes were thought to generate anomalies similar to those over sulphide mineral deposits, which have been studied more thoroughly. The goal of this research was to better understand causative mechanisms in order to define under what field conditions mapping contaminants with SP would be applicable.

### 7.1 Principle results

Three principle sources of spontaneous potentials, thermoelectric, electrokinetic and electrochemical, act simultaneously so that the signal is the sum from all sources. When investigating SP over contaminant plumes, signals of electrochemical origin are the target so contributions from the two other sources have to be accounted for and subtracted from the total signal. Anthropogenic sources also have to be identified, evaluated and subtracted. Thermoelectric sources are negligible but electrokinetic sources are thought to be significant. The electrokinetic potential is controlled by the double layer properties on the surface of sediments and we postulated that contaminants could alter these properties and affect SP. To test this hypothesis I built and calibrated a laboratory apparatus to measure the streaming potential coupling coefficient and resistivity of saturated sediment samples. These measurements can be used to determine the streaming current coupling coefficient ( $L'$ ) which is necessary for electrokinetic potential calculations. Experiments

were run with sediments from two field sites using both clean groundwater and hydrocarbon contaminated groundwater. The contamination had a significant impact on  $L'$ , which was reduced by 12-70% in 5 of the 6 tests. However, the changes in  $L'$  due to contaminants were smaller than the variation between samples. Numerical modelling that incorporated property variations on the order of those measured in the laboratory indicated that changes to streaming potential due to a contaminant plume would not have a measurable impact in the field.

To identify the field conditions necessary for effective mapping of contaminant plumes with SP, it is necessary to have detailed field data that includes both electrical and redox measurements, since these are the phenomena we are trying to link. Spontaneous potential and resistivity surveys were used to investigate two field sites with well documented degrading hydrocarbon plumes in groundwater. The thermoelectric and electrokinetic contributions to the measured SP on both sites were below the detection limit. On one of the sites it was necessary to correct the measured signal by removing anthropogenic noise. The remaining source of SP on both sites was presumably electrochemical, but there was no significant relationship between the corrected SP and measured redox conditions. This demonstrated that the link between SP and redox gradients from degrading organic contaminant plumes is not present on all sites.

When investigating causative mechanisms, field studies can be difficult to analyse because of a number of uncontrolled or unknown variables. Numerical modelling can be an effective tool for testing hypotheses if the models are credible. Two hypotheses, the diffusion and redox theoretical models, were tested by implementing them in a finite element programme. MIN3P simulation data for the biodegradation of a hypothetical toluene spill were used as input for the tests. The very high concentration gradients present in a plume because of redox reactions did not produce surface SP anomalies above survey detection limits with the diffusion model. The redox model postulates a link between SP and redox gradients with a transition zone, perhaps composed of microbial mats, where charge transfer is electronic. Using numerical modelling, I found that if the

transition zone was relatively conductive, the current stayed channelled in this zone and no potential anomaly was produced at the ground surface. To create an SP anomaly at the surface it was necessary to use a relatively resistive transition zone without changing Eh gradients. This challenges the redox model because the low conductivity in the transition zone implies low reaction rates, which do not lead to the strong redox gradients necessary to generate large surface SP anomalies.

## 7.2 Summary

Spontaneous potential has always been a difficult method because the signal magnitudes are relatively small and the signals are very sensitive to noise. When SP is used for mineral exploration, the targets are typically in remote areas where anthropogenic noise is negligible. This is not the case for environmental applications of SP. Groundwater contaminants are the result of pipeline breaks, tank leaks, landfills and other human activities so there will almost always be anthropogenic noise on these sites. This means that to perform meaningful environmental surveys anthropogenic noise must be identified and accounted for in the measured SP signal. For example, Naudet et al. (2004) identified anomalies due to cathodically protected pipelines on their survey, determined the radius of influence and disregarded the impacted data.

Numerical modelling can be used to study electrochemical SP free from anthropogenic noise. It requires a valid theoretical model and the two available, diffusion and redox currents, were unable to generate measurable surface SP anomalies under plausible circumstances. Redox currents could generate such anomalies if the model used a relatively resistive transition zone which is inconsistent with the reaction rates required for strong Eh gradients on site. Possible explanations for the failure of these models to produce measurable surface potentials are:

- 1) Other unknown mechanisms correlated with the redox gradient are creating anomalies on contaminant sites.
- 2) Redox gradients are one of several factors creating SP anomalies and there is a direct link between redox and spontaneous potentials only under special

circumstances when the redox gradient is the limiting factor. Other factors might include reaction rates.

- 3) There is no direct link between redox gradient and spontaneous potential.

If the fourteen field studies reported in literature are critically revisited, no more than a tenuous link between redox gradients due to contaminant plumes and SP can be established. Only five of the studies present redox or dissolved oxygen data, which can be used as a surrogate for redox, along with SP data. Two of these five studies did not find strong correlations between redox and SP and additionally reported infrastructure on site that could have influenced the measured signal (Naudet, 2004; Che-Alota et al., 2009). A third study incorporates anthropogenic effects since Doherty et al. (2010) produce an intricate conceptual model for their site that includes buried metallic clinker and a backfilled hole through a clay aquiclude. The conditions at this field site are unlikely to be found anywhere else and the authors do not directly correlate redox and spontaneous potentials. This leaves only two field studies with a clear correlation between SP and redox (Nyquist & Corry, 2002; Naudet et al., 2003). The field work conducted as part of this study did not produce such correlations.

The theories presently available do not seem to explain the processes creating surface spontaneous potential anomalies over organic carbon rich contaminant plumes. Neither electrokinetic, diffusion nor redox currents can create significant surface SP anomalies, except when the redox model is used with paradoxical conditions. Therefore more theoretical work is required before being able to characterize the field conditions under which mapping contaminants with SP would be applicable.

### **7.3 Future work**

A new causative mechanism must be proposed to explain the large negative surface spontaneous potential anomalies that occur on certain sites with degrading organic contaminant plumes in the ground water because the available hypotheses are unable to.

If more field studies are undertaken, steps and field characteristics which might increase chances of success are:

- 1) Beginning the SP survey with high frequency variable voltage measurements and their spectral analysis to identify and characterize sources of anthropogenic noise on site. This would allow the surveyors to determine whether the noise will be problematic and if appropriate corrections can be made.
- 2) Sites where the ground is electrically resistive because any possible electrical potential anomalies will be larger in magnitude and extent.
- 3) Sites where the redox zonation in the groundwater plume is coherent and orderly, which is more likely to occur at a site with minimal variations in groundwater flow direction.

An avenue which was not explored in this work is the role of gas production during contaminant degradation. Gas bubbles could greatly alter the electrokinetic signature (Morgan et al., 1989) or might play a role in the electrochemical signal.



## REFERENCES

- Abdel Aal, G.Z., E.A. Atekwana, S. Rossbach & D.D. Werkema, 2010, Sensitivity of geoelectrical measurements to the presence of bacteria in porous media, *Journal of Geophysical Research*, **115**(G03017): 1-11, doi:10.1029/2009jg001279.
- Abdelrahman, E.-S.M., A.A.B. Ammar, H.I. Hassanein & M.A. Hafez, 1998, Derivative analysis of SP anomalies, *Geophysics*, **63**(3): 890-897, doi:10.1190/1.1444399.
- Abdelrahman, E.M., A.A. Ammar, S.M. Sharafeldin & H.I. Hassanein, 1997, Shape and depth solutions from numerical horizontal self-potential gradients, *Journal of Applied Geophysics*, **37**(1): 31-43, doi:10.1016/S0926-9851(96)00058-4.
- Ahmad, M.U., 1964, A laboratory study of streaming potentials, *Geophysical Prospecting*, **12**(1): 49-64, doi:10.1111/j.1365-2478.1964.tb01889.x.
- Alberta Environmental Appeal Board, 2002, \*\*\*\*\* v. Director, Enforcement and Monitoring, \*\*\*\*\*, Regional Services, Alberta Environment, 119 p.
- Alexander, M., 1999, Biodegradation and Bioremediation, 2<sup>nd</sup> edition, Academic Press, San Diego, CA, U.S.A., 453 p.
- Anneser, B., F. Einsiedl, R.U. Meckenstock, L. Richters, F. Wisotzky & C. Griebler, 2008, High-resolution monitoring of biogeochemical gradients in a tar oil-contaminated aquifer, *Applied Geochemistry*, **23**(6): 1715-1730, doi:10.1016/j.apgeochem.2008.02.003.
- Antraygues, P. & M. Aubert, 1993, Self potential generated by two-phase flow in a porous medium; experimental study and volcanological applications, *Journal of Geophysical Research*, **98**(B12): 22 273-22 281, doi:10.1029/93JB02395.
- Archie, G.E., 1942, The electrical resistivity log as an aid in determining some reservoir characteristics, *Transactions of the American Institute of Mining and Metallurgical Engineers*, **146**: 54-62.
- Arora, T., N. Linde, A. Revil & J. Castermant, 2007, Non-intrusive characterization of the redox potential of landfill leachate plumes from self-potential data, *Journal of Contaminant Hydrology*, **92**(3-4): 274-292, doi:10.1016/j.jconhyd.2007.01.018.
- Asfahani, J. & M. Tlas, 2002, A nonlinear programming technique for the interpretation of self-potential anomalies, *Pure and Applied Geophysics*, **159**(6): 1333-1343.
- Asten, M.W., 1974, The influence of electrical anisotropy on mise-à-la-masse surveys, *Geophysical Prospecting*, **22**(2): 238-245.

- ASTM International, 2007, D2488-06 Standard Practise for Description and Identification of Soil (Visual-Manual Procedure), in *Annual Book of ASTM Standards*, **04.08**: 251-261.
- Atekwana, E.A., E. Atekwana, F.D. Legall & R.V. Krishnamurthy, 2005, Biodegradation and mineral weathering controls on bulk electrical conductivity in a shallow hydrocarbon contaminated aquifer, *Journal of Contaminant Hydrology*, **80**(3-4): 149-167, doi:10.1016/j.jconhyd.2005.06.009.
- Atekwana, E.A., D.D. Werkema & E.A. Atekwana, 2006, Biogeophysics: The effects of microbial processes on geophysical properties of the shallow subsurface, in *Applied Hydrogeophysics*, edited by Vereecken, H., A. Binley, G. Cassiani, A. Revil & K. Titov, Springer, Dordecht, The Netherlands, 161-193.
- Aubert, M., 1999, Practical evaluation of steady heat discharge from dormant active volcanoes: case study *Journal of Volcanology and Geothermal Research*, **92**(3-4): 413-429.
- Baas Becking, L.G.M., I.R. Kaplan & D. Moore, 1960, Limits of the natural environment in terms of pH and oxidation-reduction potentials, *Journal of Geology*, **68**(3): 243-284.
- Baker, R.J., A.L. Baehr & M.A. Lahvis, 2000, Estimation of hydrocarbon biodegradation rates in gasoline-contaminated sediment from measured respiration rates, *Journal of Contaminant Hydrology*, **41**(1-2): 175-192, doi:10.1016/S0169-7722(99)00063-7.
- Baker, S.S. & J.P. Cull, 2004, Streaming potential and groundwater contamination, *Exploration Geophysics*, **35**(1): 41-44.
- Bard, A.J., R. Parsons & J. Jordan (Eds), 1985, *Standard Potentials in Aqueous Solutions*, Marcel Dekker, Inc., New York, NY, U.S.A., 834 p.
- Bard, A.J. & L.R. Faulkner, 2001, *Electrochemical Methods. Fundamentals and Applications*, 2<sup>nd</sup> edition, John Wiley & Sons, Inc., New York, NY, U.S.A., 833 p.
- Bavusi, M., E. Rizzo & V. Lapenna, 2006, Electromagnetic methods to characterize the Savoia di Lucania waste dump (Southern Italy), *Environmental Geology*, **51**(2): 301-308, doi:10.1007/s00254-006-0327-9.
- Bear, J., 1972, *Dynamics of Fluids in Porous Media*, Dover Publications, Inc., New York, NY, U.S.A., 764 p.

- Becker, W.M. & D.W. Deamer, 1991, *The World of the Cell*, 2nd edition, Benjamin/Cummings Publishing Company, Inc., Redwood City, CA, U.S.A, 886 p.
- Bentley, L.R. & N.M. Trenholm, 2002, The Accuracy of Water Table Elevation Estimates Determined from Ground Penetrating Radar Data, *Journal of Environmental & Engineering Geophysics*, **7**(1): 37-53.
- Bernabé, Y., 1998, Streaming potential in heterogeneous networks, *Journal of Geophysical Research*, **103**(B9): 20 827-20 841, doi:10.1029/98JB02126.
- Bernabé, Y., U. Mok, A. Mainault & B. Evans, 2003, Laboratory measurements of electrical potential in rock during high-temperature water flow and chemical reactions, *Geothermics*, **32**(3): 297-310, doi:10.1016/S0375-6505(03)00020-8.
- Bérubé, A.P., 2007, A graphical 3D finite element program for modelling self-potentials generated by flow through a porous medium, *Journal of Environmental & Engineering Geophysics*, **12**(2): 185-197, doi:10.2113/JEEG12.2.185.
- Bhattacharya, B.B. & N. Roy, 1981, A note on the use of a nomogram of self-potential anomalies, *Geophysical Prospecting*, **29**(1): 102-107.
- Bhattacharya, B.B., Shalivahan, A. Jardani & A. Bera, 2007, Three dimensional probability tomography of self-potential anomalies of graphite and sulphide mineralization in Orissa and Rajasthan, India, *Near Surface Geophysics*, **5**(4): 223-230.
- Bigalke, J. & E.W. Grabner, 1997, The Geobattery model: a contribution to large scale electrochemistry, *Electrochimica Acta*, **42**(23-24): 3443-3452.
- Birch, F.S., 1993, Testing Fournier's method for finding water table from self-potential, *Ground Water*, **31**(1): 50-56.
- , 1998, Imaging the water table by filtering self-potential profiles, *Ground Water*, **36**(5): 779-782.
- Bockris, J.O.M. & A.K.N. Reddy, 1998, *Electrochemistry 1. Ionics*, 2<sup>nd</sup> edition, Plenum Press, New York, NY, U.S.A., 767 p.
- Bockris, J.O.M., A.K.N. Reddy & M. Gamboa-Aldeco, 2000, *Electrochemistry 2A. Fundamentals of Electroics*, 2<sup>nd</sup> edition, Plenum Publishers, New York, NY, U.S.A., 771-1534 p.
- Bogart, T.F., 1988, *Electric Circuits*, Macmillan Publishing Company, New York, NY, U.S.A., 840 p.

- Bogolovsky, V.A. & A.A. Ogilvy, 1970, Natural potential anomalies as a quantitative index of the rate of seepage from water reservoirs, *Geophysical Prospecting*, **18**: 261-268.
- , 1972, The study of streaming potentials on fissured media models, *Geophysical Prospecting*, **20**: 109-117.
- , 1973, Deformations of natural electric fields near drainage structures, *Geophysical Prospecting*, **21**: 716-723.
- Bølviken, B., 1979, The redox potential field of the earth, *in* Origin and distribution of the elements. Second symposium on the origin and distribution of the elements, Paris, France, May, 1977, edited by Ahrens, L.H., Pergamon International, Oxford, England, 649-665.
- Bow River Basin Council, 2005, Nurture, Renew, Protect: A Report on the State of the Bow River, report #: 0-9737429-0-9, Calgary, AB, Canada, 202 p.
- Bruckshaw, J.M., 1931, Spontaneous Polarization Method - Theoretical Considerations, *in* The Principles & Practise of Geophysical Prospecting, edited by Edge, A.B.B. & T.H. Laby, Cambridge University Press, Cambridge, England, 242-245.
- Buselli, G. & K. Lu, 2001, Groundwater contamination monitoring with multichannel electrical and electromagnetic methods, *Journal of Applied Geophysics*, **48**(1): 11-23.
- Carrigy, M.A., 1971, Lithostratigraphy of the uppermost Cretaceous (Lance) and Paleocene strata of the Alberta plains, Alberta Research Council, 161 p.
- Castermant, J., C.A. Mendonça, A. Revil, F. Trolard, G. Bourrié & N. Linde, 2008, Redox potential distribution inferred from self-potential measurements associated with the corrosion of a burden metallic body, *Geophysical Prospecting*, **56**(2): 269-282, doi:10.1111/j.1365-2478.2007.00675.x.
- Chapelle, F.H., S.K. Haack, P. Adriaens, M.A. Henry & P.M. Bradley, 1996, Comparison of  $E_H$  and  $H_2$  Measurements for Delineating Redox Processes in a Contaminated Aquifer, *Environmental Science & Technology*, **30**(12): 3565-3569, doi:10.1021/es960249+.
- Chapman, D.L., 1913, A contribution to the theory of electrocapillarity, *Philosophical Magazine*, **25**(148): 475-481.

- Che-Alota, V., E.A. Atekwana, E.A. Atekwana, W.A. Sauck & D.D. Werkema, 2009, Temporal geophysical signatures from contaminant-mass remediation, *Geophysics*, **74**(4): B113-B123, doi:10.1190/1.3139769.
- Christensen, T.H., P.L. Bjerg, S.A. Banwart, R. Jakobsen, G. Heron & H.-J. Albrechtsen, 2000, Characterization of redox conditions in groundwater contaminant plumes, *Journal of Contaminant Hydrology*, **45**(3-4): 165-241.
- Christensen, T.H., P. Kjeldsen, P.L. Bjerg, D.L. Jensen, J.B. Christensen, A. Baun, H.-J. Albrechtsen & G. Heron, 2001, Biogeochemistry of landfill leachate plumes, *Applied Geochemistry*, **16**(7-8): 659-718.
- Cockett, R., 2011, Student, Dept. of Geoscience, University of Calgary, Estimates of biofilm conductivities based on laboratory work by Regberg et al. (2011), in prep.
- Corry, C.E., 1985, Spontaneous polarization associated with porphyry sulfide mineralization, *Geophysics*, **50**(6): 1020-1034, doi:10.1190/1.1441967.
- , 1994, Investigation of ferroelectric effects in two sulphide deposits, *Journal of Applied Geophysics*, **32**(1): 55-72.
- Corwin, R.F. & D.B. Hoover, 1979, The self-potential method in geothermal exploration, *Geophysics*, **44**(2): 226-245, doi:10.1190/1.1440964.
- Corwin, R.F., 1989, Data quality for engineering self-potential surveys, in *Detection of subsurface flow phenomena*, edited by Merkle, G.-P., H. Militzer, H. Hötzl, H. Armbruster & J. Brauns, Springer-Verlag, Berlin, Germany, 51-72.
- , 1990, The Self-Potential Method for Environmental and Engineering Applications, in *Geotechnical and Environmental Geophysics*, edited by Ward, S.H., Society of Exploration Geophysicists, Tulsa, OK, U.S.A., 127-145.
- , 2005, Self-potential field data acquisition manual, report #: T992700-0205B, CEA Technologies Inc., Montréal, QC, Canada.
- Coyne, M.S. & J.A. Thompson, 2006, *Fundamental Soil Science*, Thomson Delmar Learning, Clifton Park, NY, U.S.A., 403 p.
- Cozzarelli, I.M., M.J. Baedecker, R.P. Eganhouse & D.F. Goerlitz, 1994, The geochemical evolution of low-molecular-weight organic acids derived from the degradation of petroleum contaminants in groundwater, *Geochimica et Cosmochimica Acta*, **58**(2): 863-877.
- Cozzarelli, I.M., B.A. Bekins, R.P. Eganhouse, E. Warren & H.I. Essaid, 2010, In situ measurements of volatile aromatic hydrocarbon biodegradation rates in

- groundwater, *Journal of Contaminant Hydrology*, **111**(1-4): 48-64, doi:10.1016/j.jconhyd.2009.12.001.
- Cull, J.P., 1985, Self potential and current channelling, *Geophysical Prospecting*, **33**: 460-467.
- Davies, C.W., 1962, Ion Association, Butterworths & Co. Ltd., London, England, 190 p.
- Davis, C.A., E. Atekwana, E. Atekwana, L.D. Slater, S. Rossbach & M.R. Mormile, 2006, Microbial growth and biofilm formation in geologic media is detected with complex conductivity measurements, *Geophysical Research Letters*, **33**(L18403): 1-5, doi:10.1029/2006gl027312.
- Davis, J.A., R.O. James & J.O. Leckie, 1978, Surface ionization and complexation at the oxide/water interface I. Computation of electrical double layer properties in simple electrolytes, *Journal of Colloid and Interface Science*, **63**(3): 480-499.
- Davis, J.A. & D.B. Kent, 1990, Surface complexation modeling in aqueous geochemistry, *in* Mineral-water Interface Geochemistry, edited by Hochella, M.F., Jr. & A.F. White, Mineralogical Society of America, Washington, DC, U.S.A., 177-260.
- de Witte, L., 1948, A new method of interpretation of self-potential field data, *Geophysics*, **13**(4): 606-608.
- Demir, I., 1988, The interrelation of hydraulic and electrical conductivities, streaming potential, and salt filtration during the flow of chloride brines through a smectite layer at elevated pressures, *Journal of Hydrology*, **98**(1-2): 31-52.
- Dey, A. & H.F. Morrison, 1979, Resistivity modelling for arbitrarily shaped two-dimensional structures, *Geophysical Prospecting*, **27**(1): 106-136.
- Doherty, R., B. Kulesa, A.S. Ferguson, M.J. Larkin, L.A. Kulakov & R.M. Kalin, 2010, A microbial fuel cell in contaminated ground delineated by electrical self-potential and normalized induced polarization data, *Journal of Geophysical Research*, **115**(G00G08): 1-11, doi:10.1029/2009jg001131.
- Domenico, P.A., 1977, Transport phenomena in chemical rate processes in sediments, *Annual Review of Earth and Planetary Sciences*, **5**: 287-317.
- Domenico, P.A. & F.W. Schwartz, 1998, Physical and Chemical Hydrogeology, 2<sup>nd</sup> edition, John Wiley & Sons Inc., New York, NY, U.S.A., 506 p.
- Doussan, C., L. Jouniaux & J.-L. Thony, 2002, Variations of self-potential and unsaturated water flow with time in sandy loam and clay loam soils, *Journal of Hydrology*, **267**(3-4): 173-185.

- Dukhin, S.S., 1974, Development of notions as to the mechanisms of electrokinetic phenomena and the structure of the colloid micelle, *in* Surface and Colloid Science, edited by Matijević, E., John Wiley & Sons Inc., New York, NY, U.S.A., 1-47.
- EBA Engineering Consultants Ltd., 2006, Summary of 2005 groundwater monitoring activities. Former \*\*\*\*\* Refinery, \*\*\*\*\* , Alberta, report #: 5340059.001, Calgary, AB, Canada, 15 p.
- El-Araby, H.M., 2004, A new method for complete quantitative interpretation of self-potential anomalies, *Journal of Applied Geophysics*, **55**(3-4): 211-224, doi:10.1016/j.jappgeo.2003.11.002.
- El-Naggar, M.Y., G. Wanger, K.M. Leung, T.D. Yuzvinsky, G. Southam, J. Yang, W.M. Lau, K.H. Neilson & Y.A. Gorby, 2010, Electrical transport along bacterial nanowires from *Shewanella oneidensis* MR-1, *Proceedings of the National Academy of Sciences*, **107**(42): 18127-18131, doi:10.1073/pnas.1004880107.
- Eloranta, E.H., 1988, The modelling of mise-à-la-masse anomalies in an anisotropic half-space by the integral equation method, *Geoexploration*, **25**(2): 93-101.
- Eskola, L. & H. Hongisto, 1987, A macroscopic physical model for the self-potential of a sulphide deposit, *Geoexploration*, **24**(3): 219-226.
- Eweis, J.B., S.J. Ergas, D.P.Y. Chang & E.D. Schroeder, 1998, Bioremediation Principles, McGraw-Hill, U.S.A., 296 p.
- Fitterman, D.V., 1976, Calculation of self-potential anomalies generated by Eh potential gradients, report #: OF 76-0098, U.S. Geological Survey, Reston, VA, U.S.A., 32 p.
- , 1978, Electrokinetic and magnetic anomalies associated with dilatant regions in a layered earth, *Journal of Geophysical Research*, **83**(B12): 5923-5928, doi:10.1029/JB083iB12p05923.
- , 1979, Calculations of self-potential anomalies near vertical contacts, *Geophysics*, **44**(2): 195-205, doi:10.1190/1.1440961.
- Fitterman, D.V. & R.F. Corwin, 1982, Inversion of self-potential data from the Cerro Prieto geothermal field, Mexico, *Geophysics*, **47**(6): 938-945, doi:10.1190/1.1441361.
- Fitterman, D.V., 1983, Modeling of self-potential anomalies near vertical dikes, *Geophysics*, **48**(2): 171-180, doi:10.1190/1.1441456.

- Fluke Corporation Inc., 2000, Model 187 & 189 True RMS Multimeter. User Manual, Fluke Corporation Inc., Everett, WA, U.S.A., 96 p.
- Fournier, C., 1989, Spontaneous potentials and resistivity surveys applied to hydrogeology in a volcanic area: Case history of the Chaîne des Puys (Puy-de-Dôme, France), *Geophysical Prospecting*, **37**(6): 647-668.
- Fox, R.W., 1830, On the electro-magnetic properties of metalliferous veins in the mines of Cornwall, *Philosophical Transactions of the Royal Society of London*, **120**: 399-414, doi:10.1098/rstl.1830.0027.
- Friborg, J., 1996, Experimental and theoretical investigations into the streaming potential phenomenon with special reference to applications in glaciated terrain, Ph.D. Thesis, Luleå University of Technology, Luleå, Sweden, 166 p.
- Furness, P., 1992, Modelling spontaneous mineralization potentials with a new integral equation, *Journal of Applied Geophysics*, **29**(2): 143-155.
- , 1994, A finite difference model for mineral self potentials in complex environments, *Journal of Applied Geophysics*, **32**(2-3): 235-243.
- Gibert, D. & M. Pessel, 2001, Identification of sources of potential fields with the continuous wavelet transform: Application to self-potential profiles, *Geophysical Research Letters*, **28**(9): 1863-1866, doi:10.1029/2000GL012041.
- Glover, P.W.J., P.G. Meredith, P.R. Sammonds & S.A.F. Murrell, 1994, Ionic surface electrical conductivity in sandstone, *Journal of Geophysical Research*, **99**(B11): 21 635-21 650, doi:10.1029/94JB01474.
- Gorby, Y.A., S. Yanina, J.S. McLean, K.M. Rosso, D. Moyles, A. Dohnalkova, T.J. Beveridge, I.S. Chang, B.H. Kim, K.S. Kim, D.E. Culley, S.B. Reed, M.F. Romine, D.A. Saffarini, E.A. Hill, L. Shi, D.A. Elias, D.W. Kennedy, G. Pinchuk, K. Watanabe, S.i. Ishii, B. Logan, K.H. Nealson & J.K. Fredrickson, 2006, Electrically conductive bacterial nanowires produced by *Shewanella oneidensis* strain MR-1 and other microorganisms, *Proceedings of the National Academy of Sciences*, **103**(30): 11358-11363, doi:10.1073/pnas.0604517103.
- Gouy, G., 1910, Sur la consitution de la charge électrique à la surface d'un électrolyte, *Journal de physique théorique et appliquée*, **4**(9): 457-468.
- Grahame, D.C., 1947, The electrical double layer and the theory of electrocapillarity, *Chemical Reviews*, **41**(3): 441-501.

- Greenhouse, J.P. & R.D. Harris, 1983, Migration of contaminants in groundwater at a landfill: A case study. 7. DC, VLF, and inductive resistivity surveys, *Journal of Hydrology*, **63**(1-2): 177-197.
- Guichet, X., 2002, Étude expérimentale des propriétés électriques des roches potentiels d'électrofiltration, suivi des mouvements de fluides en zones hydrothermales, Ph.D. Thesis, Université Paris 7, Paris, France, 199 p.
- Guichet, X., L. Jouniaux & J.-P. Pozzi, 2003, Streaming potential of a sand column in partial saturation conditions, *Journal of Geophysical Research*, **108**(B3): 1-12, doi:10.1029/2001JB001517.
- Guichet, X. & P. Zuddas, 2003, Effect of secondary minerals on electrokinetic phenomena during water-rock interaction, *Geophysical Research Letters*, **30**(13): 1-4, doi:10.1029/2003GL017480.
- Guichet, X., L. Jouniaux & N. Catel, 2006, Modification of streaming potential by precipitation of calcite in a sand-water system: laboratory measurements in the pH range from 4 to 12, *Geophysical Journal International*, **166**(1): 445-460, doi:10.1111/j.1365-246X.2006.02922.x.
- Hamilton, S.M., 1998, Electrochemical mass-transport in overburden: A new model to account for the formation of selective leach geochemical anomalies in glacial terrain, *Journal of Geochemical Exploration*, **63**(3): 155-172.
- , 2000, Spontaneous potentials and electrochemical cells, in *Geochemical Remote Sensing of the Subsurface*, edited by Hale, M., Elsevier International, Oxford, England, 81-119.
- Hamilton, S.M., E.M. Cameron, M.B. McClenaghan & G.E.M. Hall, 2004a, Redox, pH and SP variation over mineralization in thick glacial overburden. Part II: Field investigation at Cross Lake VMS property, *Geochemistry: Exploration, Environment, Analysis*, **4**(1): 45-58, doi:10.1144/1467-7873/03-021.
- , 2004b, Redox, pH and SP variation over mineralization in thick glacial overburden. Part I: Methodologies and field investigation at the Marsh Zone gold property, *Geochemistry: Exploration, Environment, Analysis*, **4**(1): 33-44, doi:10.1144/1467-7873/03-020.
- Hamilton, S.M. & K.H. Hattori, 2008, Spontaneous potential and redox responses over a forest ring, *Geophysics*, **73**(3): B67-B75, doi:10.1190/1.2890287.
- Hämmann, M., H.R. Maurer, A.G. Green & H. Horstmeyer, 1997, Self-potential image reconstruction: Capabilities and limitations, *Journal of Environmental & Engineering Geophysics*, **2**(1): 21-35.

- Hayashi, M., 2004, Temperature-electrical conductivity relation of water for environmental monitoring and geophysical data inversion, *Environmental Monitoring and Assessment*, **96**: 119-128.
- Hayley, K., 2007, Finite element modeling of electrical resistivity surveys, Department of Geoscience, University of Calgary, 18 p.
- Heinson, G., A. White, D. Robinson & N. Fathianpour, 2005, Marine self-potential gradient exploration of the continental margin, *Geophysics*, **70**(5): G109-G118, doi:10.1190/1.2057981.
- Heister, K., P.J. Kleingeld, T.J.S. Keijzer & J.P.G. Loch, 2005, A new laboratory set-up for measurements of electrical, hydraulic, and osmotic fluxes in clays, *Engineering Geology*, **77**(3-4): 295-303, doi:10.1016/j.enggeo.2004.07.020.
- Helmholtz, H., 1879, Studien über electrische Grenzschichten, *Annalen der Physik und Chemie*, **237**(7): 337-382.
- Hess, F.C., 1984, Chemistry Made Simple, Revised edition, Doubleday, New York, NY, U.S.A., 203 p.
- Hillel, D., 1998, Environmental Soil Physics, Academic Press, San Diego, CA, U.S.A., 771 p.
- Hirschmann, G., 1993, Seismischer Reflektor SE 1 erbohrt- und was folgt darunter?, *Kolloquium des DFG-Schwerpunktprogramms*, 63-64.
- Hostettler, J.D., 1984, Electrode electrons, aqueous electrons, and redox potentials in natural waters, *American Journal of Science*, **284**(6): 734-759.
- Ishido, T. & H. Mizutani, 1981, Experimental and theoretical basis of electrokinetic phenomena in rock-water systems and its applications to geophysics, *Journal of Geophysical Research*, **86**(B3): 1763-1775, doi:10.1029/JB086iB03p01763.
- Ishido, T., H. Mizutani & K. Baba, 1983, Streaming potential observations, using geothermal wells and in situ electrokinetic coupling coefficients under high temperature, *Tectonophysics*, **91**(1-2): 89-104.
- Ishido, T. & J.W. Pritchett, 1999, Numerical simulation of electrokinetic potentials associated with subsurface fluid flow, *Journal of Geophysical Research*, **104**(B7): 15 247-15 259, doi:10.1029/1999JB900093.
- Jackson, D.B. & J. Kauahikaua, 1987, Regional self-potential anomalies at Kilauea volcano, in *Volcanism in Hawaii*, edited by Decker, R.W., T.L. Wright & P.H.

- 
- Stauffer, U.S. Geological Survey, Professional Paper 1350, Washington, DC, U.S.A., 947-959.
- Jardani, A., J.P. Dupont & A. Revil, 2006, Self-potential signals associated with preferential groundwater flow pathways in sinkholes, *Journal of Geophysical Research*, **111**(B9204): 1-13, doi:10.1029/2005JB004231.
- Jardani, A., A. Revil, A. Bolève & J.P. Dupont, 2008, Three-dimensional inversion of self-potential data used to constrain the pattern of groundwater flow in geothermal fields, *Journal of Geophysical Research*, **113**(B09204): 1-22, doi:10.1029/2007jb005302.
- Jiang, Y.G., F.K. Shan, H.M. Jin, L.W. Zhou & P. Sheng, 1998, A method for measuring electrokinetic coefficients of porous media and its potential application in hydrocarbon exploration, *Geophysical Research Letters*, **25**(10): 1581-1584, doi:10.1029/98GL01102.
- Jouniaux, L. & J.-P. Pozzi, 1995a, Permeability dependence of streaming potential in rocks for various fluid conductivities, *Geophysical Research Letters*, **22**(4): 485-488, doi:10.1029/94GL03307.
- , 1995b, Streaming potential and permeability of saturated sandstones under triaxial stress: Consequences for electrotelluric anomalies prior to earthquakes, *Journal of Geophysical Research*, **100**(B6): 10 197-10 209, doi:10.1029/95JB00069.
- Jouniaux, L., M.L. Bernard, J.P. Pozzi & M. Zamora, 2000a, Electrokinetic in rocks: Laboratory measurements in sandstone and volcanic samples, *Physics and Chemistry of the Earth. Part A: Solid Earth and Geodesy*, **25**(4): 329-332.
- Jouniaux, L., M.L. Bernard, M. Zamora & J.-P. Pozzi, 2000b, Streaming potential in volcanic rocks from Mount Pelée, *Journal of Geophysical Research*, **105**(B4): 8391-8401, doi:10.1029/1999JB900435.
- Kassel, A., S. Faber & G.-P. Merkler, 1989, Laboratory studies on the characteristics of electrodes used for streaming-potential measurements, *in* Detection of subsurface flow phenomena, edited by Merkler, G.-P., H. Militzer, H. Hötzl, H. Armbruster & J. Brauns, Springer-Verlag, Berlin, Germany, 157-170.
- Keller, G.V. & F.C. Frischknecht, 1966, Electrical Methods in Geophysical Prospecting, Pergamon Press Inc., Oxford, England, 517 p.
- Kilty, K.T., 1984, On the origin and interpretation of self-potential anomalies, *Geophysical Prospecting*, **32**(1): 51-62.

- Kirkup, L. & B. Frenkel, 2006, *An Introduction to Uncertainty in Measurement*, Cambridge University Press, Cambridge, England, 233 p.
- Kirsch, R., 2009, Petrophysical properties of permeable and lowpermeable rocks, *in* *Groundwater Geophysics. A Tool for Hydrogeology*, edited by Kirsch, R., Springer-Verlag, Berlin, Germany, 1-22.
- Krauskopf, K.B. & D.K. Bird, 1995, *Introduction to Geochemistry*, 3<sup>rd</sup> edition, McGraw-Hill, Inc., New York, NY, U.S.A., 647 p.
- Kulesa, B., B. Hubbard & G.H. Brown, 2003, Cross-coupled flow modeling of coincident streaming and electrochemical potentials and application to subglacial self-potential data, *Journal of Geophysical Research*, **108**(B8): 1-14, doi:10.1029/2001JB001167.
- Lee, J.-Y., J.-Y. Cheon, K.-K. Lee, S.-Y. Lee & M.-H. Lee, 2001, Factors affecting the distribution of hydrocarbon contaminants and hydrogeochemical parameters in a shallow sand aquifer, *Journal of Contaminant Hydrology*, **50**(1-2): 139-158, doi:10.1016/S0169-7722(01)00101-2.
- Levine, S., J.R. Marriott, G. Neale & N. Epstein, 1975, Theory of electrokinetic flow in fine cylindrical capillaries at high zeta-potentials, *Journal of Colloid and Interface Science*, **52**(1): 136-149.
- Li, S.X., D.B. Pengra & P.Z. Wong, 1995, Onsager's reciprocal relation and the hydraulic permeability of porous media, *Physical Review E*, **51**(6): 5748-5751.
- Li, Y.-H. & S. Gregory, 1974, Diffusion of ions in sea water and in deep-sea sediments, *Geochimica et Cosmochimica Acta*, **38**(5): 703-714, doi:10.1016/0016-7037(74)90145-8.
- Lile, O.B., 1994, A contribution to the theory of self-potential anomalies over electronic conductors, *SEG Annual Meeting Technical Program Expanded Abstracts*, Los Angeles, CA, U.S.A., 374-376.
- , 1996, Self potential anomaly over a sulphide conductor tested for use as a current source, *Journal of Applied Geophysics*, **36**(2-3): 97-104.
- Lindberg, R.D. & D.D. Runnells, 1984, Ground water redox reactions: An analysis of equilibrium state applied to Eh measurements and geochemical modeling, *Science*, **225**(4665): 925-927.
- Linde, N., D. Jougnot, A. Revil, S.K. Matthaei, T. Arora, D. Renard & C. Doussan, 2007, Streaming current generation in two-phase flow conditions, *Geophysical Research Letters*, **34**(L3306): 1-5, doi:10.1029/2006GL028878.

- 
- Linde, N. & A. Revil, 2007, Inverting self-potential data for redox potentials of contaminant plumes, *Geophysical Research Letters*, **34**(L14302): 1-5, doi:10.1029/2007GL030084.
- Lindell, I.V., M.E. Ermutlu, K.I. Nikoskinen & E.H. Eloranta, 1993, Static image principle for anisotropic-conducting half-space problems: PEC and PMC boundaries, *Geophysics*, **59**(12): 1861-1864, doi:10.1190/1.1443401.
- Loke, M.H. & R.D. Barker, 1996, Rapid least-squares inversion of apparent resistivity pseudosections by a quasi-Newton method, *Geophysical Prospecting*, **44**(1): 131-152.
- Loke, M.H., 2004, *Tutorial: 2-D and 3-D electrical imaging surveys*, [cited 2006], Available from [www.geoelectrical.com](http://www.geoelectrical.com).
- Lorne, B., F. Perrier & J.-P. Avouac, 1999a, Streaming potential measurements 2. Relationship between electrical and hydraulic flow patterns from rock samples during deformation, *Journal of Geophysical Research*, **104**(B8): 17 879-17 896, doi:10.1029/1999JB900155.
- , 1999b, Streaming potential measurements 1. Properties of the electrical double layer from crushed rock samples, *Journal of Geophysical Research*, **104**(B8): 17 857-17 878, doi:10.1029/1999JB900156.
- Lovley, D.R., 2008a, Extracellular electron transfer: wires, capacitors, iron lungs, and more, *Geobiology*, **6**(3): 225-231, doi:10.1111/j.1472-4669.2008.00148.x.
- , 2008b, The microbe electric: conversion of organic matter to electricity, *Current Opinion in Biotechnology*, **19**(6): 564-571, doi:10.1016/j.copbio.2008.10.005.
- MacFarlane, D.S., J.A. Cherry, R.W. Gillham & E.A. Sudicky, 1983, Migration of contaminants in groundwater at a landfill: A case study. 1. Groundwater flow and plume delineation, *Journal of Hydrology*, **63**(1-2): 1-29.
- Maineult, A., 2004, Application de la méthode du potentiel spontané à l'hydrogéologie: expérimentation sur modèle réduit d'aquifère, Ph.D. Thesis, Université Louis Pasteur, Strasbourg, France, 208 p.
- Maineult, A., L. Jouniaux & Y. Bernabé, 2006, Influence of the mineralogical composition on the self-potential response to advection of KCl concentration fronts through sand, *Geophysical Research Letters*, **33**(L24311): 1-5, doi:10.1029/2006GL028048.

- Marino, S., M. Shapiro & P.M. Adler, 2001, Coupled transports in heterogeneous media, *Journal of Colloid and Interface Science*, **243**: 391-419.
- Marshall, D.J. & T.R. Madden, 1959, Induced polarization, a study of its causes, *Geophysics*, **24**(4): 790-816, doi:10.1190/1.1438659.
- Marshall, T.J., J.W. Holmes & C.W. Rose, 1996, Soil Physics, 3<sup>rd</sup> edition, Cambridge University Press, New York, NY, U.S.A., 453 p.
- Matrix Solutions Inc., 2006, 2005 Soil and groundwater assessment report. \*\*\*\*\* gas plant, report #: 3714-502 R0606, Calgary, AB, Canada, 21 p.
- Mayer, K.U., 1999, A Numerical Model for Multicomponent Reactive Transport in Variably Saturated Porous Media, Ph.D. Thesis, University of Waterloo, Waterloo, ON, Canada, 286 p.
- Mayer, K.U., E.O. Frind & D.W. Blowes, 2002, Multicomponent reactive transport modeling in variably saturated porous media using a generalized formulation for kinetically controlled reactions, *Water Resources Research*, **38**(9): 1174, doi:10.1029/2001wr000862.
- Mazáč, O., L. Beneš, I. Landa & A. Mašková, 1990, Determination of the Extents of Oil Contamination in Groundwater by Geoelectrical Methods, *in* Geotechnical and Environmental Geophysics. Volume II: Environmental and Groundwater, edited by Ward, S.H., Society of Exploration Geophysicists, Tulsa, OK, U.S.A., 107-112.
- Meiser, P., 1962, A method for quantitative interpretation of self potential anomalies, *Geophysical Prospecting*, **10**: 201-218.
- Mendoça, C.A., 2008, Forward and inverse self-potential modeling in mineral exploration, *Geophysics*, **73**(1): F33-F43.
- Minsley, B.J., 2007, Modeling and inversion of self-potential data, Ph.D. Thesis, Massachusetts Institute of Technology, Cambridge, MA, U.S.A., 251 p.
- Minsley, B.J., J. Sogade & F.D. Morgan, 2007a, Three-dimensional self-potential inversion for subsurface DNAPL contaminant detection at the Savannah River Site, South Carolina, *Water Resources Research*, **43**(W04429): 1-14, doi:10.1029/2005WR003996.
- , 2007b, Three-dimensional source inversion of self-potential data, *Journal of Geophysical Research*, **112**(B2202): 1-13, doi:10.1029/2006JB004262.

- Mitchell, J.K., 1991, Conduction phenomena: from theory to geotechnical practice, *Géotechnique*, **41**(3): 297-340.
- Moreau, F., D. Gibert, M. Holschneider & G. Saracco, 1999, Identification of sources of potential fields with the continuous wavelet transform: Basic theory, *Journal of Geophysical Research*, **104**(B3): 5003-5013, doi:10.1029/1998JB900106.
- Morgan, F.D., 1989, Fundamentals of streaming potentials in geophysics: Laboratory methods, in *Detection of subsurface flow phenomena*, edited by Merkle, G.-P., H. Militzer, H. Hötzl, H. Armbruster & J. Brauns, Springer-Verlag, Berlin, Germany, 133-144.
- Morgan, F.D., E.R. Williams & T.R. Madden, 1989, Streaming potential properties of Westerly Granite with applications, *Journal of Geophysical Research*, **94**(B9): 12 449-12 461, doi:10.1029/JB094iB09p12449.
- Nash, M.S., E. Atekwana & W.A. Sauck, 1997, Geophysical investigation of anomalous conductivity at a hydrocarbon contaminated site, *Proceedings of the Symposium on the Application of Geophysics to Engineering and Environmental Problems*, 675-683.
- National Instruments, 2007, NI USB-621X Specifications, Austin, TX, U.S.A., 16 p.
- Naudet, V., A. Revil, J.Y. Bottero & P. Bégassat, 2003, Relationship between self-potential (SP) signals and redox conditions in contaminated groundwater, *Geophysical Research Letters*, **30**(21): 1-4, doi:10.1029/2003GL018096.
- Naudet, V., 2004, Les méthodes de résistivité électrique et de potentiel spontané appliquées aux sites contaminés, Ph.D. Thesis, Université Paul Cézanne, Aix-en-Provence, France, 203 p.
- Naudet, V., A. Revil, E. Rizzo, J.Y. Bottero & P. Bégassat, 2004, Groundwater redox conditions and conductivity in a contaminant plume from geoelectrical investigations, *Hydrology and Earth System Sciences*, **8**(1): 8-22.
- Naudet, V. & A. Revil, 2005, A sandbox experiment to investigate bacteria-mediated redox processes on self-potential signals, *Geophysical Research Letters*, **32**(L112405): 1-4, doi:10.1029/2005GL022735.
- Naumov, G.B., B.N. Ryzhenko & I.L. Khodakovsky, 1974, Handbook of Thermodynamic Data, report #: USGS-WRD-74-001, U.S. Geological Survey, U.S.A., 328 p.
- Neidhardt, F.C., J.L. Ingraham & M. Schaechter, 1990, *Physiology of the Bacterial Cell*, Sinauer Associates, Inc., Sunderland, MA, U.S.A., 506 p.

- Nevin, K.P., H. Richter, S.F. Covalla, J.P. Johnson, T.L. Woodard, A.L. Orloff, H. Jia, M. Zhang & D.R. Lovley, 2008, Power output and columbic efficiencies from biofilms of *Geobacter sulfurreducens* comparable to mixed community microbial fuel cells, *Environmental Microbiology*, **10**(10): 2505-2514.
- Nigrini, A., 1970, Diffusion in rock alteration systems: I. Prediction of limiting equivalent conductances at elevated temperatures, *American Journal of Science*, **269**: 65-91.
- Nourbehecht, B., 1963, Irreversible thermodynamic effects in inhomogeneous media and their application in certain geoelectric problems, Ph.D. Thesis, Massachusetts Institute of Technology, Cambridge, MA, U.S.A., 121 p.
- Ntarlagiannis, D., E.A. Atekwana, E.A. Hill & Y. Gorby, 2007, Microbial nanowires: is the subsurface "hardwired"?, *Geophysical Research Letters*, **34**(L17305): 1-5, doi:10.1029/2007GL030426.
- Nyquist, J.E. & C.E. Corry, 2002, Self-potential: The ugly duckling of environmental geophysics, *The Leading Edge*, **21**(5): 446-451, doi:10.1190/1.1481251.
- Ogilvy, A.A., M.A. Ayed & V.A. Bogolovsky, 1969, Geophysical studies of water leakages from reservoirs, *Geophysical Prospecting*, **17**(1): 36-62.
- Ogilvy, A.A., E.J. Ostrovskij & E.N. Ruderman, 1989, Electrical surveys using the method of the natural electrical field; New investigations, in *Detection of subsurface flow phenomena*, edited by Merkler, G.-P., H. Militzer, H. Hötzl, H. Armbruster & J. Brauns, Springer-Verlag, Berlin, Germany, 401-462.
- Olsen, H.W., 1972, Liquid movement through kaolinite under hydraulic, electric, and osmotic gradients, *American Association of Petroleum Geologists Bulletin*, **56**(10): 2022-2028, doi:10.1306/819A41AA-16C5-11D7-8645000102C1865D.
- Onsager, L., 1931, Reciprocal relations in irreversible processes. I, *Physical Review*, **37**: 405-426.
- Parasnis, D.S., 1970, Some recent geoelectrical measurements in the Swedish sulphide ore fields illustrating scope and limitations of the methods concerned, in *Mining and Groundwater Geophysics*, edited by Morley, L.W., Geological Survey of Canada, Economic Geology Report no. 26, Ottawa, ON, Canada, 290-301.
- , 1986, *Principles of Applied Geophysics*, 4<sup>th</sup> edition, Chapman and Hall, New York, NY, U.S.A., 402 p.
- Parks, G.A., 1990, Surface energy and adsorption at mineral/water interfaces: An introduction, in *Mineral-water interface geochemistry*, edited by Hochella, M.F.,

- 
- Jr. & A.F. White, Mineralogical Society of America, Washington, DC, U.S.A., 133-175.
- Patella, D., 1997a, Self-potential global tomography including topographic effects, *Geophysical Prospecting*, **45**(5): 843-863.
- , 1997b, Introduction to ground surface self-potential tomography, *Geophysical Prospecting*, **45**(4): 653-681.
- Pengra, D.B., S.X. Li & P.-Z. Wong, 1999, Determination of rock properties by low-frequency AC electrokinetics, *Journal of Geophysical Research*, **104**(B12): 29 485-29 508, doi:10.1029/1999JB900277.
- Perrier, F. & P. Morat, 2000, Characterization of electrical daily variations induced by capillary flow in the non-saturated zone, *Pure and Applied Geophysics*, **157**(5): 785-810.
- Perry, J.W., 1997, Applications of spontaneous polarization in the detection and delineation of hydrocarbon spills from underground storage tanks, M.Sc. Thesis, University of New Hampshire, Durham, NH, U.S.A., 59 p.
- Petiau, G. & A. Dupis, 1980, Noise, temperature coefficient, and long time stability of electrodes for telluric observations, *Geophysical Prospecting*, **28**(5): 792-804.
- Petrowsky, A., 1928, The problem of a hidden polarized sphere, *Philosophical Magazine and Journal of Science*, **5**: 334-353, 914-927, 927-933.
- Pirson, S.J., 1981, Significant Advances in Magnetotelluric Exploration, in *Unconventional methods in exploration for petroleum and natural gas II*, edited by Gottlieb, B.M., Southern Methodist University Press, Dallas, TX, U.S.A., 169-196.
- Poldini, E., 1938, Geophysical Exploration by Spontaneous Polarization Methods, *Mining Magazine*, **59**: 278-282, 347-352.
- , 1939, Geophysical Exploration by Spontaneous Polarization Methods, *Mining Magazine*, **60**: 22-27, 90-94.
- Pozrikidis, C., 2005, Introduction to Finite and Spectral Methods using MATLAB, Chapman & Hall/CRC, Boca Raton, FL, U.S.A., 653 p.
- Prescott, L.M., J.P. Harley & D.A. Klein, 2005, Microbiology, 6th edition, McGraw-Hill, New York, NY, U.S.A., 992 p.

- Quincke, G., 1861, Über die Fortführung materieller Theilchen durch strömende Elektrizität, *Annalen der Physik und Chemie*, **189**(8): 513-598.
- Rabaey, K., J. Rodríguez, L.L. Blackall, J. Keller, P. Gross, D. Batstone, W. Verstraete & K.H. Neelson, 2007, Microbial ecology meets electrochemistry: electricity-driven and driving communities, *ISME Journal: Multidisciplinary Journal of Microbial Ecology*, **1**(1): 9-18, doi:10.1038/ismej.2007.4.
- Rao, R.L.N., S. Sethuram, S. Ram, B.N. Rao & K.L. Tiku, 2000, Geophysical signatures of a fracture controlled U-mineralisation: A case study from Mulapalle area, Cuddapah District, Andhra Pradesh, *Journal of the Geological Society of India*, **55**(4): 421-429.
- Regberg, A., K. Singha, M. Tien, F. Picardal, Q. Zheng, E. Roden & S.L. Brantley, 2011, Electrical conductivity as a measure of iron reduction rates in abiotic and biological systems, *in preparation*.
- Reguera, G., K.D. McCarthy, T. Mehta, J.S. Nicoll, M.T. Tuominen & D.R. Lovley, 2005, Extracellular electron transfer via microbial nanowires, *Nature*, **435**(7045): 1098-1101, doi:10.1038/nature03661.
- Reppert, P.M. & F.D. Morgan, 2001, Streaming potential collection and data processing techniques, *Journal of Colloid and Interface Science*, **233**: 348-355.
- Reppert, P.M., F.D. Morgan, D.P. Lesmes & L. Jouniaux, 2001, Frequency-dependent streaming potentials, *Journal of Colloid and Interface Science*, **234**: 194-203.
- Reppert, P.M. & F.D. Morgan, 2003, Temperature-dependent streaming potentials: 2. Laboratory, *Journal of Geophysical Research*, **108**(B11): 1-13, doi:10.1029/2002JB001755.
- Revil, A. & P.W.J. Glover, 1998, Nature of surface electrical conductivity in natural sands, sandstones, and clays, *Geophysical Research Letters*, **25**(5): 691-694, doi:10.1029/98GL00296.
- Revil, A., H. Schaefer, L.M. Cathles III & P.D. Manhardt, 1999, Streaming potential in porous media. 2. Theory and application to geothermal systems, *Journal of Geophysical Research*, **104**(B9): 20 033-20 048.
- Revil, A., L. Ehouarne & E. Thyreault, 2001, Tomography of self-potential anomalies of electrochemical nature, *Geophysical Research Letters*, **28**(23): 4363-4366, doi:10.1029/2001GL013631.

- Revil, A., D. Hermitte, E. Spangenberg & J.J. Cochemé, 2002a, Electrical properties of zeolitized volcanoclastic materials, *Journal of Geophysical Research*, **107**(B8): 1-17, doi:10.1029/2001JB000599.
- Revil, A., D. Hermitte, M. Voltz, R. Moussa, J.G. Lacas, G. Bourrié & F. Trolard, 2002b, Self-potential signals associated with variations of the hydraulic head during an infiltration experiment, *Geophysical Research Letters*, **29**(7): 1-4, doi:10.1029/2001GL014294.
- Revil, A., V. Naudet, J. Nouzaret & M. Pessel, 2003, Principles of electrography applied to self-potential electrokinetic sources and hydrogeological applications, *Water Resources Research*, **39**(5): 1-13, doi:10.1029/2001WR000916.
- Revil, A. & A. Cerepi, 2004, Streaming potentials in two-phase flow conditions, *Geophysical Research Letters*, **31**(L11605): 1-4, doi:10.1029/2004GL020140.
- Revil, A., V. Naudet & J.D. Meunier, 2004, The hydroelectric problem of porous rocks: inversion of the position of the water table from self-potential data, *Geophysical Journal International*, **159**(2): 435-444, doi:10.1111/j.1365-246X.2004.02422.x.
- Revil, A., L. Cary, Q. Fan, A. Finizola & F. Trolard, 2005a, Self-potential signals associated with preferential ground water flow pathways in a buried paleo-channel, *Geophysical Research Letters*, **32**(L07401): 1-4, doi:10.1029/2004GL022124.
- Revil, A., P. Leroy & K. Titov, 2005b, Characterization of transport properties of argillaceous sediments: Application to the Callovo-Oxfordian argillite, *Journal of Geophysical Research*, **110**(B6202): 1-18, doi:10.1029/2004JB003442.
- Revil, A., F. Trolard, G. Bourrié, J. Castermant, A. Jardani & C.A. Mendonça, 2009, Ionic contribution to the self-potential signals associated with a redox front, *Journal of Contaminant Hydrology*, **109**: 27-39, doi:10.1016/j.jconhyd.2009.07.008.
- Revil, A., C.A. Mendonça, E.A. Atekwana, B. Kulesa, S.S. Hubbard & K.J. Bohlen, 2010, Understanding biogeobatteries: Where geophysics meets microbiology, *Journal of Geophysical Research*, **115**(G00G02): 1-22, doi:10.1029/2009jg001065.
- Rice, C.L. & R. Whitehead, 1965, Electrokinetic flow in a narrow cylindrical capillary, *Journal of Physical Chemistry*, **69**(11): 4017-4024.
- Rizzo, E., B. Suski, A. Revil, S. Straface & S. Troisi, 2004, Self-potential signals associated with pumping tests experiments, *Journal of Geophysical Research*, **109**(B10203): 1-14, doi:10.1029/2004JB003049.

- Rücker, C., T. Günther & K. Spitzer, 2006, Three-dimensional modelling and inversion of dc resistivity data incorporating topography - I. Modelling, *Geophysical Journal International*, **166**(2): 495-505, doi:10.1111/j.1365-246X.2006.03010.x.
- Sailhac, P. & G. Marquis, 2001, Analytic potentials for the forward and inverse modeling of SP anomalies caused by subsurface fluid flow, *Geophysical Research Letters*, **28**(9): 1851-1854, doi:10.1029/2000GL012457.
- Sato, M. & H.M. Mooney, 1960, The electrochemical mechanism of sulfide self-potentials, *Geophysics*, **25**(1): 226-249.
- Schlumberger, C. & M. Schlumberger, 1922, Phénomènes électriques produits par les gisements métalliques, *Comptes rendus hebdomadaires des séances de l'Académie des sciences*, **174**: 477-480.
- Schriever, W. & C.E. Bleil, 1957, Streaming potential in spherical-grain sands, *Journal of the Electrochemical Society*, **104**(3): 170-176.
- Sears, A.R. & J.N. Groves, 1978, The use of oscillating laminar flow streaming potential measurements to determine the zeta potential of a capillary surface, *Journal of Colloid and Interface Science*, **65**(3): 479-482.
- Seese, W.S. & G.H. Daub, 1981, Basic Chemistry, 3<sup>rd</sup> edition, Prentice-Hall, Inc., Englewood Cliffs, NJ, U.S.A., 596 p.
- Shaw, W.J.D., 2008, Professor, Dept. of Mechanical and Manufacturing Engineering, University of Calgary, Information about cathodic pipeline protection systems and anode beds.
- Sheffer, M.R., 2005, Laboratory testing of the streaming potential phenomenon in soils for application to embankment dam seepage investigations, report #: T992700-0205B/2, CEA Technologies Inc., Montréal, QC, Canada.
- , 2007, Forward modelling and inversion of streaming potential for the interpretation of hydraulic conditions from self-potential data, Ph.D. Thesis, University of British Columbia, Vancouver, BC, Canada, 207 p.
- Sheffer, M.R. & D.W. Oldenburg, 2007, Three-dimensional modelling of streaming potential, *Geophysical Journal International*, **169**(3): 839-848, doi:10.1111/j.1365-246X.2007.03397.x.
- Shen, L. & Z. Chen, 2007, Critical review of the impact of tortuosity on diffusion, *Chemical Engineering Science*, **62**(14): 3748-3755, doi:10.1016/j.ces.2007.03.041.

- Shi, W., 1998, Advanced modeling and inversion techniques for three-dimensional geoelectrical surveys, Ph.D. Thesis, Massachusetts Institute of Technology, Cambridge, MA, U.S.A., 210 p.
- Si, H., 2003, *A Quality Tetrahedral Mesh Generator and a 3D Delaunay Triangulator*, [cited 2008], Available from <http://tetgen.berlios.de/>.
- Sill, W.R., 1982, Diffusion coupled (electrochemical) self-potential effects in geothermal areas, report #: DOE/ID/12079-73, United States Department of Energy, U.S.A., 21 p.
- , 1983, Self-potential modeling from primary flows, *Geophysics*, **48**(1): 76-86.
- Sivenas, P. & F.W. Beales, 1982, Natural geobatteries associated with sulphide ore deposits, I. Theoretical studies, *Journal of Geochemical Exploration*, **17**(2): 123-143.
- Skianis, G.A. & M.C. Hernández, 1999, Effects of transverse electric anisotropy on self-potential anomalies, *Journal of Applied Geophysics*, **41**(1): 93-104.
- Slater, L., D. Ntarlagiannis, N. Yee, M. O'Brien, C. Zhang & K.H. Williams, 2008, Electrode voltages in the presence of dissolved sulfide: Implications for monitoring natural microbial activity, *Geophysics*, **73**(2): F65-F70, doi:10.1190/1.2828977.
- Smith, D., 2007, Technician at Fluke, Communication about filtering method used for 60 Hz filter.
- Smoluchowski, M., 1903, Contribution à la théorie de l'endosmose électrique et de quelques phénomènes corrélatifs, *Bulletin international de l'acadmie des sciences de Cracovie*, **1**(Janvier): 182-199.
- Sogade, J.A., F. Scira-Scappuzzo, Y. Vichabian, W. Shi, W. Rodi, D.P. Lesmes & F.D. Morgan, 2006, Induced-polarization detection and mapping of contaminant plumes, *Geophysics*, **71**(3): B75-B84, doi:10.1190/1.2196873.
- Somasundaran, P. & R.D. Kulkarni, 1973, A new streaming potential apparatus and study of temperature effects using it, *Journal of Colloid and Interface Science*, **45**(3): 591-600.
- Sposito, G., 1990, Molecular models of iron adsorption on mineral surfaces, in *Mineral-water interface geochemistry*, edited by Hochella, M.F., Jr. & A.F. White, Mineralogical Society of America, Washington, DC, U.S.A., 261-279.

- Sprunt, E.S., T.B. Mercer & N.F. Djabbarah, 1994, Streaming potential from multiphase flow, *Geophysics*, **59**(5): 707-711, doi:10.1190/1.1443628.
- Stefánsson, A., S. Arnórsson & Á.E. Sveinbjörnsdóttir, 2005, Redox reactions and potentials in natural waters at disequilibrium, *Chemical Geology*, **221**(3-4): 289-311, doi:10.1016/j.chemgeo.2005.06.003.
- Stern, O., 1924, Zür Theorie der elektrolitschen Doppelschicht, *Zeitschrift für Elektrochemie*, **30**: 508-516.
- Stern, W., 1945, Relation between spontaneous polarization curves and depth, size and dip of ore bodies, *Transactions of the American Institute of Mining and Metallurgical Engineers*, **164**: 189-196.
- Stoll, J., J. Bigalke & E.W. Grabner, 1995, Electrochemical modelling of self-potential anomalies, *Surveys in Geophysics*, **16**(1): 107-120.
- Stumm, W. & J.J. Morgan, 1996, Aquatic Chemistry. Chemical equilibria and rates in natural waters., 3<sup>rd</sup> edition, John Wiley & Sons, Inc., New York, NY, U.S.A., 1022 p.
- Sundararajan, N. & Y. Srinivas, 1996, A modified Hilbert transform and its application to self potential interpretation, *Journal of Applied Geophysics*, **36**(2-3): 137-143.
- Suski, B., A. Revil, K. Titov, P. Konosavsky, M. Voltz, C. Dagès & O. Huttel, 2006, Monitoring of an infiltration experiment using the self-potential method, *Water Resources Research*, **42**(W08418): 1-11.
- Swan, A.R.H. & M. Sandilands, 1995, Introduction to Geological Data Analysis, Blackwell Science Ltd., Osney Mead, Oxford, England, 446 p.
- Sy, A. & R.G. Campanella, 1992, Dynamic measurements of the Becker penetration test with implications for pile driving analysis, *Proceedings of the fourth international Conference on the Application of Stress-Wave Theory to Piles*, The Hague, Netherlands, 471-478.
- Telford, W.M., L.P. Geldart & R.E. Sheriff, 1990, Applied Geophysics, 2<sup>nd</sup> edition, Cambridge University Press, U.S.A., 770 p.
- Thornber, M.R., 1975a, Supergene alteration of sulphides, II. A chemical study of the Kambalda nickel deposits, *Chemical Geology*, **15**(2): 117-144.
- , 1975b, Supergene alteration of sulphides, I. A chemical model based on massive nickel sulphide deposits at Kambalda, Western Australia, *Chemical Geology*, **15**(1): 1-14.

- Timm, F. & P. Möller, 2001, The relation between electric and redox potential: evidence from laboratory and field measurements, *Journal of Geochemical Exploration*, **72**(2): 115-128.
- Titov, K., V. Loukhmanov & A. Potapov, 2000, Monitoring of water seepage from a reservoir using resistivity and self polarization methods: case history of the Petergoph fountain water supply system, *First Break*, **18**(10): 431-435.
- Titov, K., Y. Ilyin, P. Konosavski & A. Levitski, 2002, Electrokinetic spontaneous polarization in porous media: petrophysics and numerical modelling, *Journal of Hydrology*, **267**(3-4): 207216.
- Tompkins, R., 1990, Direct location technologies: a unified theory, *Oil & Gas Journal*, **Sept. 24**: 126-134.
- Torres, C.I., A.K. Marcus, P. Parameswaran & B.E. Rittmann, 2008, Kinetic experiments for evaluating the Nernst-Monod model for anode-respiring bacteria (ARB) in a biofilm anode, *Environmental Science & Technology*, **42**(17): 6593-6597, doi:10.1021/es800970w.
- UBC - Geophysical Inversion Facility, 2005, Three Dimensional Modelling of Self-Potentials Caused by Seepage flow. Manual for the software package SP3D., University of British Columbia, Vancouver, BC, Canada, 20 p.
- van Genuchten, M.T., 1980, A Closed-form Equation for Predicting the Hydraulic Conductivity of Unsaturated Soils, *Soil Science Society of America Journal*, **44**: 892-898.
- Vanhala, H., 1997, Mapping oil-contaminated sand and till with the spectral induced polarization (SIP) method, *Geophysical Prospecting*, **45**(2): 303-326.
- Vichabian, Y. & F.D. Morgan, 1999, Self potential monitoring of jet fuel air sparging, *Proceedings of the Symposium on the Application of Geophysics to Engineering and Environmental Problems*, 549-553.
- Vichabian, Y., P.M. Reppert & F.D. Morgan, 1999, Self potential mapping of contaminants, *Proceedings of the Symposium on the Application of Geophysics to Engineering and Environmental Problems*, 657-662.
- Waterloo Hydrogeologic Inc., 2002, Visual MODFLOW User's Manual, Waterloo Hydrogeologic Inc., Waterloo, Ontario, Canada, 350 p.
- Waxman, M.H. & L.J.M. Smits, 1968, Electrical conductivities in oil-bearing shaly sands, *Society of Petroleum Engineers Journal*, **8**(2): 107-122.

- Weigel, M., 1989, Self-potential surveys on waste dumps: Theory and practice, *in* Detection of subsurface flow phenomena, edited by Merkle, G.-P., H. Militzer, H. Hötzl, H. Armbruster & J. Brauns, Springer-Verlag, Berlin, Germany, 109-120.
- Werkema, D.D., Jr., E.A. Atekwana, A.L. Endres, W.A. Sauck & D.P. Cassidy, 2003, Investigating the geoelectrical response of hydrocarbon contamination undergoing biodegradation, *Geophysical Research Letters*, **30**(12): 1-4, doi:10.1029/2003GL017346.
- Wildenschild, D., J.J. Roberts & E.D. Carlberg, 2000, On the relationship between microstructure and electrical and hydraulic properties of sand-clay mixtures, *Geophysical Research Letters*, **27**(19): 3085-3088.
- Williams, K.H., S.S. Hubbard & J.F. Banfield, 2007, Galvanic interpretation of self-potential signals associated with microbial sulfate-reduction, *Journal of Geophysical Research*, **112**(G03019): 1-8, doi:10.1029/2007JG000440.
- Wilt, M.J. & D.K. Butler, 1990, Numerical modeling of SP anomalies: Documentation of program SPPC and applications, report #: REMR-GT-6, Department of the army. US Army Corps of Engineers, U.S.A., 28 p.
- Wurmstich, B. & F.D. Morgan, 1994, Modeling of streaming potential responses caused by oil well pumping, *Geophysics*, **59**(1): 46-56, doi:10.1190/1.1443533.
- Yeung, A.T., 1990, Coupled flow equations for water, electricity and ionic contaminants through clayey soils under hydraulic, electrical and chemical gradients, *Journal of Non-Equilibrium Thermodynamics*, **15**(3): 247-267.
- Yüngül, S.H., 1950, Interpretation of spontaneous polarization anomalies caused by spheroidal ore bodies, *Geophysics*, **15**(2): 237-246, doi:10.1190/1.1437597.
- Zhang, C., D. Ntarlagiannis, L. Slater & R. Doherty, 2010, Monitoring microbial sulfate reduction in porous media using multipurpose electrodes, *Journal of Geophysical Research*, **115**(G00G09): 1-11, doi:10.1029/2009jg001157.
- Zhang, Y., T. Xu & Z. Liu, 2007, Streaming potential across a porous charged membrane in organic-aqueous solutions, *Desalination*, **212**(1-3): 183-190, doi:10.1016/j.desal.2006.10.009.
- Zienkiewicz, O.C. & R.L. Taylor, 2000, The Finite Element Method. Vol 1: The Basis, 5<sup>th</sup> edition, Butterworth-Heinemann, Oxford, Great Britain, 689 p.

ZoBell, C.E., 1946, Studies on redox potential of marine sediments, *Bulletin of the American Association of Petroleum Geologists*, **30**(4): 477-513, doi:10.1306/3D933808-16B1-11D7-8645000102C1865D.



### APPENDIX A: Streaming potential coupling coefficient measurements

Streaming potential coupling coefficient data of all samples. Each sample has three panels: LEFT: Data for the whole test. MIDDLE: Close up of data used to determine  $C$ . RIGHT: Cross-plot of  $\Delta V$  vs.  $\Delta P$  from the middle panel, used to calculate the ratio.

